Contamination-induced interfacial resistance in ohmic microswitch contacts

Submitted in partial fulfillment of the requirements for

the degree of

Doctor of Philosophy

in

Mechanical Engineering

Vitali Brand

B.S., Mechanical Engineering, Iowa State University
M.S., Materials Science and Engineering, Stanford University

Carnegie Mellon University
Pittsburgh, PA

August, 2014

ACKNOWLEDGMENTS

This work is dedicated to my fiancée Reyna Garcia. Her love and friendship helped me succeed in this journey. I am also very grateful to my family for their encouragement and support throughout my life.

I owe a depth of gratitude to Professor Ashraf Bastawros for inspiring my interest in micro- and nano-science and providing me with an opportunity to do research in that area during my college years. I am also thankful to Professor Reinhold Dauskardt and Professor Michael McGehee for overseeing my work on reliability of organic solar cells during my masters.

I am thankful and grateful to my Ph.D. advisor, Professor Maarten P. de Boer for providing me the opportunity to work on this project as well as for his excellent and effectively guidance. I would also like to thank him for serving as the chair of my thesis committee. I want to thank my other thesis committee members: Professor C. Fred Higgs, III, Professor Gianluca Piazza, and Professor Robert W. Carpick for their help and advice for my work. I would also like to thank Professor Paul Steif for fostering my interest in teaching while I was his teaching assistant.

I want to thank Chris Hertz for answering all of my questions about degree requirements over the years. I am thankful to Michael Scampone, Christine Lambrou, Melissa Hyzy, Ginny Barry and Bobbi kostyak for their help in processing my lab equipment purchases and conference reimbursements. I would like to thank Ed Wojcichowski, Jim Dillinger and John Fulmer for machining parts for my experimental setup.

I am thankful to Sandia National Labs for supporting this project. Specifically, Mike S. Baker for frequent consultations, Dr. Keith Ortiz for his supporting role in this project, and the

technical staff at the Microelectronics Development Laboratory for fabricating and packaging the parts used in this thesis.

I am also thankful to the General Electric Corporation for funding the parts I needed for building my experimental chamber and the National Science Foundation for partially supporting this work under Grant No. CMMI 1334572.

Finally, I would like to thank my lab mates Sidharth S. Hazra, Emrecan Soylemez, Mohamed Saleh, Ryan Pocratsky, Sameer Shroff, and Ramesh Shrestha for their help and friendship.

ABSTRACT

Ohmic nanoswitches have been recently regarded to complement transistors in applications where electrical current leakage is becoming a problem. Although the solid state metal oxide silicon field effect transistor (MOSFET) has fueled a global technology revolution, it is now reaching its performance limits because of device leakage. To avoid electric field-induced damage in MOSFETs, operating voltage and hence threshold voltage must be reduced as linewidth is reduced. However, below a limit, the current cannot be turned off. The ohmic switch approach solves this problem because an air gap that separates the electrical contacts provides excellent electrical isolation when the relay is open. Some applications require these relays to perform billions to trillions of cycles, yet typical devices that are exposed to ambient environment degrade electrically after just a few thousand cycles. A critical challenge here is that trace amounts of volatile hydrocarbons in air adsorb on the electrical contact surfaces for a large variety of coating materials, causing an insulating deposit to form that prevents signal transmission during switch closure. We address this challenge by exploring the interactions of hydrocarbon contaminants with contact materials and operating environment on device lifetime. Our materials of choice are Pt, a common contact material in switch applications due to its resistance to wear, and RuO_2, which is believed to be somewhat resistant to hydrocarbon adsorption. We test our devices in N_2 and O_2 background environments with controlled hydrocarbon contaminant concentrations. We illustrate that the insulating hydrocarbon deposit can be electrically broken down and its resistance lowered. We show how electrical contacts that have degraded electrically due to contamination can have their performance restored to the original level by actuating them in clean N_2-O_2 environment. It is then shown how this process creates a highly conductive carbonaceous deposit that protects the contact from wear. It is also

demonstrated that RuO_2 does not exhibit contaminant-induced degradation even at very high hydrocarbon presence, as long as O_2 is also present. These results show that even though the contaminant is ubiquitous in the environment, there are many ways to reduce its effect on ohmic switches.

TABLE OF CONTENTS

List of tables

List of figures

Chapter I: Introduction

1.1 MOTIVATION

Microelectromechanical Systems (MEMS) are becoming ubiquitous; they are used as accelerometers, gyroscopes, environmental sensors, microphones, optics, and chemical sensors. This is because they offer high performance at low cost. The different categories of MEMS are [1]:

Class I - Devices with no moving parts such as accelerometers.

Class II - Devices with moving parts but without rubbing or impacting surfaces such as gyroscopes and resonators.

Class III - Devices with moving parts and impacting surfaces such as relays or Texas Instruments′ Digital Mirror Device [2].

Class IV - Devices with moving parts as well as impacting and rubbing surfaces such as optical switches.

Almost all commercial MEMS are Class I and II. Once Class III devices such as ohmic switches become sufficiently reliable for widespread commercialization, they will be of great interest in a variety of applications that require high electrical isolation and low-power consumption. These include radio frequency communications [3-5] and power management (these switches can open much faster than circuit breakers, thereby avoiding downstream electrical damage) [6]. Low power digital computing is perhaps the most alluring application, especially as the evolution of solid state switches is approaching physical limits [7]. Ohmic switch digital logic has already been demonstrated on the microscale and it can be reduced to the nanoscale [7].

Scaling of the silicon metal-oxide-semiconductor field-effect transistor (MOSFET) has enabled an exponential increase in computing power over the past decades. However, this technology is quickly reaching its performance bounds. As MOSFET gate length shrinks below 100 nm, static power dissipation due to electrical leakage becomes considerable because of a high subthreshold voltage swing of ~ 70 mV/decade [8, 9]. When reducing MOSFET dimensions, the supply voltage should also be scaled. This maintains a constant electric field, which prevents device damage by hot electron effects [10]. To scale its current drive characteristic, the threshold voltage must also be decreased. This means that in MOSFETs the current cannot be turned off, but instead must be managed [11], with a tradeoff in increased static power. These limits establish a lowest practical supply voltage on the order of one volt, a value already used in current MOSFET technology [7, 12]. The static power dissipation has become equal to dynamic power consumption, which is proportional to the square of the supply voltage [13]. This highlights the need to find alternative switch technologies to continue increasing computing power.

Complementing MOSFETs with ohmic nanoswitches can address these challenges [7, 14-17]. When an ohmic switch is "open", an air gap physically separates the electrical contacts, preventing virtually all electrical leakage [18, 19]. Furthermore, piezoelectric ohmic nanoswitches can be closed with as little as 10^{-3} V with a subthreshold voltage swing of less than 1 mV/decade [18]. Such a nanoswitch can be actuated with as little as ~10^{-6} of the power needed to actuate a MOSFET and with zero static power dissipation. Not only does this approach circumvents the scalability problem faced by MOSFETs, but is also attractive for portable applications such as smart-phones where low-power switching can substantially improve battery

life. The reduced need for thermal management of these devices can also be useful in high performance computing.

The subject of this dissertation is the reliability of ohmic switches. The main challenge is in limiting the degradation of electrical contacts. Specifically, the electrical resistance of the contacts, R_c, can increase and hinder the devices ability to transmit signals. The issues that cause this are wear or contamination. The contact resistance consists of two components:

$$R_c = R_{c,intrinsic} + R_{c,interface} \ , \qquad (1.1)$$

where $R_{c,intrinsic}$ is the contribution from clean contact interactions and can capture effects of wear, while $R_{c,interface}$ is the contribution due to contaminant formation. The majority of work in ohmic switch reliability addresses $R_{c,intrinsic}$. **Little has been done to address $\boldsymbol{R_{c,interface}}$ and very little is known about it. The focus of this dissertation is on addressing the $\boldsymbol{R_{c,interface}}$ problem.**

The experimental work performed here is on microswitches, however the device degradation mechanisms addressed are relevant on all size scales, though they become more severe as dimensions shrink.

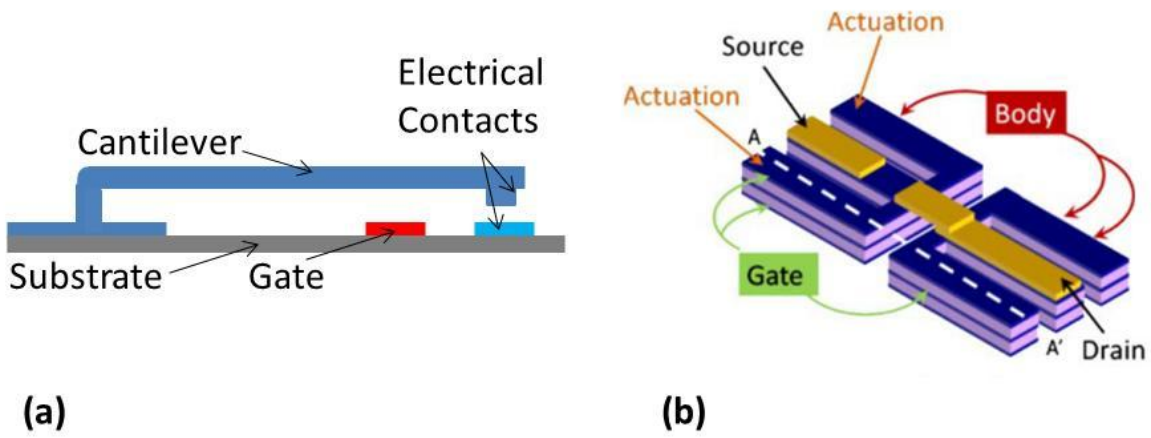

Figure 1.1: (a) Electro-static switch (b) Piezoelectric switch [19], © 2009 IEEE.

1.2 BACKGROUND

The most common and simplest ohmic switch is the electrostatically actuated cantilever beam design shown in Fig. 1.1a [20]. Applying voltage to the gate induces an electrostatic force that pulls the cantilever down, thereby closing the switch. This enables a signal to be passed through the electrical contacts. There are other variations of electrostatically actuated switches such as the significantly faster fixed-fixed beam switch [21]. The main drawback in the electrostatic switch design is the relatively high voltage required to operate it. The piezoelectric switch requires very low operating voltages and actuation time can also be in the ns realm. In this design, the piezo-electric effect induces actuation (Fig. 1.1b) [19]. The device used in this research is the thermally actuated switch shown in Fig. 2.1. This switch design is known for the high loads it can apply, though the feature most important to us is the ability to easily vary the contact material without altering other fabrication steps (as will be discussed in Chapter II).

Ohmic micro- and nano-switches need to withstand trillions of actuation cycles in the most demanding applications; however, such operational lifetimes have been difficult to achieve. Extensive [3, 22-31] and preliminary [17] investigations of micro- and nanoswitch reliability,

respectively, have been reported. Two types of technical challenges, both related to the interface that is formed when a switch closes, limit the reliability of these devices. The first challenge arises when the contact surfaces are clean as they may wear and/or adhere to each other [3, 22, 32-34]. Repeated closing and opening of the switch (cycling) may produce wear particles that interfere with switch closure, thereby increasing the electrical resistance of the contacts. Cycling also causes asperity flattening of the contacts. This increases the effective contact area, potentially leading to permanent contact adhesion. Generally, issues with clean contacts have been managed by using harder (wear resistant) contact materials such as the Pt group metals and/or by providing sufficient restoring force to the switch to reduce adhesion [35, 36].

While wear and adhesion have been widely studied in the literature [3, 22, 32-34], there is another critical problem for which there exists no fundamental understanding. That is, an organic deposit accumulates on the contacting surfaces under repetitive mechanical loading. This "tribopolymer" deposit ***(TP)*** increases contact resistance, in the term identified as $R_{c,interface}$. ***Gaining insight into experimental parameters that affect the nucleation, growth and behavior of the TP deposit is the subject of this work.***

A review of what is known about the origin of the TP deposit follows. Trace amounts of volatile hydrocarbons in air are known to adsorb on a large variety of surfaces [37, 38]. For example, a 20-40 Å layer adsorbs on Au despite its being chemically inert [24, 39]. The adsorbent is then transformed into a complex mixture of cross-linked high molecular weight deposits. It is hypothesized that catalytically active metals polymerize the adsorbent [27, 37, 40]. In applications where the contacts are rubbing against each other, a mechanical wiping action (associated with sliding contacts during switch closure) is assumed to move the polymer to a different location, thereby enabling new polymer to be formed at the original site. Upon

repeating this process many times, a considerable deposit is accumulated, and is thus called 'friction polymer' [37]. The polymerization mechanisms remain unknown, however [27, 41]. Note that the deposit formed in the experiments in this study is called "tribopolymer" as opposed to "friction polymer" because here devices experience normal loading and unloading as opposed to lateral loading.

The deposit will reduce problems associated with wear and adhesion, but will increase the switch electrical resistance as cycling continues [42]. As switch dimensions reduce to micrometers [5, 20] and nanometers [13, 21], devices become far more susceptible to contamination because the contact area decreases with the square of the dimension. Indeed, microswitch reliability investigations with *predominantly normal contact* (i.e. no rubbing) implicate hydrocarbons as the source of increasing resistance [24, 28, 42, 43]. In those studies the hydrocarbon source was from laboratory air [24, 28, 43] or from a vacuum pump [42] and was not introduced in a controlled fashion. The studies [37, 42, 44] indicate that an insulating film forms from hydrocarbon contamination, reducing the metal to metal contact area, thereby increasing the resistance. It is generally believed that if the resistance is finite, mechanical penetration of this film at some contacting asperities enables local transmission of current [37, 41, 42]. However, as will be shown in this dissertation, the deposit itself can become conducting.

The Pt group metals are known to be catalysts that are suspected to promote organic deposit accumulation [27], but some of these metals (Rh, Ru, Ir, Re) can be oxidized to form conducting oxides [45]. The catalytic properties of these oxides, in particular RuO_2 and Rh_2O_3 were believed to be deactivated [46]. Hinohora et al. found that the transition metal oxide Rh_2O_3, which has low resistivity (~50 μΩ•cm), effectively hindered hydrocarbon adsorption and

polymer formation [46]. Magnetically-actuated mm-scale relay contacts coated by this material were shown to operate without resistance degradation for up to 100 million cycles *in clean air,* after pre-exposure to benzine (a petroleum derivative) [46].

Even if the adsorbent is removed, surface contamination inevitably develops even in ultra-high vacuum conditions [29, 38]. Therefore, any material will have some surface contamination when exposed to atmosphere, and switch reliability needs to be considered in the context of this layer. Both the materials that make contact and the environment in which they operate can be varied. ***A central hypothesis of this work is that reliable switches can be made by formulating suitable combinations of materials and environment.*** In this research, we address the interplay between electrical resistance, materials and environment in the presence of a contaminant.

The tolerance to resistance increase depends on the switch application. In radio frequency applications, only a few Ω is acceptable [47], while in digital logic, several kΩ [7] can be managed.

For the purposes of this study, the microscale size of the switches is convenient for surface analysis of the contacts. Nanoswitches are also commonly produced by similar thin film deposition and etching techniques [21] and therefore have approximately the same surface roughness. While the forces and contact areas are quite different, in both micro- and nanoswitches the real contact areas are much smaller than the nominal contact areas. The local pressures are on the order of GPa and will be limited by material hardness [3]. The electrical current densities are also approximately the same in micro- and nano-switches [48] (see Appendix I). Therefore, the degradation mechanisms are likely to be similar.

The beginning of this thesis refers to the then unidentified carbonaceous contaminant deposit as TP, however, our later studies revealed it to be an amorphous carbon, so the later chapters refer to it as an amorphous carbon deposit. It is important to clarify that both TP deposit and amorphous carbon deposit refer to the same thing. The choice of the term used in each chapter is consistent with how it was presented in our published work.

1.3 RESEARCH OVERVIEW AND KEY RESULTS

There are few literature reports in which contaminants have been introduced in microswitches in a controlled way. In a recent microswitch study with Au and RuO_2 interface materials, a doubling of electrical resistance at *first switch closure* versus dodecane vapor pressure was seen at a partial pressure as low as 10^{-5} Torr [30]. It was also found that switch cycle lifetime was greater in a pure nitrogen environment than in vacuum.

To expand on the research reported in [30], we investigate in this thesis how the contaminant deposit accumulates with device cycling using different materials in both N_2 and N_2:O_2 backgrounds. We also investigate the effects of cold switching versus mechanical cycling (to be defined below). To accomplish this, we have developed a microswitch platform [31] and experimental test chamber [48] to explore the effect of cycling in clean and contaminated environments with different materials. **The experimental setup will be detailed in Chapter II.**

In Chapter III, we intentionally accelerate the contact contamination process by introducing a very high level of gaseous contaminant (up to 2,500 parts per million) into the test chamber, such that the degradation is readily observable within the timeframe of the experiment. We compare the resistance versus cycle count characteristic of Pt- and RuO_2-coated contacts, where the catalytically-deactivated materials (RuO_2) would be presumably less prone to contamination. The contaminant of choice is benzene (C_6H_6) because it is a known bad actor [37]. A key result is that RuO_2 is highly effective at resisting TP buildup, but only in an O_2 environment. For cold switching in N_2-0.25% C_6H_6 (N_2 environment with 0.25% by volume benzene), both Pt- and RuO_2-coated microswitches produced carbonaceous deposit with a corresponding degradation in electrical resistance that can reach and exceed a value of 1 kΩ.

The RuO_2-coated microswitches, contrary to expectations, produce significantly more TP than the Pt-coated microswitches. In N_2-0.25% C_6H_6:O_2 (N_2:O_2 environment with 0.25% by volume benzene), the performance of both microswitches is greatly improved relative to the N_2-0.25% C_6H_6 environment. Now, however, the RuO_2-coated microswitches tolerated the contamination much better than the Pt-coated microswitches.

To place the results in perspective, a resistance rise of ~ 1 Ω would be significant in a microswitch but because electrical signal delays are much shorter than mechanical delays in nanomechanical device logic, resistance at the ~1 kΩ level can be tolerated in logic applications [49]. The RuO_2 switches tested here in 1:1 N_2-0.25% C_6H_6:O_2 plateau after a resistance increase of 40 Ω.

In Chapter III we also explore the effect of applied voltage across the contacts on device performance. We test the switches in "cold-switching" and "mechanical-cycling" modes. In cold switching, the contacts are closed, and then voltage is applied across them. Voltage is removed before opening the contacts. In mechanical cycling, the switch is opened and closed without applying voltage. It is found that TP buildup is far larger in cold switching than in mechanical cycling, but also that the TP formed in cold switching is rather conductive compared to that formed in mechanical cycling.

In Chapter IV, we probe the effect of temperature on contaminant buildup and evaluate whether temperature rise due to electrical current affects deposit growth. We test Pt-coated switches in the temperature range from 25℃ to 200 ℃ in the presence of 2,500 parts per million (PPM) C_6H_6 to see how temperature effects deposit growth. It was expected that higher temperature would enhance its growth rate because in Chapter III it was shown that cold

switching produces more deposit than mechanical cycling. Instead it was found that increased temperature reduces deposit accumulation in mechanical cycling and delays the deposit accumulation in cold switching. Therefore, the temperature rise induced by the current is not responsible for increased TP formation.

In Chapter V, we probe the contamination thresholds of Pt and RuO_2 coatings. We test both coatings in different contamination levels, ranging from <0.1 PPM to 2,500 PPM of benzene, with the most effective background gas for each material (N_2 and N_2:O_2 for Pt, and RuO_2, respectively). This type of data is critical for industrial applications because when contamination is unavoidable, it is necessary to know the thresholds for reliable device operation. We find that TP builds up on Pt even at the lowest introduced level of benzene (0.02 PPM), while RuO_2 is resistant to TP buildup even up to 400 PPM.

In Chapter VI, we demonstrate that devices that degraded due to high contamination can recover their electrical performance. We examine how these pre-contaminated devices can recover their electrical performance in clean environments (pure N_2 or N_2:O_2). We show how the chemical structure of the contaminant changes with its electrical conductivity.

An important question relates to the role of gaseous O_2. Although it was shown that O_2 can accelerate wear-induced degradation of Pt contacts in contaminant-free conditions [31], we found that O_2 plays an important role in reducing the amount of deposit created and the resistance increase when contaminant was present [48]. Identifying its role may be especially important because MEMS and NEMS devices are commonly packaged in an N_2 environment. We find that O_2 plays a highly beneficial role in that it not only reduces TP production, but

actually transforms the TP into a highly conducting graphitic-like layer which can passivate the surface and substantially increase the switch longevity by limiting wear.

In Chapter VII, further results are presented and directions for follow-on experiment are suggested. For the additional results, the electrical resistance recovery of pre-contaminated RuO_2 contacts is discussed first. Then the spallation problem in RuO_2 coating is addressed. Afterwards, it is shown that Au against RuO_2 contacts have no significant advantage in performance over RuO_2 against RuO_2 contacts. Next, data showing the oxygen induced acceleration of wear in both Pt and RuO_2 contacts is provided. Then, the effect of increasing contact force on accelerating electrical degradation onset is addressed. This is followed by a brief discussion on the interpretation of the different Raman spectroscopy results that were presented in previous chapters.

The rest of this chapter discusses directions for future work. One avenue of interest is to investigate how mechanical stress effects deposit growth by altering contact hardness while not changing other surface properties. Another study would look into measuring the I-V characteristics of the TP deposit. Finally, we propose to investigate contaminant buildup in "hot-switching", in which contacts are opened and closed while voltage is applied. This switching mode would be used in logic applications. This is a secondary objective because advanced logic supply voltage levels are on the order of 1 V or less. Since this is less than the work function of most materials [27], hot switching degradation may be similar to cold-switching. However, it would be important to investigate whether this speculation is correct.

In Chapter VIII, conclusions and suggestions for future work are presented.

In the Appendices, brief reports and calculations on related work are provided. Appendix I relates microswitch data to nanoswitches. Appendix II discusses flammability concerns with respect to the benzene contaminant. Appendix III shows a sample procedure for the safe use of benzene in experiments. Appendix IV shows the chip layouts for Pt and RuO_2 switches. Appendix V discusses minimum actuation voltages for our switches and provides experimental evidence of cold switching. Appendix VI estimates the time it takes to close the switch.

1.4 REVIEW OF RELATED SCIENCE

This part of the chapter will introduce the scientific phenomena essential for understanding the research problem at hand. The aim is to provide a comprehensive and concise summary of the relevant topics that should be kept in mind while interpreting the results and discussion in the forthcoming chapters.

1.4.1 Adsorption:

The adsorption of volatile hydrocarbon on the surface of electrical contacts is the source of the contamination. Although the details of processes that could happen during adsorption were not investigated here, it is important to discuss the key concepts of this phenomenon as it applies to this work.

Gases that are below or even above their critical temperature (the temperature above which neither a solid nor liquid can exist) will adsorb on surfaces. Adsorption in general can be categorized into two forms; physisorption and chemisorption. In physisorption, a gas molecule becomes trapped on the surface when its kinetic energy is exceeded by the van der Waals energy of attraction to the surface and it is held in place only by van der Waals forces. This is similar to the process of condensation of a vapor to a liquid and is therefore affected by pressure and temperature. In physisorption the adsorbed molecules remain intact, while in chemisorption the adsorbed molecules may dissociate on the surface into parts that can chemically bond with the surface. In other words, if the adsorption energy is as large as the chemical bond energy than the molecule can be considered chemisorbed [50].

Chemisorption does not readily occur at low surface temperatures and it usually does not happen directly. Generally the species will first physisorb on the surface and then will begin to chemically interact with the surface as the temperature is increased. However, if the translational energy of an incoming gas molecule is increased sufficiently (e.g. by accelerating it) then chemisorption can happen and even at a low temperature [51]. In most cases direct chemisorption readily occurs at temperatures that are higher than the critical temperature of the adsorbate [50].

As the surface temperature increases, the adsorbate molecules gain more kinetic energy and it becomes more likely that they desorb. Therefore the overall surface coverage by the adsorbate is reduced [51, 52]. The rate of chemisorption depends on the quantity of adsorbates, the amount of time each of these molecules spend on the surface and whether sufficient energy is available for a chemical reaction. As the surface temperature is increased, more energy becomes available to establish chemical bonds with the surface, however, the amount of time an adsorbate molecule resides on the surface is decreased [51]. Another key distinction between physisorption and chemisorption is that although several monolayers are generally physisorbed onto the substrate, only the first monolayer can be chemisorbed [50].

Although it will not be implemented in this work, introducing a more quantitative description of adsorption will show how key parameters such as pressure, temperature, surface and gas properties affect it.

If a gas molecule approaches a surface and there are no attractive forces between the molecule and the surface, then the amount of time this molecule will spend in the vicinity of the

surface is on the order of 10^{-13} seconds, roughly its vibration time. If attractive forces exist, then the average time of stay, τ, of the molecule on the surface is

$$\tau = \tau_0 e^{Q/RT} \quad , \quad (1.2)$$

where $\tau_0$is 10^{-12} to 10^{-13} seconds, Q is the energy of adsorption in kcal/mol, R is the ideal gas constant ($1.987 \cdot 10^{-3}$ kcal/mol•K), and T is the gas temperature in K. Adsorption is considered to have occurred if τ is larger than several vibration periods. The surface adsorbate concentration, Γ, is defined as

$$\Gamma = Z\tau \quad , \quad (1.3)$$

where Z is moles of collisions per square centimeter per second. It is assumed that all molecules colliding with the surface stick to it. Table XVII-1 from Adamson and Gast [50] (labeled here as **Table 1.1**) summarizes the adsorption behavior at 25 ℃ as a function of the energy of adsorption.

Table 1.1: Adsorption behavior as a function of energy of adsorption at room temperature. Reproduced from [50] with permission from Wiley (Copyright © 1997 by John Wiley & Sons, Inc. All rights reserved).

Q (kcal/mol)	τ, 25 ℃ (sec)	Γ, net (mol/cm^2)	Comments
0.1	10^{-13}	0	Negligible adsorption
1.5	10^{-12}	0	Region of physical adsorption
3.5	$4 \cdot 10^{-11}$	10^{-12}	Region of physical adsorption
9.0	$4 \cdot 10^{-7}$	10^{-8}	Region of physical adsorption
20.0	100	Not accurate	Region of chemisorption
40.0	10^{17}	Not accurate	Region of chemisorption

This table shows that at very low Q values the surface concentration is practically zero. For intermediate Q values (1.5 through 9 kcal/mol), corresponding to physical adsorption, the surface

concentration approaches the monolayer level. When the Q values are in the chemisorption region, τ becomes very large, corresponding to unrealistically high Γ values. The source in the error is the assumption that all molecules colliding with the surface stick to it. In reality, as the surface coverage approaches a monolayer, more and more molecules will collide with occupied sites and not experience the full adsorption energy of the surface. The Langmuir adsorption isotherm sets the groundwork for correcting this inaccuracy.

Adsorption is a function of temperature T and pressure P, such that the amount adsorbed is $n = f(P, T)$. Because it can be experimentally convenient to hold temperature constant, an adsorption isotherm can be defined as $n = f_T(P)$. The Langmuir isotherm basically describes equilibrium between the rate of evaporation and the rate of condensation of a gas on a surface such that it is possible to deduce the fraction of the surface covered, θ, by the adsorbate:

$$\theta = \frac{bP}{1+bP} \quad , \qquad (1.4)$$

where P is the gas pressure and b is the ratio of evaporation and condensation rate constants. These can be expressed as:

$$b = \frac{N_0 \sigma^0 \tau_0 e^{QR/T}}{(2\pi MRT)^{1/2}} \quad , \qquad (1.5)$$

where N_0 is the number of molecules on the surface, σ^0 is the area per adsorption cite and M is the molar mass of the gas.

If several adsorbates are competing for the surface then the fraction of total coverage for the i^{th} adsorbate (θ_i) is

$$\theta_i = \frac{b_i P_i}{1+\sum_j b_j P_j} \quad . \qquad (1.6)$$

Although the Langmuir equation is limited by many simplistic assumptions, it was found to fit reasonably well with experimental data. Other more sophisticated models that fit certain experimental data better are available; however, they are usually still based on the Langmuir approach.

We are now in a better position to comment on how these concepts apply to the adsorption of hydrocarbons on contact surfaces. At low temperatures, most hydrocarbons physisorb on the surfaces of transition metals (such as Pt). However, this process is often irreversible because when the surface temperature is increased, rather than fully desorbing, only some hydrogen is desorbed, leaving partially dehydrogenated carbon on the surface. For example, ethylene (C_2H_4) that was adsorbed on Rh(111) surface stays intact at 77 K. However, upon raising the surface temperature to 220 K, it dissociates into H and CCH_3. Adsorbed C_2H_4 on Pt(111) is intact at 202 K but becomes dissociated into H and CCH_3 at 300 K. As the temperature increases further, more dehydrogenation occurs, forming polymeric C chains terminated with H. Eventually, the concurrent polymerization and dehydrogenation create a graphene layer on the surface [38].

This understanding supports the Hermance and Egan hypothesis from the 1950s [37] where they propose that the "friction polymer" is formed as a result of the catalytic action of the metal surface. A catalyst after all is a material that participates in a chemical reaction by acting as an intermediate (a stepping stone to the final product) without being consumed by it. In the present case, the transition metal helps create the graphene layer by dehydrogenating and polymerizing the adsorbent without remaining as a part of the final chemical compound.

Benzene (C_6H_6) molecules adsorb on Pt(111), with the ring being parallel to the surface. They experience a similar dehydrogenation and polymerization process; however, it begins at

temperatures higher than 350 K. Hence C_6H_6 remains intact on the surface at room temperature. This is likely similar to what is happening in our experiments where benzene physisorbs on the polycrystalline Pt contact surface. However, considering that the critical temperature of benzene is 562 K (289 ℃) and that some experiments described in Chapter IV were performed at surface temperatures near that level, it is possible that in those cases some benzene was chemisorbed.

1.4.2 Mechano-chemical reactions:

As mentioned above, chemical catalysis may contribute to the polymerization of the adsorbed hydrocarbons on the contact surfaces. However, the repeated loading and unloading of the contacts during switch cycling undoubtedly plays a role in deposit growth as it only happens at locations that experienced mechanical contact.

As intriguing as it may sound, chemical reactions induced by mechanical pressure (stress) are fairly common and have been investigated and understood for some time, yet they remain largely unnoticed in modern chemistry textbooks and other literature. In fact, the first record of the phenomenon dates back to the times of Aristotle when his students showed how rubbing native cinnabar in a brass mortar with a brass pestle in the presence of vinegar produces metallic mercury ($HgS + Cu \rightarrow Hg + CuS$). The underlying idea is that strong covalent bonds are activated by applying an external pressure [53].

1.4.2.1 Chemical degradation of organic polymers under mechanical stress

For the case of organic polymers under *tensile* stress, the hemolytic cleavage (i.e. electrons from the bond divided equally between products) of the C-C bonds in the macromolecule backbones was observed [53-58]. It has also been shown that stress-induced bond ruptures produce free radicals [53, 59, 60]. These radicals likely cause further chemical reactions in the polymer that degrade its structure. It has been demonstrated that increasing tensile stress or temperature causes an exponential increase in the formation of free radicals [61-64]. An equation by Zhurkov [65, 66] describing the breakdown of solids shows how the rate of bond-cleavage (K) depends on the applied tensile stress (σ) and temperature (T):

$$K = K_0 e^{-(E_A - \alpha\sigma)/RT} \quad . \qquad (1.7)$$

Here σ is in N/m^2, T is in K, K_0 is the Arrhenius frequency factor (Hz), α is a coefficient with the dimension of m^{3}mol^{-1}, and E_A is the activation energy of the breakdown reaction. Notice that the numerator in the exponent term becomes smaller with increased tensile stress, indicating that less energy is required for a reaction to initiate (i.e., stress effectively reduces the activation energy).

The forces required to cleave covalent bonds are measured to be in the range of several nN, agreeing with theoretical estimates. The bond cleavage tends to happen at the center of the polymer backbone because that is where the maximum viscous force is reached. This means that a local thermal activation can be ruled out as the reason for bond cleavage because a thermal activation cannot be that selective. Furthermore, the temperature required for radical formation is much too high to be feasible. The broad implications of these results are that whenever materials containing macromolecules undergo a mechanical process involving fracture or cutting of some sort, covalent bonds are cleaved resulting in formation of free radicals [53].

The initial understanding of mechanochemical reactions was that the mechanical energy is accumulated and stored in a particular bond until it cleaves. It is now known that this energy is in fact stored in the environment such as in a stretched spring and that not all of the energy necessary for bond cleavage has to go into the bond for the cleavage to occur. The addition of mechanical energy to a potential energy reservoir in the system is conceptually similar to the addition of electrical energy for example.

1.4.2.2 Mechano-chemical polymerization of hydrocarbons

When hydrocarbons experience increasing *compressive* stress, their volume is reduced and interatomic and intermolecular distances are also reduced. This leads to increased overlap between molecular orbitals, thereby changing the electronic structure of the molecules involved and initiating a chemical reaction. In other words, increasing compressive stress increases the density and kinetic energy of the electrons involved in the chemical bonds. When the kinetic energy overcomes the attractive interactions, the system becomes thermodynamically unstable, inducing chemical bond reorganization that minimizes the free energy. This happens by exchanging double and triple bonds and weak intermolecular bonds for single bonds that favor more efficient packing. This corresponds with Le Chatelier's principle that states that at increasing pressure, the system evolution towards smaller volume is preferred [67].

A series of experiments was performed by Schettino et al. on a variety of hydrocarbons to show how pressure affects their structure and chemistry. The hydrocarbon samples were tested in the diamond anvil cell (DAC), where the sample is compressed by two diamonds and constrained laterally by a steel diamond-coated gasket, as shown in **Figure 1.2** below [67].

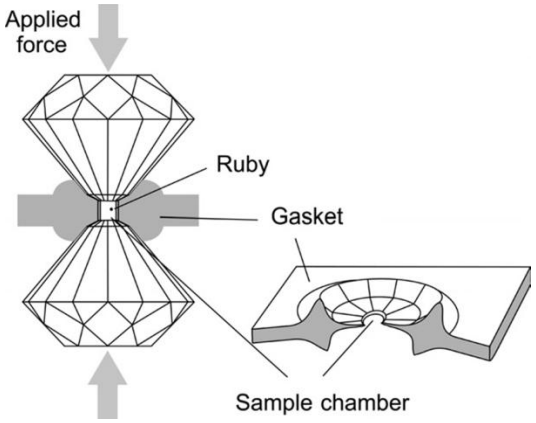

Figure 1.2: Diamond anvil cell is used to compress a laterally constrained sample (Reproduced in part from [67] with permission of The Royal Society of Chemistry).

The results from such tests will be addressed here. Special attention is given to how benzene behaves under compression because it is the contaminant of choice in our microswitch contact reliability studies.

It has been known for several decades that benzene irreversibly transforms into highly cross-linked carbonaceous materials under high pressure and temperature conditions [68, 69]. The path to this point can be seen in the benzene phase diagram in **Figure 1.3** where the material's response to pressure and temperature is illustrated. The melting point of benzene is 5.5 ℃ at atmospheric pressure, so it is a liquid at SATP (standard ambient temperature and pressure). Upon being compressed to 0.07 GPa at room temperature (298 K), it transitions to what is known as a phase I solid that has an orthorhombic $Pbca(D_{2h}^{15})$ crystal structure [70]. Upon increasing the pressure to 1.4 GPa at room temperature a transition to phase II happens, which has the monoclinic $P2_1/c$ structure. As the pressure increases further to values above 23 GPa at room temperature, a chemical transformation of benzene into a hydrogenated amorphous carbon (a-(C:H)) is realized. Notice that such a transformation can occur at lower pressures when compression is performed at higher temperatures. The rate of the amorphization reaction at room temperature is on the order of hours when the sample is under constant compression. Although the reaction can start quickly, the concentration of a-(C:H) within the compressed sample continues to increase beyond 24 hours into the experiment. No influence of compression rate in the range of 1 to 10 GPa per hour on the reaction was observed [71].

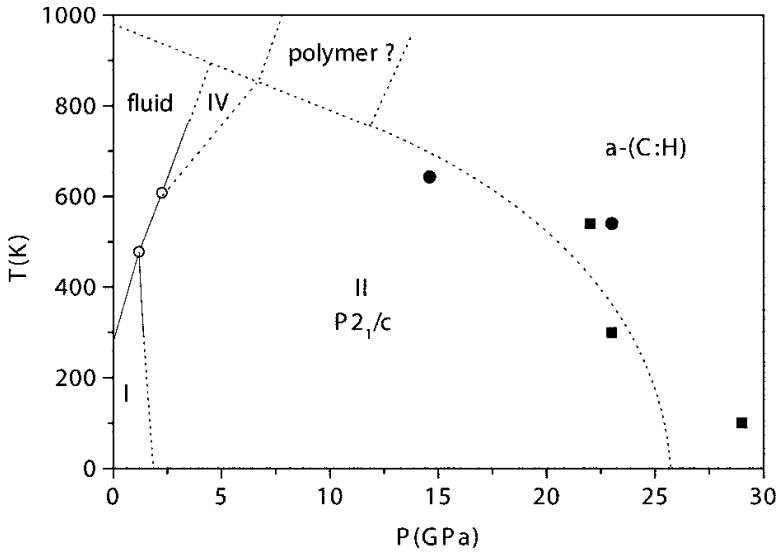

Figure 1.3: The phase diagram of benzene and its chemical stability boundary are shown [70]. The dotted lines represent the phase boundaries. The full lines represent the melting boundary and the I-II phase boundary. The empty circles represent the two triple-points. The filled circles and squares correspond to conditions in which benzene was tested in related previous studies discussed by [70]. (Reprinted figure with permission from [70]. © 2005 by the American Physical Society).

It is known that the transformation of benzene into a-(C:H) begins with the opening of the benzene ring and that the resulting a-(C:H) does not have graphitic regions. The same reaction can be induced at 15 GPa and room temperature when the material is excited optically (with a 458 nm 70 mW laser focused to a 80 μm diameter spot size [72]), suggesting that an excited electronic state plays an active role or even triggers the reaction mechanism.

It has been observed that at any given pressure greater than the amorphization threshold for a given temperature (see phase diagram), the benzene transformation into a-(C:H) transpires only partially. However, the rest of the transformation occurs during the decompression from the maximum pressure of the given experiment. Notably, the decompression greatly accelerates this process. It is believed that although the benzene molecules have been irreversibly distorted under high pressure, their ring opening is hindered while density is high because of the

constraints on movement of atoms and molecules in the system. During decompression the average molecular volume is increased, thereby allowing restructuring of chemical bonds (i.e. further ring opening and amorphization) [72]. In other words, volume constraints at high pressure set energy barriers that prevent the complete reorganization of the bonds. As the pressure is reduced, more space becomes available for reaction completion [73].

The recovered a-(C:H) is metastable and is a white solid. However, upon heating its color changes to orange at 510 K and black at 600 K. It was also possible to induce the color change by increasing the applied pressure [72]. This material was shown to be an insulator with a density of 1.4 g/cm^3, an optical gap of 2.8 eV and a refractive index of 1.47. Because no hydrogen was released during the reaction, the C:H ratio of this material is about the same as in benzene. IR spectroscopy of the recovered sample showed its sp^3/sp^2 ratio is about 75%.

Molecular dynamics simulations of benzene compression help explain the aforementioned experimental observations. They indicate that molecular deformation is substantial and that the electronic energy levels can be broadened to an extent where the gap between the Highest Occupied Molecular Orbital and the Lowest Unoccupied Molecular Orbital (HOMO-LUMO) disappears. They also predict that the high pressure causes charge separation in pairs of nearest-neighbor benzene molecules, enabling the formation of benzene dimers (two molecules that become chemically bonded). Those dimers have been suggested to be nucleation sites for the transformation of benzene to a-(C:H).

Simulations showed that the benzene transformation reaction will occur only if the intermolecular carbon-carbon spacing is less than 2.6 Å, (for comparison, the spacing between two adjacent carbon atoms in a benzene molecule at atmospheric pressure and room temperature

is 1.4 Å). However, when the applied pressure is 41 GPa at room temperature, the shortest C-C separation is 2.726 Å, yet it was shown experimentally that it only takes 23 GPa to initiation amorphization. When benzene is in the solid state, its molecules are energetically confined to fixed sites in the crystal lattice. Their mobility is limited to vibrations of atoms within the molecule and the vibrations of the molecule as a whole, where the amplitude of motion depends on the temperature. It turns out that when these vibrations are taken into account, the C-C separation can temporarily shorten to 2.552 Å at room temperature, which is sufficiently low (and the duration is sufficiently long) for a reaction to happen [73].

Non aromatic hydrocarbons require less pressure to induce polymerization (typically 1 – 6 GPa) because they have a less stable structure [72]. For example, at room temperature, butadiene polymerizes at 0.7 GPa [67], ethylene polymerizes at 3 GPa [74], acetylene polymerizes at 3.5 GPa, while Acrylic acid polymerizes at 8 GPa [75]. Styrene and Furane, which are aromatics, polymerize at 10 GPa, while thiophene (another aromatic) polymerizes at 16 GPa [67]. It is also generally true that unsaturated hydrocarbons (i.e. those that have double or triple bonds) require less pressure to initiate polymerization. In all cases, optical excitation can reduce the pressure at which polymerization happens.

In our experiments, amorphous carbon with presumably high sp^3/sp^2 ratio is formed from benzene at contact pressures as low as ~5 GPa. It could be so because the benzene-metal surface interaction helps strain its bonds, thereby lowering the activation energy barrier to a level where a 5 GPa contact stress is sufficient to overcome it. Significant shear stresses exist when asperities come into contact. In silicon, it has been shown that shear significantly reduces the average stress necessary to convert from the wurtzite to the beta-tin structure [76].

1.4.3 Contact mechanics

Having explored above how hydrocarbons (in particular benzene) adsorb on switch contact surfaces, as well as how the catalytic action of the surface and the applied mechanical stress on the adsorbent trigger its polymerization, it is now time to discuss the mechanical nature of surface interactions. Understanding where the mechanical load is applied on the surface and how it is distributed will shed light on how the contaminant deposit will evolve. The apparent area of contact during switch closure in this thesis is defined by the contact dimensions (i.e. 2 µm X 50 µm). However, the real area of contact is defined only by the interacting surface asperities and will therefore be orders of magnitude smaller, as shown in **Figure 1.4**. Considering that the polymerized hydrocarbon contaminant has only been found near these contacting asperity sites, it is important to have an estimate of the effective contact area.

The outermost tip of each asperity can be approximated with a sphere of radius R, as shown in **Figure 1.4**. When two asperities contact elastically, as could happen upon switch closure, they form a region of contact that can be approximated by the circular contact area of two contacting spheres that was first described by Hertz [77].

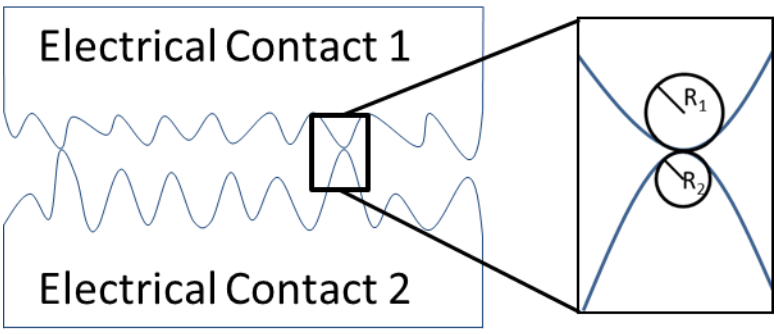

Figure 1.4: Hertzian contact of two spheres can be used to approximate the contact of each asperity pair.

1.4.3.1 Hertzian mechanics [77-79]

Hertz predicted that when two spheres with radii R_1 and R_2 are pressed against each other with load P as shown in **Figure 1.5a**, the radius, a, of the resulting circular contact area is defined by

$$a = \left(\frac{3PR_e}{4E_e}\right)^{1/3} \quad , \quad (1.8)$$

where R_e and E_e is the effective radius and effective elastic modulus, respectively. These values are found as follows:

$$R_e = \left(\frac{1}{R_1} + \frac{1}{R_2}\right)^{-1} \quad \text{, and} \quad (1.9)$$

$$E_e = \left(\frac{1-\nu_1^2}{E_1} + \frac{1-\nu_2^2}{E_2}\right)^{-1} \quad , \quad (1.10)$$

where E_1 and E_2 are the elastic moduli of each of the two spheres in **Figure 1.5**, and ν_1 and ν_2 are the respective Poisson ratios of each sphere. For this study, both spheres are made of the same material so they have the same elastic modulus, E, and Poisson ratio, ν. Notice that if one of the spheres has an infinite radius, the contact described is that of a sphere on flat geometry, as shown in **Figure 1.5b**. The amount by which the two spheres in **Figure 1.5a** are compressed elastically or the elastic displacement of the tip in **Figure 1.5b** is δ:

$$\delta = \frac{a^2}{R_e} \quad (1.11)$$

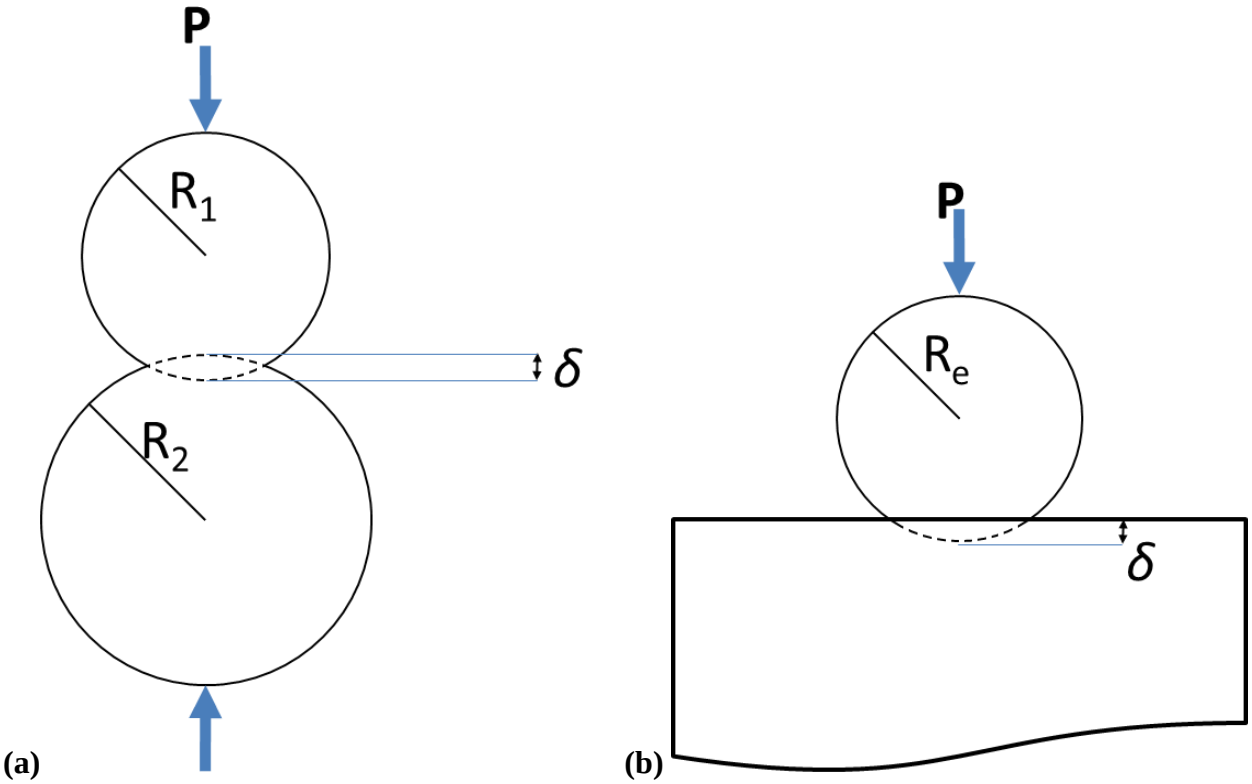

Figure 1.5: Hertzian elastic contact for (a) sphere on sphere geometry and (b) sphere on flat geometry.

The stress distribution, $\sigma(r)$, at the circular contact spot with radius a (**Figure 1.6a**) as a function of the distance from the center of that spot, r, is defined as (**Figure 1.6b**):

$$\sigma(r) = \sigma_0 \left(1 - \left(\frac{r}{a}\right)^2\right)^{1/2}, \qquad (1.12)$$

where σ_0 is the stress at the center of the contact spot, such that

$$\sigma_0 = \left(\frac{3P}{2\pi a^2}\right) \qquad . \qquad (1.13)$$

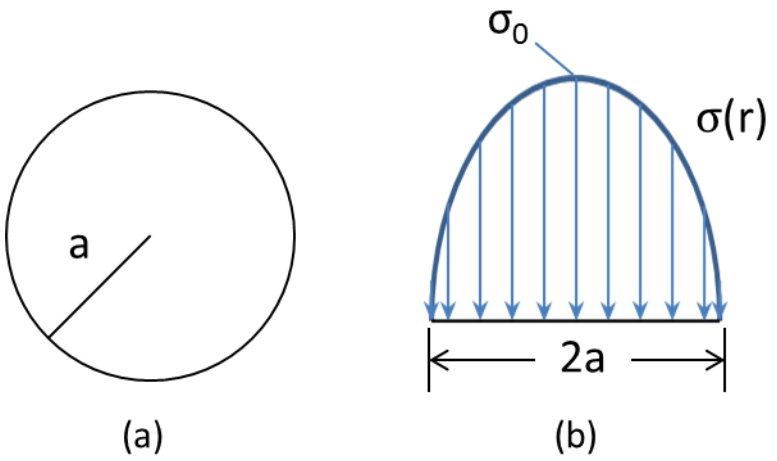

Figure 1.6: (a) Resulting spot size at Hertzian contact and (b) the corresponding normal stress distribution.

The other two principle stresses at the location of σ_0 have a magnitude of $\sigma_0 * (1 + 2\nu)/2$. The shear stress there is much smaller, being $\sigma_0 * (1 - 2\nu)/4$. The largest surface shear stress occurs at the periphery of the circular contact area [80] and it has a magnitude of

$$\tau_{max} = \frac{\sigma_0 * (1-2\nu)}{3} \quad . \quad (1.14)$$

These surface stresses are important in the nucleation of the tribopolymer deposit from the adsorbed hydrocarbon layer. The discussion in Section 1.4.2 above cited that at least 23 GPa of hydrostatic pressure was required to polymerize benzene. However, because the shear stress is zero under hydrostatic conditions, it is unknown how much shear stress would be needed to induce such a transformation. Because the shear strength of most sp^2-hybridized carbon structures (such as benzene) is relatively low, it may take just a small shear stress to induce polymerization, so it is important to be aware of this parameter.

Finally, with reference to **Figure 1.5**, the required displacement to induce a desired load and vice versa can be found from the following relation:

$$P = \left(\frac{4E_e R_e^{1/2}}{3}\right)\delta^{3/2} \quad . \qquad (1.15)$$

It is important to keep in mind that Hertzian contact is purely elastic and therefore does not account for plasticity or surface forces (such as van der Waals). Nevertheless, this approach provides an introduction to the contact phenomena and serves as a necessary starting point for derivation of other more complicated contact mechanics models.

1.4.3.2 Greenwood and Williamson model [77-79, 81]

The Greenwood and Williamson model expands upon Hertz's model to find the real contact area between two touching rough surfaces such as those shown in **Figure 1.4**. The model assumes that all asperities have the same spherical radius at the tip, R_e, and that all contact is Hertzian. It also assumes that the contact is between a rigid smooth plane and a rough surface of apparent area A_0 with a large number of asperities N, as shown in **Figure 1.7**. Upon contact, the smooth plane and rough surface are separated by a distance d, which is taken from the smooth plane to the mean asperity height. If d<0, it means that the flat smooth plane was pushed under the mean asperity height. Additionally, if an asperity height z>d, it contacts the smooth rigid plane. Finally, all asperities are far enough apart to be mechanically independent.

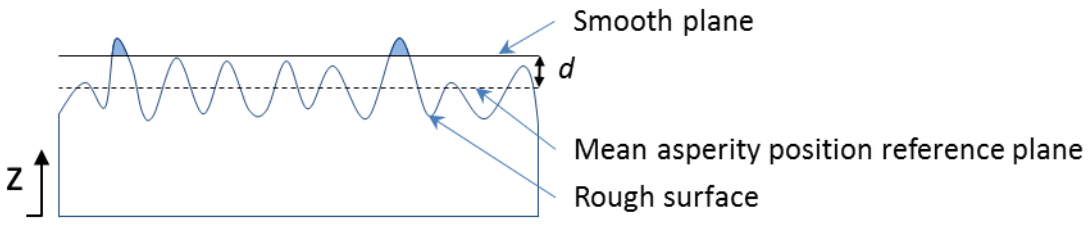

Figure 1.7: Greenwood and Williamson rough-surface and smooth-plane contact.

The probability for a given asperity of height z from the mean rough surface (measured from the mean roughness reference plane) to make contact with the smooth flat plane is:

$$prob(z > d) = \int_d^\infty \varphi(z)dz \quad , \qquad (1.16)$$

where $\varphi(z)dz$ is the probability for an asperity to have a height between z and $z + dz$:

$$\varphi(z) = \frac{1}{\sigma\sqrt{2\pi}} \exp\left(-\frac{z^2}{2\sigma^2}\right) \quad , \qquad (1.17)$$

where σ is the standard deviation of the Gaussian height distribution of the asperities.

Hence the expected quantity of contacting asperities is:

$$n = N \int_d^\infty \varphi(z)dz \quad . \qquad (1.18)$$

The normalized asperity separation is:

$$h = d/\sigma \quad , \qquad (1.19)$$

and the density of asperities on the surface is:

$$\eta = N/A_0 \qquad (1.20)$$

The number of asperities in contact with the smooth plane, the total load, P, and the real contact area, A_r, can now be written as:

$$n = \eta A_0 F_0(h) \quad \text{, and} \qquad (1.21)$$

$$P = \frac{4}{3}\eta A_0 E_e R_e^{1/2} \sigma^{3/2} F_{3/2}(h) \quad \text{, and} \qquad (1.22)$$

$$A_r = \pi\eta A_0 \eta R_e \sigma F_1(h) \quad , \qquad (1.23)$$

where

$$F_n(h) = N \int_h^{\infty} (z^* - h)^n \varphi^*(z^*) dz^* \quad . \qquad (1.24)$$

Here $\varphi^*(z^*)$ is the normalized asperity height distribution:

$$\varphi^*(z^*) = e^{-z^*} \quad , \qquad (1.25)$$

and

$$z^* = \frac{z-m}{\sigma} \quad , \qquad (1.26)$$

where m is the mean of the height distribution.

Key results of this model are that there is a linear dependence between contact force and real contact area as well as the number of contact spots. Also, the mechanical stress at contact and the mean size of the contact spots are independent of applied load. The mechanical stress is approximately equal to the contact hardness [35]. Despite the simplifying assumptions of the Greenwood and Williamson model, its overall accuracy was found to be good. McCool modeled surfaces with randomly distributed anisotropic elliptical asperties and found strong agreement with Greenwood and Williamson [82]. Furthermore, Greenwood and Tripp modeled two rough contacting surfaces (instead of a rough surface against a smooth one) and showed the results were equivalent to those of Greenwood and Williamson [35].

1.4.3.3 Abbott Firestone approach [35, 83]

It is important to consider that the switch contacts experience substantial plastic deformation at the asperities. This is observable experimentally when electrical contact resistance drops during the first ~10 cycles. During this time, the real contact area increases to a steady value that will typically be maintained for a prolonged number of cycles. Abbott and Firestone included the effects of plastic asperity deformation in their model and derived a simple result to estimate the real contact area. The key assumption is that the contact stress is large enough and has been applied for long enough for material creep to be exhausted. The real contact area can be thought of here as a circle that has an area equal to the sum of all the individual contact areas from each pair of contact asperities on the surface. The total circular area has an effective radius, r_{eff}:

$$r_{eff} = \sqrt{\frac{F_c}{H\pi}} \quad , \quad (1.27)$$

where F_c is the contact force and H is the hardness of the surface (load divided by projected area of an indentation). In the case of our switch contacts, the hardness is 5 GPa for Pt coatings and 20 GPa for RuO_2 coatings. For a 100 μN load, the resulting r_{eff} values are 90 nm for Pt and 45 nm for RuO_2. Hence the real contact area, A_r, is:

$$A_r = \pi r_{eff}^2 \quad , \quad (1.28)$$

which is $2.5 \cdot 10^4$ nm^2 for a Pt coating and $6.3 \cdot 10^3$ nm^2 for a RuO_2 coating.

1.4.3.4 JKR and DMT models [77, 79]

A critical topic in the mechanics of contacts that has not been addressed above is contact adhesion. In clean operating conditions micro and nano-switch contacts can become permanently stuck upon closure. Although this topic is beyond the scope of this dissertation because such a failure mechanism is rarely observed in the presence of contaminants, it is nevertheless worthwhile to introduce the concept for completeness.

Hertzian mechanics does not address the problem of contact adhesion and predicts that the contact area between two spheres would be zero when the load is zero. Two approaches that address this shortcoming and assume a ball on flat contact geometry will be now discussed. The Johnson-Kendall-Roberts (JKR) model modifies the Hertz theory to include the surface energy of the solids (Dupre energy of adhesion), ω. The attractive forces are only considered in the region of contact and are not considered in nearby areas where contact has separated. Hence, to find the contact radius as a function of applied load, we use:

$$a = \left(\frac{R_e}{K}\left(P + 3\pi\omega R_e + (6\pi\omega R_e P + (3\pi\omega R_e)^2)^{1/2}\right)\right)^{1/3} , \qquad (1.29)$$

where

$$K = \frac{4}{3}\frac{1-\nu^2}{E} . \qquad (1.30)$$

To find the contact radius as a function of displacement we use:

$$a = \left(\delta R_e + \left(\frac{8\pi\omega a R_e^2}{3K}\right)^{1/2}\right)^{1/2} , \quad \text{and} \qquad (1.31)$$

$$\delta = \frac{a^2}{R_e} - \left(\frac{8\pi\omega a}{3K}\right)^{1/2} . \qquad (1.32)$$

The pull-off force and pull-off displacement are P_c and δ_c, respectively, according to:

$$P_c = \frac{3}{2}\pi\omega R_e \quad \text{, and} \tag{1.33}$$

$$\delta_c = \left(\frac{3}{4}\frac{\pi^2\omega^2 R_e}{K^2}\right)^{1/3} \quad . \tag{1.34}$$

The limitation of JKR is that it works best for soft contact materials that have a large surface energy. Hard contact materials with low surface energy are best described by Derjaguin-Muller-Toporov (DMT) model. This model assumes Hertzian contact at the contact region but includes the contribution of attractive forces around the Hertzian contact. The surface energy contribution is not considered at the contact because there is a competition between the higher contacting asperities pushing each other apart and the lower contacting asperities pulling each other together and these affects are argued to largely cancel each other. Hence, to find the contact radius as a function of applied load:

$$a = \left(\frac{R_e}{K}(P + 2\pi\omega R_e)\right)^{1/3} \quad , \tag{1.35}$$

while as a function of displacement it is:

$$a = (R_e\delta)^{1/2} \quad . \tag{1.36}$$

Finally the DMT pull off force is:

$$P_c = 2\pi\omega R_e \quad . \tag{1.37}$$

For comparison, the normalized load as a function of normalized displacement were plotted by Maugis as shown in **Figure 1.8** for the Hertz, JKR and DMT models. As can be seen the difference between the three models is not very large when the contacts are loaded. However,

unlike the Hertz model, the other two models show adhesive forces when the displacement is zero.

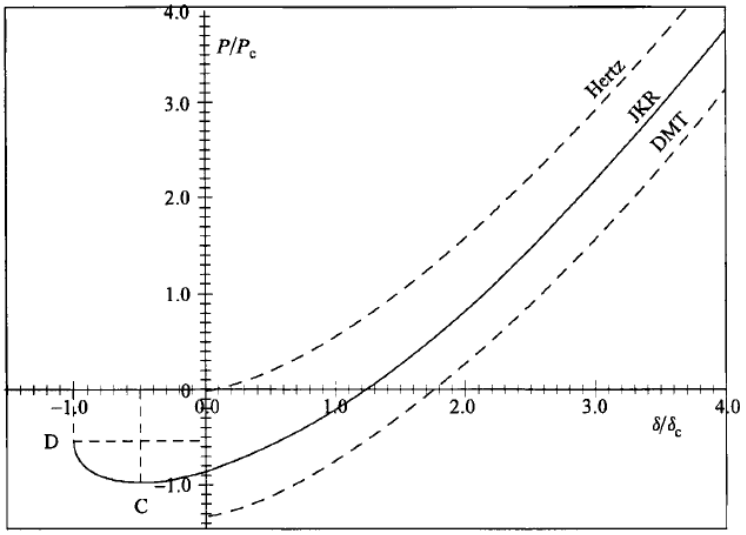

Figure 1.8: Relation between load and penetration (Adapted from [77] with permission of Taylor and Francis, www.tandfonline.com).

1.4.4 Regimes of electrical contact resistance

When the microswitch is closed, the measured resistance is the sum of the contact resistance, R_c, and all other resistance contributions in the circuit outside the contact, R_{trace}:

$$R_{measured} = R_c + R_{trace} \qquad (1.38)$$

The value for R_{trace} in our devices is about 10 Ω, which is actually larger than the contact resistance for clean contacts, being 4 Ω for Pt-coated contacts or 9 Ω for RuO_2-coated contacts. When the real contact area is sufficiently large and the contact is clean, the contact resistance is known as Maxwell resistance, R_{cM}, and it depends on just the resistivity of the contact material, ρ, and the effective contact radius, r_{eff} (which is found using the Abbott and Firestone's approach that assumes plastic deformation, as described at the end of the last section) [84]:

$$R_{cM} = \frac{\rho}{2r_{eff}} \qquad (1.39)$$

This relation holds only when the electron transport through the contact is diffusive which means the electron scatters many times during its path through the contact, as shown in **Figure 1.9a**. Diffusive electron transport occurs when the contact area through which electrons pass is much larger than the electrons elastic mean free path, l_e. Most metals have a mean free path of about 50 nm [85].

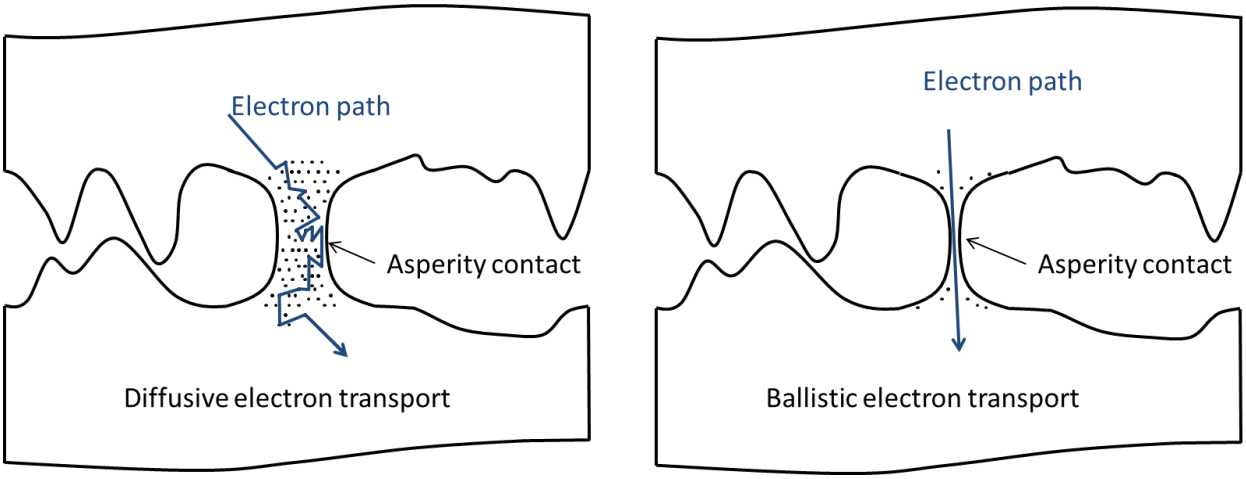

(a) **(b)**

Figure 1.9: (a) The left image shows diffusive electron transport through a conductor while (b) the right image shows ballistic electron transport.

If the contact radius is lower than l_e. than the electron transport through the contact is in the ballistic regime, where the electron does not interact with other atoms while passing through the contact, as shown in **Figure 1.9b**. The contact resistance for the case of ballistic transport is called the Sharvin resistance, R_{cS} [32, 86]:

$$R_{cS} = \frac{4\rho K}{3\pi r_{eff}} \quad , \qquad (1.40)$$

where K is the Knudsen number:

$$K = \frac{l_e}{r_{eff}} \quad . \qquad (1.41)$$

However, if the effective radius is on the order of l_e, then the electron transport is in the quasi-ballistic regime. For such a case, Wexler interpolated between the diffusive and ballistic electron transport regimes. The Wexler contact resistance, R_{cW}, is [87]:

$$R_{cW} = \frac{4\rho K}{3\pi r_{eff}}\left[1 + \frac{3\pi}{8}\Gamma(K)\frac{r_{eff}}{l_e}\right] \quad , \qquad (1.42)$$

where $\Gamma(K)$ is the Gamma function of unity order:

$$\Gamma(K) \approx \frac{2}{\pi}\int_0^{\infty} e^{-Kx} sinc(x)dx \quad . \quad (1.43)$$

Mikrajuddin et al wrote the Gamma function the plot of which is shown in **Figure 1.10** [88]. As will be addressed in Chapter 5, the Wexler approach appears to be the most appropriate theoretical approach to estimate the electrical contact resistance for clean electrical contacts.

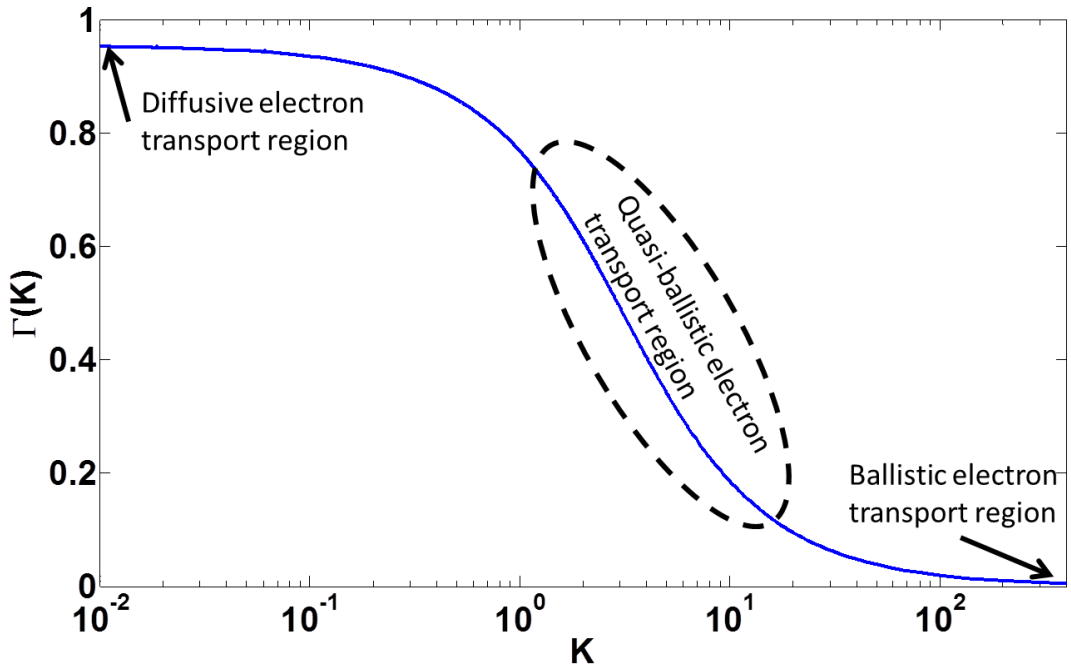

Figure 1.10: Plotted gamma function from Mikrajuddin et al., a similar plot is shown in ref. [35]

In reality, however, there is a contaminant film that is either partially or completely separating the electrical contact, so the resistance would be larger. When the amount of contaminant covering the contact surface is very small, some asperities may break through the layer establishing clean contact. If the contaminant is a poor conductor, it would be more

difficult to estimate contact resistance because it is not known what fraction of the asperities are penetrating the layer to establish clean contact.

If the contaminant is thick enough, it would effectively establish a series resistance with the electrical contacts. Hence, the contact resistance R_c, actually has the form:

$$R_c = R_{c,intrinsic} + R_{c,interface} \quad , \qquad (1.44)$$

where $R_{c,intrinsic}$ is the intrinsic contact resistance due to spreading resistance (e.g. Maxwell or Sharvin), whereas $R_{c,interface}$ is the interface resistance, being by far the dominant component in our experiments (i.e. the intrinsic component is always under 10 Ω, while the interface component occasionally exceeds 1,000 Ω). Understanding $R_{c,interface}$ and how to manipulate it is a key focus of this dissertation.

1.4.5 Temperature rise due to passage of electric current through the contacts

The flow of electric current and the flow of heat obey similar laws. While voltage is the driving force for current, temperature difference is the driving force for heat flow. The heat generated due to electric current flows in the same path as the current. Using the assumption by Greenwood and Williamson that in an electrical contact, an equipotential surface is also isothermal and the Wiedermann-Franz law (which relates the thermal conductivity, electrical conductivity and temperature), it is possible to relate voltage and contact temperature [84]:

$$T_{max} = \sqrt{\frac{V_C^2}{4L} + T_0^2} \quad , \qquad (1.45)$$

where, V_c is the voltage across the contacts, $L = 2.45 \bullet 10^{-8}$ WΩ/K^2 is the Lorentz constant, and T_0 is the ambient temperature.

Jensen et al. [42] suggested that the Holm temperature estimate may not be accurate for microswitches. The assumption that all electron transport through the contact is diffusive (i.e. R_C is dominated by Maxwell resistance) and thus is responsible for driving the temperature up was questioned. When the contact radius is less than the electron mean free path (~50 nm), there must also be ballistic electron transport (responsible for the Sharvin resistance component in R_C), which does not cause a temperature increase. Considering that the total effective contact area has a radius of ~90 nm for our switches [89], which realistically consists of several smaller contact regions, individual contacting asperities are likely to have contact radii under 50 nm. This means the Jensen picture applies better here. Jensen modified the Holm equation to account for ballistic electron transport, such that R_C, is equal to the sum of the Maxwell component, R_m, and the Sharvin component, R_s, thus giving the relation [42]:

$$L(T_{max}^2 - T_0^2) = \left(\frac{1+0.83\left(\frac{\lambda}{a}\right)}{1+1.33\left(\frac{\lambda}{a}\right)}\right)\frac{R_m}{4R_c}V_c^2 \quad , \qquad (1.46)$$

where λ is the mean free path (in Pt ~40 nm), and $a = 90$ nm is the contact radius (in the worst case scenario that will yield the highest temperature), while $R_m = \rho/(2a)$ where ρ is the resistivity of the material.

When the contacts are contaminated to an extent that there is no metal-on-metal contact and instead occurs through the contaminant layer, the aforementioned approach to estimate temperature does not apply. In that case the power, $I^2 \bullet R_c$ (where I is electrical current) is the heat source that needs to be accounted for in order to calculate the change in contact temperature.

The shape factor heat transfer analysis [90] for a disk of contaminant deposit sandwiched between two semi-infinite bodies (the electrical contacts), as shown in **Figure 1.11**, was found to be the most suitable approach. The relation is:

$$q = 2Sk(T_{max} - T_0) \quad , \quad (1.47)$$

here, q is the power generated (in watts), S is the shape factor and k is the thermal conductivity of the contact. We approximate the contaminant deposit as a disk on the semi-infinite body (the contact surface), thus having a shape factor of $2D$, where D is the diameter of the disk [90]. The factor of two on the right side of the equation signifies that heat is dissipated into two semi-infinite bodies.

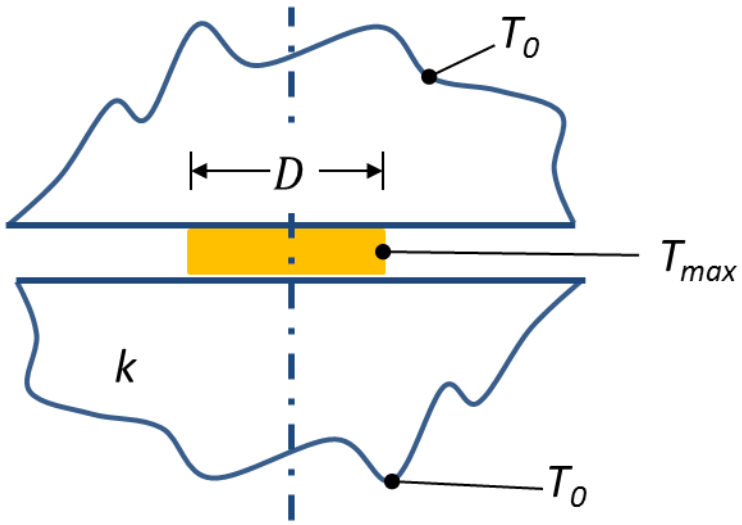

Figure 1.11: Geometry for the shape factor heat transfer analysis. Contaminant deposit is sandwiched between two semi-infinite bodies (that represent the electrical contacts).

1.4.6 Dielectric breakdown

1.4.6.1 Mechanisms

The carbonaceous contaminant deposit that builds up on the surface of the electrical contact can be fully electrically insulating or highly conducting. Operationally, this largely depends on whether or not a voltage is applied across the contacts during switch closure. When the switch is cycled without any voltage being applied across the contacts, such that only mechanical interactions occur at the contacts, the deposit is electrically insulating. When electrical voltage is applied during each cycle (in this thesis 5 V was always applied across the contacts and a series resistor), a contaminant layer still builds up but now it is electrically conductive. However, its resistance is still relatively high. This suggests that the application of voltage induces a dielectric breakdown. In a dielectric breakdown of a solid, the chemistry and/or structure of the insulating material is usually changed to make it permanently conductive. For example, when applying a sufficiently large electric field to diamond like carbon, which originally has an electrically insulating sp^3 structure, upon dielectric breakdown its structure changes to sp^2, which is electrically conducting.

A general overview of the dielectric breakdown mechanisms is provided here. First, intrinsic, avalanche type dielectric breakdown is described. The time scale for this process is on the order of 10 ns. Upon application of a sufficiently high electric field, electrons in an insulator can be excited from the valence band to the conduction band, which then travel from the cathode to the anode. The electric field will accelerate these electrons and collisions with other electrons at atomic lattice sites will occur. When such collisions energize the lattice-site electrons above the ionization potential, those electrons become liberated. These liberated electrons in turn also

become energized and liberate yet more electrons, eventually triggering an electron avalanche that induces dielectric breakdown [27, 91].

Another dielectric breakdown mechanism is known as thermal breakdown. When an insulator is subject to an electric field, an electric current, even if extremely small flows through the material. This current heats up the material. The system remains in equilibrium as long as the amount of heat generated can be dissipated by the material to the surrounding (i.e. heat input equals heat output). If the heat produced exceeds the heat dissipated, the temperature of the material will increase, eventually inducing thermal disintegration of the material [92].

Electromechanical breakdown is particularly common in very thin dielectric films and in self assembled monolayers [93]. In this mechanism, high electric fields induce compressive electrostatic forces that effectively pinch through the insulator to establish electrode on electrode contact. This is the only dielectric breakdown mode where the insulator is not altered chemically or structurally.

It is important to note that dielectric breakdown is not necessarily limited to a single mechanism, it could in fact be a result of several mechanisms happening concurrently [93].

1.4.6.2 **Dielectric breakdown in polymers** [92]

The dielectric breakdown of polymers depends on material properties such as chemical structure and structural defects and irregularities, as well as physical parameters such as temperature and pressure. The electric strength of most polymers is in the range of 100 to 900 MV/m at room temperature. The electric strength tends to drop when temperature is increased.

For example increasing the temperature from -200 ℃ to 150 ℃ can reduce the dielectric strength by nearly a factor of 10. The enhanced molecular mobility and electron transport associated with temperature increase could be responsible for the corresponding reduction in electric strength.

The polymer dielectric breakdown mechanisms can also be categorized into the three types discussed above. That is, the electronic breakdown processes (which includes avalanche process), thermal breakdown, and electromechanical breakdown. The particular breakdown mechanism involved depends on the physical state of the material, which in turn depends on the temperature. For instance, when the polymer is in a glass-like state (at low temperature), it tends to have higher breakdown strength and experiences an electron avalanche breakdown process. When the temperature is increased and the polymer transitions to a rubber-like state, it is more likely to experience a thermal breakdown. When a further increase in temperature enables plastic flow, an electromechanical breakdown becomes possible.

There are several factors that can affect the electric strength. Introducing polar molecules increases the electric strength in the glass-like phase. Increasing molecular weight increases the electric strength in the rubber-like and plastic-flow regimes, likely due to the higher glass transition temperature. Cross-linking increases strength in the plastic-flow regime, again, this is likely due to the higher glass transition temperature. Whereas increasing crystallinity reduces strength in the glass-like regime, while increasing it in the rubber-like and plastic flow regimes. Adding electrically conductive impurities to the

polymer can reduce its resistivity and reduce its electric strength in the rubber-like and plastic-flow regimes.

An important phenomenon in polymer dielectric breakdown is known as treeing. During the breakdown process gaseous channels are formed through the dielectric between the two electrodes. These channels have a tendency to branch out into other channels and the resulting structure eventually resembles a tree or a bush. The channel walls can become electrically conductive. Treeing happens presumably because the electron avalanche or thermal breakdown process induces a gas discharge along the electron path. The velocity of channel growth is on the order of 10^3 m/s.

1.4.7 Surface analysis techniques

1.4.7.1 Scanning electron microscopy (SEM)

The basic principle of operation in SEM is an electron beam scanning (rastering) the surface to generate a topographical image. The electrons are emitted from the filament (the electron gun) once they gain enough energy as a result of an applied voltage bias, this is known as field emission. The electric field guides the electrons towards the sample in the form of a beam. On its way to the sample, the electron beam is focused with a set of electromagnetic condenser lenses and the scanning motion is enabled and controlled via deflection coils that are located near the sample. The resulting spot size on the sample is typically 0.5 to 5 nm in diameter. Sample scanning is generally performed under medium vacuum (~10^{-5} Torr) so that gas does not interfere with the electron beam (although environmental SEMs can operate at much higher pressures). As the electron beam hits the surface, some of the electrons scatter elastically (back-scattered) off the surface, while other electrons induce photon-emission or scatter inelastically from the surface. Those inelastically scattered electrons are ejected from the k-shell of the atoms in the sample and are known as secondary electrons. These secondary electrons are typically utilized in image formation. Secondary electrons originate from within several nanometers of the surface due to their low energy. The main benefit of the SEM as compared to optical microscopy is that its' resolution is not restricted by the diffraction limits of visible light and it can therefore be used to obtain images of up to a magnification of 500,000 times. In this work, the Quanta 600 SEM from FEI was used to examine nearly every microswitch after it was tested. SEM helped identify contact failure locations and mechanisms [94].

1.4.7.2 Energy dispersive X-ray spectroscopy (EDS)

Many SEMs, including the instrument used for this research, have energy dispersive X-ray spectroscopy (EDS) capabilities. EDS can be used to quantify the atomic composition of the surface or spot being analyzed. The basic principle is that an incoming high energy electron (i.e. from the SEM electron beam) collides with an inner-shell electron of an atom in the sample, as shown in **Figure 1.12**. This interaction energizes and ejects the inner shell electron, creating a hole. At this point, an electron from a higher energy level (higher electron shell) drops down to fill the hole, emitting an x-ray in the process. The energy of this x-ray is equal to the energy difference between these two shells in that particular element. The energy of the x-ray is measured by the detector, identifying the element from which it came. EDS has the surface resolution of the spot size used by the SEM and it provides quantitative elemental composition of the sample. However, a major disadvantage of the technique is that it is not surface sensitive - the signals can come from as far as 2 μm below the surface. Also, the technique does not provide information on the bond structure between elements [94].

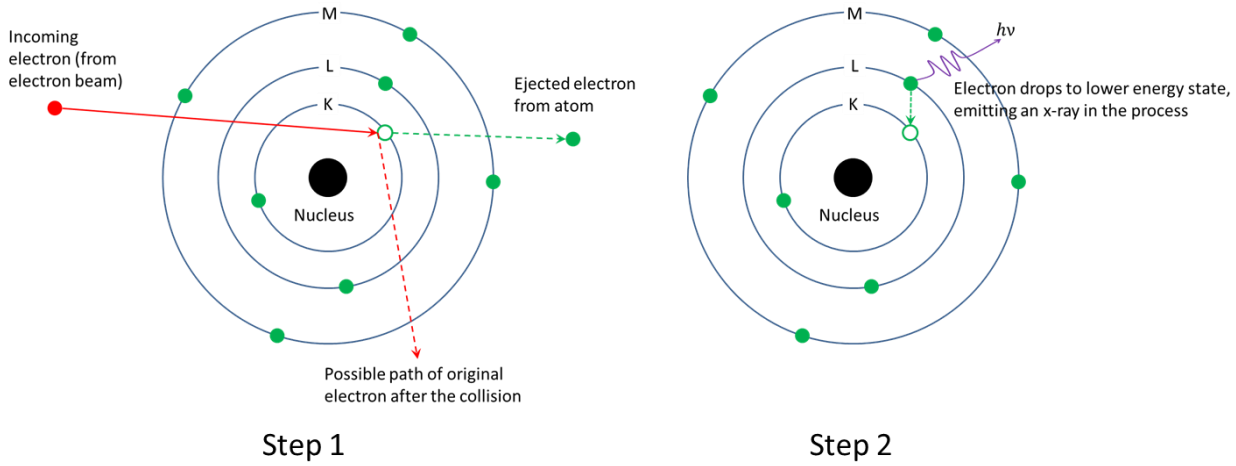

Figure 1.12: In EDS, an incoming electron knocks off an inner shell electron, creating a hole (step 1). Then an upper shell electron fills the lower energy hole, emitting an x-ray with energy equal to the energy difference between the two shells (step 2).

1.4.7.3 Auger electron spectroscopy (AES)

Auger electron spectroscopy (AES) has a major advantage over EDS because it is much more surface sensitive. Its analysis depth is generally less than 10 nm below the surface. Also it has some capability of distinguishing bond structure, especially in carbonaceous materials. For instance, it is capable of distinguishing diamond and graphite and in in some cases it can find the sp^2/sp^3 ration of carbon in the sample. The instrument used for this research was the PHI Model 700 Scanning Auger Nanoprobe LS (located at the Massachusetts Institute of Technology). The Auger emission process is initially similar to what is happening in EDS, as shown in **Figure 1.13**. That is, an electron (as in this case) or a photon knocks off an inner-shell electron, generating a hole. An outer shell electron then drops to the lower energy level to fill the hole. The energy released during this transition can be coupled with an excitation of a second outer shell electron. If the energy transferred to this electron is greater than the binding energy of the orbital, the electron is emitted. This final ejected electron is known as the Auger electron and it has the characteristic energy of the element (and possibly bonding structure) from where it was emitted [95].

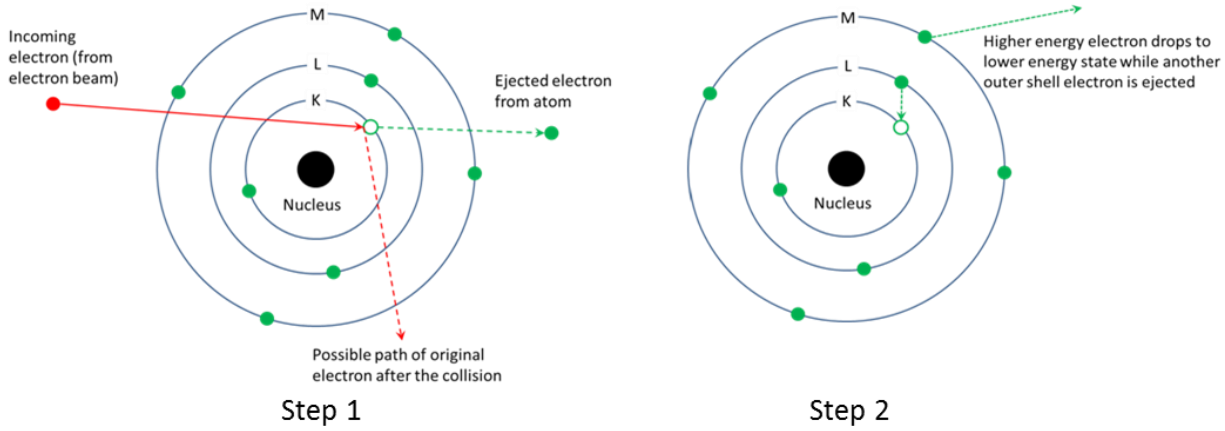

Figure 1.13: In AES, an incoming electron knocks off an inner shell electron, creating a hole (step 1). Then an upper shell electron fills the lower energy hole while potentially transferring energy to another outer shell electron (step 2). If the transferred energy is sufficiently high, the electron will be ejected. This ejected electron is an Auger electron.

1.4.7.4 X-ray photoelectron spectroscopy (XPS)

X-ray photoelectron spectroscop (XPS) uses X-rays to irradiate a surface. Electrons with energies specific to atoms and orbitals are emitted. In essence, the X-rays are absorbed by electrons in the surface and if the electron absorbs enough energy it leaves its orbital. As these photoelectrons enter a detector, their kinetic energy is measured and since the energy of the X-ray that liberated them is known, the energy of the orbital from which they came can be found. This technique is relatively surface sensitive because the analysis depth does not exceed 10 nm. XPS quantifies the elemental composition of the surface, however, it also provides bonding information and can be used to identify molecular structure. A drawback of this technique is that most instruments have a smallest spot size of about 10 μm, and this turned out to be too large to effectively characterize microswitch contact surfaces [95].

1.4.7.5 Raman Spectroscopy

In this technique a monochromatic light source (a laser) is directed at the sample where it interacts with phonons, vibrational and rotational modes of the molecules. Most of the laser light that impinges on the sample is scattered elastically (known as Rayleigh scattering). This means the light is first absorbed by the molecule, exciting it from the ground state to what is known as a virtual energy state (an unstable state or a temporary unobservable quantum state), as the molecule returns to the ground state, it re-emits light with the original frequency. Elastic scattering provides no information on the vibrational modes of the molecule and therefore it is filtered out by the detector. If the re-emitted light either has a slightly higher or a slightly lower frequency than the original incident laser light, it means that it was scattered inelastically and can therefore provide valuable information on the vibrational modes of the molecule with which it interacted. Raman signals are due Stokes or Anti-Stokes scattering. Stokes scattering occurs when the re-emitted photon has a lower frequency than the original photon, meaning that when it was re-emitted, the molecule did not relax to its ground state. Anti-Stokes scattering occurs when the re-emitted photon has a higher frequency than the original photon. This can happen if the molecule was already at an excited state when it absorbed the photon and it relaxed to the ground state when it re-emitted it. The three different scattering modes are illustrated schematically in **Figure 1.14** below. The Raman effect is different from fluorescence, where a molecule is excited to a distinct (not virtual) electronic state, as shown in right side of **Figure 1.14**. To put this in perspective, inelastic scattering happens in only 1 out of 10^7 incident photons, the rest are scattered elastically. Out of those that are inelastically scattered, most interactions are of the Stokes type [96].

In this thesis, Raman spectroscopy was used to identify the carbonaceous contaminant deposit formed on microswitch contacts, as well as the degree of disorder in that deposit. The data was then correlated to and interpreted in terms of its electrical conductivity. This technique has a spot size of 0.5 µm. The instrument used was a Horiba Scientific Model LabRAM HR Evolution located at RJ Lee, Inc. Monroeville, PA.

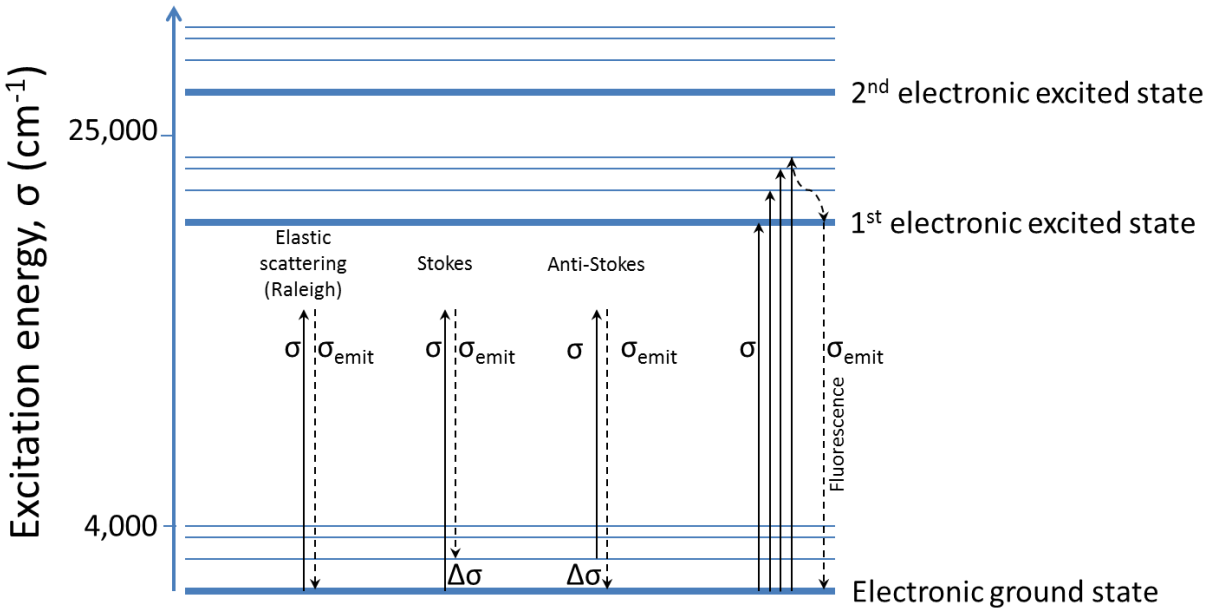

Figure 1.14: Scattering modes of monochromatic light on a sample. In Elastic, Stokes and Anti-Stokes scattering, the molecules are temporarily excited to virtual electronic states. This is different from fluorescence where the molecule is excited to distinct electronic states. (Source: http://www.ccmr.cornell.edu/igert/modular/docs/Raman_Scattering.pdf).

1.5 CONTRIBUTIONS

We identify contributions to date and expected contributions in the technical area of Ohmic microswitch reliability. A number of new results have been found thus far. They have been published in Tribology Letters [97] and Journal of Microelectromechanical Systems [89]. Two other papers, listed below, have been submitted.

The main contributions of this thesis are:

- It is possible to build a system that can test switches in clean and contaminated environments. The test system can be cleaned by an ultrahigh vacuum (UHV) bakeout after it has been contaminated.
- Normal contact in a contaminated environment induces the nucleation and growth of tribopolymer (TP) both in mechanical cycling and in cold switching conditions.
- The TP is an amorphous carbon.
- The TP remains electrically conducting.
- TP growth can be accelerated with high levels of benzene.
- TP growth can be inhibited by increasing temperature.
- Environmental oxygen greatly reduces the nucleation and/or growth of the tribopolymer.
- RuO_2 is highly resistant to TP nucleation and/or growth if oxygen is in the gas background.
- TP forms readily on RuO_2 if no oxygen is present in the background.
- The background contamination threshold level for TP nucleation and growth is much higher for RuO_2 in an N_2:O_2 background than Pt in a N_2 background (both tested in their best backgrounds).

- Even if degraded electrically in N_2-C_6H_6, the contact resistance can be restored to a clean level by re-introducing O_2 into the gas mixture.
- The presence of O_2 improves the electrical conductivity of the deposit by increasing its graphitic contact during cycling.
- When a device is pre-contaminated by cycling it in N_2-C_6H_6 and then cycled in clean N_2:O_2, a passivating, highly electrically conductive layer is created that protects the contact surface from wear and can extend device life by 10^3 times.

Journal contributions to date:

1) Brand V, Baker M S and de Boer M P 2013 Impact of Contact Materials and Operating Conditions on Stability of Micromechanical Switches *Tribol Lett* **51** 341-56
2) Brand V, Baker M S and de Boer M P 2013 Contamination Thresholds of Pt- and RuO2-Coated Ohmic Switches *J Microelectromech S* **22** 1248-50
3) Brand V and de Boer M P 2014 Oxygen-induced graphitization of amorphous carbon deposit on ohmic switch contacts improves their electrical conductivity and protects them from wear (to appear at the Journal of Micromechanics and Microengineering)
4) Brand V, Saleh M and de Boer M P 2014 Effect of temperature and electrical current on contamination of ohmic microswtich contacts (submitted)

Chapter II: Experimental setup and testing procedure

In this chapter we describe the microswitch test platform chosen for this project as well as the processing required to fabricate it. We then detail the construction of a state-of-the-art chamber for testing the reliability of the devices in clean and contaminated conditions and with different gas backgrounds. Finally, we discuss the procedure used to test the switches. Although these procedures apply to all of our work, the procedural specificities of experiments in subsequent chapters will be mentioned to prevent confusion.

Some of the material below is reprinted from [48] with permission from Springer

2.1 THERMALLY ACTUATED MICROSWITCH TEST PLATFORM

A significant complication in comparing contact materials in Ohmic microswitches is that for each material the entire fabrication process must be repeated [22]. This means that processing variations, for example uncontrolled photoresist residue, besides the material itself may affect the results. We resolve this problem by fabricating polycrystalline silicon (polysilicon) microswitch substructures [31]. In our design, a self-shadowing mask provides in-plane isolation when coated by a blanket metal sputter deposition. Therefore, the only processing difference is in the final coating step, in which the material is varied depending on the sputter target.

The device design and processing are detailed in ref. [31]. The device is schematically represented in **Figure 2.1a** and the top view optical image of the region surrounding the contacts

is shown in **Figure 2.1b**. The circled region in Figure 2.1b shows a contact pair, and all forthcoming images of the contacts will correspond to such a location. A zoomed-out optical view of **Figure 2.1b** and **Figure 2.2a** that shows the entire switch is illustrated in **Figure 2.2b.**

The switching motion is due to a thermal actuator (TA), as seen in **Figure 2.1a**. The TA is mechanically connected to a contact bar through a central shuttle. Joule-heating of the TA legs causes the contact bar to close against the traces. Electrical cross-talk between the legs and the contacts is prevented by a nitride insulator that is built into the shuttle. The SUMMiT V^{TM} process drawing in **Figure 2.2c** illustrates the TA legs and the shuttle, which are under a polysilicon cover. The circuit diagram of the switch is shown in **Figure 2.3**. The TA legs have a total electrical resistance of ≈1000 Ω. There is a 500 Ω resistor in series with the electrical contacts. The voltage applied across the TA (V_{TA}) is always 8 V. The voltage across the contacts ($V_{contact}$) is 5 V unless stated otherwise, whereas V_{out} is the actual voltage across the contacts. V_{out} depends on the measured contact resistance.

The TA is shielded by the polysilicon cover so that its characteristics are not affected by the blanket metal deposition. The polysilicon was sputter-coated by either a 50 nm/450 nm Ti/Pt coating or a 50 nm/450 nm Ti/RuO_2 coating. The sputter target is at a 60 degree angle relative to the switch so that its sidewalls, where mechanical/electrical contact is made, are also covered. The self-shadowing mask structures that prevent electrical shorting of the switch during the metal blanket deposition are shown in cross-section of the contact illustrated by a dashed line from **Figure 2.4a** in **Figure 2.4b**.

After coating, chips are attached to 24 pin dual inline packages (DIPs), shown in **Figure 2.5**, with a Au-Sn eutectic that does not outgas during a subsequent bakeout. Aluminum bond wire

connects the switches to the DIP, but the package is not lidded. All traces and contact pads to which the Al wires are connected can be seen in **Figure 2.2b**. The initial electrical resistance of the devices in this work is on the order of tens of ohms. This is dominated by trace resistance – actual initial contact resistance is 4 to 10 Ω [31].

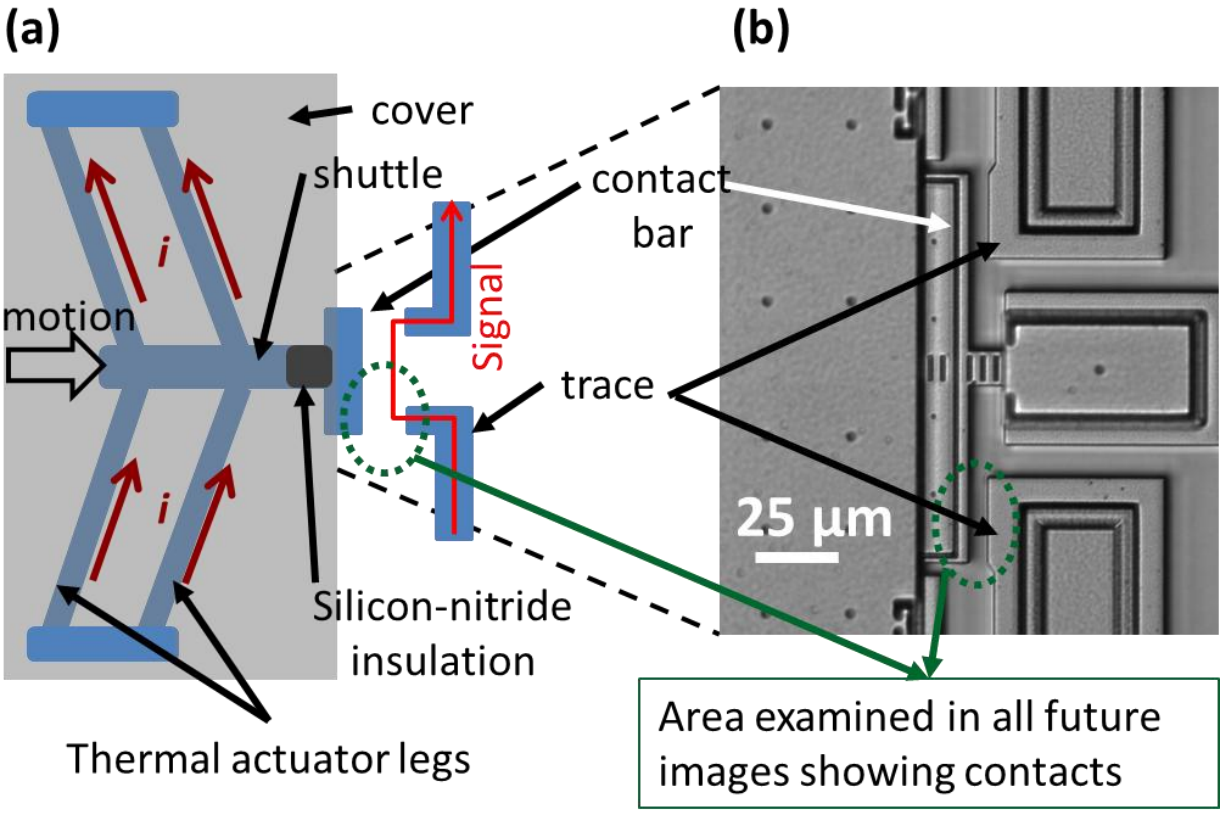

Figure 2.1: (a) Voltage applied across the thermal actuator legs causes joule heating induced thermal expansion of the legs (a silicon-nitride insulator electrically isolates the contact bar from the TA legs). (b) Close-up of area near contact bar (optical image).

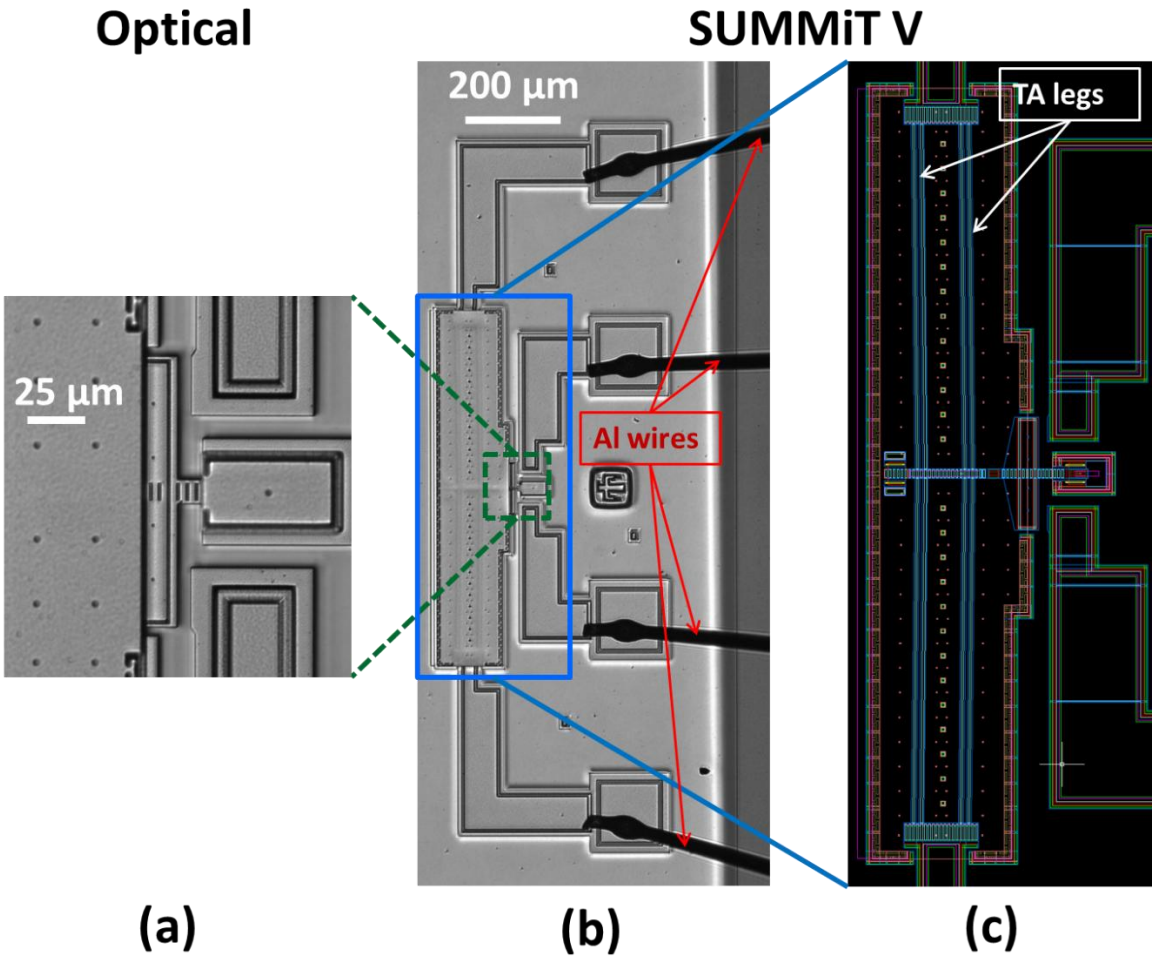

Figure 2.2: (a) The optical image from **Figure 2.1b** is shown again for reference. (b) Zoomed-out version of the previous image shows the entire switch, including the contact pads to which Al wire leads are connected. (c) The SUMMiT V^{TM} drawing shows what the thermal actuator legs and shuttle look like under the polysilicon cover.

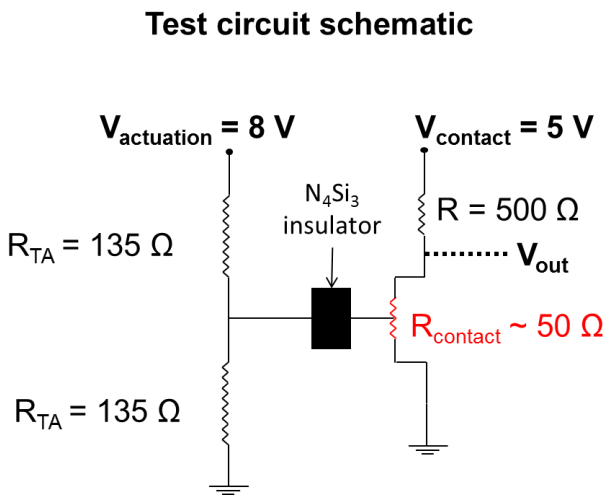

Figure 2.3: Circuit diagram of the ohmic switch.

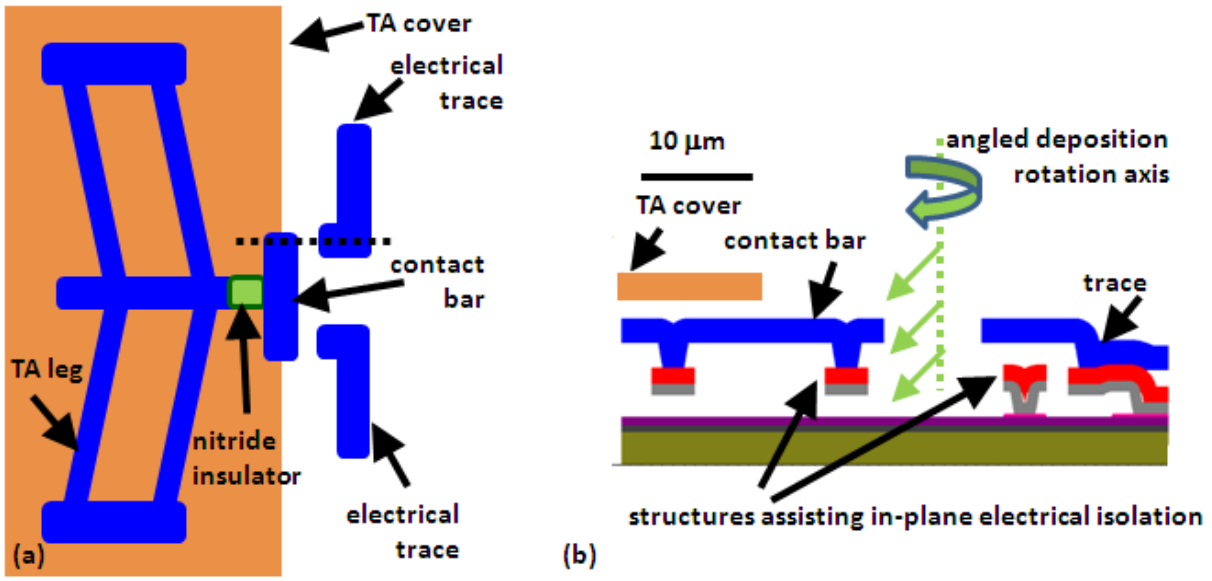

Figure 2.4: (a) Ohmic microswitch schematic with dotted line for the (b) cross section through the contacts that shows how the contact bar and trace overhang and in-plane isolation structures prevent in-plane electrical shorting during metal coating deposition. (Source: [31], reproduced by permission of IOP Publishing).

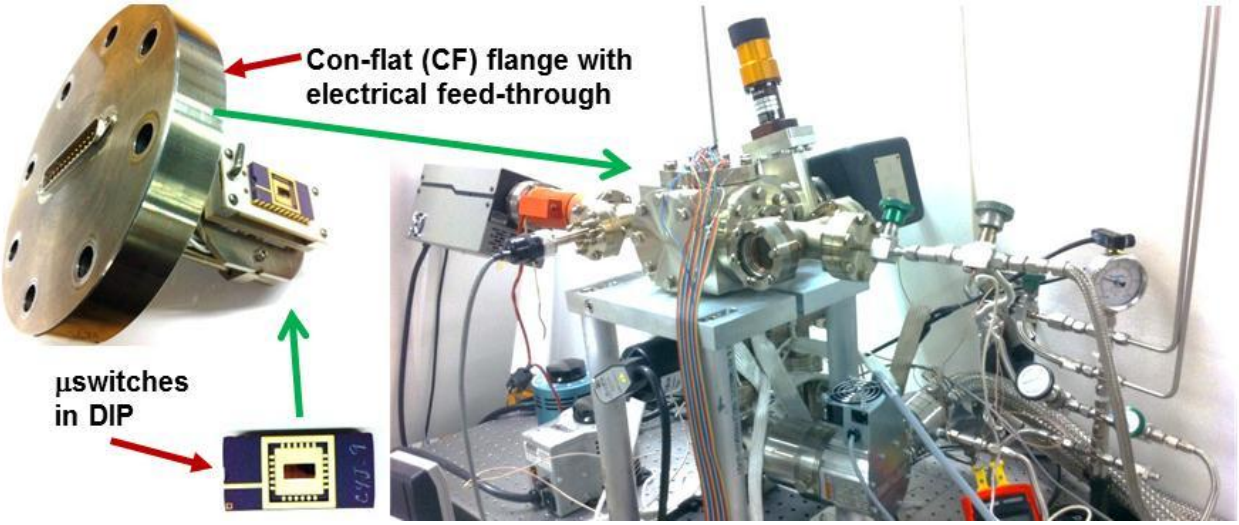

Figure 2.5: Image of main components of the test system.

2.2 SELECTION OF SWITCH MATERIALS, CONTAMINANT SPECIES AND GAS BACKGROUND

We have selected to coat the switch contacts with RuO_2, a conductive oxide, because it is catalytically inactive [46] and so we expect it would not be contaminated easily. RuO_2 also has a high hardness (20 GPa [98]), making it resistant to wear. The cross-section scanning electron microscope image (SEM) of the switch contact in **Figure 2.6a** shows how the RuO_2 layer coats the polysilicon substrate. Notice that the layer thickness on the sidewall contact is roughly half of that on the top surface. Also notice how in **Figure 2.6b**, the cross-section under an overhang shows the thinning of the RuO_2 layer due to the angled deposition. SEM images of the contact sidewall surface of a RuO_2 coated switch that was tested for $300 \bullet 10^6$ cycles are shown in **Figure 2.7**. There is some asperity flattening on the sidewall surface shown in **Figure 2.7c**.

For comparison purposes, we also decided to test Pt coated devices. Pt and other Pt group metals are commonly used in relays [36] because these materials have relatively high hardness and are therefore wear resistant (Pt has a hardness of 5 GPa [99]). Pt is also catalytically active, converting hydrocarbons to cross-linked polymers and potentially graphite [38]. SEM images of the surfaces of two opposing Pt contact sidewalls are shown in **Figure 2.8**. Notice that there is more severe asperity flattening on Pt surfaces (**Figure 2.8**) compared to RuO_2 surfaces (**Figure 2.7**), showing that RuO_2 is more wear resistant.

We decided to use benzene (C_6H_6) as the contaminant in our experiments because it is known to be a strong adsorbent [38]. Furthermore, in the Hermance and Egan telephone relay contacts study [37] it was shown to be amongst the worst contaminants because it produced more deposit than most other volatile hydrocarbons. We chose to use N_2 and N_2:O_2 (1:1 ratio) as the

background gases because the first gas is inert while the latter is similar to air, which is a possible operating environment in real applications. It is also important to compare the two background environments to understand how oxygen effects deposit formation.

Considering that benzene is flammable in the presence of oxygen and because electrostatic sparks or the high temperature of the thermal actuator could potentially become and ignition source, we made sure that the benzene concentrations used in this research were well below the flammability limit. The analysis used to ensure that the experimental setup will be safe is presented in Appendix II.

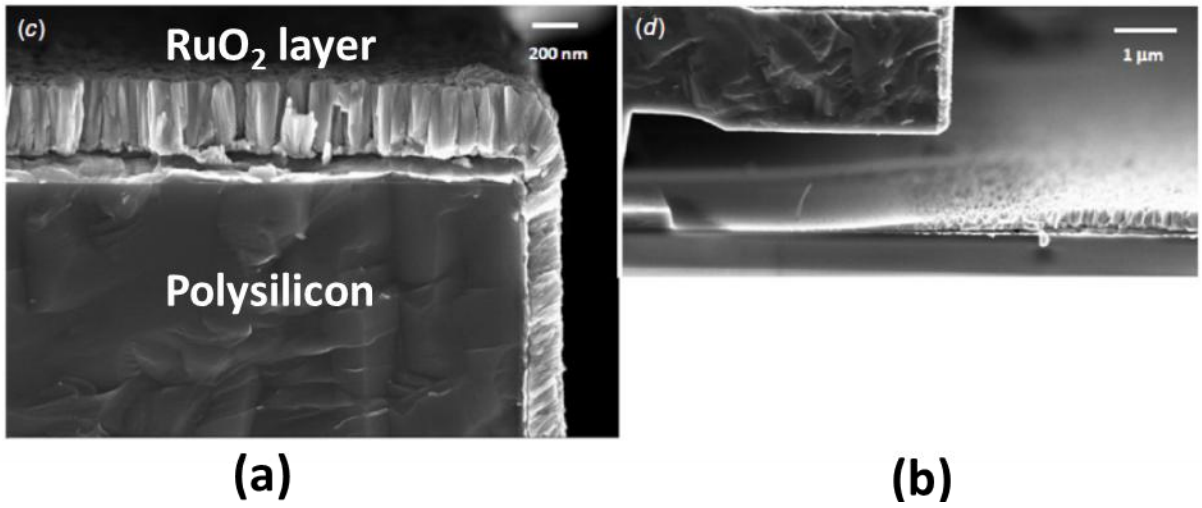

Figure 2.6: (a) A cross-section of a RuO_2 coated contact is showing the polysilicon structure and the RuO_2 layer coating it. (b) The structural overhang causes the thinning of the RuO_2 coating under it during angled sputter deposition (Source: [31], reproduced by permission of IOP Publishing).

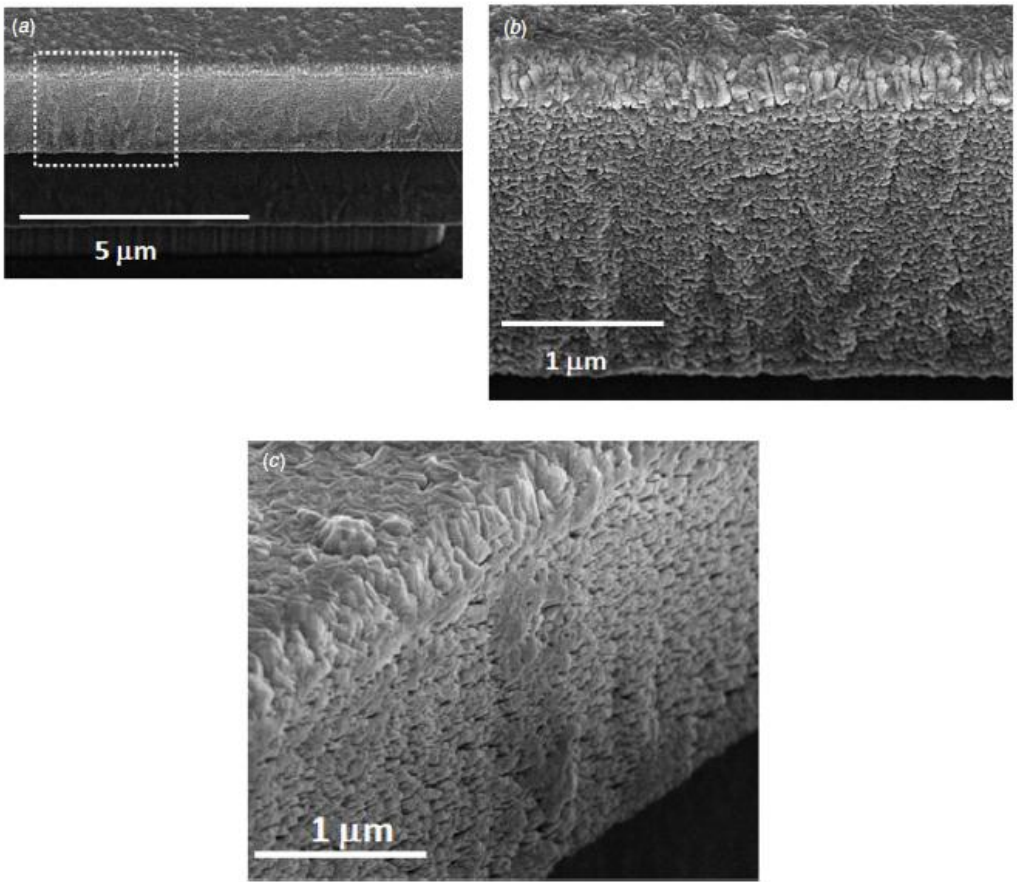

Figure 2.7: The SEM images of RuO_2 coated switch contacts that were cycled for $300 \bullet 10^6$ times are showing some asperity flattening (Source: [31], reproduced by permission of IOP Publishing)

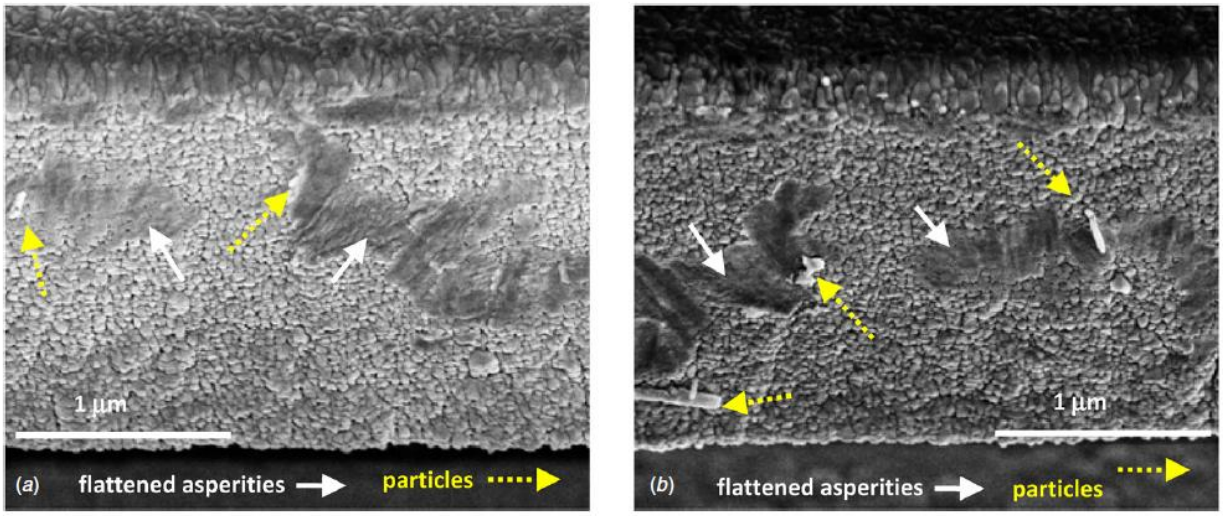

Figure 2.8: The SEM images of the Pt coated contacts show more severe asperity flattening and wear than the RuO_2 contacts in **Figure 2.6** (Source: [31], reproduced by permission of IOP Publishing).

2.3 TEST SYSTEM

To conduct experiments in which surfaces initially can be vacuum baked and in which the background gas and contaminant can be varied, we constructed a test chamber with ultra-high vacuum (UHV) capabilities. The test system and specimen preparation are discussed next with reference to the schematic in **Figure 2.9**. A flange equipped with a 25-pin D-sub connector feedthrough provides the electrical interface to a dual inline package (DIP). **Figure 2.5** shows the DIP package, a ceramic zero insertion force (ZIF) insert is mounted to the conflat flange, which is connected to the test chamber and sealed by a copper O-ring. UHV pressure was first attained as described below in Section 2.4 using roughing, turbomolecular, and ion pumps. The vacuum level was measured with thermocouple and cold cathode pressure sensors, while system temperature was monitored with an internal thermocouple probe. The chamber was then refilled with ultra-high purity gas (UHP), by contaminated gas, or with both. The cylinders with the UHP gases are shown in **Figure 2.10a**, while the one with the contaminant is shown in **Figure 2.10b** (notice it is in a fumehood). **Figure 2.11** shows the leak valve used to control the amount

of contaminant gas that can be introduced into the chamber; it is located in the back of the experimental system. **Figure 2.12** shows the power supplies and other instrumentation used to control the pumps and sensors in the experimental setup.

During an experiment, custom electronics controlled by Labview software measure the electrical resistance (up to $2 \cdot 10^6$ Ω, which is subsequently referred to as the open state) of each switch as a function of the cycle count.

Although most of the experiments discussed in this thesis were performed in an environment that contained the benzene contaminant, it was necessary to have a clean system to begin each experiment in order to maintain a high level of control and repeatability of the testing conditions. Furthermore, most of the devices were pre-tested in UHP gas conditions to establish a resistance baseline value and verify their suitability for the subsequent experiment.

To confirm the presence of benzene and to show that it could also be removed after an experiment, the chamber was pumped to $5 \cdot 10^{-7}$ Torr after filling it with ½ atm N_2-0.25% C_6H_6 (no bakeout). Then, residual gas analysis showed a C_6H_6 peak (**Figure 2.13a**). Another UHV bakeout was performed. The residual gas analysis at this point is shown in **Figure 2.13b**, indicating that benzene is fully removed by the bakeout.

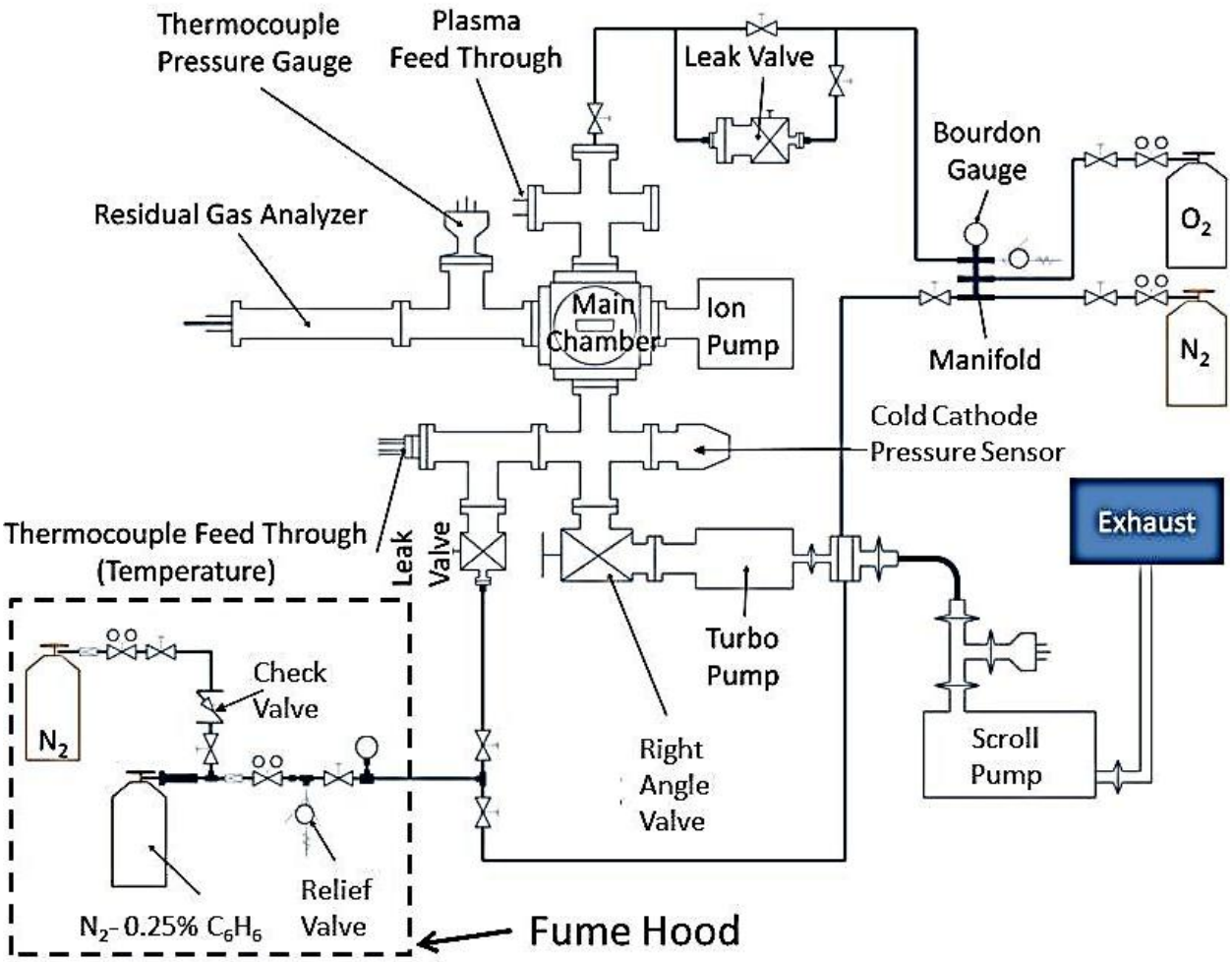

Figure 2.9: Test system schematic.

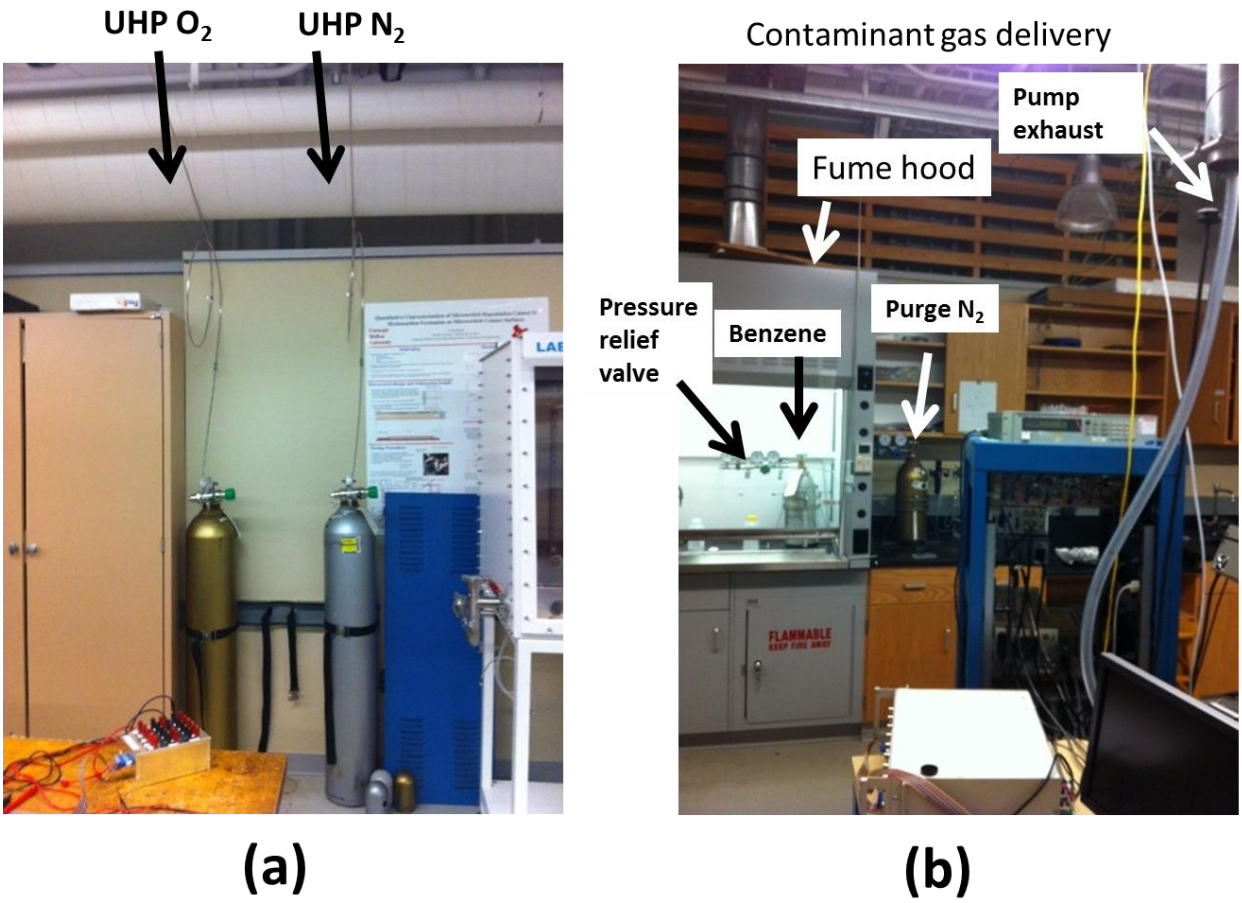

Figure 2.10: (a) UHP O_2 and UHP N_2 delivery. (b) Contaminant gas delivery

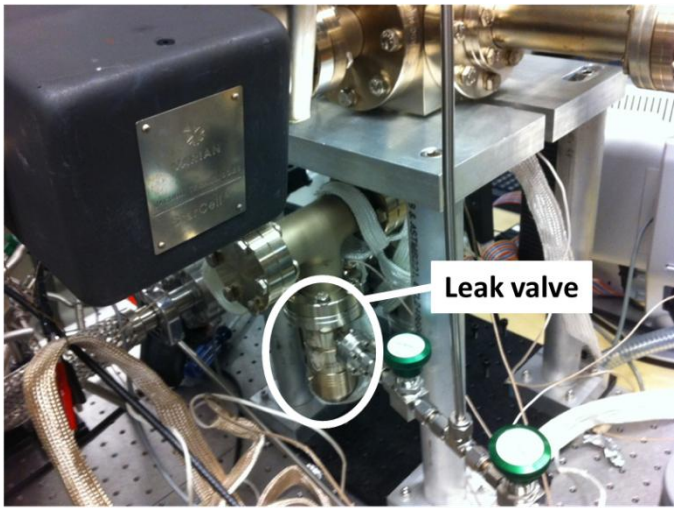

Figure 2.11: Image of the back side of the system, showing the leak valve that can be used to control the quantity of contaminant being introduced into the chamber.

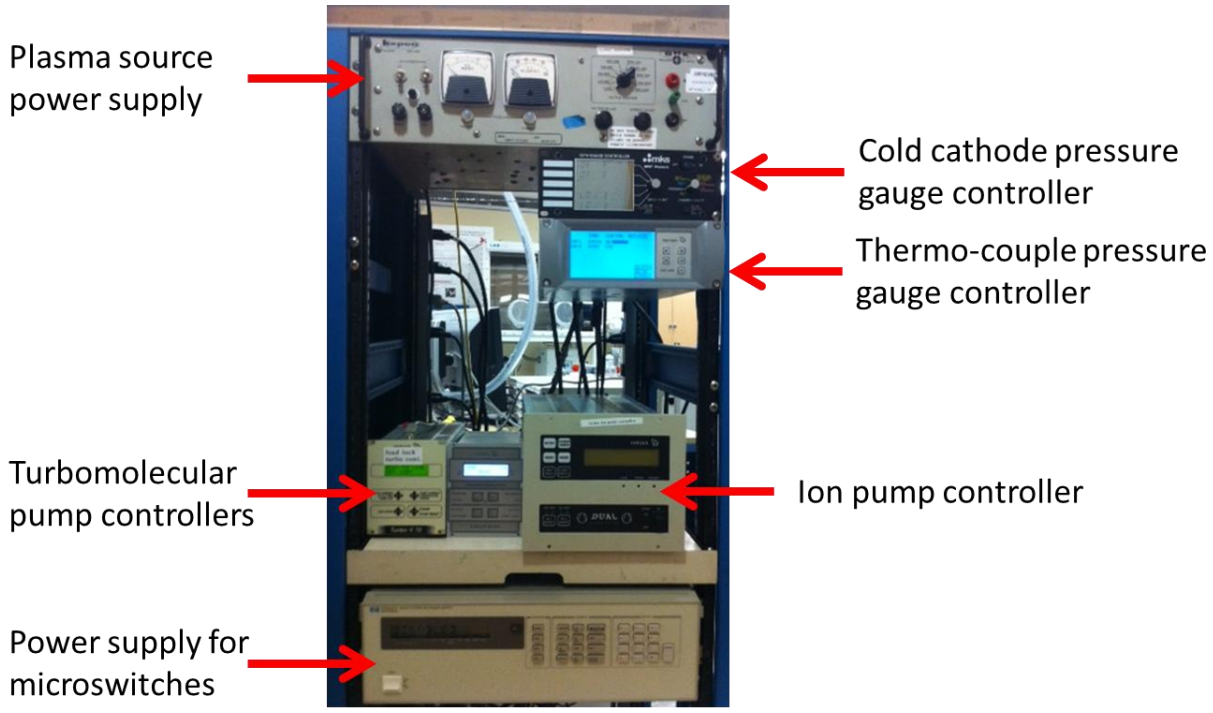

Figure 2.12: Image of the instrumentation used to control the experiments, including power supplies, turbo and ion pump controllers and pressure gauges.

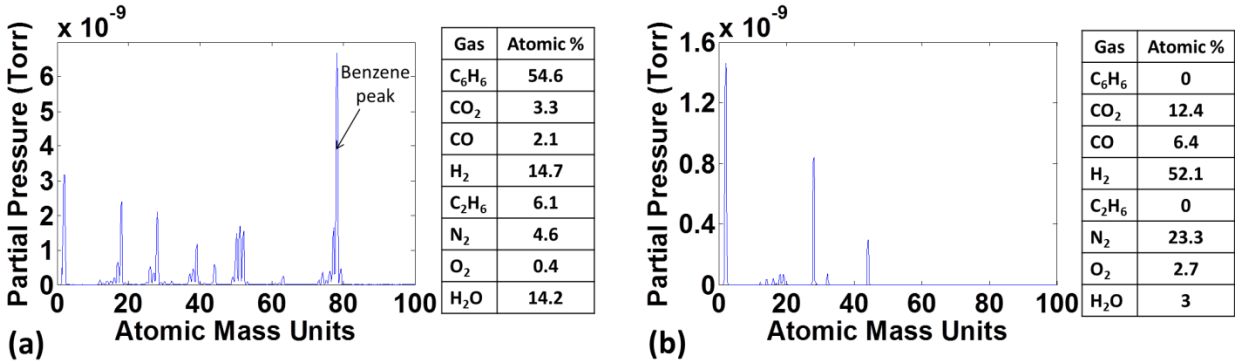

Gas	Atomic %
C_6H_6	54.6
CO_2	3.3
CO	2.1
H_2	14.7
C_2H_6	6.1
N_2	4.6
O_2	0.4
H_2O	14.2

Gas	Atomic %
C_6H_6	0
CO_2	12.4
CO	6.4
H_2	52.1
C_2H_6	0
N_2	23.3
O_2	2.7
H_2O	3

Figure 2.13: (a) The RGA measures substantial quantities of benzene when the system is pumped down to high vacuum after an experiment in a benzene containing environment. (b) Benzene is no longer detected in the system once a bakeout has been done on the chamber.

2.4 TEST PROCEDURE

The test protocol for each experiment began by loading the switches into the chamber and evacuating it with the roughing, turbomolecular, and ion pumps. The chamber was then baked out at 200 ℃ for 24 hours to desorb contaminants. This was followed by cooling the chamber to 25 ℃ and waiting until the system pressure dropped below 10^{-8} Torr.

The experiments were performed at a pressure of ½ atm to avoid opening a system safety check valve that was installed in a fume hood (**Figure 2.9**). To perform experiments in N_2-0.25% C_6H_6 (2,500 PPM C_6H_6), the chamber was filled directly from the N_2-0.25% C_6H_6 cylinder to ½ atm. For the experiments that were performed in N_2-0.25% C_6H_6:O_2 (1,250 PPM C_6H_6), the chamber was filled to ¼ atm from the N_2-0.25% C_6H_6 cylinder and then with an additional ¼ atm from the UHP O_2 cylinder. For experiments that required lower concentrations of C_6H_6, the chamber was filled from the N_2-0.25% C_6H_6 cylinder to a pre-determined level of C_6H_6 (controlled by the leak valve) and then with the UHP N_2 and O_2 to a total pressure of ½ atm such that the N_2:O_2 ratio is about 1:1. A sample procedure for safely filling the test chamber with contaminant is presented in Appendix III. **Table 2.1** presents the abbreviations for gas mixtures used in this thesis.

Table 2.1: The abbriviations for the different gas mixtures used are presented below:

Gas mixture	**Abbreviation**
UHP N_2	N_2
1:1 ratio UHP N_2 : UHP O_2	$N_2 : O_2$
0.25% by volume of C_6H_6 in N_2	N_2-C_6H_6
1:1 mixture of 1 part 0.25% by volume of C_6H_6 in N_2 with 1 part UHP O_2	N_2-C_6H_6:O_2

In all experiments, the switches were closed by applying 8 V across the thermal actuator legs. The resulting contact force was ~200 μN per contact pair [100]. This load is spread over the contact area of 25 x 2 μm^2, though the effective contact area is due to contacting surface asperities and is therefore much smaller, being ~0.0254 μm^2, which is equivalent to a circle with radius of 0.09 μm. The switch layouts for Pt coated devices and RuO_2 coated devices is presented in their respective chips is presented in Appendix IV. While the device response at different actuation voltages is presented in Appendix V.

Two modes of switch operation were used in these studies, namely *cold switching* and *mechanical cycling*. In cold switching experiments, a 5 V cold switch signal was applied across the mechanically closed contacts every cycle. The current was limited by a 500 Ω resistor in series with the switch trace (as shown in **Figure 2.3**), and the electrical resistance measurement was a value calculated from a voltage divider circuit. The resistance was measured each cycle for the first 100 cycles, 100 times per decade until 10,000 cycles and every 1,000 cycles thereafter. In mechanical cycling experiments, no voltage was applied across the contacts except once per decade, when an electrical resistance measurement was made. When testing resistance,

the cycling frequency was 8 Hz, and during cycling it was 250 Hz. This enabled roughly 16 million cycles in a 20 hour test.

After testing, the chamber was evacuated, and the gases were pumped into house exhaust. Post-experimental analysis was performed with scanning electron microscopy (SEM, FEI Model Quanta 600 FEG), Auger spectroscopy (PHI Model 700 Scanning Auger Nanoprobe LS), and Raman spectroscopy (Horiba Scientific Model LabRAM HR Evolution). A 10 kV electron beam was used for SEM, while 5 kV beam with a ~100 nm lateral and <10 nm depth resolution was used for Auger. Raman spectroscopy was performed with a 473 nm (blue) 38 μW laser with a spot size of 0.5 μm.

Chapter III: Impact of contact materials and operating conditions on stability of micromechanical switches

In this chapter, we describe the first experiments [48] using the test platform and test chamber detailed in Chapter II. In particular, we present results on and discuss the cycling of Pt- and RuO_2-coated switches in clean and highly contaminated conditions. Previous literature assumed that hydrocarbons from an uncontrolled environmental source were responsible for creating carbonaceous deposit. Here we introduce the hydrocarbons in a controlled manner to verify this result, and show that deposit growth can be accelerated by a high benzene concentration. We find that in N_2-C_6H_6 both Pt and RuO_2 coated devices experience severe degradation due substantial contaminant buildup, though the RuO_2 devices experience the worst degradation. However, when oxygen is present the RuO_2 coated devices are relatively resistant to contaminant buildup.

We also explore and analyze results for both cold switching and mechanical cycling. We find that in the absence of electrical current a small quantity of highly insulating deposit forms. However, in the presence of electrical current the quantity of deposit produced is greatly augmented, though it is now much more electrically conductive.

Most of the material below is reprinted from [48] with permission from Springer

3.1 EXPERIMENTAL DETAILS

Pt and RuO_2- coated devices were tested in N_2-C_6H_6, where there was ~2,500 PPM C_6H_6. Pt and RuO_2- coated devices were also tested in 1:1 N_2-C_6H_6:O_2, where there was ~1,250 PPM C_6H_6.

Hereafter, N_2-C_6H_6 shall signify a 0.25% by volume benzene in N_2, while N_2-C_6H_6:O_2 shall signify a 1:1 mixture of one part 0.25% by volume of C_6H_6 in N_2 with one part O_2. Pt- and RuO_2–coated devices were cold switched in N_2-C_6H_6 as well as in N_2-C_6H_6:O_2. Both types of devices were also cycled mechanically in the said environments. The experiments performed in this study are summarized in **Table 1**.

Table 3.1: Experiments performed and associated figures

Testing Type	**Pt Coating**	**RuO_2 Coating**
Cold Cycling	N_2-C_6H_6 Fig. 3.1	N_2-C_6H_6 Fig. 3.3
Cold Cycling	N_2-C_6H_6:O_2 Fig. 3.2	N_2-C_6H_6:O_2 Fig. 3.4
Mech. Cycling	N_2-C_6H_6 Fig. 3.5	N_2-C_6H_6 Fig. 3.7
Mech. Cycling	N_2-C_6H_6:O_2 Fig. 3.6	N_2-C_6H_6:O_2 Fig. 3.8

N_2-C_6H_6 signifies 0.25% by volume of C_6H_6 in N_2

N_2-C_6H_6:O_2 signifies a 1:1 mixture of 1 part 0.25% by volume of C_6H_6 in N_2 with 1 part O_2

3.2 RESULTS AND DISCUSSION

3.2.1 Cold switching

3.2.1.1 N_2-C_6H_6 environment/Pt coating

We begin by presenting data on three Pt-coated switches tested in N_2-C_6H_6 for $15 \cdot 10^6$ cycles (**Figure 3.1a**). The electrical resistance, starting at about 15 Ω, began rising after the first 100 cycles, eventually reaching ~300-800 Ω. This increase can be associated with the presence of benzene for two reasons. First, previous data in N_2 only indicated that the resistance remained around 15 Ω up to 100,000 cycles [31]. Furthermore, the switches in **Figure 3.1a** were first cycled for 5000 cycles in N_2 only, and no increase in resistance from the 15 Ω value was observed. The SEM image in **Figure 3.1b** is for one of the tested switches and it shows a deposit accumulation in the contacting area on the sidewalls as well as substantial deposit above and below the contacting surface. EDS indicated much more carbon on the deposit than on any deposit-free area, thereby establishing the carbonaceous nature of the deposit. Note that the majority of the deposit seems to be below the contacting surface, as if it was displaced into the adjacent (non-contacting) sidewall underneath it. There however remains a significant amount of deposit covering the entire thickness of the contacting sidewall inside the circled region of **Figure 3.1b**. It can be difficult to see because it is only slightly darker than the clean regions to the left of the dashed circle. Because the deposit is carbonaceous, it is not a Pt wear product but rather a buildup resulting from the cycling procedure in the presence of the C_6H_6. The SEM images for the other tested switches showed similar quantities of deposit.

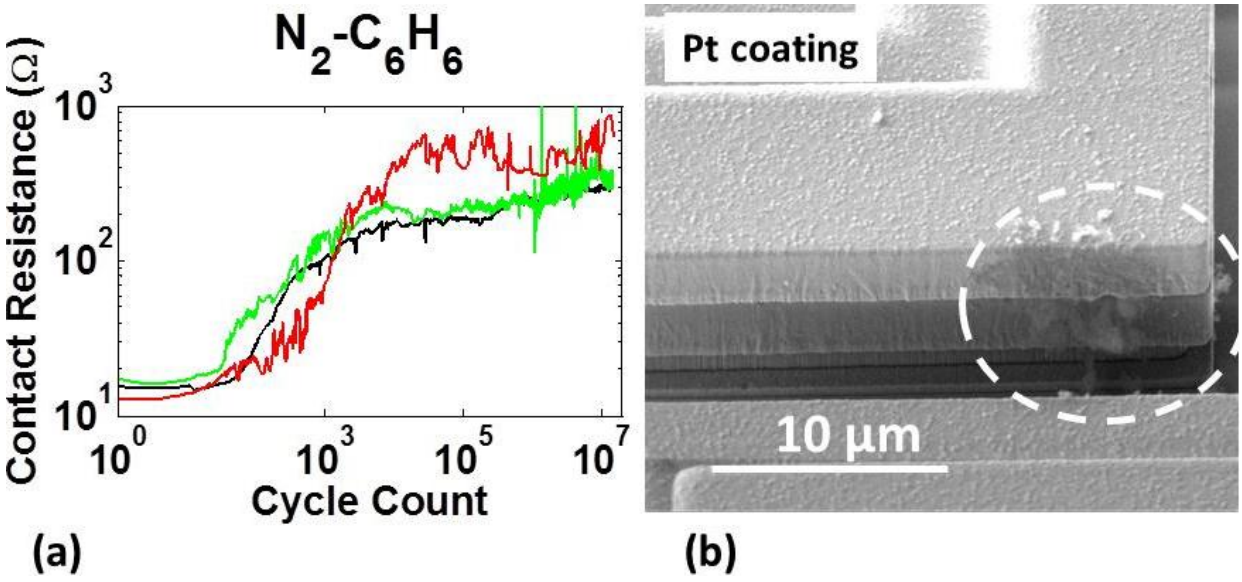

Figure 3.1: (a) Resistance versus cycle count data (cold switching) for three Pt-coated µswitches in N_2-C_6H_6. (b) Post-test SEM image.

3.2.1.2 N_2-C_6H_6:O_2 environment/Pt coating

The next two Pt-coated devices were tested in the presence of N_2-C_6H_6:O_2 for $15 \cdot 10^6$ cycles and the electrical data is illustrated in **Figure 3.2a**. Here the resistance increased to approximately 150 Ω, noticeably less than the 300 to 800 Ω increase observed in the N_2-C_6H_6 experiment. The SEM image in **Figure 3.2b** again shows deposit, but now mainly on the contacting surface and the total amount of buildup appears to be somewhat lower than in the previous case (compare to **Figure 3.1b**). EDS revealed only carbon in the deposit. Tests on Pt-coated devices were also conducted in O_2 only, and resistance increased to ~100 Ω after only ~100 cycles due to oxide buildup. This corroborated previously published data [31]. Therefore, the resistance increase in **Figure 3.2a** cannot exclusively be attributed to the presence of the carbonaceous deposit.

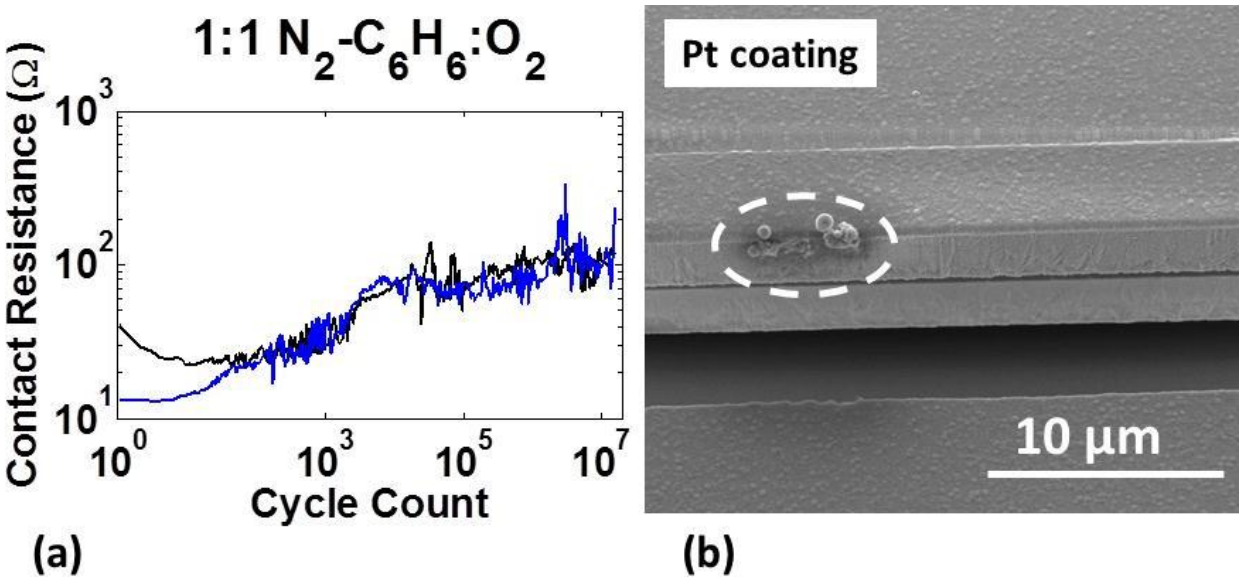

Figure 3.2: (a) Resistance versus cycle count data (cold switching) for two Pt-coated µswitches in 1:1 N_2-C_6H_6:O_2. (b) Post-test SEM image.

3.2.1.3 N_2-C_6H_6 environment/RuO_2 coating

Subsequently, four RuO_2-coated devices were tested in N_2:C_6H_6 for $15 \cdot 10^6$ cycles. As shown in **Figure 3.3a**, the electrical data begins at 25-40 Ω. This initial resistance is higher than the typical initial resistance for Pt-coated devices of 15-20 Ω because of resistance leading up to the contact (trace resistance). This is because the resistivity of RuO_2 is ~50 µΩ-cm, which is roughly five times higher than Pt [31]. Over the course of the experiment, the resistance of each switch approached and then exceeded 10^3 Ω. The SEM image in **Figure 3.3b** shows a large amount of carbonaceous deposit buildup in the vicinity of the contact surface (in comparison to **Figure 3.1b**), correlating with the relatively high resistance increase.

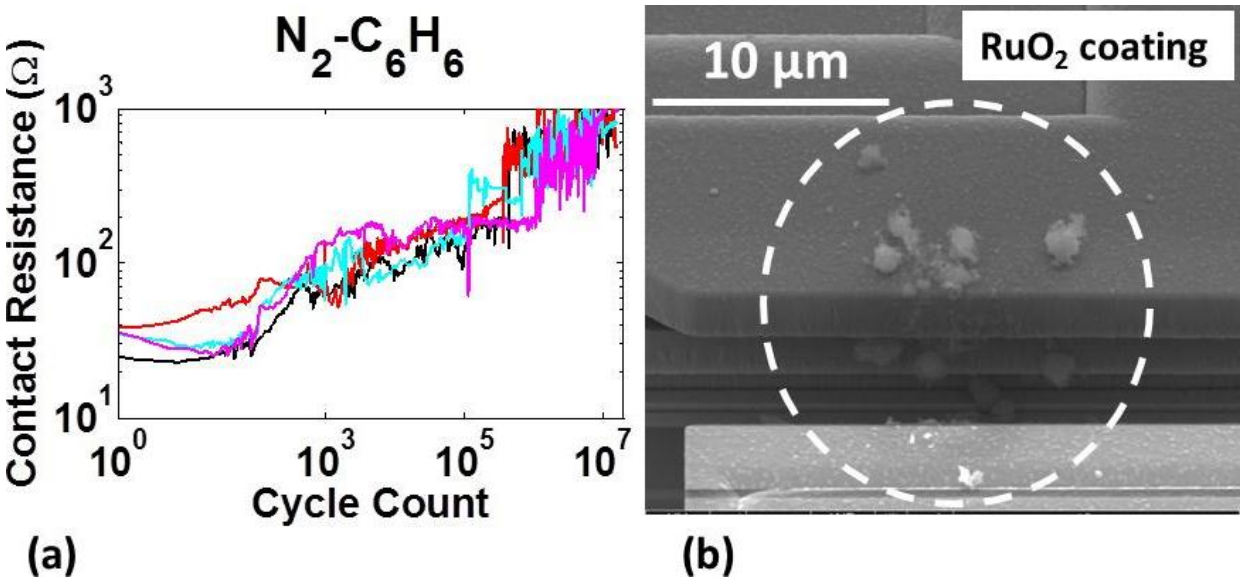

Figure 3.3: (a) Resistance versus cycle count data (cold switching) for four RuO_2-coated µswitches in N_2-C_6H_6. (b) Post-test SEM image.

3.2.1.4 N_2-C_6H_6:O_2 environment/RuO_2 coating

Four RuO_2 coated switches were tested in N_2-C_6H_6:O_2 with a cycle count reaching $7.5 \cdot 10^6$. Starting at 30-40 Ω, the resistance increased moderately during the first 10^3 cycles as seen in **Figure 3.4a**, reaching a plateau at only ~70 Ω that remained constant for the remainder of the experiment. The corresponding SEM image (**Figure 3.4b**) shows a contact surface that is much cleaner than in any of the previously discussed experiments, although a small amount of contaminant can still be observed. This result suggests that if O_2 is present in the system, RuO_2-coated switches are significantly less vulnerable to deposit buildup than Pt coated devices.

3.2.1.5 Summary of cold switching results

To summarize the results thus far, in the absence of O_2, the RuO_2-coated switches are more susceptible to resistance increase and deposit buildup than the Pt-coated devices. However,

when O_2 is present, the RuO_2 contacts are more resistant to resistance increase and deposit buildup compared to the Pt contacts. Furthermore, the resistance of RuO_2 contacts plateaus at the beginning of the experiment (in N_2-C_6H_6:O_2), while for Pt contacts it keeps rising gradually throughout the experiment. EDS showed the deposit is carbonaceous in all cases without revealing details on molecular structure.

Given that 5000 cycles of stable resistance were measured before the contaminant gas was introduced, and resistance increased typically within 10-100 cycles after its introduction, it is clear that the degradation process is accelerated by this test procedure.

The results illustrate that switch performance depends on the background gases involved as well as the switch coating material being used. An important question now arises: To what extent can these effects be attributed to the electrical current being passed through the contacts?

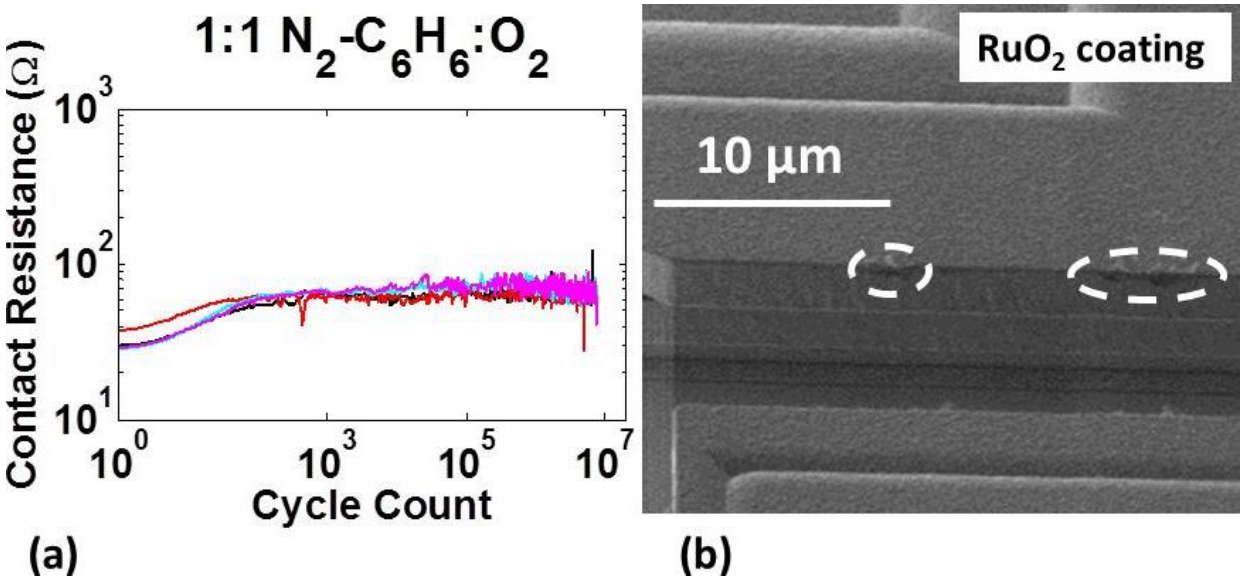

Figure 3.4: (a) Resistance versus cycle count data (cold switching) for three RuO_2-coated µswitches in 1:1 N_2-C_6H_6:O_2. (b) Post-test SEM image.

3.2.2 Mechanical cycling

Current transmission through the contacts may potentially affect deposit formation by increasing temperature (due to joule heating at the contacts) or by inducing an electrical breakdown of the buildup. Therefore, we repeated the above experiments in the absence of current transmission, i.e., by mechanical cycling. To quantify how the resistance changes at the contacts we still needed to pass current through the contacts to measure it, but of course the objective was to limit electrically-induced phenomena. As a compromise, we took electrical measurements only once per decade (i.e. 1^{st} cycle, 10^{th} cycle, 100^{th} cycle, etc.) instead of passing current during every time the switch is closed as is done in cold switching.

3.2.2.1 N_2-C_6H_6 environment/Pt coating

In mechanical cycling of a Pt-coated switch in N_2-C_6H_6, resistance rose gradually until abruptly attaining the open state after 10^4 cycles, as seen in **Figure 3.5a**. Switch data from the corresponding cold switching experiment (from **Figure 3.1a** above) is also included to illustrate how it compares with this experiment; notice how the resistance rise for the first 10^3 cycles is of similar magnitude in both cases, but behaves rather differently later on. In the SEM image of the mechanically cycled switch (**Figure 3.5b**), we see a darker region at the center of the contact that is in fact the carbonaceous deposit (confirmed by EDS).

Also, two additional Pt-coated switches were mechanically cycled in the same environment but without any electrical measurements. The SEM images of those switches after testing showed about the same amount of similar looking deposit as on the mechanically-cycled switch that experienced electrical measurements once per decade. This demonstrated that the

occasional electrical measurements did not noticeably change the amount of deposit in this type of experiment. The amount of deposit associated with mechanical cycling was small compared to the deposit created in the corresponding cold switching experiments that were done in the same environment (see **Figure 3.1b**). However, this small amount of deposit was apparently sufficient to electrically insulate the contacts, whereas the comparatively profuse deposit accumulation observed in **Figure 3.1b** merely increased resistance by several hundred ohms.

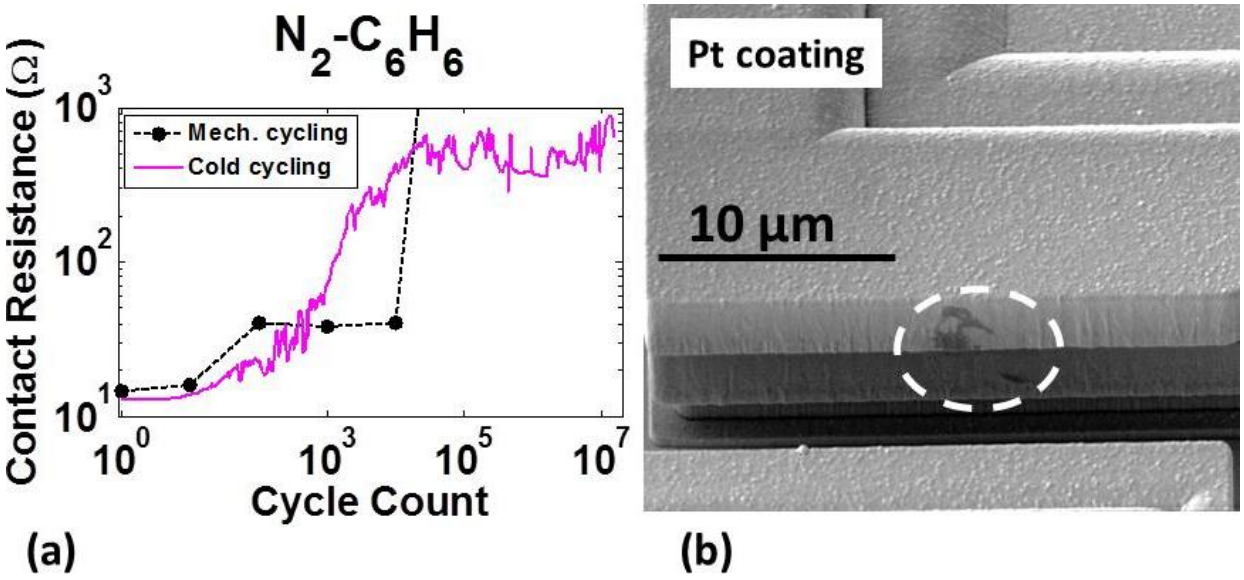

Figure 3.5: (a) Resistance versus cycle count data (mechanical cycling) for one Pt-coated µswitch in N_2-C_6H_6 (device from **Figure 3.1a** also shown for comparison). (b) Post-test SEM image.

3.2.2.2 N_2-C_6H_6:O_2 environment/Pt coating

The same experiment was now performed on two Pt-coated switches in N_2-C_6H_6:O_2. As shown in **Figure 3.6a**, the resistance rose gradually to 95 Ω after $15 \cdot 10^6$ cycles for one device and to the open state for the other. The corresponding cold-switching experiment (as shown by the solid line in **Figure 3.6a**– taken from **Figure 3.2a**) had a comparable resistance increase though it never achieved the open state. The SEM image corresponding to the mechanically-

cycled switch that reached 95 Ω (**Figure 3.6b**) again showed a significantly smaller amount of deposit than what was observed in the cold switching experiment that was done on a Pt-coated switch in the same environment (compare with **Figure 3.2b**). We note that the image for the other mechanically-cycled switch looked very similar.

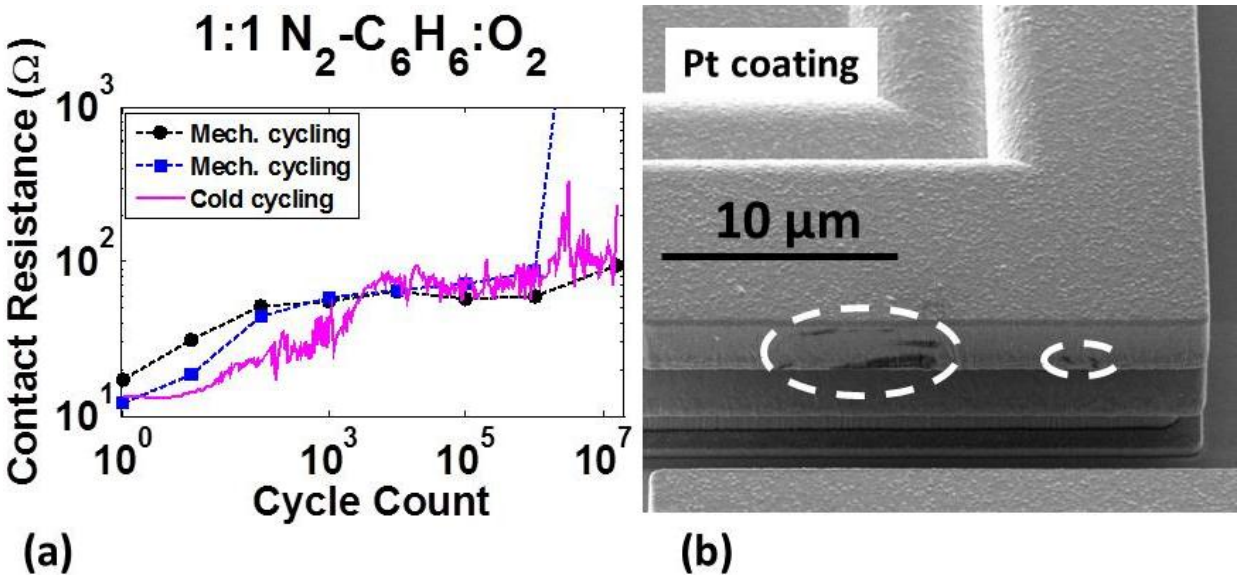

Figure 3.6: (a) Resistance versus cycle count data (mechanical cycling) for two Pt-coated µswitches in N_2-C_6H_6:O_2 (device from **Figure 3.2a** also shown for comparison). (b) Post-test SEM image.

3.2.2.3 N_2-C_6H_6 environment/RuO_2 coating

Next, two RuO_2 coated switches were tested by cycling them mechanically in N_2-C_6H_6 and again we measured the resistance only once per decade, as shown in **Figure 3.7a**. The resistance for both switches started under 40 Ω and after only 10^3 cycles it increased to the open state. By comparison, a RuO_2 device that was cold switched in the same conditions showed a steadily rising resistance that never abruptly reached open state (solid line in **Figure 3.7a** – taken from **Figure 3.3a**). The SEM image for one of the mechanically tested switches (**Figure 3.7b**) shows a small amount of deposit that is significantly lower than what can be found in the corresponding

image for the cold switching experiment (**Figure 3.3b**). Furthermore, the observed buildup (from mechanical cycling) has the form of a transparent 'flake' that is suspended from the edge of the contact. In comparison the corresponding cold switching experiment image showed comparatively large pieces of deposit that are often assembled into a spherical or elliptical shapes.

Also, for one of the mechanically tested switches in **Figure 3.7a**, the resistance dropped from open state to ~200 Ω, suggesting the deposit was broken down electrically during the measurement process.

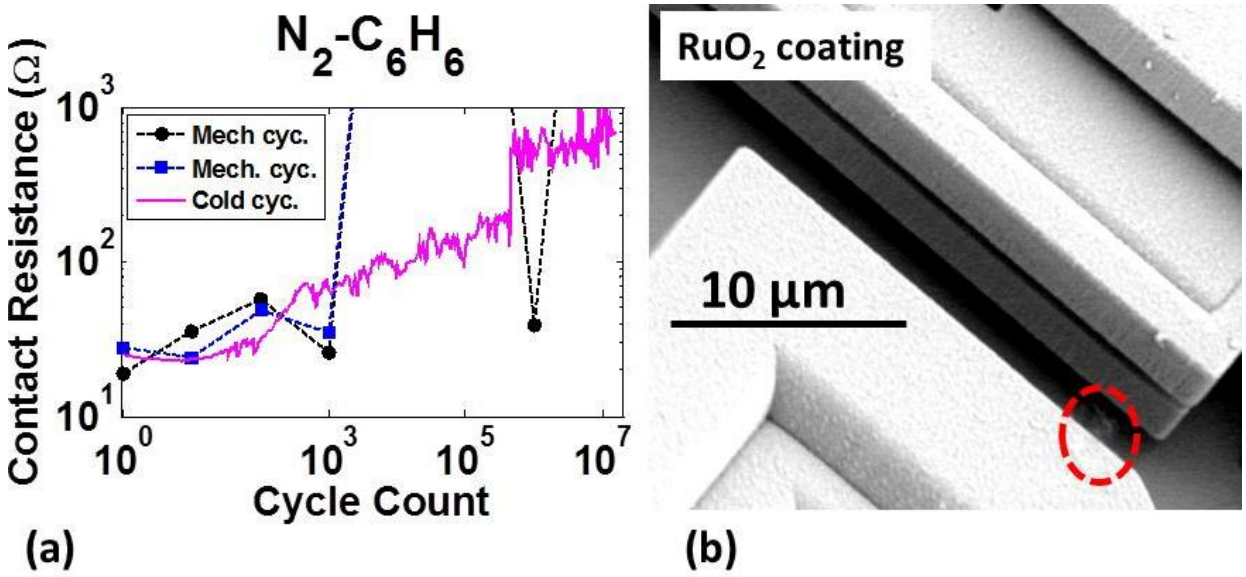

Figure 3.7: (a) Resistance versus cycle count data (mechanical cycling) for two RuO_2-coated µswitches in N_2-C_6H_6 (device from **Figure 3.3a** also shown for comparison). (b) Post-test SEM image.

3.2.2.4 N_2-C_6H_6:O_2 environment/RuO_2 coating

Finally, the same experiment was repeated on three RuO_2-coated switches in N_2-C_6H_6:O_2, as shown in **Figure 3.8a**. The resistance started at ~35 Ω and reached the open state after 10^5

cycles for two devices and after 10^6 for the third. Prior to the abrupt electrical failure, the resistance increase in all three devices did not exceed the values found in the corresponding cold switching experiment, as shown by the solid line in **Figure 3.8a**. From the SEM image of the mechanically tested switches (**Figure 3.8b** shows one of them) it is not clear where the buildup occurred. Considering that no other defects are visible on the surface of the contact, it may be suggested that a small amount of carbonaceous deposit is present and that it was sufficient to drive the resistance up to the open state.

3.2.2.5 Summary of mechanical cycling results

In these mechanical-cycling experiments our most significant observations are that the amount of deposit buildup is much lower for the mechanically-cycled switches than for the cold switched ones but that mechanically-cycled devices generally exhibit a larger resistance increase.

We also see that, until they attain the open state, the mechanical cycling experiments show electrical degradation trends that generally follow those of the cold switching experiments (see **Figures. 3.5-3.8**). For example, referring to **Figures. 3.5a & 3.6a**, which show both mechanical cycling and cold switching electrical results for Pt, the switches degrade more quickly and severely in N_2-C_6H_6 than in N_2-C_6H_6:O_2. **Figures 3.7a and 3.8a** show both mechanical cycling and cold switching electrical results for the RuO_2-coated switches. In this case, switches tested in N_2-C_6H_6 (**Figure 3.7a**) exceed 100 Ω in fewer cycles than the devices tested in N_2-C_6H_6:O_2 (**Figure 3.8a**).

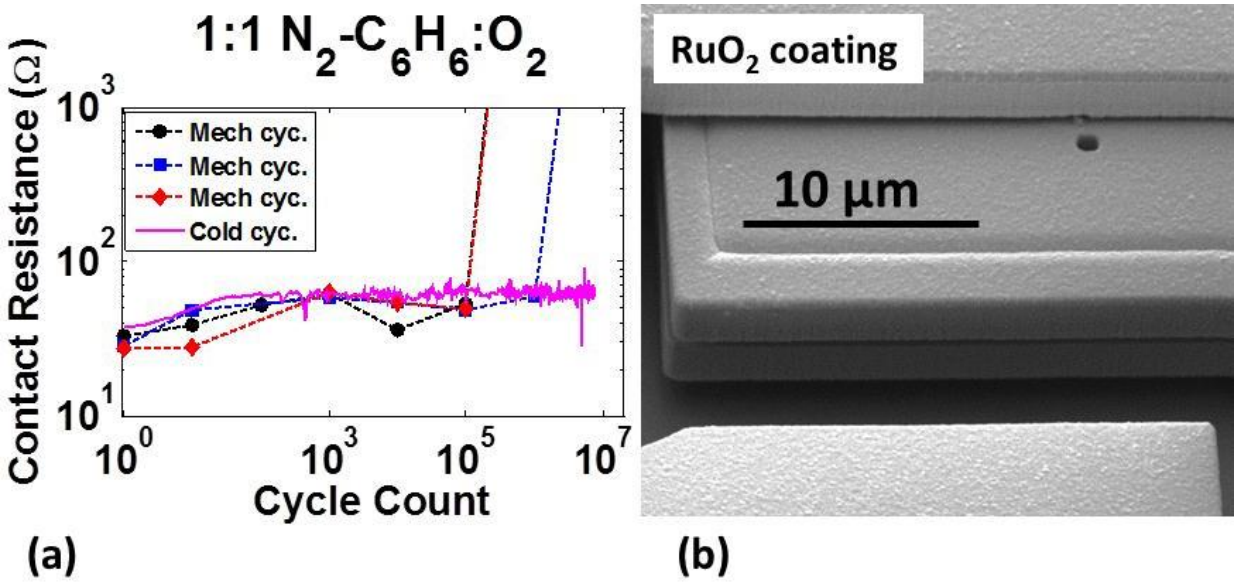

Figure 3.8: (a) Resistance versus cycle count data (mechanical cycling) for three RuO_2-coated µswitches in N_2-C_6H_6:O_2 (device from **Figure 3.4a** also shown for comparison). (b) Post-test SEM image

3.3 ANALYSIS AND INTERPRETATIONS

3.3.1 Carbonaceous deposit becomes electrically conducting after dielectric breakdown

The deposit produced in mechanical cycling was sufficient to increase the contact resistance to open state during nearly every experiment. This result strongly suggests that the deposit is an electrical insulator, agreeing with literature [37, 44]. However, the maximum resistance values achieved in the cold switching experiments rarely exceeded 10^3 Ω, despite producing a much larger quantity of deposit than mechanically cycled devices. We know from EDS that the deposit contains carbon. Considering that this deposit forms only in the presence of mechanical loading, it is most likely polymeric as identified in other literature [37]. However, as there is no rubbing (or wiping) involved here (since the contacts experience normal loading during switch closure) we decided to refer to this deposit as tribopolymer (as opposed to friction-polymer [37]).

3.3.1.1 Unambiguous evidence that tribopolymer becomes conducting during cold switching

The top view optical image in **Figure 3.9** illustrates a RuO_2-coated switch in the un-actuated (nominally open) state that was cold-switched in N_2-C_6H_6 for $15 \cdot 10^6$ cycles. Enough deposit was created to establish tribopolymer bridges across both contacts. The length of each bridge is ~3.5 μm. Taking into account that this length is half of what it normally would be for a clean (untested) switch in the open state, it is clear that the two bridges are able to prevent the contact bar from retreating all the way back to its relaxed state. In this un-actuated position, the electrical resistance across the switch is 505 Ω, unambiguously demonstrating that the tribopolymer itself becomes conducting. This proves that mechanical penetration of asperities through the contaminant film is not necessary to transmit current in cold switching. When this switch was actuated, the resistance dropped to 474 Ω, likely because bridge cross-sectional area increases.

Considering that the initial resistance of this switch was 36 Ω, the tribopolymer (TP) resistance in the un-actuated state is R_{TP}=469/2=235 Ω (accounting for two resistors in series). Using this information and the geometry of the buildup, the resistivity, ρ_{TP} of the deposit can be estimated as

$$\rho_{TP} = R_{TP}\frac{A}{l} \qquad (3.1)$$

where A is the cross sectional area of the bridge and l is its length in the un-actuated state. Detailed SEM images of this region (see inset in **Figure 3.9** for a top view image) enabled us to

approximate *A* as a rectangular cross section of ~1 μm width and thickness ~1 μm. Using these values we obtain a resistivity of $6.7 \cdot 10^{-5}$ Ω*m, being on the order of the resistivity of graphite [101]. It is well known that the electrical breakdown of polymers transforms their original molecular structure into a conductive material [92]. This is likely accomplished with an electric-field induced electron avalanche [92]. For example, the electrical breakdown of polyethylene can produce a conducting graphite path through the polymer [102].

It is important to distinguish the electrically broken-down tribopolymer described here from the conducting carbon deposit observed in higher voltage hot switching [43, 103, 104]. In hot-switching, arcing that occurs before the switch is closed or when it opens, thermally disintegrates adsorbed hydrocarbons into a pure carbon deposit that has a resistivity of the same order measured here [104].

As will be shown in Section 3.3.2, the temperature rise experienced by the contacts in our cold-switching experiments is too low to cause thermal disintegration of the tribopolymer. Furthermore, the voltage bias across our contacts is a maximum of 5 volts, being too low to initiate arcing [84].

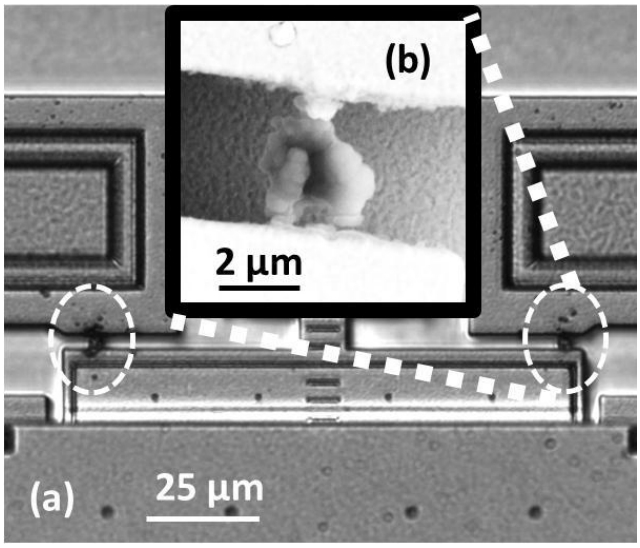

Figure 3.9: (a) (Optical image) Tribopolymer electrically connects the trace to contact bar demonstrating that initially insulating tribopolymer undergoes an electrical breakdown. (b) Inset (SEM image).

3.3.1.2 The tribopolymer is conducting due to electrical breakdown even in mechanical cycling

Even for switches cycled mechanically, the resistance measurements may cause a dielectric breakdown of the tribopolymer, especially during the first few measurements when the amount of deposit is still a very thin layer. To gauge this, we conducted an experiment on Pt-coated switches in N_2-C_6H_6. Here, a given switch was *only* mechanically cycled until the end of the test. Before cycling, the resistance was ~10 Ω. Once cycling started, the electrical measurement was *only* after the final cycle for each device, which was after 200, 10^4, $3•10^5$ and $16•10^6$ cycles. After 200 cycles, the resistance was 35 Ω, and after 10^4 cycles it was 68 Ω. After $3•10^5$ cycles, the resistance measured an open circuit. To check this result, we repeated the measurement twice on that switch. The first repeat still gave an open state, but the second gave 582 Ω, suggesting an electrical breakdown. At $16•10^6$ cycles the resistance remained in the open state even after several measurements.

This discussion helps explain why the resistance values obtained during mechanical testing (**Figures 3.5-3.8**) closely resemble the trends seen in cold switching up until the open state resistance measurement. Specifically, during the first few cycles, when the amount of deposit is still a very thin layer, the resistance measurements provide enough electric field to break down this insulating layer. However, as the measurements became less frequent (due to their logarithmic occurrences), sufficient tribopolymer built up to prevent electrical breakdown, thereby causing the abrupt rise in resistance (i.e. the open state).

It is worth noting that the fluctuation in the resistance data (as seen in **Figures 3.1-3.8**) most likely reflects the amount of electrically broken-down tribopolymer at the contacting interface during the particular measurement. The resistance rises as more tribopolymer is created but can also drop when tribopolymer pieces flake off from the contact interface. Notice how in **Figure 3.3b** numerous pieces of deposit are found above and below the contacting interface. The large number of switch cycles inevitably provides numerous opportunities for the interface to be randomly altered.

3.3.2 Is temperature rise responsible for increased tribopolymer production in cold switching?

The increase in tribopolymer production during cold switching relative to mechanical cycling could be the consequence of a possible temperature rise at the contacts. In this section we will demonstrate that this temperature rise is too small to affect tribopolymer production.

The classical approach for estimating a temperature rise was presented by Holm in 1967 [84] and it entails using the initial contact temperature (before passing current) and the voltage bias

across the contacts to calculate the new temperature. Here, diffusive electron transport through a narrow constriction (i.e. the contacting asperities) takes place. The voltage across this constriction in turn correlates with contact temperature. This approach, although developed for large scale contacts, was implemented recently by Broue et al. for microswitches [105]. Upon trying to utilize this method with our devices we obtained a reasonable number for our lowest resistance measurements but unrealistic values on the order of 10^4 K when the contact resistance was 500 Ω.

Jensen et al. proposed a modified Holm approach that will be valid for contact radii that are smaller than the electron mean free path [42]. Then, electron transport through the contact is ballistic rather than diffusive. Less electron scattering generates less heat, therefore temperature difference is less. This model predicts a much lower temperature change for a given voltage than the Holm model. However, the model requires a key assumption which is that metal to metal contact remains. In our experiments this assumption cannot hold because we clearly see a tribopolymer deposit separating the contacts in cold switching.

The resistance measured is a sum of the trace resistance and the contact resistance, R_c, which is of the form [47]

$$R_c = R_{c,intrinsic} + R_{c,interface} \qquad (3.2)$$

where $R_{c,intrinsic}$ is the intrinsic contact resistance due to spreading resistance, whereas $R_{c,interface}$ is the interface resistance, being by far the dominant component in our experiments (i.e. the intrinsic component is always under 10 Ω, while the interface component occasionally exceeds 1,000 Ω). Hence, $I^2 \cdot R_c$ (where I is electrical current) is the heat source that we need to account for in order to calculate the change in contact temperature.

The shape factor heat transfer analysis [90] was found to be the most suitable approach. The relation is:

$$T_{max} - T_0 = \frac{q}{Sk} \qquad (3.3)$$

Here T_{max} is the temperature of the contact surface, T_0 is room temperature (~22 ℃), q is the power being generated (in watts), k is the thermal conductivity of the contact (50.0 and 71.6 W/m•K for RuO_2 and Pt, respectively) and S is the shape factor. We approximate the tribopolymer deposit as a disk on the semi-infinite body (the contact surface), thus having a shape factor of $2D$, where D is the diameter of the disk (we estimate it to be $2 \cdot 10^{-6}$ m on average) [90]. The power generated at the contacts is:

$$q = I^2 R_c = \left(\frac{V}{R_{series}+R_c}\right)^2 R_c \qquad (3.4)$$

where V designates the 5 V applied across contacts (that have resistance R_c) *and* the 500 Ω current limiting resistor in series with the contacts (R_{series}), as discussed in Section 2.1 of Chapter II. We must divide $I^2 \cdot R_c$ by four to account for the fact that there are two semi-infinite bodies to which the 'tribopolymer disk' is conducting heat (introducing a factor of 1/2) and that there are two pairs of contacting surfaces that comprise R_c (introducing another 1/2 factor). By combining the last two equations we get:

$$T_{max} - T_0 = \frac{R_c}{4Sk}\left(\frac{V}{R_{series}+R_c}\right)^2 \qquad (3.5)$$

This simple relationship enables us to plot the contact temperature rise as a function of measured contact resistance, the range of which is selected to be between 0 and 3,000 Ω to reflect our data. Notice that as R_c approaches open state, $\Delta T = T_{max} - T_0$ approaches zero. This

analysis shows that the maximum temperature rise after switch closure for the RuO_2 switch is 16^0C, while for the Pt switch it is 11 ^{0}C. In both cases it reaches that level as R_c approaches 500 Ω, as shown in **Figure 3.10**. These calculations imply that the temperature difference between RuO_2 and Pt coated switches does not exceed 5 ^{0}C.

The highest contact temperature estimates attained in this analysis (38 ℃ for RuO_2 and 33 ℃ for Pt) suggest that heat does not contribute to tribopolymer growth and its electrical conductivity onset, especially in light of evidence that frictional polymer formation is not affected by temperature in the range from -60^{0}C to 150^{0}C [37].

Hence, we conclude that temperature rise is unlikely to be the reason for why more tribopolymer forms during cold-switching than mechanical switching. More work is needed to understand why this happens.

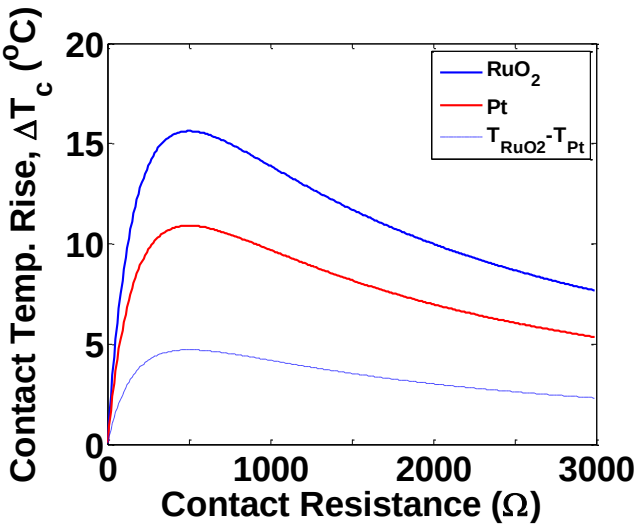

Figure 3.10: Shape factor analysis to estimate the temperature increase at the contact surface as a function of resistance for Pt and RuO_2 contacts (the dashed line illustrates the temperature difference between RuO_2 and Pt contacts).

3.3.3 Energy balance can explain the increase in tribopolymer production during cold switching

When mechanical cycling or cold switching in N_2-C_6H_6, the benzene adsorbs on the surface of the contacts and then polymerizes at the contact interface to form the deposit we see in **Figures 3.1-3.8**. It appears that mechanical loading is critical to tribopolymer formation because the deposit does not form away from the area where the mechanical loading occurs. Furthermore, the tribopolymer is found near certain locations on the contact rather than being spread out throughout the entire contact surface (see **Figure 3.2b** for example), thereby suggesting it originated at the surface asperities that form contact. This result could be rationalized by a lower energy state of the formed tribopolymer as compared to the adsorbed benzene, where the mechanical load helps overcome the activation energy barrier between the two states. Though intriguing, the effect of mechanical loading on chemical reactions is a well-established phenomenon. Porter and Casale [106] and Caruso et al. [107] summarize research exploring how mechanical stress enables chemical reactions by breaking and reforming bonds in many different polymers.

We conjecture that the underlying reason why more tribopolymer forms after electrical breakdown is that an even larger energy drop for the final products from initial reactants occurs during deposit buildup. Hence the higher thermodynamic driving force causes more deposit to be created. We illustrate this concept schematically in **Figure 11**, where the Gibbs free energy of formation is plotted against the reaction coordinate. We propose that the original (insulating) tribopolymer has a lower Gibbs free energy of formation than the adsorbed benzene and that the electrically broken down (or conducting) tribopolymer has the lowest Gibbs free energy of formation. We then suggest that the mechanical stress at contact closure enables the system to

overcome the first activation energy barrier and that the passage of electrical current through the contacts helps overcome the second barrier. Finally, the conducting tribopolymer, being energetically the most stable, remains. Both parts of this process can be summarized with the dashed heavy line shown to present a more general model that could be applicable to cold switching and mechanical cycling.

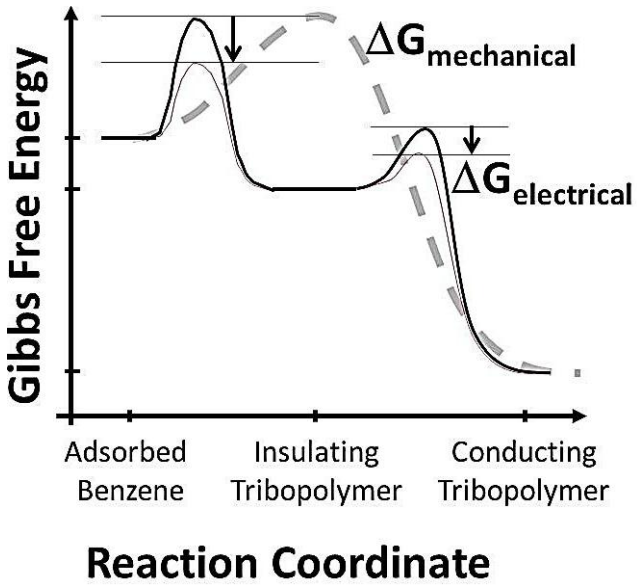

Figure 3.11: Schematic model that is consistent with the experimental data showing how the activation energy barrier to form tribopolymer is reduced by mechanical stress and then again by the electrical current.

We expand upon this qualitative model in **Figure 12a**. Once again the abscissa is the reaction coordinate, while the ordinate is the Gibbs free energy. The fact that cold-switched RuO_2 coated devices produce more tribopolymer (and see higher resistance) than Pt coated devices could be related to their respective hardness values (20 GPa for RuO_2 [98] and 5 GPa for Pt [99]). The higher hardness of RuO_2 would result in a smaller effective contact area and correspondingly a higher mechanical stress than in the case of Pt [27]. This higher mechanical stress would therefore reduce the polymerization activation energy for RuO_2 coating more than

for the Pt coating ($\Delta G_{RuO2}(N_2) > \Delta G_{Pt}(N_2)$), thus enabling more tribopolymer build-up on the RuO_2 contact.

It is worth noting that another residue buildup mechanism was proposed [26] where charged molecules or molecules with appreciable dipole moments migrated towards the contacts due to the local electric field. That work suggested that current flow through the contacts ionized or induced a dipole on a self-assembled monolayer (SAM) and the affected molecules then migrated towards the contacts where the electric field was greatest. A ball-on-flat contact geometry undergoing hot switching was used.

This mechanism is not likely to operate here because firstly we see tribopolymer buildup at the contacts (during mechanical cycling) when no electric field is present. Secondly, if this tribopolymer undergoes dielectric breakdown during a resistance measurement (as discussed in Section 3.3.1.2), the resistance values are close to cold-switching data at the corresponding number of cycles (see **Figures 3.5-3.8**). This resemblance would suggest that cold-switching residue is merely electrically broken-down tribopolymer rather than an agglomeration of migrated hydrocarbon molecules.

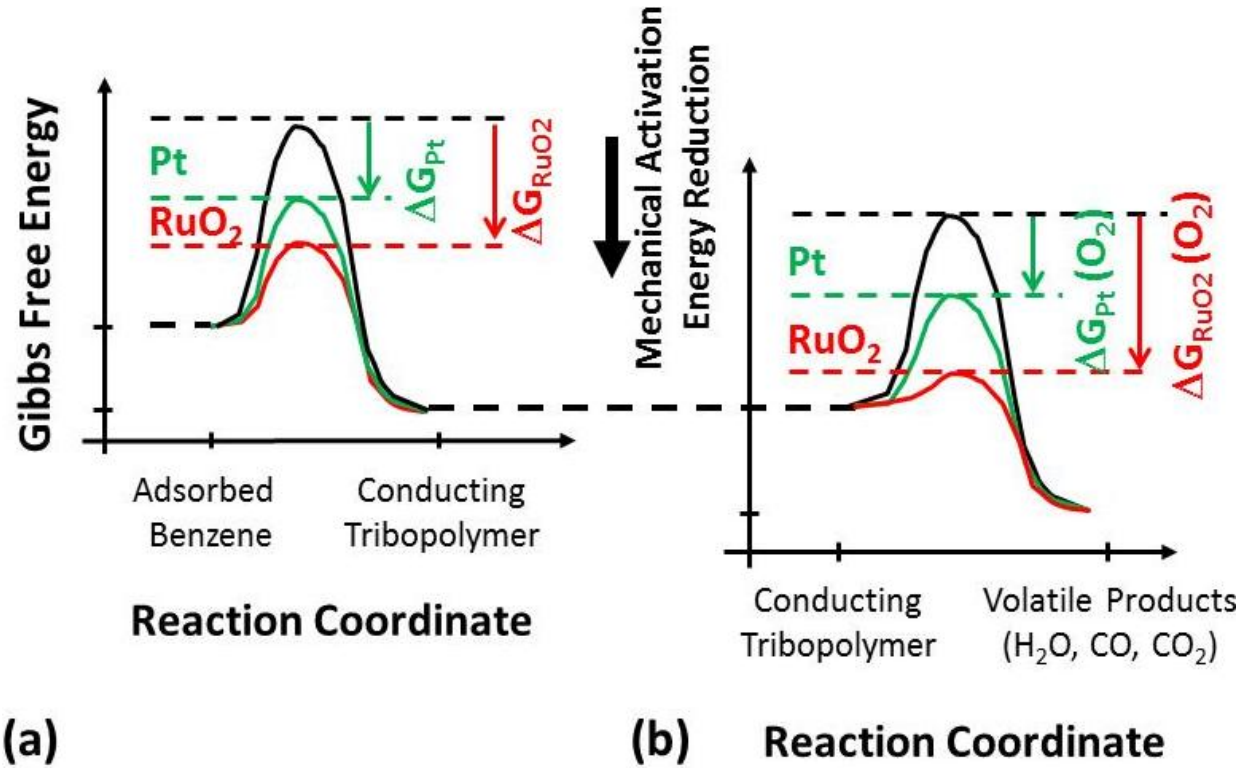

Figure 3.12: (a) Schematic model representing how activation energy to form (a) tribopolymer and (b) volatile products can be reduced by mechanical stress.

3.3.4 Tribopolymer growth is reduced with O_2; RuO_2 performs very well in O_2

For both Pt-coated and RuO_2-coated switches, when cold-switching is performed in N_2-C_6H_6:O_2, there is less tribopolymer buildup (and less resistance rise) than when it is done in N_2-C_6H_6. For the case of RuO_2, this difference is considerable. The lower quantities of tribopolymer formed in these experiments are not associated with having less (by half) benzene in N_2-C_6H_6:O_2 as compared to N_2-C_6H_6. We have performed experiments with both Pt and RuO_2-coated devices in environments with variable benzene concentrations [submitted], where we show that it is necessary to reduce the concentration of benzene by several orders of magnitude to notice such a significant change in tribopolymer buildup.

The governing mechanism could involve the adsorbed benzene first polymerizing and then oxidizing if O_2 is present. This idea was supported by cold-switching in a N_2-C_6H_6:O_2 environment after creating conducting tribopolymer in N_2-C_6H_6. In that case, resistance reduced after just 2 cycles to typical N_2-C_6H_6:O_2 levels. Also, the tested samples have been exposed to room air for several days before being examined in the SEM, yet deposits persisted. Therefore, the deposit is not removed by atmospheric oxygen in the absence of mechanical loading.

Figure 12b shows the reaction of tribopolymer to volatile products. The standard Gibbs free energy of formation (ΔG_f°) is much higher for the majority of hydrocarbons and their polymers (-50.75 to 338.58 KJ/mole) [108] as compared with typical hydrocarbon oxidation reaction products such as CO (-137.3 KJ/mole), CO_2 (-394.4 KJ/mole) and H_2O (-228.6 KJ/mole) [109]. This suggests that the standard Gibbs free energy of reaction ($\Delta G_{reaction}^\circ = \sum \Delta G_{f\_products}^\circ - \sum \Delta G_{f\_reactants}^\circ$) [109] for oxidation reactions would be lower than for polymer forming reactions. Therefore, the volatile products in **Figure 12b** are represented by the lowest energy. This could be why switches tested in the presence of oxygen are comparatively clean.

Once again, the higher mechanical stresses experienced by RuO_2 contacts than by Pt contacts correlate with the larger reduction in the activation energy of the oxidation reaction for RuO_2 contacts than for Pt contacts (i.e., $\Delta G_{RuO2}(O_2) > \Delta G_{Pt}(O_2)$). This could be why RuO_2 contacts are cleaner than Pt contacts.

3.3.5 Tribopolymer formation aided by catalysis is possible for Pt coated devices but is not likely for RuO_2 coated switches

The mechanism of hydrocarbon polymerization on electrical contacts is admittedly a poorly understood phenomenon which thus far has been generally attributed to catalysis associated with the contact material [27, 37, 41]. However, there is also a substantial body of evidence that contradicts catalysis being the dominant mechanism. Most notably, Hermance and Egan pointed out that the most effective catalytic poisons for the Pt group metals did not prevent or reduce the friction polymer buildup [37]. They also demonstrated that the frictional polymer was forming despite the absence of direct metal on metal contact (the only contact was between the organic films coating the metal contacts) and that there was no temperature dependence on polymer formation between (-) 60 ^{0}C to (+) 150 ^{0}C. Considering that chemical reactions catalyzed by Pt group metals usually need to have direct interaction with the metal and have strong rate dependence on temperature within the aforementioned range, these results show evidence against the catalytic process. Furthermore, as was discussed by Chaikin [110], the carbonaceous high molecular weight products formed from adsorbed hydrocarbons are completely inconsistent with the known products of reactions over Pt group metals. Finally, the formation of friction polymer from an organic vapor was observed on semiconductors [111, 112] as well as ceramics such as Al_2O_3 on Al_2O_3 [113] and SiO_2 on SiO_2 [114] without the presence of catalysts.

Given that Pt is a well-known catalyst, it is plausible that it plays a role in the chemistry despite the evidence presented just above against the catalysis mechanism. As with regard to RuO_2, several papers by Over and others that are summarized in references [115, 116] suggest that the most catalytically active RuO_2 surface is grown thermally to a thickness of 1.6 nm on Ru(0001) at 600 K O_2 environment. For this catalyst to be active, the coordinately unsaturated

cus-Ru sites need to be exposed and ready to interact with incoming molecules. Thicker RuO_2 films are however catalytically deactivated because the cus-Ru sites are not exposed. The RuO_2 film coating our contacts is a 500 nm reactively sputtered layer that is therefore most likely catalytically deactivated when O_2 is present. In the absence of O_2 in the environment, the RuO_2 layer is also catalytically inactive. Furthermore, the relatively low temperatures at the contact during switch closure would not be adequate for efficient chemical catalysis.

Hence our interpretation is that mechanical stress rather than chemical catalysis is playing the dominant role in both production of tribopolymer as well as its removal when oxygen is present. Future careful and creative experiments and models are necessary to elucidate the relative importance of mechanical stress and surface catalysis as a function of material.

3.4 SUMMARY:

We have investigated ohmic microswitch degradation due to hydrocarbon residue accumulation at electrical contacts as a function of material and environment. A high concentration of benzene (~1 part per 1000) was used to accelerate the growth of tribopolymer. Its accumulation rate is reduced if oxygen is present, and is reduced further if the surfaces are coated by RuO_2 rather than by Pt. It was confirmed that applied voltage caused an electrical breakdown of the tribopolymer, making it conductive. This result may be of substantial importance for nanoswitches because the resistance of the formed tribopolymer can be reduced to an acceptable level for these devices. It was further observed that when a voltage was applied across the switch while the mechanical load was still present, the amount of deposit produced

was augmented. A model invoking the view that the activation energy is reduced by mechanical pressure is qualitatively consistent with the observed results.

Other potential parameters in tribopolymer formation, namely temperature and catalytic activity at the contacts, were considered. The temperature rise was estimated to be too low to affect the surface chemistry. As with regards to catalytic activity, it was surmised that while the catalytic effects of the Pt coating may contribute to the polymerization and oxidation reactions, the RuO_2 coating is catalytically deactivated.

Chapter IV: Effects of electrical current and temperature on contamination induced degradation in ohmic switch contacts

In the previous chapter we found that deposit formed on the contacting asperities in the absence of electrical current being passed through the contacts. However, when current was passed, the amount of deposit formed was greatly augmented. Then, the deposit was much more electrically conductive. We suggested that the temperature rise associated with the electrical current was too low to be responsible for the large increase in deposit produced.

In this chapter we test this suggestion experimentally by observing how contaminant growth is affected by increasing the temperature in both mechanical cycling and cold-switching conditions. We demonstrate that increasing the contact temperature delays electrical degradation and inhibits deposit formation. Therefore, the temperature rise induced by the current is indeed not responsible for increased deposit formation [117].

4.1 EXPERIMENTAL DETAILS

All experiments were performed in N_2 containing 2,500 parts per million (PPM) benzene at 0.5 bar. This high concentration ensures that deposit formation is favored over other potential failure mechanisms such as wear [3] or adhesion [22]. For experiments that were performed at 100 ℃ or 200 ℃, the chamber was heated to the desired temperature and the excess gas (namely N_2- C_6H_6) was controllably released through a valve until the chamber pressure dropped back to 0.5 bar. With this procedure we controlled the contaminant and its concentration, thereby

isolating the experiment to the effect of temperature rather than any contribution due to other contaminants or environmental oxygen.

4.2 RESULTS

After baking the samples and introducing the N_2-C_6H_6 mixture, $R \approx 20\ \Omega$ in the first cycle. Switches that were *mechanically-cycled* for $16 \bullet 10^6$ times in N_2- C_6H_6 always grew an electrically insulating deposit that created an open circuit. This deposit is barely visible by optical microscopy (top view, **Figure 4.1b**), but it can be clearly seen with an SEM (45^0 tilt view of the contact sidewall, **Figure 4.1c**). When switches were *cold switched* for $16 \bullet 10^6$ times in N_2- C_6H_6, the amount of deposit produced was always greatly augmented, as shown in optical and SEM images of **Figure 4.1d** and **4.1e**. Yet this deposit was electrically conductive (with a final R value of $\approx 800\ \Omega$). We reported similar results earlier [48]. Therefore, these effects are repeatable.

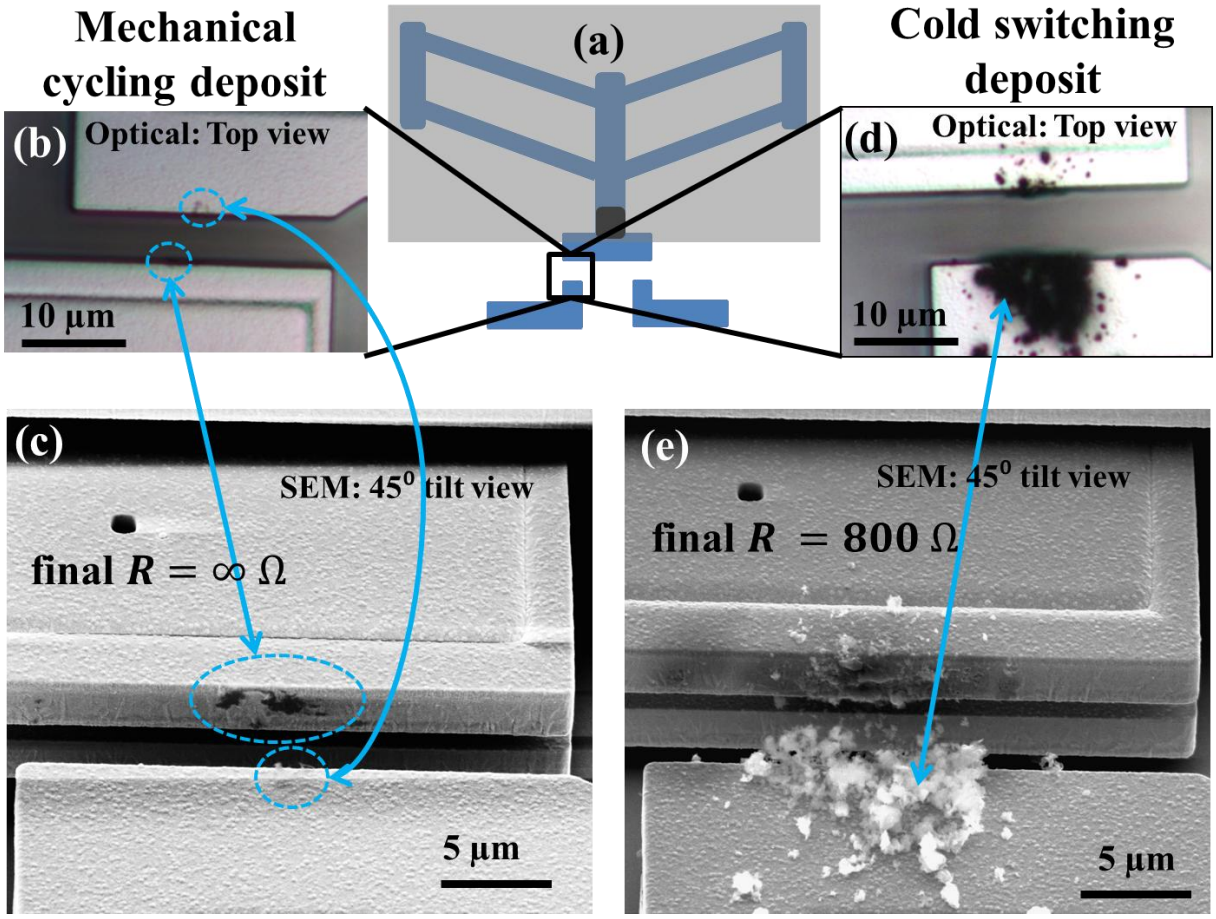

Figure 4.1: (a) Schematic of switch indicating location of (b)-(e). (b) Top view optical image of mechanically cycled contacts shows a small protruding piece of electrically insulating deposit accumulated in N_2-C_6H_6 environment. (c) A tilted SEM view shows the deposit in more detail. (d) Top view optical image of the contacts shows more deposit is produced In cold-switching, though it is now somewhat electrically conductive. (e) The tilted-view SEM image shows deposit in more detail.

Two key questions can be posed: Because increasing the temperature can increase the rate of chemical reactions, does the temperature increase associated with joule heating at the contacts induce the observed increase in deposit formation? If not, can it clearly be associated with the flow of electrical current? These questions motivated the following experiments.

The *R* rise as a function of cycle count for *mechanically-cycled* devices was measured for $16 \cdot 10^6$ cycles at three different chamber temperatures. As seen in **Figure 4.2a**, two switches tested at room temperature (24 ℃) attain the open circuit condition ($>10^6$ Ω) after 10^5 cycles.

The switch tested at 100 ℃ achieves a final R of 310 Ω after $16 \cdot 10^6$ cycles, while not experiencing open circuit. The switch tested at 200 ℃ achieves a final R of 170 Ω, also not experiencing an open circuit condition. As there are only a few data points per experiment, it cannot be ascertained whether temperature affects the onset of electrical degradation. However, it is clear that no open circuit is observed at 100 ℃ and 200 ℃. Also, it appears that the final R value was reduced with increasing temperature. The SEM image of the contacting sidewall of the device tested at 24 ℃ (**Figure 4.2b**) shows much more deposit (inside the circled region) than for the device tested at 200 ℃ (**Figure 4.2c**), perhaps helping to explain the lower R in the latter.

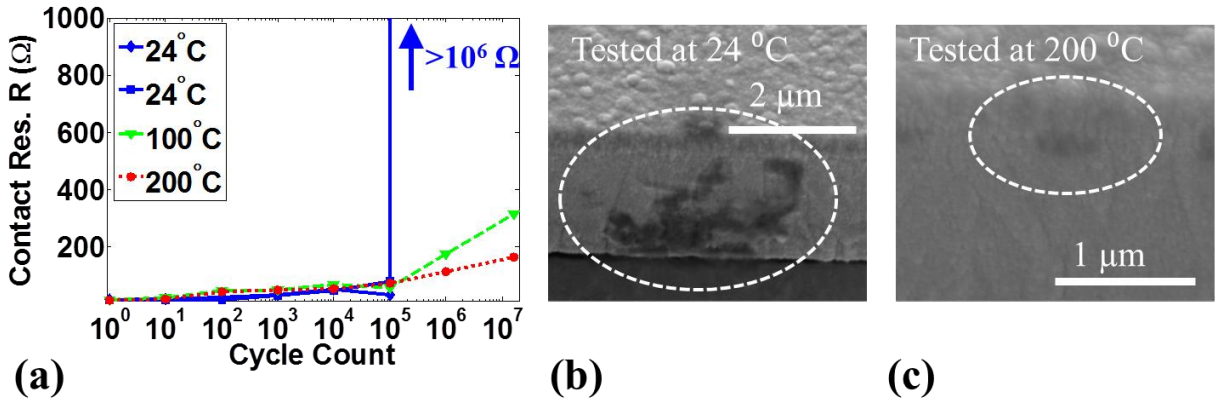

Figure 4.2: Mechanical-cycling was performed at three different temperatures. Increasing the temperature reduces deposit buildup, improving switch performance. (b) Looking in the circled region, notice that the amount of deposit produced on the contacts at 24 ℃ is much larger than the amount produced at (c) 200 ℃.

Next, the R rise as a function of cycle count for *cold-switched* devices was measured for $16 \cdot 10^6$ cycles at the same three temperatures. As seen in **Figure 4.3a**, two devices cold switched at room temperature (25 ℃) showed a steep rise in R beginning at $\sim 1 \cdot 10^3$ cycles; this was followed by R fluctuation around $5 \cdot 10^2$ Ω that eventually reached 10^3 Ω. Two devices that were cold-switched at ~100 ℃ showed a steep R increase beginning at $\sim 2 \cdot 10^3$ cycles; this was again

followed by R fluctuation around $5 \cdot 10^2$ Ω that eventually reach 10^3 Ω. For two devices cold switched at 200 ℃, the steep increase in R has begun after ~$1 \cdot 10^4$ cycles and was also followed by R fluctuations around $5 \cdot 10^2$ Ω, eventually reaching 10^3 Ω. As can be seen, the onset of electrical degradation (rise in R) is significantly delayed with increasing test temperature. The SEM images of the contacting sidewalls show about the same amount of deposit at 24 ℃ (**Figure 4.3b**) and 200 ℃ (**Figure 4.3c**). Each SEM image was taken after the $16 \cdot 10^6$ cycles.

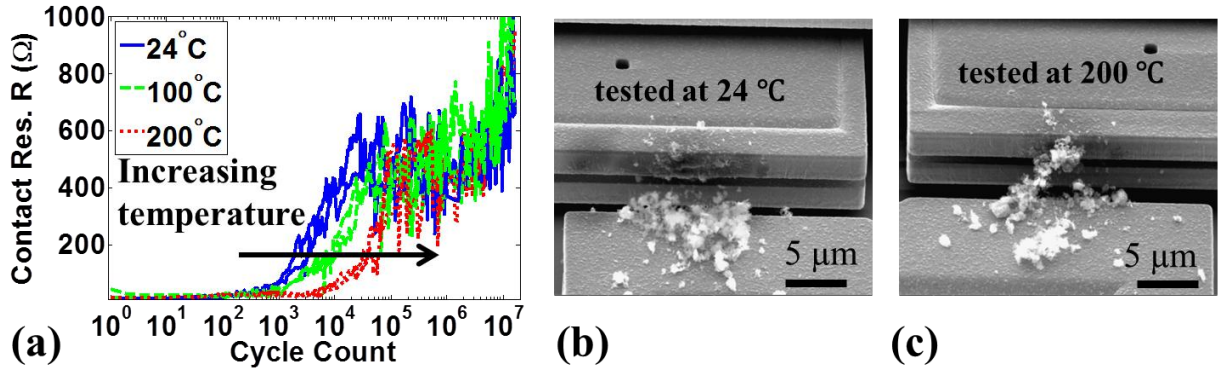

Figure 4.3: (a) Cold-switching was performed at three different temperatures. Increasing the temperature delays the onset of electrical degradation which is determined when the contact resistance begins to rise. The amount of deposit produced on the contacts at (b) 24 ℃ and (c) 200 ℃ is about the same.

The significant differences in electrical conductivity of the deposit created at 24 ºC in mechanical cycling as compared to that in cold switching suggest that the chemical composition or structure of those deposits may be different. Energy dispersive x-ray spectroscopy (EDS) and Auger electron spectroscopy (AES) showed that the chemical composition of the deposits was the same in all N_2-C_6H_6 experiments and consisted of carbon [48, 118]. Thus, we sought to distinguish the different deposit types with Raman spectroscopy as this technique is frequently applied in studying carbonaceous materials [96].

A Raman spectrum plots signal intensity as a function of Raman shift (cm^{-1}). The four Raman spectra in **Figure 4.4a** were collected at four different locations on the deposit produced in mechanical cycling at 24 ºC (shown in **Figure 4.1b**). The peak located at roughly 1330 cm^{-1} is known as the 'D' peak, whereas the peak at about 1580 cm^{-1} is the 'G' peak [96, 119, 120]. The peak intensity ratio (I_D/I_G) was calculated for each spectrum. The average value is 0.60 with a standard deviation of 0.024. The Raman spectra in **Figure 4.4b** were collected at four different locations on the deposit produced in cold switching at 24 ºC (shown in **Figure 4.1d**). The I_D/I_G ratios were again calculated for each spectrum and the average value is 0.84 with a standard deviation of 0.067. The peak intensity ratio is clearly higher for the cold-switched devices as compared to the mechanically-cycled ones. In Pt regions where there was no deposit, only noise was observed at the wavenumbers associated with the D and G peaks.

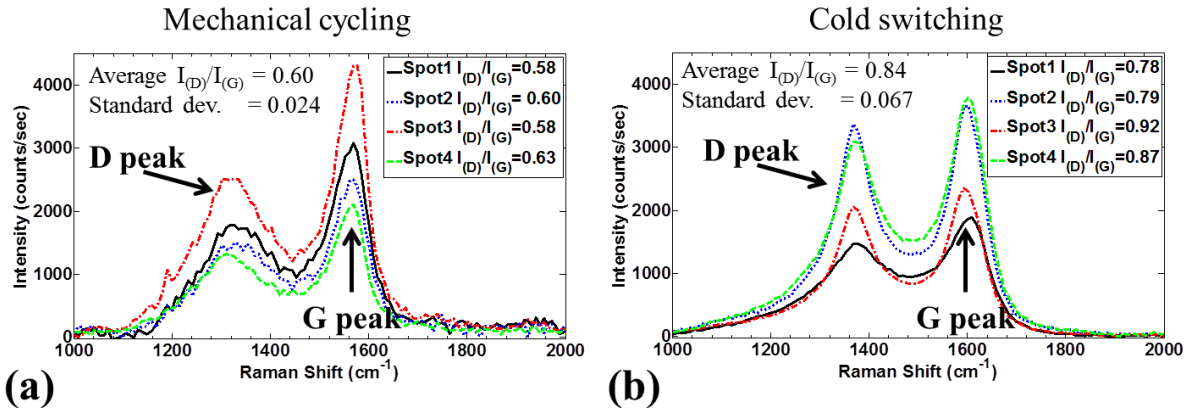

Figure 4.4: Raman spectra at four different locations on the deposit produced at room temperature in (a) mechanical-cycling (**Figure 4.1b**) where the average peak intensity ratio is 0.60, and (b) in cold switching (**Figure 4.1d**) where the average peak intensity ratio is 0.84.

Raman spectroscopy is more difficult to perform on mechanically-cycled devices because less deposit is produced at the contacting sidewalls. Unless this deposit makes its way to the top of the switch contact from the sidewall, it cannot be accessed with the instrument. At 100 ºC and 200 ºC, the mechanical cycling experiments did not produce enough deposit for it to be moved to

the top of the contact. Raman measurements could be performed on cold-switched devices that were tested at 100 ºC and 200 ºC. Although the I_D/I_G ratio may have reduced slightly with increasing temperature, there was no statistically significant difference compared to the spectra in **Figure 4.4b**.

4.3 DISCUSSION

4.3.1 Overview of phenomena in mechanical cycling versus cold switching

We surmise that the following sequence of events takes place in mechanical cycling. The electrically insulating carbonaceous deposit layer grows slowly with cycling. As long as it remains thin, the contact voltage (V_c=5 V) that is applied during the R measurement is sufficient to break down the dielectric electrically, and the R value remains low. When it reaches sufficient thickness, the electric field due to V_c is no longer large enough to cause breakdown, and R abruptly increases to the open circuit condition. Because the layer grows more slowly as temperature increases, the change to the open circuit condition is delayed to higher (yet to be determined) cycle counts at 100 ºC and 200 ºC.

In cold switching, current passes through the film every cycle. Therefore, the film is converted into a conductor in each cycle. Any subsequent layer that is deposited may be insulating, but remains thin and breaks down again. This apparently also enables a much higher growth rate of the deposit.

The dielectric breakdown mechanism could involve a process where free electrons in the insulator are accelerated by the electric field, ionizing atoms in its path and initiating an electron

avalanche [27]. Alternatively, assuming that each switching cycle creates about a monolayer of deposit [37], electron tunneling could be the method of current transmission [121, 122]. Either mechanism will permanently alter the structure of the deposit such that it becomes conductive. Perhaps sp^3-hybridized carbon, which is not electrically conductive, becomes converted to graphitic sp^2-hybridized carbon in the process [122], which is conductive.

We now consider the underlying deposit formation mechanisms and associated temperatures in more detail.

4.3.2 Raman spectroscopy of deposit

The Raman spectra of the deposit produced in cold switching as well as the deposit produced in mechanical cycling are characteristic of amorphous carbons [96, 120]. The D peak is attributed to the breathing mode of the six-fold aromatic rings. This mode does not exist in perfect graphene or graphite but becomes active in the presence of disorder in the crystal structure. This means that as the average size of graphitic crystallites in a carbonaceous deposit decreases, the intensity of the D peak increases [123]. However, as the concentration of aromatic rings present in the deposit reduces, the intensity of the D peak will also reduce [96]. The G peak corresponds to the in-plane bond-stretching motion of pairs of sp^2-hybridized carbon atoms, and does not require the aromatic ring structure to be present [96].

The data could be interpreted as suggesting that the deposit formed in mechanical cycling has larger graphitic crystallites [124] and more graphitic order [123] than the deposit formed in cold switching because the former has a significantly lower I_D/I_G ratio. However, if the deposit produced in mechanical cycling were more graphitic, it would be expected to exhibit higher

electrical conductivity [123]. On the contrary, this mechanically-cycled deposit (which was created at 24 ℃ ambient conditions) is a very good electrical insulator despite its small amount. In contrast, the large quantity of the deposit produced with cold switching is highly conducting by comparison, with maximum R values of ~10^3 Ω.

A more likely interpretation is that the mechanically-cycled deposit is electrically insulating because it primarily consists of sp^3-rich amorphous carbon. The lower I_D/I_G ratio observed in mechanical cycling deposit is therefore associated with the presence of fewer aromatic rings. For example, Ferrari and Robertson [125] show spectra for tetrahedral (sp^3-rich) amorphous carbon (ta-C) deposit in their Fig. 48. There, the I_D/I_G ratio is lower than what we see for the deposit produced in our mechanical cycling experiments, suggesting theirs has even fewer aromatic rings. They classify ta-C as a wide band gap semiconductor. As such, it would be expected to be an electrical insulator. In cold switching conditions, the sp^3-rich amorphous carbon might still be produced upon mechanical contact but is then electrically broken down during each cold switching pulse, thereby creating electrically conducting graphitic pathways in the deposit. Thus, the increased presence of aromatic rings in the amorphous carbon matrix increases the intensity of the D mode, thereby increasing the I_D/I_G ratio. Robertson and Ferrari also show that when the sp^3-rich ta-C follows an ordering trajectory to graphite, its peak intensity ratio increases [96]. Visible Raman spectroscopy is far more sensitive to sp^2-carbon than sp^3-carbon, so it is difficult to accurately measure the sp^2/sp^3 ratio with this method.

4.3.3 Effects of temperature on deposit formation

The observations of **Figure 4.2** indicate that for mechanical cycling experiments, increasing the temperature reduces deposit buildup and electrical degradation. From **Figure 4.3**, it is clear that increasing temperature also significantly delays contaminant-induced degradation in cold switching. These results can be rationalized as follows: When a gas molecule collides with a surface, it will become trapped (adsorbed) on the surface if its kinetic energy is exceeded by the van der Waals energy of attraction to the surface [50]. Similarly, an adsorbed molecule might be able to desorb from the surface if it gains enough kinetic energy to overcome the surface attraction. Increasing the temperature increases the kinetic energy of the benzene molecules, thereby reducing their concentration on the surface of the contacts. This means that the amount of available deposit-forming reactants is reduced, so the rate of deposit formation is also reduced. Indeed it is well known that adsorption of gases (including volatile hydrocarbons) on a variety of surfaces reduces with increasing temperature [51, 126, 127], while desorption increases [51, 52].

4.3.4 Estimating true contact temperature

We have already demonstrated that higher temperature is unlikely to be the reason why more deposit is produced in the presence of electrical current through the contacts. However, it is important to estimate the *steady state* temperature increase due to joule heating to compare it to the chamber temperature differences. Furthermore, it is important to estimate the *transient* contact temperature increase associated with mechanical impact during switch closure, as well as the contribution due to conduction from the thermal actuator legs to the contact surface.

We begin by considering the contact temperature before deposit accumulates, that is, the first few cycles when little if any deposit has accumulated. At this early stage, it is assumed that

asperities break through a thin adsorbed contaminant layer upon switch closure, establishing metal on metal contact. This scenario is relevant because it sheds light on the temperature when the deposit first nucleates.

An early approach to estimate the maximum temperature (T_{max}) at the contact asperities due to joule heating was presented by Holm [84] for macroscale contacts. Jensen et al. [42] suggested that the Holm temperature may not be accurate for microswitches because it assumes that electron transport through the contact is diffusive (i.e. R is dominated by Maxwell resistance due the electron scattering). However, when the contact radius is less than the electron mean free path (~40 nm), there must also be ballistic electron transport through the contact, which causes less temperature increase. The total effective contact area has a radius of ~90 nm for these switches [89]. This area consists of several smaller contact regions, in which individual contacting asperities are likely to have contact radii under 40 nm. This means that the Jensen model applies better here.

It is now convenient to define $R_C = R - 10\ \Omega$ as the *real* contact resistance, where the extra ~ 10 Ω associated with contributions from features such as wire bonds and ribbon cable is subtracted from the measured contact resistance R. Jensen modified the Holm equation to account for ballistic electron transport, such that R_C is equal to the sum of the Maxwell component, R_m, and the Sharvin component, R_s. Hence, the joule-heating temperature is

$$T_{JH} = \sqrt{\left(\frac{1 + 0.83\left(\frac{\lambda}{a}\right)}{1 + 1.33\left(\frac{\lambda}{a}\right)}\right)\frac{R_m}{4R_c}\frac{V_c^2}{L} + T_0^2} \quad , \qquad (1)$$

where V_c =0.04 V is the voltage across the contacts, L=2.45•10^{-8} W•Ω/K^2 is the Lorentz constant, T_0=297 K is the ambient temperature and λ is the mean free path in Pt (~40 nm). Also, R_C≈5 Ω for a clean Pt contact, while $R_m = \rho/2 \bullet a$ where ρ is the resistivity of Pt (10 μΩ-cm). The value of the contact radius, a, is taken to be 90 nm to give an upper bound estimate on the temperature. This results in the maximum possible contact temperature to be T_{JH}=299.6 K, or a joule-heating induced increase of ΔT_{JH}=2.6 ºC.

After substantial deposit has built up on the contacts such that it separates them during closure, the Jensen model is not applicable. The joule-heating induced temperature rise was instead estimated using the shape-factor heat transfer analysis and shown to not exceed a 10 ºC increase [48].

The analysis thus far indicates that the differences from 24 ºC to 100 ºC and to 200 ºC chamber temperatures dominate the effects of temperature increase associated with steady-state joule heating at contacts. This reinforces the conclusion that the augmentation of deposit growth in cold switching is not attributed to the steady-state joule-heating induced temperature increase.

However, two transient effects should also be considered. First, impact during mechanical closure raises the local temperature due to internal friction associated with plastic deformation. An upper bound estimate for the temperature rise can be found by assuming a constant heat flux irradiating a semi-infinite body as a result of the plastic deformation of two asperities during contact [128]:

$$\Delta T_{pl} = \frac{F}{2}\sqrt{\frac{\Delta t}{\pi k \rho c}} \quad . \qquad (2)$$

The energy flux dissipated during deformation is $F = \sigma_n v$, where σ_n is normal stress during contact and v is the velocity of the contact bar at impact. The value of σ_n is approximately 5 GPa, the hardness of Pt [48], while v is ≈ 0.23 m/s (see Appendix VI). The duration of impact (Δt) is estimated to be the asperity deformation divided by the velocity. If we assume an asperity with height (h) of 50 nm (an upper bound) protruding from the contact surface, then a rough estimate for Δt is $h/v \approx 2.2 \cdot 10^{-7}$ s. The thermal conductivity of Pt is k_{Pt} =71.6 W/(m•K), its specific heat is c_{Pt}=1230 J/(Kg•K) and its density is ρ_{Pt}=21,500 kg/m^3. Inserting these values into Equation 1 yields an upper bound temperature rise of ΔT_{pl}=3.5 ºC.

Because the 5 V is applied across the contacts 0.7 ms after contact is made (which takes ~25 μs, see Appendix VI), the temperature excursion due to impact will have subsided considering the large thermal mass of the trace and contact bar compared to the asperity.

Second, the contact bar itself is hot due to heat conduction from the TA legs. Referring to **Figure 2.1**, during switch closure at 24 ℃, steady state finite element analysis (using ANSYS) indicates the maximum temperature due to joule heating in the thermal actuator legs is ≈138 ℃. At the leg to shuttle connection points, the temperature is ≈116 ℃. Due to the thermal conduction through the gas to the substrate, the temperature is ≈75 ℃ at the contact bar. When the switch is closed, the contact temperature rapidly reduces to that of the substrate because the trace is attached to it. This does however mean that the transient temperature at the contact interface would be as much as 50 ℃ higher than the ambient temperature at the instant of switch closure. While the amount of adsorbent on the hot contact bar is significantly lower (due to the inverse exponential dependence on temperature [50]) compared to the amount on the trace, the

heat in the contact bar will flow through the adsorbent on the trace. This heat flow may assist in the polymerization of the adsorbent.

Hence the transient temperature excursion is governed by the maximum of that from impact (ΔT_{pl}=3.5 ºC) or joule heating in the TA legs and conduction to the contact bar (ΔT≈50 ºC). The value is then ΔT_{max}≈50 ºC. However, the effect of transient-induced temperature rise, which subsides long before electrical current flows through the contacts, must be small. This can be inferred from **Figure 4.2**, where it is seen that increasing chamber temperature reduces the deposit buildup when only mechanical cycling. Therefore, it is likely that transient temperatures do not play a strong role. Rather, the deposit growth can unambiguously be associated with the passage of electrical current.

4.3.5 Comments on deposit evolution

We next discuss factors that may influence electrically-induced deposit nucleation and growth. From diamond anvil experiments, in which hydrostatic pressure is applied, it is found that when bulk benzene is compressed to ~23 GPa at room temperature, it transforms into hydrogenated amorphous carbon that is ~75% sp^3 [67, 72]. Although the compressive stress in our Pt contacts of ~5 GPa (due to the hardness of Pt) is insufficient to initiate such a reaction by itself, the benzene-Pt interface interaction may reduce the required pressure.

It is well known that when hydrocarbons adsorb on transition metals such as Pt at room temperature, they can chemically interact with the surface by becoming polymerized and dehydrogenated [38]. They are essentially turning into graphite, though factors such as their chemical stability and surface temperature determine the degree of polymerization and whether

they eventually become graphite. Benzene is one of the more stable hydrocarbons due to its aromatic nonpolar structure and on Pt it begins to polymerize and dehydrogenate at temperatures above 80 ºC. Even though it stays intact on the contacts at room temperature (and at 75 ºC on the contact bar prior to switch closure), it inevitably interacts with the surface. Perhaps this surface interaction enables it to polymerize at only 5 GPa of pressure. In other words, at room temperature, the benzene-Pt interaction lower the activation energy barrier for polymerization and the mechanical pressure pushes the benzene over this barrier to polymerize. It is known however that benzene polymerizes on Pt with the help of mechanical rubbing at room temperature [37]. In our experiments we show that the deposit produced in mechanical cycling is an amorphous carbon that is highly electrically insulating, suggesting it is sp^3-rich. It therefore resembles the product from compressing benzene as opposed to the sp^2-rich deposit formed by surface-induced polymerization of benzene.

The fact that our amorphous carbon deposit only formed at locations that experienced mechanical contact (i.e. the contacting asperities) further supports the idea that stress and surface energy are working together to create it.

To rationalize how electrical current augments deposit formation, let us assume that the adsorbed C_6H_6 molecules exhibit a distribution of energies. The mechanical stress and substrate-adsorbent interaction could be raising the energy of all the adsorbed C_6H_6 molecules at the contact site (or equivalently lowering the activation energy barrier for adsorbent polymerization), thereby increasing the fraction of these molecules with sufficient energy to overcome the activation barrier and to be polymerized. Applying electrical current during contact (as in cold switching) further facilitates deposit formation by enabling a much larger fraction of the C_6H_6 molecules adsorbed at the contact site to overcome this activation energy barrier [48].

4.4 CONCLUSIONS

Cycling microswitches in a N_2-C_6H_6 environment results in a contaminant-induced electrical degradation of their contacts. Mechanically cycling the switches in the N_2-C_6H_6 environment produced a small amount of deposit. The increase in the amount of deposit in cold switching was not related to the temperature rise associated with joule-heating of the contacts. On the contrary, higher contact temperatures inhibited deposit formation and delayed electrical degradation. This was explained by the reduced adsorption and increased desorption of the volatile contaminant with increasing temperatures. Instead, in cold switching the deposit is conductive due to an electrical breakdown that transpires each cycle. The passage of electrical current augments its formation.

Chapter V: Contamination thresholds of Pt- and RuO_2-coated switches

In this chapter, we test Pt- and RuO_2-coated switches in increasing benzene contamination levels to determine if a threshold level for contamination can be found and whether it depends on the material [89]. It is seen that Pt is sensitive to a benzene contaminant at a concentration as low as 0.02 PPM (OSHA permissible exposure limit is 1 PPM for humans), while RuO_2 exhibits immunity even at the 130 PPM level. The data may also provide useful insight for nanoswitches because the current densities involved are of the same order in nano- and microswitches (see Appendix III).

5.1 EXPERIMENTAL DETAILS

Pt- and RuO_2-coated switches were tested in their best backgrounds, N_2 and 1:1 N_2:O_2, respectively [97], with benzene concentrations ranging from <0.1 to 2,500 PPM.

5.2 RESULTS AND DISCUSSION

The initial electrical contact resistance (R_c) values were 4 and 10 Ω for the Pt- and RuO_2-coated switches, respectively, as in previous results [31]. In **Figures 5.1a** and **5.2a** (Pt- and

RuO_2-coated switches, respectively), the R_c data was initially zeroed by subtracting the first resistance measurement from each subsequent measurement. Thus, the data indicates changes in R_c. To separate experiments performed in different benzene concentrations, the data sets were offset by 200 and 100 Ω for Pt- and RuO_2-coated switches, respectively. Two to four devices were tested at each contamination level.

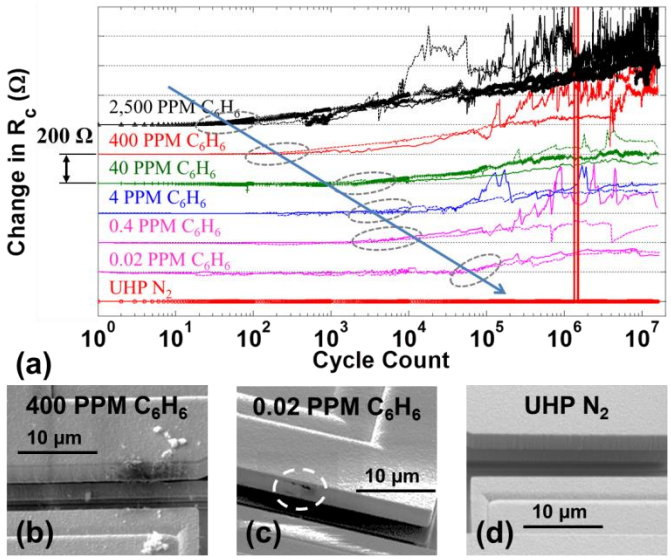

Figure 5.1: Pt switches tested in decreasing concentrations of C_6H_6 with N_2 background. Note that the y-axis scale is twice that of **Figure 3**. (a) Onset of electrical degradation initiates later with decreasing C_6H_6 concentration. (b) TP easily forms on contacts at 400 PPM C_6H_6. (c) Some TP forms even at 0.02 PPM C_6H_6. (d) Contact surface is clean after pure N_2 experiment.

As seen in **Figures 5.1a**, at 2,500 PPM benzene, electrical degradation of four Pt-coated switches began at ~$3•10^1$ cycles with an R_c rise of up to 10^3 Ω. At 400 PPM of benzene, the degradation began at ~$3•10^2$ cycles with an R_c rise of 400 to 700 Ω. The SEM image of the contacts in both switches (one of which is in **Figures 5.1b**) showed a large amount of residue on the electrical contacts, as well as sizable residue above and below the contact sidewalls. This residue was confirmed with EDS to be TP (due to its higher carbon content). At 40 PPM benzene, the R_c degradation onset began at ~$1•10^3$ cycles and its rise was 150 to 400 Ω. At 4

and 0.4 PPM benzene the degradation onset occurred at ~$2 \bullet 10^3$ cycles and a resistance rise of 150 to 500 Ω was observed.

Merely 0.02 PPM benzene caused two different Pt-coated switches to begin degrading electrically at ~$8 \bullet 10^4$ cycles (**Figures 5.1a**). For both switches, the resistance increased by about 150 Ω. The corresponding SEM image of the contacts (**Figures 5.1c**) showed TP.

Finally, two switches that were tested in UHP N_2 showed no electrical degradation besides an open circuit event for one of the devices, as shown in **Figures 5.1a**. The corresponding SEM images of all the contacts showed a clean Pt surface with no detectable carbonaceous deposit or wear (one contact pair is illustrated in **Figures 5.1d**).

The onset of degradation is highly consistent for the different Pt-coated switches for a given contamination level. This onset tends to occur at a larger cycle count as benzene concentration decreases, possibly indicating a controlled nucleation phenomenon for the TP. This would explain the observation that the contamination threshold for R_c increase depends on the number of cycles.

After the degradation onset, the R_c can vary significantly. This variation is likely due to the flaking-off and regrowth of TP, as noted for **Figures 5.1b**. The R_c remains finite, however, because the TP becomes conducting [97].

RuO_2-coated devices were nearly impervious to these extremely high levels of benzene (note that the y-axis in **Figures 5.2a** is expanded by a factor of two compared to **Figures 5.1a**). The four RuO_2 devices tested in 1,300 PPM of benzene experienced an average R_c rise of only ~35 Ω. This occurred during the first 10^3 cycles and then stabilized. As seen in **Figures 5.2b**, these switches exhibited a lesser amount of TP than the Pt-coated devices cycled at 400 PPM (compare

to **Figures 5.1b**). They revealed about the same amount of TP as the Pt-coated devices cycled at 0.02 PPM (**Figures 5.1c**). Furthermore, their R_c change is ~five times less than in the 0.02 PPM experiment with Pt-coated switches.

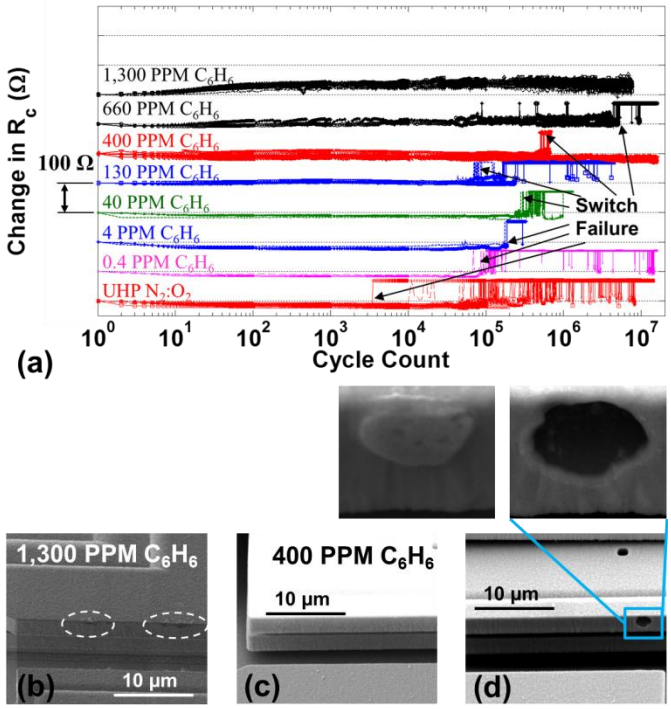

Figure 5.2: RuO_2-coated switches tested in decreasing concentrations of C_6H_6 in 1:1 N_2:O_2 background. (a) C_6H_6 concentrations above 400 PPM induce minor degradation. (b) Some TP forms at 1,300 PPM. (c) Contact surface is clean at 400 PPM of C_6H_6. (d) Spallation-induced electrical failure is the likely cause of the abrupt resistance rise.

At 660 PPM of benzene there was a smaller R_c increase of ~20 Ω during the first 100 cycles and it remained at that value or below until 10^5 cycles. However, beginning at 10^5 cycles there were several abrupt open circuit failure events, followed by a permanent open circuit condition after $4 \cdot 10^6$ cycles (to avoid obscuring data, open circuit failure was designated with data points at 70 Ω in **Figures 5.2a** as switch resistance rise never exceeded that value otherwise).

At 400 PPM, one switch initially experienced a slight resistance increase of ~10 Ω, while the other three showed no such resistance rise. Beginning at $5 \cdot 10^5$ cycles, open circuit failures were

observed in two devices (though the other two switches never failed). No TP buildup was observed in any of the devices (as in **Figures 5.2c**). At 130 PPM, the R_c change was less than 10 Ω, however, open circuit occurred at ~$7 \cdot 10^4$ cycles.

At 40, 4, 0.4 PPM benzene and in UHP N_2:O_2, the R_c change was always negative. This can be attributed to asperity flattening, reducing $R_{intrinsic}$. However, the open circuit condition was observed within $3 \cdot 10^3$ to $2 \cdot 10^5$ cycles.

All switches that experienced the abrupt resistance failure had cavities in one contact side (**Figures 5.2d**) such that the material taken out of that cavity was transferred to the opposite contact. EDS confirmed the transferred material was RuO_2 and that there was no detectable presence of TP residue. In fact, the only switches that showed any TP were the ones tested in 1,300 PPM of benzene. These results demonstrate the remarkable ability of RuO_2 contacts to remain clean if O_2 is present in the environment. The material transfer and the fact that RuO_2 is brittle suggest a susceptibility to spallation fracture. We are investigating the cause of this failure mechanism.

To place the results in the context of nanoswitches, consider that ΔR_c is much greater than the initial R_c value in **Figures 5.1 and 5.2**. If nanoswitch resistance cannot change by more than say 50 % (this number depends on the circuit implementation), then Pt in UHP N_2 or RuO_2 in N_2:O_2 with ≤ 40 PPM would be acceptable. It will be important to test this assessment on actual nanoswitches. In any case, it can be considered that RuO_2 in N_2:O_2 is much more tolerant of benzene contamination than Pt is in N_2.

5.3 CONCLUSIONS

Because hydrocarbons are difficult to eliminate and because micro- and nanoswitches must survive billions to trillions of cycles, it is useful to find materials and gas backgrounds that are not susceptible to TP formation. We find for Pt in N_2 at a benzene concentration as low as 0.02 PPM that $R_{interface}$ increases substantially due to TP. Also, the onset of degradation occurs sooner and its severity increases with more contaminant. However, RuO_2 in N_2:O_2 is a robust material with respect to TP formation, revealing only a small increase in $R_{interface}$ at a benzene concentration as high as 1,300 PPM. Future work entails finding mechanisms to toughen RuO_2 with respect to the spallation failure.

Chapter VI: Oxygen-induced graphitization of amorphous carbon deposit on ohmic switch contacts improves their electrical conductivity and protects them from wear

In this chapter, we manipulate the operating environment with an aim of controlling and understanding the deposit growth and its electrical characteristics [129]. An important question relates to the role of gaseous O_2. Although it was shown that O_2 can accelerate wear-induced degradation of Pt contacts in contaminant-free conditions [31], we found in chapter III that O_2 plays an important role in reducing the amount of deposit created and the resistance increase when contaminant was present [48]. Identifying its role may be especially important because MEMS and NEMS devices are commonly packaged in an N_2 environment. We find that O_2 plays a highly beneficial role in that it not only reduces deposit production, but actually transforms the deposit into a highly conducting graphitic-like layer which can passivate the surface and substantially increase the switch longevity by limiting wear.

6.1 EXPERIMENTAL DETAILS

Prior to the first experiment on a given switch, it was baked in high vacuum inside a testing chamber by setting the chamber temperature to 200 ºC for 24 hours as described in the experimental section. It was then filled with the desired testing environment to a total pressure of 0.5 bar. The testing environments used were N_2-C_6H_6 (~2500 PPM C_6H_6), 1:1 N_2-C_6H_6:O_2 (~1250 PPM C_6H_6), *clean* 1:1 N_2:O_2 or *clean* N_2. Devices that were tested again in a subsequent experiment in a different environment were not baked out a second time. In those cases, the

chamber was merely pumped down to ~1•10^{-7} Torr to purge the previous environment and then refilled with the subsequently desired environment.

6.2 RESULTS

We first describe results which show that the environment enables a certain degree of control on the measured electrical contact resistance (R_c) values. Then, we report on the results of Auger and Raman spectroscopic analysis of the deposit produced under different environmental conditions.

6.2.1 Electrical, Optical and SEM Data

After establishing an N_2-C_6H_6 environment in the test chamber, two microswitches were cold-switched. After purging the environment, two different devices were cold-switched in N_2-C_6H_6:O_2. As seen in **Figure 6.1a**, R_c for all four switches was initially between 10 and 20 Ω. The two switches tested in N_2-C_6H_6 experienced an R_c rise after just 5 to 20 cycles. The R_c reached 500 Ω to 700 Ω after 10^4 cycles where it remained through 6•10^6 cycles and eventually approached 1,000 Ω near 16•10^6 cycles. For the two N_2-C_6H_6:O_2 experiments, R_c began to increase after just 10 to 20 cycles. It reached 100 Ω within 10^4 cycles and fluctuated between 100 Ω and 200 Ω from 0.5•10^6 to 16•10^6 cycles. In both environments, the deposit is conducting, and the repeated buildup and self-removal of the film cause the fluctuations in R_c [48].

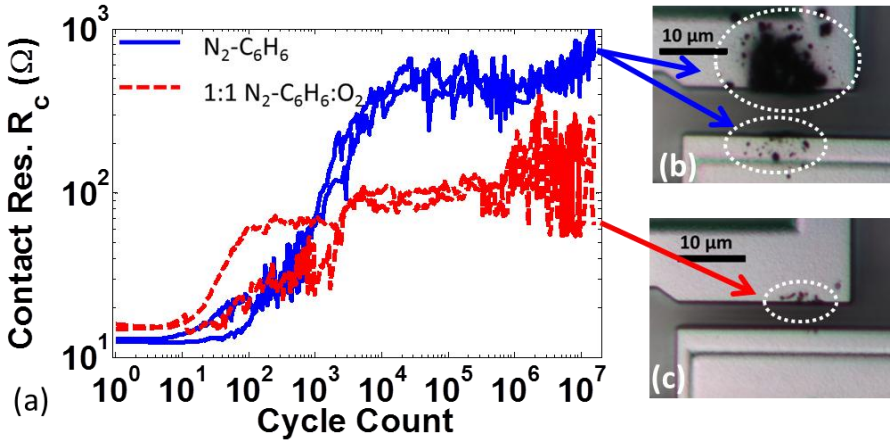

Figure 6.1: (a) R_c versus cycle count while cold-switching in N_2-C_6H_6 and N_2-C_6H_6:O_2. The optical images on the right indicate the quantity of deposit produced in (b) N_2-C_6H_6 and (c) N_2-C_6H_6:O_2.

For comparison, in *clean* N_2, R_c typically remains low and nearly constant until 10^5 to 10^7cycles [31, 89, 130]. Hence the rapid R_c increase in N_2-C_6H_6 can be unambiguously associated with the high contaminant level. In *clean* N_2:O_2, R_c typically remains low and nearly constant until 10^2 to 10^3cycles [31]. Although not as dramatic, the rapid R_c increase in N_2-C_6H_6:O_2 can again be attributed to the presence of C_6H_6.

Not only do the devices tested in N_2-C_6H_6 achieve a higher R_c than those cycled in N_2-C_6H_6:O_2, but by comparing the optical images of **Figures 6.1b and 6.1c**, it is seen that they also accumulate substantially more deposit. **Figures 6.1b and 6.1c** only shows the top view of the switch contacts. The deposit forms in the contacting sidewalls (which are perpendicular to the plane of view in **Figure 6.1b and 6.1c**) and is then squeezed out or ejected from the sidewalls during switch closure [48].

The results in **Figure 6.1** are qualitatively consistent with previously published data in the same two environments [48], and therefore the effects of (i) greater deposit produced and (ii)

higher R_c in N_2-C_6H_6 than N_2-C_6H_6:O_2, are repeatable. However, it is not clear why the gas environment plays such a strong role. One important question that can be asked is whether it is possible to transition from the R_c values measured in N_2-C_6H_6 to those measured in N_2-C_6H_6:O_2. To address this question, a device was first cold-switched in N_2-C_6H_6 **(Figure 6.2a)**. Here the device is seen to reach ~300 Ω at 10^6 cycles, similar to the ~400 Ω seen in **Figure 6.1a** at that cycle count. (The small decrease at ~40 cycles may be due to an initial deposit buildup which subsequently moved away from the contact area). The test chamber was then purged by pumping to 10^{-7} Torr, and the N_2-C_6H_6:O_2 gaseous environment was introduced. As seen in **Figure 6.2b**, during cycling the switch R_c decreased after 10^4 cycles to the values typically seen in N_2-C_6H_6:O_2 experiments of **Figure 6.1**. To enable direct comparison, **Figure 6.2b** also shows the data from the **Figure 6.1a** devices that were only cold-switched in N_2-C_6H_6:O_2.

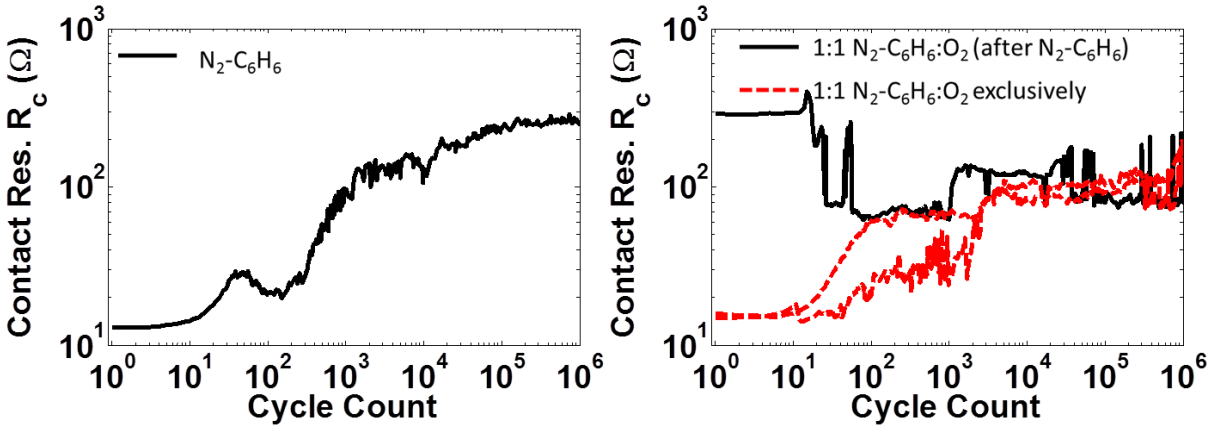

Figure 6.2: (a) A device cold-switched in N_2-C_6H_6 shows the typical R_c increase versus cycle count. (b) The same device subsequently cold-switched in N_2-C_6H_6:O_2 shows a moderate drop in R_c that converges with a rise in R_c experienced by virgin devices that were simultaneously tested in N_2-C_6H_6:O_2.

If the deposit is first created by cycling in N_2-C_6H_6, but further testing is conducted in *clean* N_2:O_2 (i.e., no background contamination), will R_c reduce below the level to which it stabilized in N_2-C_6H_6:O_2? Six devices were first cold-switched in N_2-C_6H_6. As seen in **Figure 6.3a**, they

showed the usual R_c rise after 10^6 cycles, often exceeding 500 Ω. The test chamber was then purged and *clean* N_2:O_2 was introduced. For some devices, the initial R_c values in **Figure 6.3b** (in the new environment) were higher than the final R_c value in the previous environment, perhaps because gas flow in the test chamber during the purging process displaced the deposit. However, all switches showed a large drop in R_c to ~20-40 Ω within 10^3 to $2 \cdot 10^5$ cycles, a level at which they remained up to 10^6 cycles. (Subtracting 10 Ω, the interface resistance is initially about 6 Ω for the two series contacts in **Figure 6.3a**. After 10^6 cycles in **Figure 6.3b**, it is 6 to 30 Ω).

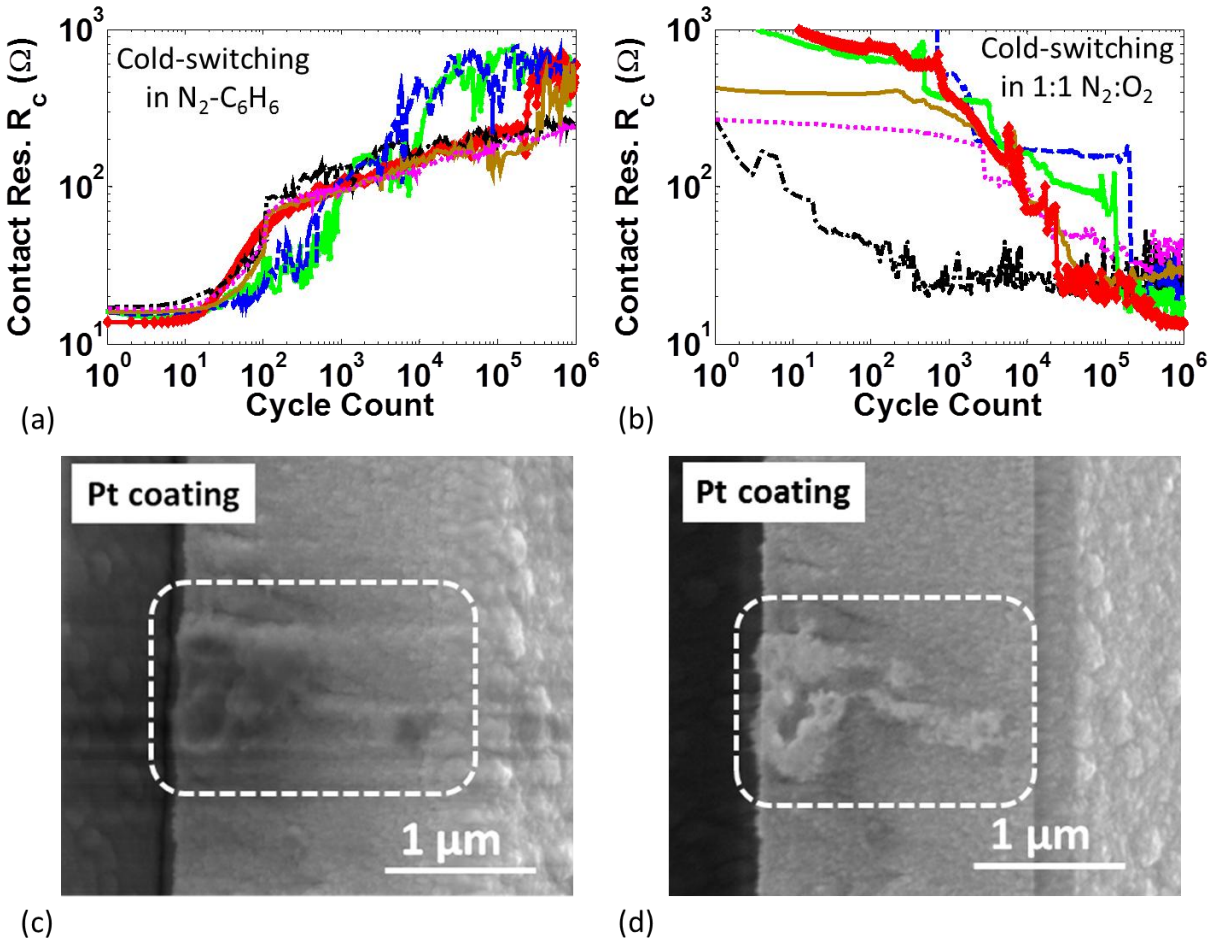

Figure 6.3: The six devices in (a) and (b) are each represented by different colors. (a) Devices cold-switched in N_2-C_6H_6 show typical electrical degradation. (b) Upon subsequent cold switching in *clean* N_2:O_2 (after chamber pumped to 10^{-7} Torr vacuum and refilled with N_2:O_2), all six devices experienced a large drop in R_c. (c) Image of a device contact after 10^5 cycles in N_2-C_6H_6 shows deposit (R_c = 400 Ω). (d) Image of same device after 10^5 additional cycles in clean N_2:O_2 shows that the deposit remains (R_c = 16 Ω).

The final R_c values in **Figure 6.3b** have decreased substantially and sometimes became as low as those observed for switches *before* they become contaminated. Does the gaseous O_2 oxidize and volatilize the deposit during cycling, hence re-creating a pristine surface? To address this question, the contacting sidewalls from each device were imaged in SEM (at a 45

degree tilt from the top view of the switch such that the contact sidewall is visible) after the **Figure 6.3b** experiment. In each case, deposit remained. A new device was cold-switched for 10^5 cycles in N_2-C_6H_6 (attaining a final R_c of 400 Ω). Its contacting sidewall was then imaged with SEM (again at 45 degree tilt) as shown in **Figure 6.3c**. Next, this *same* device was cold-switched in *clean* N_2:O_2 for an additional 10^5 cycles (attaining a final R_c of 16 Ω) and imaged again, as shown in **Figure 6.3d**. The images show the same deposit on the contact sidewall. Hence, it does not volatilize in *clean* N_2:O_2. The deposit bears the entire load upon switch closure such that there is no direct metal on metal contact. This point will become clearer in **Figure 6.4** below.

While the deposit does not volatilize, it evidently transforms chemically or structurally to become more electrically conductive. One may postulate that this occurs due to the passage of electrical current through the deposit. Indeed cold-switching pre-contaminated devices in *clean* N_2 caused R_c to drop to 100 Ω after 10^6 cycles) and even to 30 Ω (within 30 cycles) in another experiment. However, the drop in R_c in *clean* N_2 did not always reduce to ≤40 Ω as in *clean* N_2:O_2.

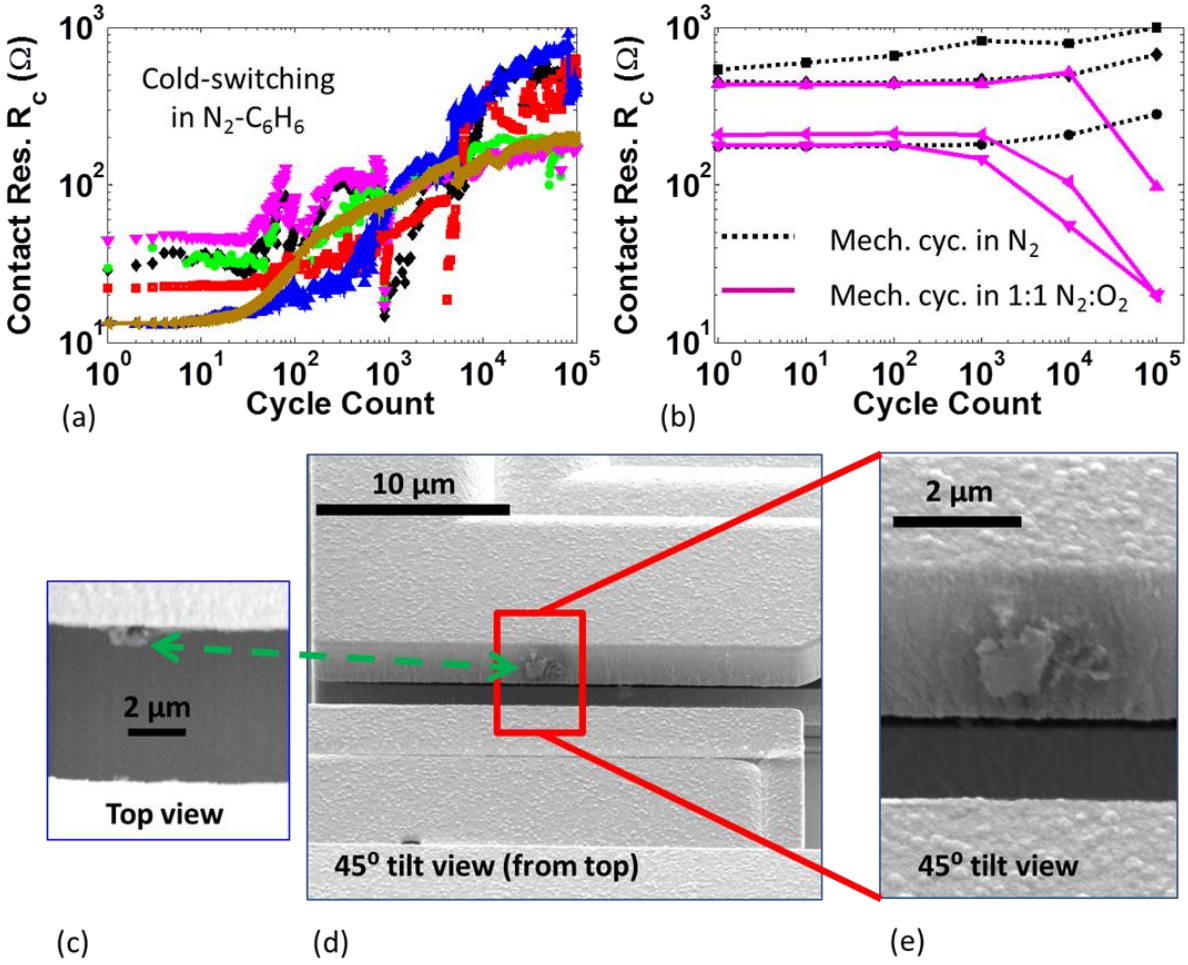

Figure 6.4: (a) Six devices cold-switched (each represented by a different color) in N_2-C_6H_6 for 10^5 cycles show a typical R_c increase. (b) Subsequent 10^5 mechanical cycling of three switches in *clean* N_2 showed further R_c increase. The other three switches that were mechanically cycled in *clean* N_2:O_2 experienced a large drop in R_c. (c) Top view and (d) close-up with (e) inset of a switch that was mechanically cycled in *clean* N_2:O_2. The images indicate that contact must occur through the now highly conducting deposit since it protrudes by 0.5 um.

To address the role of O_2 in more detail, six devices were cold-switched simultaneously in N_2-C_6H_6 for 10^5 cycles, again attaining the typical R_c increase, as seen **Figure 6.4a**. Three of these devices, which are designated by a dashed black line in **Figure 6.4b**, were then mechanically cycled (i.e. no current through contacts) in *clean* N_2 for 10^5 cycles. The resistance increased further by 120 to 400 Ω.

The other three devices, which are designated by a solid magenta line in **Figure 6.4b**, were mechanically cycled in *clean* N_2:O_2 for 10^5 cycles. Two of the devices experienced an R_c drop of ~200 Ω, achieving a final value of 20 Ω, while the third device experienced a larger R_c drop of ~300 Ω. Upon an additional 10^6 cycles in N_2:O_2, this third device achieved an R_c value of 20 Ω as well (data point not shown). The post-experimental SEM images of this third device are shown in **Figure 6.4c, 6.4d and 6.4e** (**6.4c** shows the top view while the view tilted at 45 degrees from the top is provided in **56.4d** and **6.4e**). Notice that a single large piece of deposit on the contacting sidewall protrudes much further (by ~ 0.5 μm) than any other asperity, clearly indicating it formed the only conduction path through the contacts during switch closure.

6.2.2 Chemical and Structural Characterization of Deposit

Auger spectroscopy was used to characterize the elemental composition of the deposits from each of the aforementioned experiments. Each deposit showed roughly the same composition. Data from three representative regions are presented. **Figure 6.5** shows SEM images of the contact surface (at a 30 degree tilt from the top view) with circled crosshairs indicating the locations where elemental composition was sampled. Each deposit consists of primarily C (96 to 99 atomic percent) and a small but detectable quantity of O (1 to 4 atomic percent). The surrounding deposit-free area has a large amount of Pt (36 to 52 atomic percent), a similar amount of O (1 to 2 atomic percent) and less C (45 to 63 atomic percent). These locations indicate physisorbed O and C on the Pt surface. As will be elaborated in the discussion section, Auger spectroscopy indicates that the different deposits were carbonaceous, but it does not

explain why the R_c values vary from 600 Ω to 20 Ω under cycling conditions in different environments.

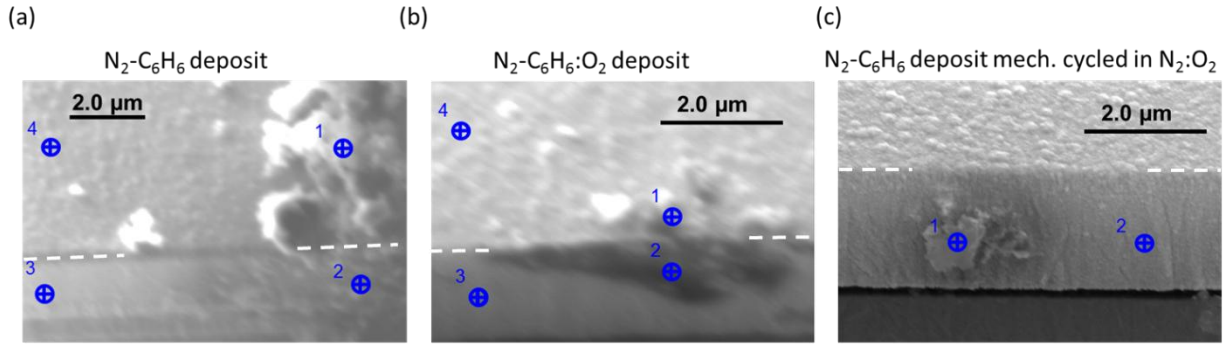

	At % C	At % O	At % Pt
Point 1	98.4	1.6	0
Point 2	98.8	1.2	0
Point 3	51.7	1.7	46.6
Point 4	58.8	1.5	39.7

	At % C	At % O	At % Pt
Point 1	96.1	3.9	0
Point 2	96.3	3.7	0
Point 3	52.5	1.6	45.9
Point 4	45.2	2.4	52.4

	At % C	At % O	At % Pt
Point 1	98.6	1.4	0
Point 2	62.5	1.5	36.0

Figure 6.5: Scanning Auger microscope analysis results. Dashed lines in SEM images above indicate the vertical contact edge. (a) Points 1 and 2 indicate that the N_2-C_6H_6 deposit is mostly elemental C with a trace of O. (b) The N_2-C_6H_6:O_2 deposit is also mostly C though it has slightly more O. (c) The N_2-C_6H_6 deposit that experienced mechanical cycling in N_2:O_2 has the same composition as the N_2-C_6H_6 deposit, despite the much lower R_c.

Raman spectroscopy has been applied frequently to gain information on carbonaceous materials [96]. Here, Raman spectra ideally would be collected on the structure sidewalls, as was done with Auger, but it is difficult to obtain reliable optical spectroscopy results from such a small area on a tilted specimen. However, cycling in both N_2-C_6H_6 and N_2-C_6H_6 O_2 cause deposit to migrate to the top surface as seen in **Figure 6.1b**. Therefore, the material on the top surface is likely the same as the material that was created at the contacting interface.

Raman spectra were collected from a rectangular region on the deposits in **Figure 6.1b** and **6.1c**. Basis spectra are shown in **Figure 6.6**, where the signal intensity (I) is plotted as a function of Raman shift (vibrational frequency). They were generated from scans of the

rectangular regions in **Figure 6.1** (also outlined in **Figure 6.7**). There, a spectrum was collected at each pixel of 0.5•0.5 μm^2 area. In each spectrum, the peak located at ~1330 cm^{-1} is known as the 'D' peak, while the peak located at ~1580 cm^{-1} is known as the 'G' peak [96, 119, 120]. The solid blue basis spectrum in **Figure 6.6** is generated from the pixel with the highest D to G peak ratio ($I_D/I_G \cong 0.9$), while the dashed red basis spectrum in **Figure 6.6** is generated from the pixel with the lowest D to G peak ratio ($I_D/I_G \cong 0.6$).

A third spectrum, designated in dotted green in **Figure 6.6**, was collected in the deposit-free area on the Pt surface (away from a deposit). This spectrum shows only noise fluctuations, thereby indicating that the red and blue spectra are in fact unique to the deposits. The Raman spectra from the *deposit-free Pt surfaces* of switches tested in both N_2-C_6H_6 and N_2-C_6H_6:O_2 show roughly the same noise fluctuations.

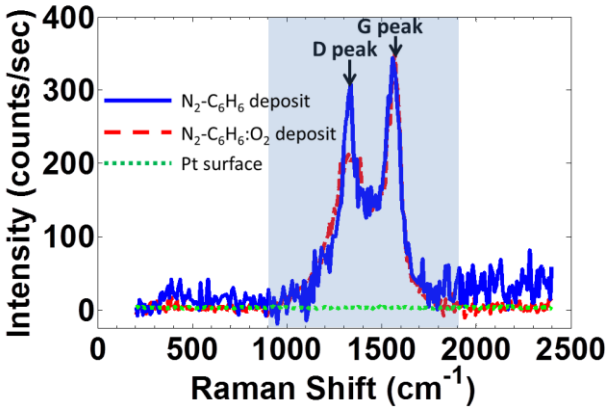

Figure 6.6: Raman basis spectra determined from scan of regions in **Figures 2(b) and 2(c)**.

The color-coded Raman maps in **Figure 6.7** indicate how the spectra vary throughout each deposit. They were created using the basis spectra from **Figure 6.6**. The color of the pixel indicates whether its spectrum is closer in shape to the blue, red, or green spectrum from **Figure 6.6**. More specifically, each spectrum is approximated with a linear combination of the three

basis spectra from **Figure 6.6** by using a classical least squares (CLS) fitting algorithm. The color of the pixel is determined by the percentage that each of the three basis spectra contributed. To limit the contribution of noise in the CLS algorithm, the span of each basis spectrum was truncated to be between the frequencies 900 and 1900 cm^{-1}, i.e., the highlighted region in **Figure 6.6**. It can be seen that the Raman map of the deposit created in N_2-C_6H_6 is mostly blue (**Figure 6.7a**) while the map of the deposit created in N_2-C_6H_6:O_2 is mostly red (**Figure 6.7b**). Hence the Raman spectra are nearly uniform within each deposit.

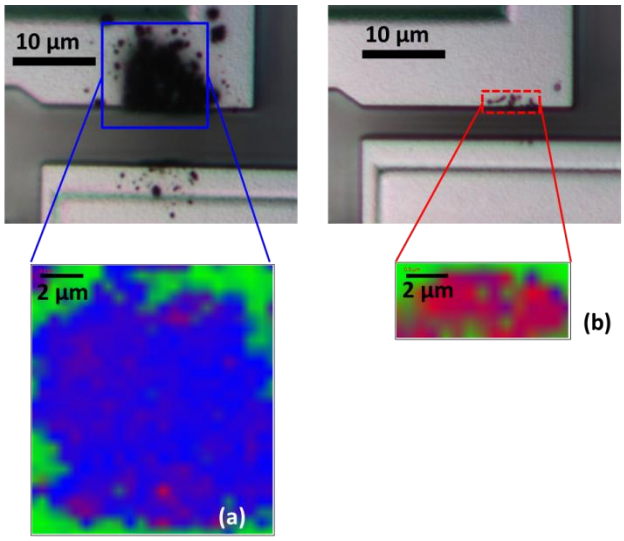

Figure 6.7: Raman spectroscopy maps of deposits created in (a) N_2-C_6H_6 and (b) N_2-C_6H_6:O_2 environments. Each map shows the corresponding regions from **Figure 2b and 2c**.

6.3 DISCUSSION

The higher R_c values found in **Figure 6.1** for the N_2-C_6H_6 experiment as compared to the N_2-C_6H_6:O_2 experiment could be due to the larger amount of deposit created in the former case. However, only the deposit at the contacting asperities on the sidewall affects R_c, not the copious amount found on top of the contacts in **Figure 6.1b**. The sidewall itself usually retains only part of the total deposit produced because as it grows inside the contact, it is continually squeezed or

ejected upon impact at switch closure. In neither experiment does the sidewall show more deposit (see **Figure 6.5a & 6.5b**). Furthermore, images from similar experiments in our previous work tend to show more deposit on the contact sidewall from the N_2-C_6H_6:O_2 case than the N_2-C_6H_6 case [48], despite the N_2-C_6H_6:O_2 case having a much lower R_c. This suggests that the difference in R_c exists primarily because each type of experiment produces different kinds of chemical bonding structure in the deposits, even though Auger spectroscopy indicates similar elemental makeup.

The decrease in the R_c values from cycling in N_2-C_6H_6 to cycling in N_2-C_6H_6:O_2, as shown in **Figure 6.2**, either suggests a deposit transformation takes place, or that the N_2-C_6H_6 deposit is gradually removed and replaced by the N_2-C_6H_6:O_2 deposit. The experimental evidence, reviewed next, indicated that transformation is the more likely process.

First, in **Figure 6.3**, it was seen that the deposit remains in place after cold switching in *clean* N_2:O_2. Next, in **Figure 6.5**, mechanically cycling the deposit created in N_2-C_6H_6 caused an R_c drop in *clean* N_2:O_2 but not in *clean* N_2. In the *clean* N_2:O_2 case the large protruding piece of deposit unambiguously demonstrated not only that the deposit remains but that it must provide the conduction path as it would keep the two metal contacts from touching each other during switch closure **(Figure 6.4c)**. The low R_c means that the deposit becomes highly conducting in O_2 because its chemical makeup and/or its structure changes. This point also suggests that the deposit created in N_2-C_6H_6 that was then cycled in N_2-C_6H_6:O_2 **(**see **Figure 6.2)** is transformed into, rather than replaced by, the N_2-C_6H_6:O_2 deposit.

The **Figure 6.4b** experiments also indicate that electrical current is not necessary for R_c to drop. Although electrical current was passed six times during both N_2 and N_2:O_2 experiments

(during the once per decade R_c measurements), the drop in R_c of the deposit occurred in the latter case only. This indicates that the presence of O_2 is the critical factor in recovery of R_c.

Using Auger spectroscopy, we attempted to explain the O_2-induced chemical or structural changes in the deposit. Although all deposits showed similar elemental compositions, we note that the N_2-C_6H_6 deposit had 1.2 to 1.6 atomic % O compared to the 3.7 to 3.9 atomic % O found in the N_2-C_6H_6:O_2 deposit **(Figures 6.5a & 6.5b)**. Before attempting to correlate the lower R_c in the N_2-C_6H_6:O_2 deposit with the higher amount of O, it is important to consider that the transformed N_2-C_6H_6 deposit from **Figure 6.5c (and Figure 6.4e)**, which has the lowest R_c by far, had only 1.4 % O (similar to N_2-C_6H_6 deposit). For that reason it seems unlikely that the variations in the amount of O can explain the variation in the corresponding R_c for each type of deposit. While the O found on the N_2-C_6H_6 deposit physisorbed upon the post-experimental exposure to air, for the N_2-C_6H_6:O_2 deposit the O may have been physisorbed on successively-formed layers of deposit while it was growing during the experiment. Perhaps this explains why there was more O in the latter case.

The Auger elemental composition analysis showed each type of deposit was carbonaceous and found no significant elemental distinction between the highest R_c N_2-C_6H_6 deposit and the lowest R_c transformed N_2-C_6H_6 deposit, suggesting each could involve different carbon allotropes. Hence, Raman spectroscopy was used to gain further insight. The spectra collected from the N_2-C_6H_6:O_2 and N_2-C_6H_6 deposits **(Figure 6.6)** indicate these are amorphous carbons [96, 120]. The D peak at 1330 cm^{-1} is associated with disordered carbon in the deposit structure [96, 119], whereas the G peak at 1580 cm^{-1} is associated with sp^2-hybridized carbon as found in graphite [96, 119, 120]. The lower I_D/I_G ratios in the spectra of the N_2-C_6H_6:O_2 deposit suggests a more graphitic (i.e., ordered carbon) character than in the N_2-C_6H_6 deposit [120]. Given that

sp^2 hybridized (graphitic) carbon is largely responsible for electrical conductivity within amorphous carbons, a higher percentage of graphitic carbon in the deposit would correspond to lower electrical resistivity [131, 132] and hence lower R_c. This could explain the lower R_c values in the N_2-C_6H_6:O_2 deposit.

Just as the N_2-C_6H_6 deposit is likely transformed into the more graphitic N_2-C_6H_6:O_2 form **(Figure 6.2, 6.6 and 6.7)**, it may be transformed in **Figure 6.3 and 6.4** into an even more graphitic form in *clean* N_2:O_2. Although a Raman measurement could not be made to confirm this (the contacting sidewalls were not accessible with Raman), its very low R_c and carbonaceous composition (undistinguishable in Auger from the high R_c N_2-C_6H_6 deposit), imply that this is the case.

We now turn our attention to the mechanism for the higher conductivity deposit that is attained in the *clean* N_2:O_2 environment. We suggest that O_2 selectively oxidizes the disordered carbon in the deposit during cycling while ordered graphitic clusters, which are energetically more stable, remain largely intact. Thus, the percentage of disordered carbon in the deposit is reduced. This in turn increases the electrical conductivity of the deposit because the electron hopping mechanism between neighboring graphitic islands in the deposit becomes more efficient [131, 133]. A similar phenomenon, selective thermal oxidation of amorphous carbon found on double-walled carbon nanotubes, has been documented [134]. In the present situation, however, mechanical stress at the contact during switch closure is a likely driving force for this oxidation.

Let us now consider the application of this study to an actual micro- or nanoswitch. In **Figure 6.3** it is seen that after cycling a deposit formed in N_2-C_6H_6 in *clean* N_2:O_2, the deposit's resistance is significantly reduced, and in fact attains nearly the level of a pristine surface. We

conjectured that the transformed deposit would provide protection from wear over an extended period. A *clean* device cold-switched in *clean* N_2:O_2 experiences wear-induced degradation, typically reaching 100 Ω within only 10^3 cycles. This is seen in **Figure 6.8** (black solid line). The appearance of Pt wear particles is the cause of this resistance increase [31]. However, the R_c of the transformed deposit cold-switched in *clean* N_2:O_2 is shown in **Figure 6.8** to drop from ~400 Ω to ~ 30 Ω within $5 \cdot 10^4$ cycles, where it remains for over $2 \cdot 10^6$ cycles. Hence, the transformed deposit can passivate the interface and delay the cycle count of wear-induced rise in R_c by three orders of magnitude.

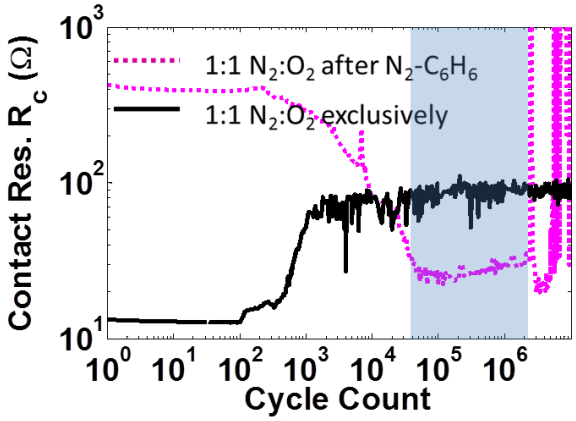

Figure 6.8: The transformed deposit maintains low R_c for over 2 million cycles, while a clean contact experiences degradation after several hundred cycles.

The approach to solving the contact contamination problem has traditionally focused on investigating contact materials that are less prone to carbonaceous deposit growth, such as Au and Ag [27, 37, 48]. However, these materials are particularly prone to wear [22]. Thus, exploitation of the deposit formed here may provide a new approach and a potential path towards solving the perplexing problem of ohmic switch reliability for micro- and nanoswitches [24, 27, 28, 37, 42, 43]. The discovery of a uniform and process-compatible method of deposition of this material that creates a suitably conducting carbonaceous layer without the need for cycling

would be of great interest. If successful, the catalytic activity and resistance of the underlying metal then would no longer be critical. Further work in characterizing the mechanical and electrical integrity of the material would also be necessary.

6.4 CONCLUSIONS

This work has demonstrated that the contact contamination issue can be reduced by transforming the highly resistive contaminant layer into a conductive one and that the wear issue can be mitigated with this protective transformed layer.

A large R_c drop in Pt-coated microswitches was observed during cycling of pre-contaminated devices in a *clean* N_2:O_2 environment. This was explained by an increase in sp^2-hybridzed carbon content of the amorphous carbon deposit on the contacts. Specific conclusions and recommendations follow:

- A contaminant-induced R_c increase in Pt-coated microswitches can be accelerated by introducing high levels of hydrocarbons into the gas background. The R_c increases correlate with the physical production of a deposit. The degree to which the R_c increases depends strongly on whether the background gas contains N_2 only, or a N_2:O_2 mixture.
- The R_c attained in N_2-C_6H_6 (~500 Ω) can be reduced to that attained in N_2-C_6H_6:O_2 (~100 Ω) after several thousand cold-switching cycles by cycling in N_2-C_6H_6:O_2. The R_c attained in N_2-C_6H_6 can be reduced to 15 to 40 Ω, nearly as low as that of a pristine surface (~15 Ω) by cycling in *clean* N_2:O_2.

- These R_c reductions are likely due to a transformation of the deposit from a disordered carbonaceous film to a more graphitic carbonaceous film. The mechanism for this transformation may be associated with a selective oxidation of the disordered components of the carbonaceous film.
- The implications of this result are firstly that ohmic switches that experienced electrical performance degradation due to contamination can be revived by cycling them in *clean* N_2:O_2. Secondly, the now graphitized, highly conducting deposit was shown to protect the contact surface from wear. Further research is needed to determine if the lifetime of this beneficial passivation layer can be increased.

Chapter VII: Current work and follow-up suggestions

Preliminary results for other work currently in progress are discussed in this chapter. Suggestions for next steps are made for each topic.

7.1 ELECTRICAL RESISTANCE RECOVERY IN RuO_2 CONTACTS

A detailed investigation of electrical contact resistance recovery of pre-contaminated Pt contacts in the presence of oxygen was presented in Chapter VI. Now we address the resistance recovery of RuO_2 contacts in the presence of oxygen.

Two RuO_2 switches were prepared for testing using the procedure described in Section 6.1 of Chapter VI. After the system bakeout, the devices were cold-switched in N_2-C_6H_6 for 100,000 cycles to accumulate contaminant. Both switches experienced a resistance rise as shown in **Figure 7.1a**, suggesting contamination. Next, the N_2-C_6H_6 gas was purged (to 10^{-7} Torr vacuum) and the chamber was refilled with 1:1 N_2-C_6H_6:O_2. One of the tested devices (the one designated in red) was now cycled in the new environment for 100,000. The fact that the resistance dropped at the first cycle for that switch (it was 135 Ω at the end of experiment one and immediately dropped to 70 Ω in experiment two), as shown in **Figure 7.1b**, demonstrates just how effective the presence of O_2 can be on device performance. As cycling progressed the resistance dropped slightly more, eventually settling at a plateau around 60 Ω, which is similar to the result obtained in **Figure 3.4a**.

After the experiment, both switches were imaged with SEM. The device that was cycled in N_2-C_6H_6 only shows a darker spot in the vicinity of the contact, as shown in **Figure 7.1c**. It could be TP, but there was not enough deposit to be identified with EDS. The SEM image of the device tested in N_2-C_6H_6 and then 1:1 N_2-C_6H_6:O_2 (**Figure 7.1d**) also shows a very slight amount of TP, though it may be as much as in **Figure 7.1c**. Hence, although device performance clearly improves upon introduction of O_2 into the system, there is not enough deposit created to visually identify this improvement. The advantage of having a small amount of deposit is that it precisely marks the contact spot, which in turn makes it possible to examine the chemistry of that location with Auger (unlike EDS, it is surface sensitive). Had these devices been cycled in N_2-C_6H_6 for longer to create more TP, it would have been more difficult to accurately pin-down the contact region.

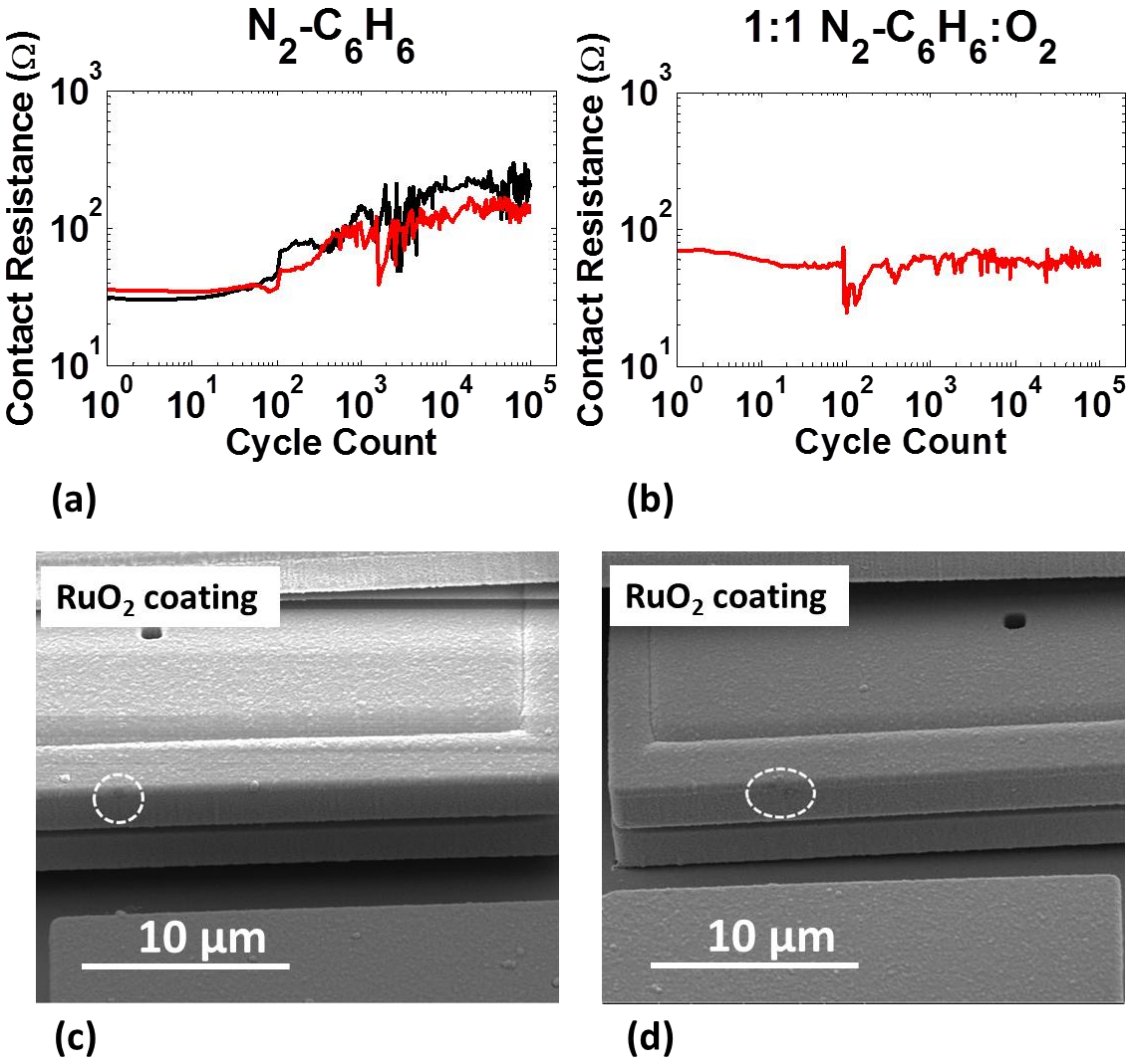

Figure 7.1: (a) 'black' and 'red' switches cycled in N_2-C_6H_6. (b) 'red' switch later cycled in N_2-C_6H_6:O_2. (c) SEM of 'black' switch after testing in N_2-C_6H_6. (d) SEM of 'red' switch after testing in N_2-C_6H_6:O_2.

To see whether additional performance recovery is possible, two fresh devices were pre-contaminated by cold-switching in N_2-C_6H_6 for 10^6 cycles, reaching resistance values of ~ 10^3 Ω (**Figure 7.2a**), and then subsequently tested in clean 1:1 N_2:O_2 (**Figure 7.2b**). Although the lowest achieved resistance values were comparable to those seen in clean devices, the resistance often fluctuated to open circuit. This fluctuation is indicative of spallation of the contact. Indeed, spallation was observed in the post experimental SEM images, as shown in **Figure 7.2c**.

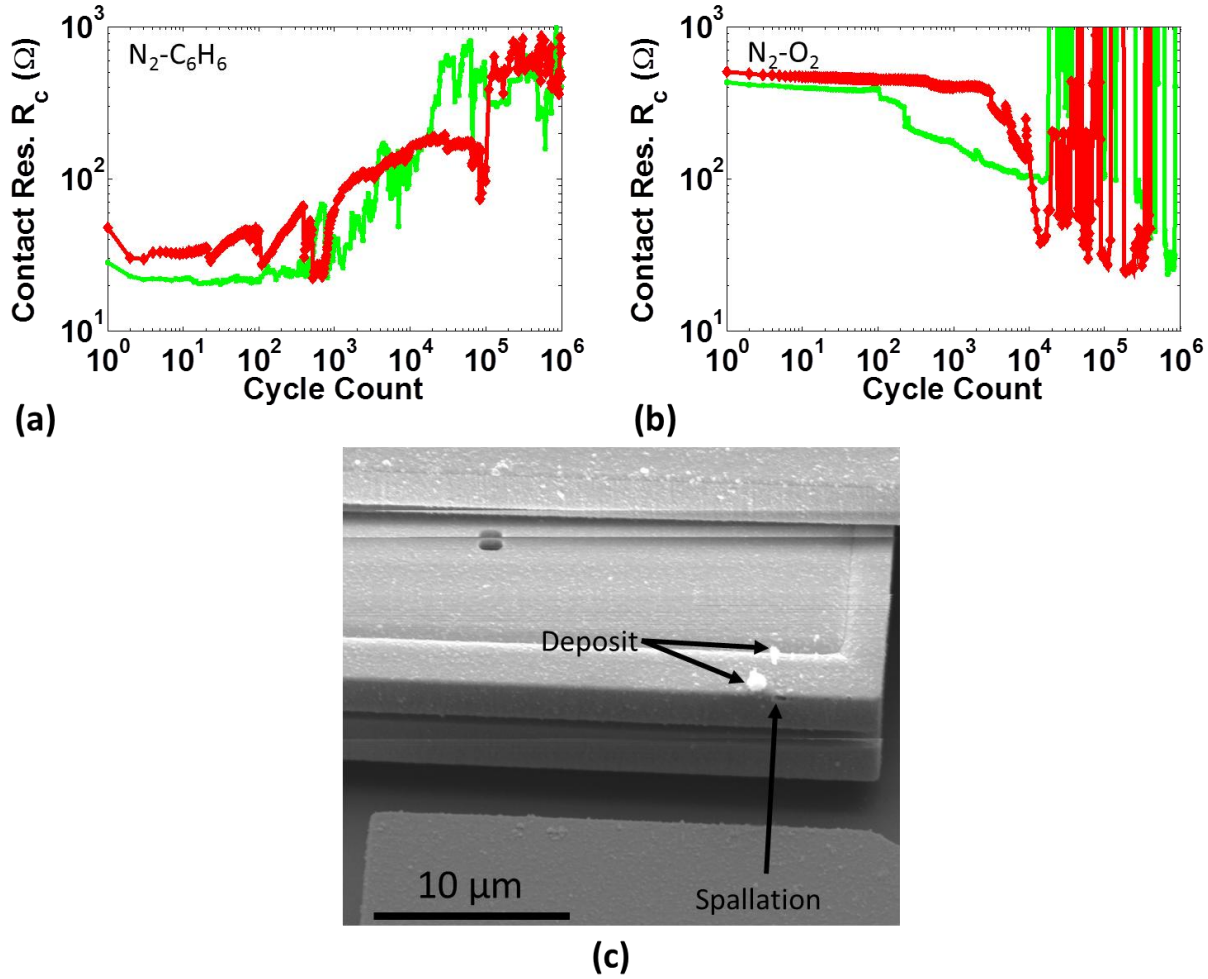

Figure 7.2: (a) Two devices cold-switched in N_2-C_6H_6 for 10^6 cycles. (b) Same two devices then cold switched in 1:1 N_2:O_2. (c) SEM image showing the contact from one of the switches after the experiments.

Devices that were cold switched for $16 \cdot 10^6$ cycles in N_2-C_6H_6 (**Figure 7.3a**) and then mechanically cycled in either UHP N_2 or 1:1 N_2:O_2 (**Figure 7.3b**) did not show any resistance recovery, though spallation was avoided as well. The post-experimental SEM image in **Figure 7.3c** corresponds to the UHP N_2 device, while the image in **Figure 7.3d** corresponds to the clean 1:1 N_2:O_2 device. Both images show about the same amount of deposit.

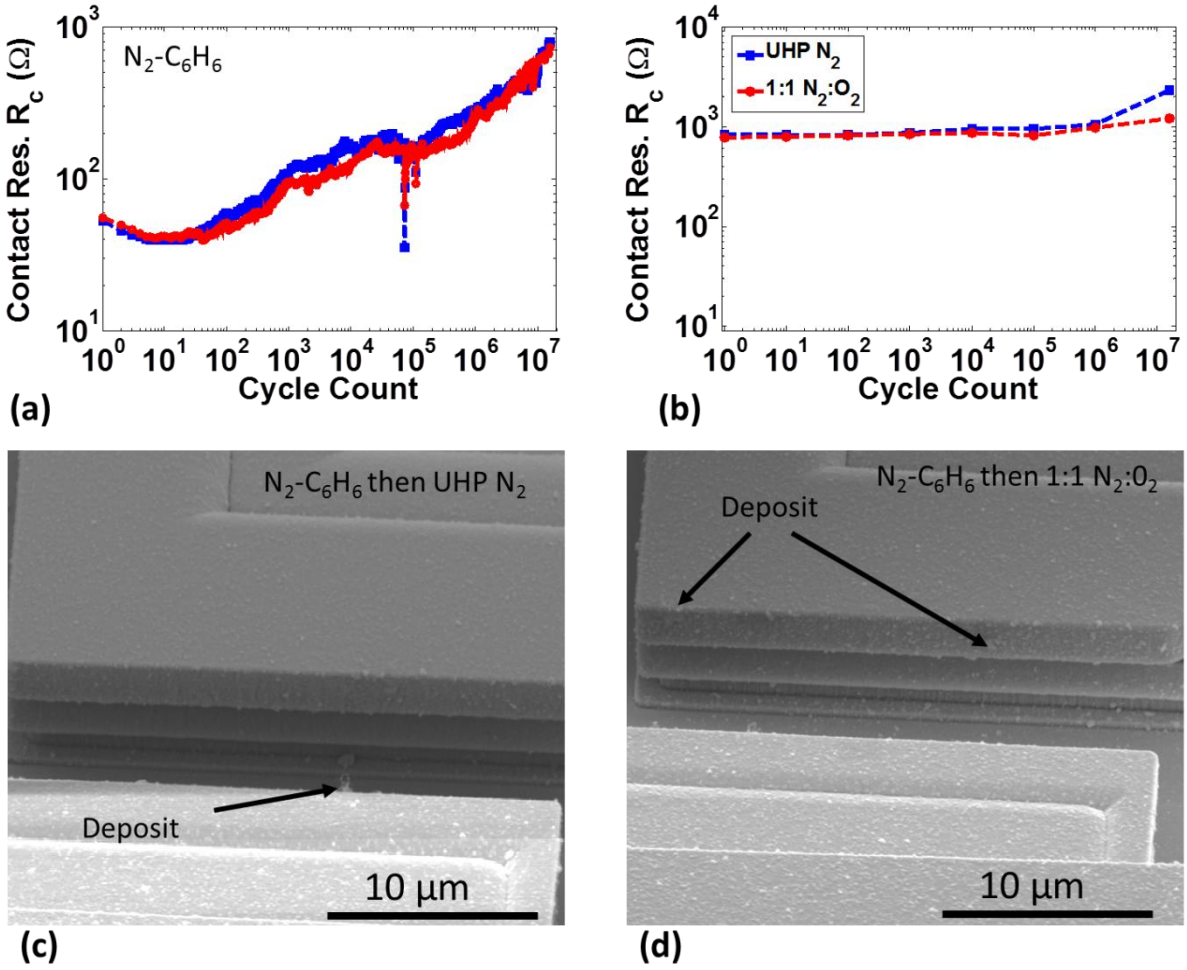

Figure 7.3: (a) Two devices cold-switched in N_2-C_6H_6 for $16 \cdot 10^6$ cycles. (b) Same two devices were then mechanically cycled; one in UHP N_2, the other in 1:1 N_2:O_2.

The mechanism of the oxygen-induced resistance recovery, when it occurs, can be likely explained by the same principle outlined in Section 6.3 of Chapter VI. That is, mechanical pressure at the contacts (during switch closure) in the presence of oxygen encourages selective oxidation of disordered carbon in the deposit, leaving the more stable graphitic carbon intact, and thereby increasing the conductivity of the deposit. Auger and Raman spectroscopy needs to be performed on the deposit created in each type of experiment to confirm this.

It is necessary to find a way to increase the lifetime of the electrical contacts after performance recovery. Perhaps cold switching the RuO_2 contacts in N_2-C_6H_6 for 10^7 cycles (10 times longer than in **Figure 7.2a**) will generate sufficient deposit to better protect the surface from wear and the subsequent graphitization of this deposit in N_2:O_2 will make it sufficiently conductive.

7.2 THE SPALLATION PROBLEM IN RuO_2 CONTACTS

As was described in **Figure 5.2d** in Chapter V, RuO_2, devices that were cold-switched typically experienced fractures at the contact surfaces. These fractures look like a piece of RuO_2 film from one contact was transferred to the opposite contact and were called spallations. The spallation problem was correlated with the onset of the open circuit failure condition. In the results of the previous section (as well as other occasions) it was observed that observed that open circuit failure and spallation did not occur in mechanical cycling. It was therefore suspected that electrical current is causing or facilitating this failure mechanism.

To test how the current effects open circuit failure, after the standard experimental preparations outlined in Chapter II, seven devices that had a RuO_2 coating and were cold switched for $16 \cdot 10^6$ cycles in clean 1:1 N_2:O_2. Two of these devices had 1 V applied across the contacts, three of them had 5 V applied across the contacts and the last two had 10 V applied across the contacts, as shown in **Figure 7.4a**. The two devices with the lowest contact voltage (1 V) performed the best. Although they experienced some resistance increase (from ~30 Ω to ~50 Ω for the most part), they never reached open circuit. The three devices tested with 5 V across the contacts reached the open circuit condition after $1.5 \cdot 10^4$, $6.5 \cdot 10^4$ and $6.8 \cdot 10^4$ cycles. These numbers are generally consistent with similar 5 V experiments performed in our previous studies, where most devices survived $6 \cdot 10^4$ cycles but some failed much sooner. The devices tested with 10 V across the contacts appeared to fare the worst. One achieved open circuit after $1.1 \cdot 10^4$ cycles, while the other after $2.9 \cdot 10^4$ cycles. The SEM image of the 1 V experiment, as shown in **Figure 7.4b**, showed spallation, just as the image of the 10 V experiment in **Figure 7.4c**.

It is surprising that although all three experiment types showed spallation failure, only the 5 V and the 10 V experiments reached open circuit. It means that although open circuit has always been correlated with spallation failure, the spallation failure does not necessarily imply the open circuit condition. It is important to emphasize again that such spallations were not observed in switches that have been mechanically cycled, so it still appears that electrical current is facilitating their formation.

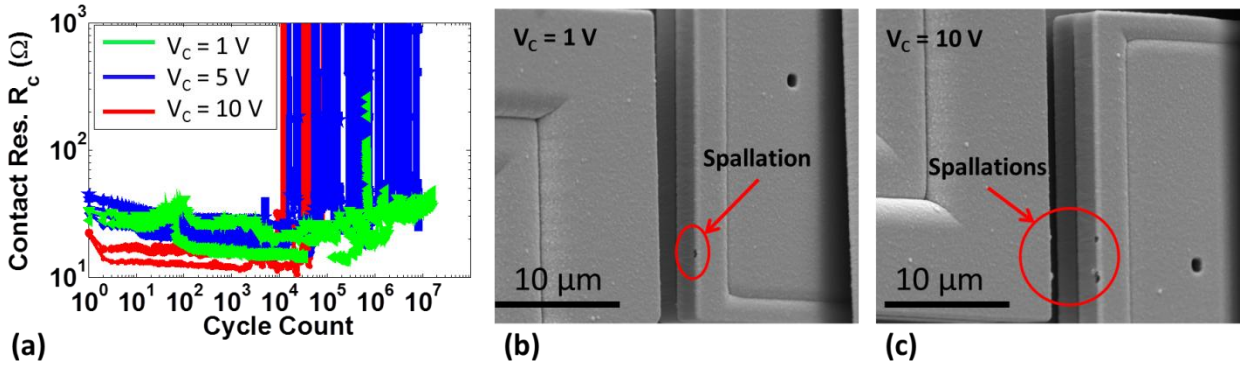

Figure 7.4: (a) Seven RuO_2 coated devices were cold switched in clean 1:1 N_2:O_2 with contact voltages of 1,5 and 10 volts, where increasing the contact voltage generally corresponded with earlier open circuit failure. (b) Although the devices with 1 V contact voltage did not experience open circuit failure, they still showed contact spallation. (c) The devices with 10 V across the contacts experienced open circuit failure and showed contact spallation.

The cause of open circuit failure is not clear. Perhaps after spallation happens, a particle from the fractured surface eventually gets in the way of contact closure such that only one of the two contact pairs experiences real contact, effectively creating an open circuit. However, as can be seen in that data of **Figure7.4a**, low resistance contact is frequently re-established after the initial open circuit failure, suggesting that the re-alignment of that particle allowed the closure of the circuit. Perhaps the spallation happens sooner at higher voltages (and consequently higher currents), explaining why we see open circuit failure sooner in those cases.

The cause of spallation could be associated with a local temperature increase at contacting asperities that creates fracture-inducing thermal stresses. Alternatively, current-induced material transfer could explain this phenomenon. In nearly all cases where this failure mode has been observed, the two spallation regions on the contact bar at the sites of the two respective contacts have opposite spallation types. One side of the contact bar has a "hole" in it (the opposing trace contact has the removed material), as shown in **Figure 7.5a**, while the other side of the same contact bar has an extra piece of material (taken out of the opposing trace contact), as shown in **Figure 7.5b**. Given that during switch closure current enters the contact bar at one contact site and exits the bar from the other site, the trend in material transfer suggests a dependence on electron path.

If the materials transfer is indeed current based, it would be worthwhile to reverse the direction of current flow every so many cycles or even use alternating current to see whether the problem persists. Since it was shown that deposit buildup protects the contacts from spalling, it may be worth-while to work on developing a method where highly conductive protective deposit is built-up. The conducting graphitized deposit discussed in Section 7.1 may be a capable of creating such a protective layer. It may be also worth exploring different adhesive interfaces between the RuO_2 and the polysilicon to see whether they can hold the structure together better. This last approach does not seem particularly promising because we have already shown that an Al interlayer did not reduce spallation.

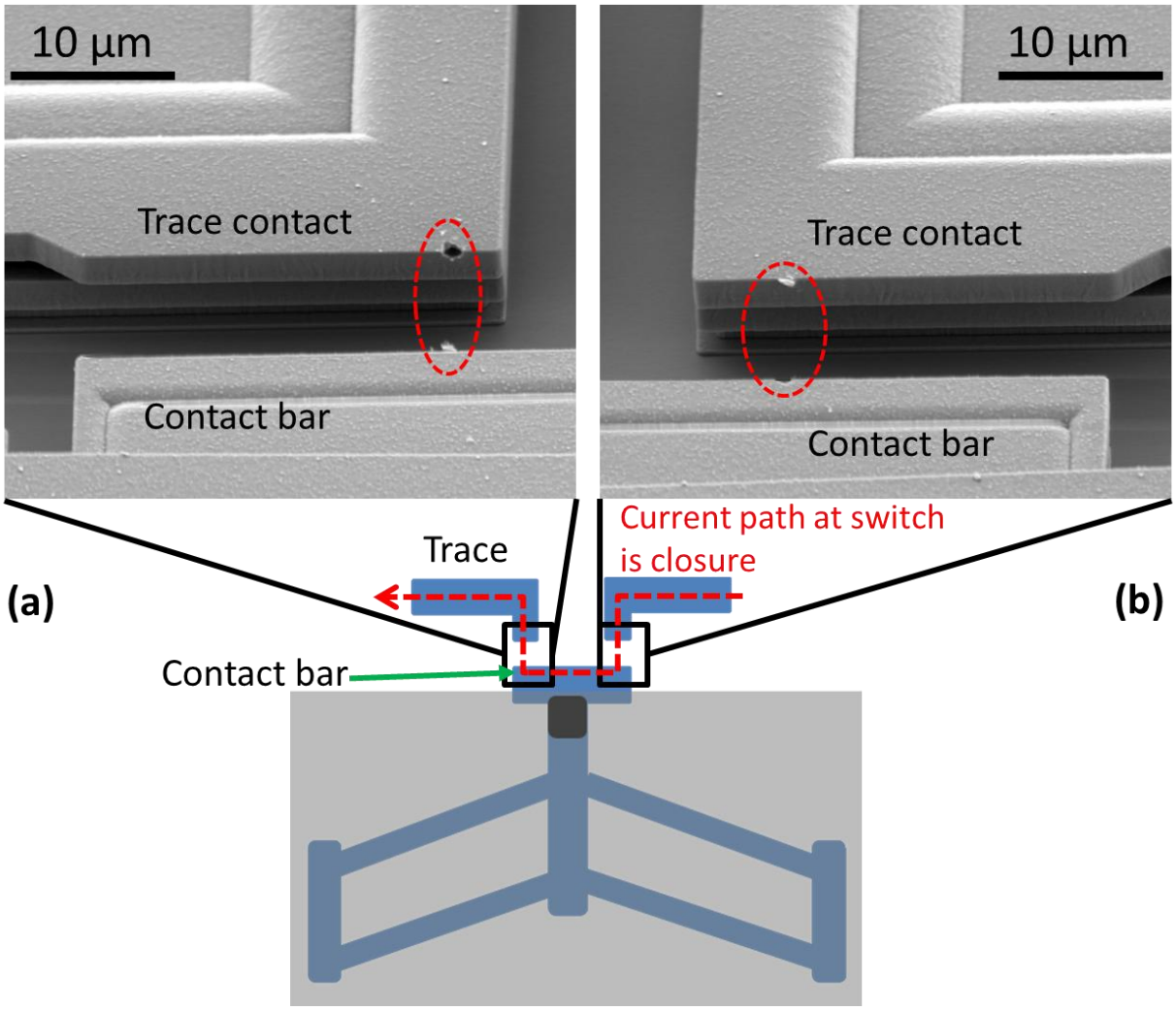

Figure 7.5: Material transfer appears to be related to the path of electrical current through the contacts. (a) Material is transferred from the trace to the contact bar. (b) Material is transferred from the contact bar to the trace.

Nanoindentation experiments were performed to be able to comment further on the role of mechanical loading in spallation failure. Although extensive cycling as in switch contacts was not implemented here, it was worthwhile to find loading conditions under which plastic deformation and fracture of the coating can happen.

The chip containing the switches was bonded with stiff epoxy to the sample chuck of the nanoindenter in order to limit sample compliance during indentation. The chip itself is a 500 µm

thick [111] silicon substrate that is coated with a 1 μm thick polycrystalline RuO_2 film. A set of relatively deep and optically visible indents were performed on a flat region of the chip to calibrate for sample compliance and indentor positioning. A diamond cube-corner nanoindenter tip was used.

Indentation testing was performed on the chip surface at flat locations that are at least 50 μm away from the MEMS switches so as to avoid interference with the indent-induced deformation zone. As shown in **Figure 7.6**, the indentation experiment involved five loading/unloading cycles on the same location with increasing maximum loads of 0.625 mN, 1.25 mN, 2.5 mN, 5 mN, and 10 mN. The maximum depth of penetration was 4 μm, being substantially larger than the 1 μm RuO_2 coating thickness. This means that the coating was either penetrated by the indenter or it was pushed downwards with the substrate without being penetrated. The time of the entire experiment was 272 seconds.

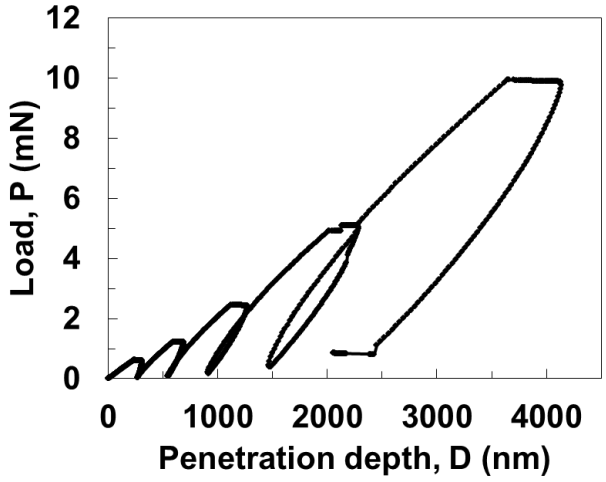

Figure 7.6: Nanoindentation of 1 μm thick RuO_2 coating on a 500 μm thick silicon substrate.

The 10 mN load of the indentation is 50 times as large as the 200 uN load applied on each contact during switching. Although permanent deformation was observed after the indentation, as shown in **Figure 7.7a**, it resembles plastic deformation without any form of fracture of the RuO_2 film. However the much larger calibration indent showed a deeper imprint in the RuO_2 film as well as what looks like delamination of the film and channel cracking (**Figure 7.7b**).

This means that uniform loading alone is unlikely to induce spallation of the RuO_2 layer at the contacts. The dynamic aspect of contact cycling may be necessary for instigating the structural failure of the contact. However, passing electrical current through the contacts appears to be critical for such failure to materialize since it has not been observed in mechanical cycling.

It would be important to check whether spallation can happen during constant loading in the presence of current but in the absence of cycling. In such an experiment, the switch would be held closed while current is being passed through it for a duration of 24 hours (a time frame that is roughly equivalent to $1.6 \bullet 10^7$ switch cycles).

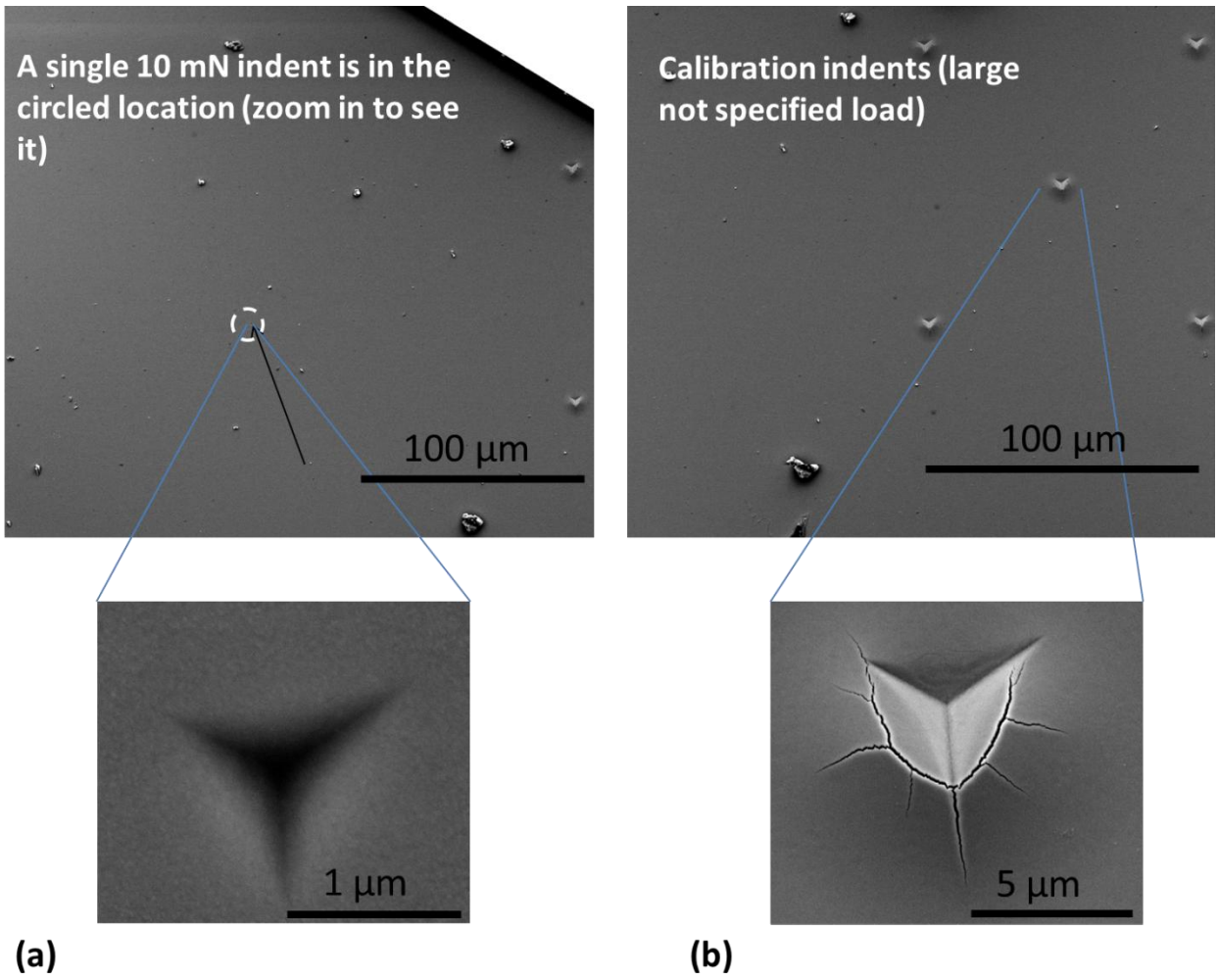

Figure 7.7: (a) The 10 mN indentation shows plastic deformation but no signs of fracture. (b) The much larger calibration indent shows what appears to be delamination and channel cracks

7.3 OXYGEN-INDUCED ACCELERATION OF WEAR (FOR BOTH Pt and RuO_2 CONTACTS)

When switches with Pt-coated contacts are tested in clean operating conditions (after undergoing the standard cleaning procedure outlined in Chapter II), they still experience a rise in contact resistance. This increase in R_C has been associated with contact wear. In cold-switching experiments performed on four switches in UHP N_2 (where devices were tested for at least

$16 \cdot 10^6$ cycles) a rise in R_C was observed after 10^5 to 10^6 cycles, as shown in **Figure 7.8a**. However, for cold-switching experiments performed in clean 1:1 N_2:O_2 on three switches (where devices were tested for at least $16 \cdot 10^6$ cycles), electrical degradation started much sooner -- after just 10^3 cycles, as shown in **Figure 7.8a**. The post experimental SEM images of the UHP N_2 test (**Figure 7.8b**) and the 1:1 N_2:O_2 test (**Figure 7.8c**), showed wear products that were confirmed with EDS to be mostly Pt and to not differ in chemical composition from the surrounding regions. Auger spectroscopy was also performed on the wear products of the 1:1 N_2:O_2 test, again confirming they are made of Pt and that their chemical composition does not differ from the surrounding region.

Our initial interpretation for as to why the presence of oxygen causes such a rapid onset of degradation was that an electrically resistive oxide is formed at contacting asperities. However, Auger spectroscopy conclusively showed that this is not the case because the amount of oxygen on the wear products was very small and did not differ from surrounding Pt surfaces away from the contact. It is therefore not clear why oxygen accelerates wear. It is possible that oxygen somehow embrittles Pt.

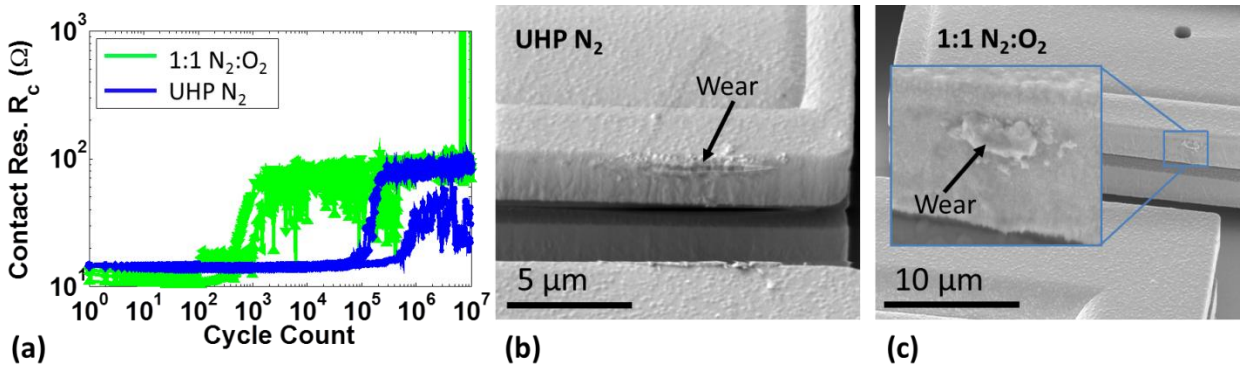

Figure 7.8: (a) Seven Pt devices were tested in clean environments. Four were tested in UHP N_2 and the other three were tested in 1:1 N_2:O_2, the latter three experienced electrical degradation much sooner. (b) A post-experimental SEM image of a device tested in UHP N_2. (c) A post-experimental SEM image of a device tested in 1:1 N_2:O_2.

A similar effect was observed on RuO_2-coated switch contacts. A total of nine switches were tested in clean conditions after undergoing the standard cleaning procedure outlined in Chapter II. Six of these devices were cold-switched in UHP N_2 for $16 \cdot 10^6$ cycles experienced open circuit failure after $\sim 2 \cdot 10^6$ cycles, as shown in **Figure 7.9a**. However, the three devices that were cold-switched in 1:1 N_2:O_2 for $16 \cdot 10^6$ cycles, all experienced open-circuit failure before 10^5 cycles, as shown in **Figure 7.9a**. The post-experimental SEM image in **Figure 7.9b** of the device tested in UHP N_2 shows a typical spallation failure. The device tested in 1:1 N_2:O_2 also experienced the spallation failure, as shown in **Figure 7.9c**.

Again, it is clear that the presence of oxygen accelerates wear-induced (that appears in the form of spallation here) electrical degradation, though it is not clear why that happens. It would be worthwhile to test whether oxygen accelerates degradation in the absence of electrical current. For example one device could be mechanically cycled in clean N_2 while another device could be mechanically cycled in N_2:O_2 and the electrical performance data from both experiments would be compared.

It could be worthwhile to measure the mechanical properties of wear products from each environment using nanoindentation or AFM. A thorough literature review of oxygen-induced embrittlement may also shed light on potential relevant mechanisms.

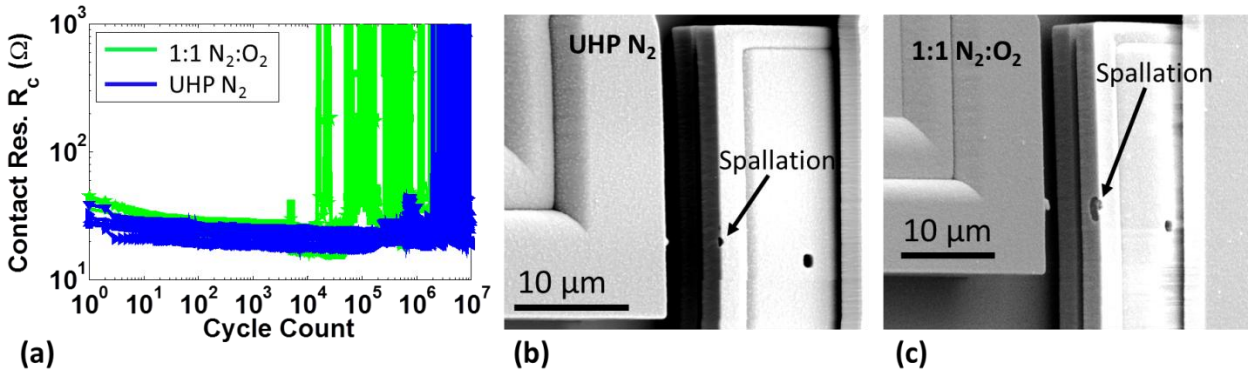

Figure 7.9: (a) Nine RuO_2 devices were tested in clean environments. Six were tested in UHP N_2 and the other three were tested in 1:1 N_2:O_2, the latter three experienced open circuit failure much sooner. (b) A post experimental SEM image of a device tested in UHP N_2. (c) A post experimental SEM image of a device tested in 1:1 N_2:O_2.

7.4 THE FORCE EFFECT

After undergoing the standard cleaning preparations outlined in Chapter II, four devices were cold-switched in N_2-C_6H_6 (2,500 PPM C_6H_6) for 10^5 cycles, all of these devices experienced a resistance rise as shown in **Figure 7.10**. The only difference between those switches was however, that the two devices designated by red had twice as many thermal actuators legs as compared to those designated in green (four versus two). This means that the contacts of the red device experienced twice the load (250 µN per contact surface) as compared to the green device (125 µN per contact surface). Electrical degradation initiated in the red devices after the first 20 cycles, whereas in the green devices degradation initiated after ~200 cycles. Hence, devices undergoing the larger contact load experience electrical degradation sooner. Although this contact-loading effect is repeatable (we observed it in up to 90 % of ~40 pairs of switches), it is typically less noticeable than what is shown in **Figure 7.10**. One reason this load dependence is weak is because at this scale, the contact stress is largely governed by material hardness instead of the applied load.

It is worth noting that the devices with the lower load appear to reach a higher R_C value towards the end of the experiment, however, had these switches been tested longer, they would all likely have reached the same level.

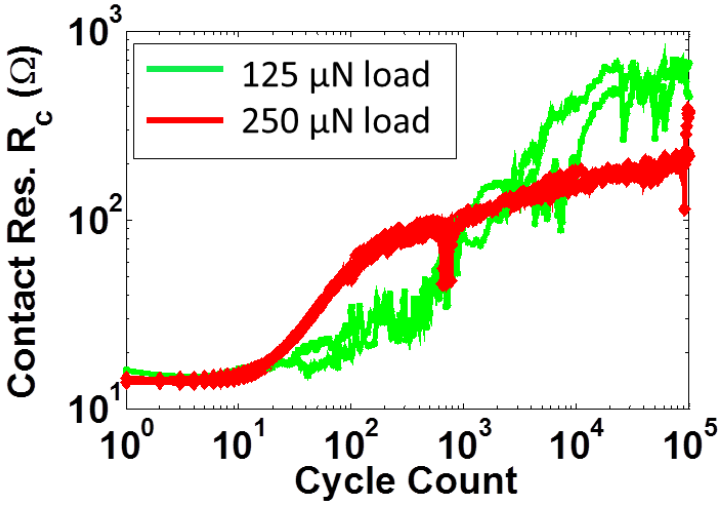

Figure 7.10: Electrical degradation happens at a lower cycle count when the load is higher

7.5 ELECTRICAL PERFORMANCE OF Au-RuO_2 CONTACTS

With the intent of limiting the spallations seen in RuO_2-RuO_2 contacts, two dissimilar metal contacts, namely, Au on one contact and RuO_2 on the opposing contact were cold-switched in clean O_2. It was hoped that the softer Au will cushion the impacts at contact during cycling and reduce spalling in the RuO_2 coating. The contact resistance vs. cycle count data for this coating combination turned out to be rather similar to what was seen previously in RuO_2-RuO_2 contacts. Data for five devices is shown in **Figure 7.11**. Four devices experienced an abrupt open circuit failure between $1.5 \cdot 10^5$ and $2.5 \cdot 10^5$ cycles, though the fifth devices failed after just $2.3 \cdot 10^4$ cycles.

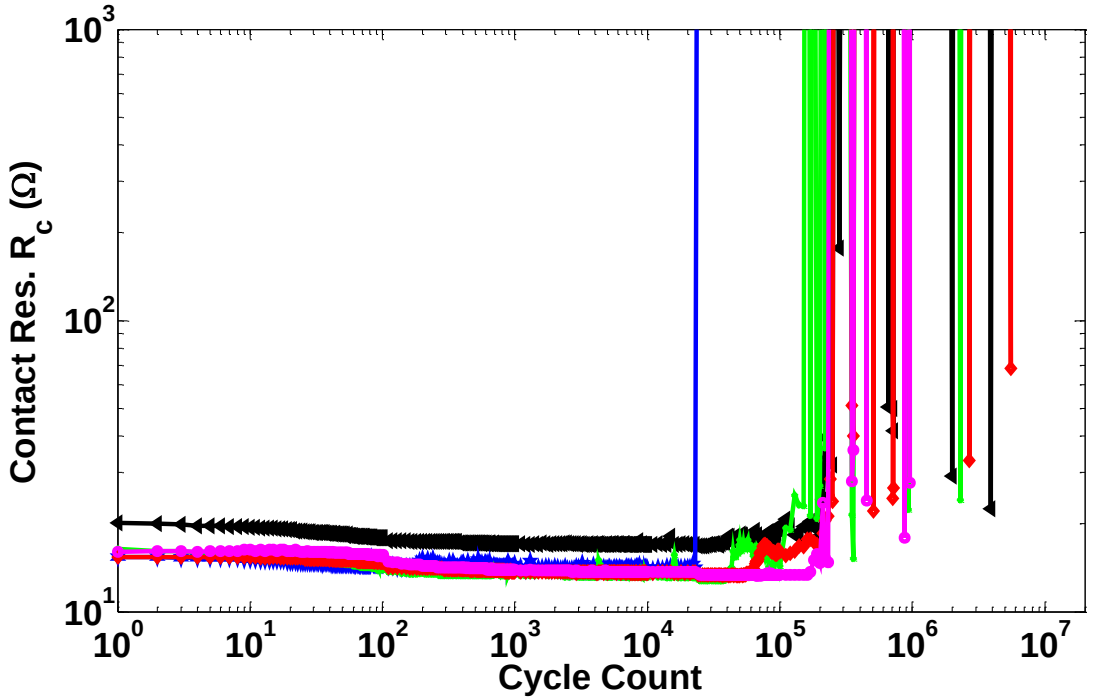

Figure 7.11: Five Au-RuO_2 devices tested in clean O_2.

The reason for the open circuit failure can likely be associated with what appears to be substantial material transfer seen in **Figure 7.12**. As in the RuO_2-RuO_2 contact spallation problem, a large particle stuck in between one contact pair may be preventing the other contact pair from closing, effectively causing open circuit. It is also noticeable that while the left side of the RuO_2 contact bar (which is opposite the left trace contact) in **Figure 7.12a** has a Au deposit, the right side of the same contact bar (opposite the right trace contact) in **Figure 7.12b** has a hole. This may suggest that the direction of DC current flow through the contacts affected the material transfer direction.

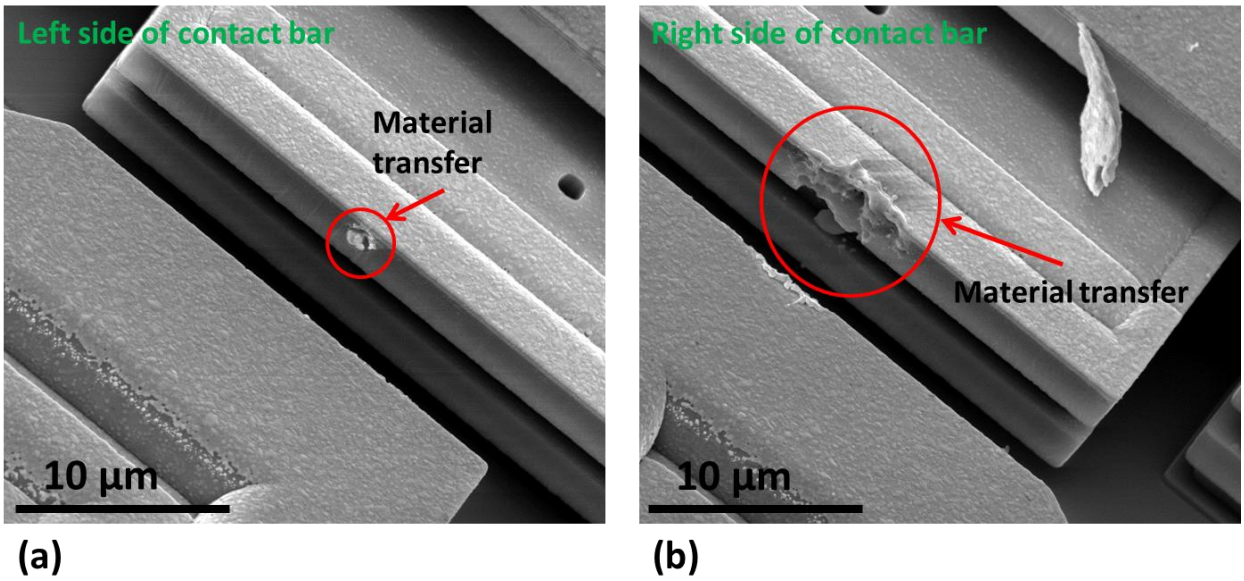

Figure 7.12: (a) The left side of the RuO_2 contact bar has Au deposit transferred from the opposing trace contact. (b) The right side of the same contact bar has a hole.

Another notable difference for this experiment is that the thermal actuator voltage used was 9 V rather than the 8 V used in all other experiments discussed in this dissertation. The initial experiments I did when I was starting my PhD work were performed at 9 V in clean conditions. The Au-RuO_2 devices were amongst these first experiments. However, in trying to limit wear (in switches with all coating types), the actuation voltage was then reduced to 8 V. Although this voltage reduction turned out to have an insubstantial effect on wear, the 8 V level was maintained in all experiments thereafter for the sake of consistency.

Future work could entail investigating this phenomenon in N_2 environment to see whether oxygen also accelerates wear for this material combination (see oxygen-induced acceleration of contact wear discussion in Section 7.3).

7.6 FINAL COMMENTS ON DEPOSIT FORMATION AND RAMAN DATA

In Chapter IV it was concluded that the larger Raman peak intensity ratio (I_D/I_G) of the deposit produced in cold-switching as compared to that produced in mechanical cycling was due to an increased amount of disordered carbon in the former (**Figure 4.4**).

It was suggested that in both switching modes, the same type of electrically-insulating sp^3-rich deposit is produced at the beginning of each actuation cycle. However, the application of voltage that occurs in the cold-switching mode *after contact is formed* electrically breaks down the deposit. This electrical breakdown transforms some sp^3-carbon into graphitic sp^2-carbon (which is electrically conducting), making the deposit conductive. The higher concentration of aromatic rings within the sp^3-rich and amorphous structure gives rise to the higher I_D/I_G ratio.

In Chapter VI it was observed that the deposit produced in N_2-C_6H_6 and then cycled in the presence of oxygen experienced a reduction in its I_D/I_G ratio (**Figures 6.6 and 6.7**). It was concluded that this was related to its graphitization (increase in fraction of graphitic sp^2-carbon). It was suggested that disordered carbon in the deposit was selectively oxidized while the energetically more stable graphitic sp^2-carbon remained, thus its fraction of deposit content increased. Since there was now less disorder, the I_D/I_G ratio was also lower. The increasing electrical conductivity of the deposit provided evidence for that.

The different reasons given to explain lower I_D/I_G ratio in Chapters IV and VI need not contradict each other. The low concentration of aromatic rings (as in sp^3-rich amorphous carbon), which are necessary for the Raman D-mode to be active, can correspond to low I_D/I_G ratio, as can low amount of disorder in the structure (the I_D/I_G ratio is zero in perfect graphite

because the D-mode is forbidden in the absence of disorder). Additional information such as the electrical resistance of the deposit can be used to find the correct explanation for each scenario.

Future work with Raman spectroscopy could involve the study of experiments where only small quantities of deposit were produced that inevitably remained on the contact sidewall surfaces. The deposit in those experiments is not accessible with the Raman instrument when the switch contact is in its natural position (see discussion in Section 6.3). Special preparations would be needed to extract the contact surface (possibly cutting it out using focused ion beam) to make it accessible to Raman. Specifically, it would be worthwhile to prove that the deposit produced in N_2:O_2 performance recovery experiments (see Section 6.3) is indeed highly graphitized. It would be also interesting to perform Raman on the deposit produced by mechanically cycling Pt contacts in N_2-C_6H_6 at 100 ℃ and 200 ℃, as discussed in Section 4.2.

Another avenue would be to do Raman spectroscopy on deposits produced on experiments involving RuO_2 contacts and compare that to the corresponding experiments with Pt contacts.

7.7 INVESTIGATE HOW MECHANICAL STRESS EFFECTS DEPOSIT GROWTH

It would be useful to test the effect of mechanical stress on deposit formation by varying contact hardness while keeping the surface chemistry largely the same. When polycrystalline metals are annealed, their grains grow and their hardness drops. The Pt coating will work for this experiment because it has a well-established grain size to hardness relationship [135]. For example, by annealing bulk Pt at 800 ℃, its hardness can drop by more than a factor of three. In our specimens, this hardness drop could be quantified with nanoindentation testing of a rigid (but

Pt coated) region near the actual switch. We hypothesize that the softened Pt will produce a lower amount of TP and will also have a lower resistance. The specimens could be annealed at the desired temperature in an oven or more simply by joule heating of the contacts. The Jensen temperature model from equation 4.3 in Chapter IV, predicts that by passing 0.1 A through the contacts with a resistance of 10 Ω, a temperature of ~ 1,000 ℃ would be established.

It is important to keep in mind however that the cycling of Pt undoubtedly cold-works the surface to some extent. This may harden it noticeably and thus somewhat reverse the softening effect of annealing. It would need to be determined whether cold-working would change the hardness substantially at that scale.

Another method to control the hardness of the Pt film is by controlling the layer underneath it. The mechanical behavior of a very thin film is affected by the layer underneath [136]. Thus, for example if we coat a hard substrate with ~ 10 nm of Pt, the Pt will resemble the hardness of the substrate to a large extent. Using this technique to study the effects of hardness on TP formation would largely circumvent the issue associated with cold-working. Furthermore, controlling the under-layer material and annealing could potentially enable an even broader range of contact hardness values to work with.

7.8 REVISED QUALITATIVE MODEL AND COMMENTS ON DEPOSIT FORMATION

The discussion in Chapter III provided a simple qualitative model (Figure 3.11 and Figure 3.12) that describes how factors such as mechanical stress and electrical current can lower the activation energy of tribopolymer deposit formation from adsorbed benzene. The discussion in Chapter IV provides additional information on how the surface-adsorbent interaction is likely to

contribute to tribopolymer deposit formation and addresses the relative contribution of other factors such as electrical current and heat. Here, a modified model for the simplest experimental scenario, where Pt-coated switches were tested in N_2-C_6H_6 is proposed with reference to **Figure 7.13**.

The mechanical cycling deposit is produced at the contacting asperity sites, so it is clear that mechanical interaction is critical for deposit formation. However, as was discussed in Chapter IV, at least 25 GPa of pressure is required induce the polymerization of the deposit, so this alone cannot be sufficient for deposit formation. Chapter IV also discussed that the Pt-benzene surface-adsorbent interaction can induce the polymerization of the adsorbent at temperatures above 80 ℃, however, the temperature of the electrical contacts does not reach that level in a standard experiment. It is therefore evident that neither mechanical stress nor surface-adsorbent interactions alone can create the deposit. Hence, the combined effect of these factors is likely the reason why TP deposit forms in mechanical cycling.

It is appropriate to assume that the adsorbed C_6H_6 molecules exhibit some distribution of energies. The mechanical stress and substrate-adsorbent interaction could be raising the energy of all the adsorbed C_6H_6 molecules at the contact site (or equivalently lowering the activation energy barrier for adsorbent polymerization as shown in **Figure 7.13**), thereby increasing the fraction of these molecules with sufficient energy to overcome the activation barrier and to be polymerized. Because applying electrical current during contact (as in cold switching) greatly augments the amount of deposit produced (as compared to mechanical cycling), it likely significantly raises the energy of the adsorbed C_6H_6 molecules to enable a much larger fraction of them to overcome this activation energy barrier (hence the relatively large barrier reduction illustrated by the red arrow in **Figure 7.13**). Although increasing the contact temperature would

further reduce the activation energy, it also desorbs the reactants and for that reason the overall effect is a reduction in amount of deposit produced, as was shown experimentally in Chapter IV. The most substantial contribution to the reduction in activation energy seemingly comes from the electrical current, as shown in **Figure 7.13**, however, it is not clear large the other contributions are in comparison.

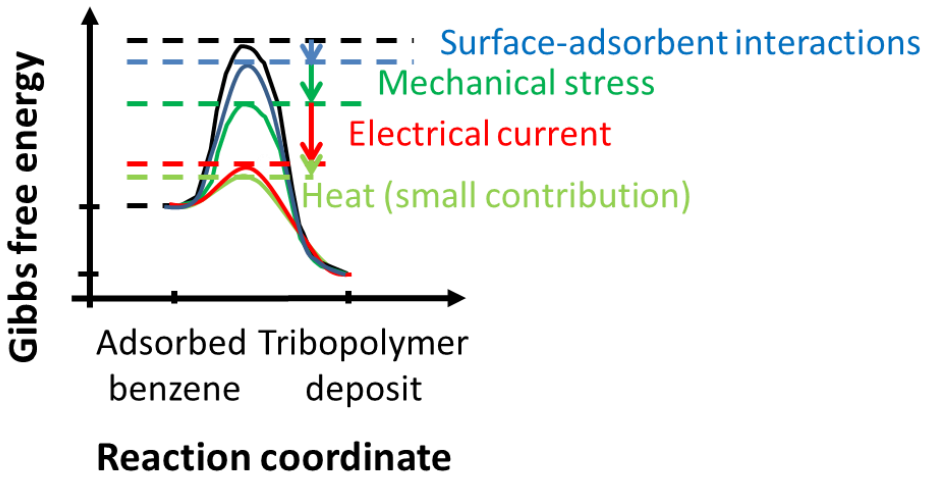

Figure 7.13: Qualitative model illustrating how four different factors lower the activation energy barrier separating.

A comprehensive picture that addresses all experimental scenarios can become quite complex and further work needs to be done to establish it.

7.9 TRIBOPOLYMER I-V MEASUREMENTS

Considering that it would be close to impossible to keep the electrical contacts completely polymer-free in real applications, it is necessary to understand how the resistance of this polymer depends on the voltage applied across it. It is worth saying that this relationship is not likely to

be linear for TP, since it is not linear for most polymers. For this reason it would be useful to create current-voltage plots for the tribopolymers we create in the different testing conditions.

7.10 HOT SWITCHING

The experimental framework we established and used for cold-switching can also be utilized for hot-switching. Considering that many ohmic switching applications, logic circuits in particular, would prefer to utilize the hot-switching mode, it would be very useful to take hot-switching contact reliability data.

Chapter VIII: Summary and suggestions for future work

First the major findings from Chapters III through VI are summarized. Then future avenues that may be worthwhile to pursue are suggested.

This dissertation explores and addresses the electrical performance degradation of ohmic microswitch electrical contacts due to the buildup of an electrically-resistive carbonaceous contaminant layer at their interface. The source of the contamination is trace amounts of volatile hydrocarbons in the environment. These hydrocarbons adsorb on the electrical contact surfaces thereby initiating the degradation process.

It has been demonstrated that a system can be built to test switches in clean and contaminated environments. The test system can be cleaned by an ultrahigh vacuum bakeout after it has been contaminated.

The contaminant of choice in this study was benzene because it is known to readily induce carbonaceous deposit growth on switch contacts. Very high concentrations of benzene were used to accelerate deposit growth to manageable time scales and to minimize the wear contribution to contact resistance increase.

It was shown that normal mechanical contact in a contaminated environment caused the nucleation and growth of electrically insulating tribopolymer (TP) deposit in the adsorbed benzene layer. When electrical current was passed through the TP, as in cold switching, the TP deposit became conducting. Furthermore, the passage of electrical current through the deposit greatly augmented its production, though this was found to not be associated with a joule-heating

induced temperature increase. In fact, increasing the temperature of the experiment was found to reduce and inhibit deposit growth.

Chemical analysis of the TP deposit with EDS, Auger and Raman spectroscopies identified it to be an amorphous carbon. Raman spectroscopy provided insight on the relative degree of disorder in the carbon structure for TP deposits produced under different experimental conditions. The TP produced in mechanical cycling had a more sp^3-rich carbon structure than the electrically broken down TP produced in cold switching, which had more sp^2 carbon in the form of aromatic ring clusters. Also, the TP produced in N_2-C_6H_6:O_2 likely had more of a graphitic structure than the TP produced in N_2-C_6H_6.

The effect of the interplay between operating environment and contact materials on switch performance was investigated. Pt and RuO_2 contacts were tested in N_2-C_6H_6 and N_2-C_6H_6:O_2 environments. It was found that both materials experienced rapid degradation in N_2-C_6H_6, though degradation was more severe for RuO_2. While both materials showed less TP deposit buildup in N_2-C_6H_6:O_2, RuO_2 experienced virtually no electrical degradation. In fact it was shown that as long as oxygen was present, at least 400 PPM of benzene (a very high concentration) was necessary to initiate contaminant-induced degradation in RuO_2 contacts. Whereas only 0.02 PPM of benzene in N_2 background (no O_2), which is much less than the total hydrocarbon load found in air, initiated electrical degradation in Pt contacts. In the presence of O_2, Pt contacts degrade very quickly due to wear, even before contaminant begins building up.

Despite the promising contamination-resistant qualities of RuO_2, this coating was found to be prone to spallation failure that was associated with an open circuit. It was shown that this open

circuit failure was dependent on the voltage applied across the contacts, where a larger voltage accelerates degradation.

While oxygen was found to accelerate contact wear under clean conditions for both contact materials used in this work, this effect was particularly pronounced for the Pt coating. However, when Pt devices were pre-contaminated by cold switching in N_2-C_6H_6 and then were cycled in clean N_2:O_2, their electrical performance recovered fully or nearly so. This performance recovery was attributed to the graphitization of the TP deposit. The now transformed highly conductive deposit was shown to protect the surface from wear.

Future work could entail finding or developing methods to efficiently grow this highly conductive graphitic coating on the contacts. Not only does this approach present a promising start to solving the wear problem, but it can also prevent or limit degradation due to contaminant buildup. This is because a carbonaceous layer has a much lower affinity for adsorbing hydrocarbons than a metal surface.

It would also be worthwhile to investigate the performance of other contact materials as well as the effect of other contaminants on device reliability.

Bibliography:

[1] A. D. Romig, M. T. Dugger, and P. J. McWhorter, "Materials issues in microelectromechanical devices: science, engineering, manufacturability and reliability," *Acta Materialia,* vol. 51, pp. 5837-5866, Nov 25 2003.

[2] L. J. Hornbeck, "Multi-level digital micromirror device," United States Patent 5,583,688, 10 Dec. 1996, 1996.

[3] R. A. Coutu, P. E. Kladitis, K. D. Leedy, and R. L. Crane, "Selecting metal alloy electric contact materials for MEMS switches," *Journal of Micromechanics and Microengineering,* vol. 14, pp. 1157-1164, Aug 2004.

[4] J. B. Hacker, R. E. Mihailovich, M. Kim, and J. F. DeNatale, "A Ka-band 3-bit RF MEMS true-time-delay network," *Ieee Transactions on Microwave Theory and Techniques,* vol. 51, pp. 305-308, Jan 2003.

[5] G. M. Rebeiz, *RF MEMS: Theory, Design, and Technology*. New York: John Wiley & Sons, 2004.

[6] C. Keimel, G. Claydon, B. Li, J. Park, and M. E. Valdes, "Microelectromechanical system (MEMS) based switches for power applications," presented at the Industrial and Commercial Power Systems Technical Conference (IEEE I&CPS 2011), Niskayuna, NY, USA, 2011.

[7] M. Spencer, F. Chen, C. C. Wang, R. Nathanael, H. Fariborzi, A. Gupta, *et al.*, "Demonstration of Integrated Micro-Electro-Mechanical Relay Circuits for VLSI Applications," *IEEE Journal of Solid-State Circuits,* vol. 46, pp. 308-320, Jan 2011.

[8] S. Narendra, V. De, S. Borkar, D. A. Antoniadis, and A. P. Chandrakasan, "Full-chip subthreshold leakage power prediction and reduction techniques for sub-0.18-mu m CMOS," *IEEE Journal of Solid-State Circuits,* vol. 39, pp. 501-510, Mar 2004.

[9] M. Alioto, "Understanding DC Behavior of Subthreshold CMOS Logic Through Closed-Form Analysis," *IEEE Transactions on Circuits and Systems I-Regular Papers,* vol. 57, pp. 1597-1607, Jul 2010.

[10] R. H. Dennard, F. H. Gaensslen, H. N. Yu, V. L. Rideout, E. Bassous, and A. R. Leblanc, "Design of Ion-Implanted Mosfets with Very Small Physical Dimensions," *Ieee Journal of Solid-State Circuits,* vol. Sc 9, pp. 256-268, 1974.

[11] M. Alioto, "Understanding DC behavior of subthreshold CMOS logic through closed-form analysis," *IEEE Transactions on Circuits and Systems I: Regular Papers,* vol. 57, pp. 1597-1607, 2010.

[12] S. Hanson, M. Seok, D. Sylvester, and D. Blaauw, "Nanometer device scaling in subthreshold logic and SRAM," *IEEE Transactions on Electron Devices,* vol. 55, pp. 175-185, Jan 2008.

[13] R. Parsa, M. Shavezipur, W. S. Lee, S. Chong, D. Lee, H. S. P. Wong, *et al.*, "Nanoelectromechanical relays with decoupled electrode and suspension," in *Micro Electro Mechanical Systems (MEMS), 2011 IEEE 24th International Conference on*, 2011, pp. 1361-1364.

[14] T. J. K. Liu, D. Markovic, V. Stojanovic, and E. Alon, "The Relay Reborn," *IEEE Spectrum,* vol. 49, pp. 38-43, Apr 2012.

[15] J. O. Lee, Y.-H. Song, M.-W. Kim, M.-H. Kang, J.-S. Oh, H.-H. Yang, *et al.*, "A sub-1-volt nanoelectromechanical switching device," *Nature nanotechnology,* 25 November 2012.

[16] P. Clarke. (2012) IBM, ST go back to the future with nanorelay logic. *Electronic Engineering Times*. 30.
[17] O. Y. Loh and H. D. Espinosa, "Nanoelectromechanical contact switches," *Nature Nanotechnology,* vol. 7, pp. 283-295, May 2012.
[18] N. Sinha, Z. Guo, V. Felmetsger, and G. Piazza, "100nm Thick Aluminum Nitride Based Piezoelectric Nano Switches Exhibiting 1mV Threshold Voltage Via Body-Biasing," in *Proceedings of 2010 Solid-State Sensors, Actuators, and Microsystems Workshop (Hilton Head 2010),* 2010.
[19] N. Sinha, T. S. Jones, Z. J. Guo, and G. Piazza, "Body-Biased Complementary Logic Implemented Using AlN Piezoelectric MEMS Switches," *Journal of Microelectromechanical Systems,* vol. 21, pp. 484-496, Apr 2012.
[20] G. M. Rebeiz and J. B. Muldavin, "RF MEMS switches and switch circuits," *Microwave Magazine, IEEE,* vol. 2, pp. 59-71, 2001.
[21] D. A. Czaplewski, G. A. Patrizi, G. M. Kraus, J. R. Wendt, C. D. Nordquist, S. L. Wolfley, *et al.*, "A nanomechanical switch for integration with CMOS logic," *Journal of Micromechanics and Microengineering,* vol. 19, Aug 2009.
[22] Z. Y. Yang, D. J. Lichtenwalner, A. S. Morris, J. Krim, and A. I. Kingon, "Comparison of Au and Au-Ni Alloys as Contact Materials for MEMS Switches," *Journal of Microelectromechanical Systems,* vol. 18, pp. 287-295, Apr 2009.
[23] R. A. Coutu, P. E. Kladitis, L. A. Starman, and J. R. Reid, "A comparison of micro-switch analytic, finite element, and experimental results," *Sensors and Actuators a-Physical,* vol. 115, pp. 252-258, Sep 21 2004.
[24] S. T. Patton and J. S. Zabinski, "Fundamental studies of Au contacts in MEMS RF switches," *Tribology Letters,* vol. 18, pp. 215-230, Feb 2005.
[25] S. T. Patton and J. S. Zabinski, "Failure mechanisms of capacitive MEMS RF switch contacts," *Tribology Letters,* vol. 19, pp. 265-272, Aug 2005.
[26] S. T. Patton, K. C. Eapen, J. S. Zabinski, J. H. Sanders, and A. A. Voevodin, "Lubrication of microelectromechanical systems radio frequency switch contacts using self-assembled monolayers," *Journal of Applied Physics,* vol. 102, Jul 15 2007.
[27] P. G. Slade, *Electrical Contacts: Principles and Application*. New York: Marcel Dekker, Inc., 1999.
[28] J. W. Tringe, T. A. Uhlman, A. C. Oliver, and J. E. Houston, "A single asperity study of Au/Au electrical contacts," *Journal of Applied Physics,* vol. 93, pp. 4661-4669, Apr 15 2003.
[29] M. Walker, C. Nordquist, D. Czaplewski, G. Patrizi, N. McGruer, and J. Krim, "Impact of in situ oxygen plasma cleaning on the resistance of Ru and Au-Ru based rf microelectromechanical system contacts in vacuum," *Journal of Applied Physics,* vol. 107, Apr 15 2010.
[30] M. J. Walker, D. Berman, C. Nordquist, and J. Krim, "Electrical Contact Resistance and Device Lifetime Measurements of Au-RuO2-Based RF MEMS Exposed to Hydrocarbons in Vacuum and Nitrogen Environments," *Tribology Letters,* vol. 44, pp. 305-314, Dec 2011.
[31] M. P. de Boer, D. A. Czaplewski, M. S. Baker, S. L. Wolfley, and J. A. Ohlhausen, "Design, fabrication, performance and reliability of Pt- and RuO2-coated microrelays tested in ultra-high purity gas environments," *Journal of Micromechanics and Microengineering,* vol. 22, Oct 2012.

[32] S. Majumder, N. E. McGruer, G. G. Adams, P. M. Zavracky, R. H. Morrison, and J. Krim, "Study of contacts in an electrostatically actuated microswitch," *Sensors and Actuators a-Physical*, vol. 93, pp. 19-26, Aug 25 2001.
[33] N. E. McGruer, G. G. Adams, L. Chen, Z. J. Guo, and Y. Du, "Mechanical, Thermal, and Material Influences on Ohmic-Contact-Type MEMS Switch Operation," in *Micro Electro Mechanical Systems, 2006. MEMS 2006 Istanbul. 19th IEEE International Conference on*, 2006, pp. 230-233.
[34] R. P. Hennessy, A. Basu, G. G. Adams, and N. E. McGruer, "Hot-switched lifetime and damage characteristics of MEMS switch contacts," *Journal of Micromechanics and Microengineering*, vol. 23, May 2013.
[35] R. A. Coutu, "Electrostatic radio frequency (RF) microelectromechanical systems (MEMS) switches with metal alloy electric contacts," DTIC Document2004.
[36] S. Majumder, J. Lampen, R. Morrison, and J. Maciel, "MEMS switches," *IEEE Instrumentation & Measurement Magazine*, vol. 6, pp. 12-15, Mar 2003.
[37] H. W. Hermance and T. F. Egan, "Organic Deposits on Precious Metal Contacts," *Bell System Technical Journal*, vol. 37, pp. 739-776, 1958.
[38] G. A. Somorjai and Y. Li, *Introduction to surface chemistry and catalysis*. New York: John Wiley & Sons, 2010.
[39] D. Hyman and M. Mehregany, "Contact physics of gold microcontacts for MEMS switches," *Ieee Transactions on Components and Packaging Technologies*, vol. 22, pp. 357-364, Sep 1999.
[40] B. T. Reagor and L. Seibles, "Structural-Analysis of Deuterated and Non-Deuterated Frictional Polymers Using Fourier-Transform Infrared-Spectroscopy and Pyrolysis-Gas Chromatography-Mass Spectroscopy," *Ieee Transactions on Components Hybrids and Manufacturing Technology*, vol. 4, pp. 102-108, 1981.
[41] M. Antler, "Electrical effects of fretting connector contact materials: A review," *Wear*, vol. 106, pp. 5-33, 11// 1985.
[42] B. D. Jensen, L. L. W. Chow, K. W. Huang, K. Saitou, J. L. Volakis, and K. Kurabayashi, "Effect of nanoscale heating on electrical transport in RF MEMS switch contacts," *Journal of Microelectromechanical Systems*, vol. 14, pp. 935-946, Oct 2005.
[43] D. J. Dickrell and M. T. Dugger, "Electrical contact resistance degradation of a hot-switched simulated metal MEMS contact," *IEEE Transactions on Components and Packaging Technologies*, vol. 30, pp. 75-80, Mar 2007.
[44] W. E. Campbell and R. E. Lee, "Polymer Formation on Sliding Metals in Air Saturated with Organic Vapors," *A S L E Transactions*, vol. 5, pp. 91-104, 1962/01/01 1962.
[45] D. B. Rogers, R. D. Shannon, A. W. Sleight, and J. L. Gillson, "Crystal Chemistry of Metal Dioxides with Rutile-Related Structures," *Inorganic Chemistry*, vol. 8, pp. 841-&, 1969.
[46] T. Yokokawa, T. Yano, C. Kawakita, K. Hinohara, and A. Nagai, "A Study on the Surface Deactivation Treatment of Rhodium-Plated Contact Reed Switches," *Ieee Transactions on Components Hybrids and Manufacturing Technology*, vol. 9, pp. 124-127, Mar 1986.
[47] R. A. Coutu, J. R. Reid, R. Cortez, R. E. Strawser, and P. E. Kladitis, "Microswitches with sputtered Au, AuPd, Au-on-AuPt, and AuPtCu alloy electric contacts," *Ieee Transactions on Components and Packaging Technologies*, vol. 29, pp. 341-349, Jun 2006.

[48] V. Brand, M. S. Baker, and M. P. de Boer, "Impact of Contact Materials and Operating Conditions on Stability of Micromechanical Switches," *Tribology Letters,* vol. 51, pp. 341-356, Sep 2013.
[49] M. Spencer, F. Chen, C. C. Wang, R. Nathanael, H. Fariborzi, A. Gupta, *et al.*, "Demonstration of integrated micro-electro-mechanical relay circuits for VLSI applications," *IEEE Journal of Solid-State Circuits,* vol. 46, pp. 308-320, 2011.
[50] A. W. Adamson and A. P. Gast, *Physical chemistry of surfaces*: Wiley, 1997.
[51] S. M. Wetterer, D. J. Lavrich, T. Cummings, S. L. Bernasek, and G. Scoles, "Energetics and kinetics of the physisorption of hydrocarbons on Au(111)," *Journal of Physical Chemistry B,* vol. 102, pp. 9266-9275, Nov 12 1998.
[52] F. Mittendorfer, C. Thomazeau, P. Raybaud, and H. Toulhoat, "Adsorption of unsaturated hydrocarbons on Pd(111) and Pt(111): A DFT study," *Journal of Physical Chemistry B,* vol. 107, pp. 12287-12295, Nov 6 2003.
[53] M. K. Beyer and H. Clausen-Schaumann, "Mechanochemistry: The mechanical activation of covalent bonds," *Chemical Reviews,* vol. 105, pp. 2921-2948, Aug 2005.
[54] H. Staudinger and E. O. Leupold, "On isoprene and caoutchuc, 18. Announcement: Viscosity-research on Balata.," *Berichte Der Deutschen Chemischen Gesellschaft,* vol. 63, pp. 730-733, 1930.
[55] H. Staudinger and H. F. Bondy, "On isoprene and caoutchuc, 19. Announcement: On the molecular size of caoutchuc and Balata.," *Berichte Der Deutschen Chemischen Gesellschaft,* vol. 63, pp. 734-736, 1930.
[56] H. Staudinger, "On isoprene and cautschuc, 20. Announcement.: On the nature of colloids of coutchuc and balata.," *Berichte Der Deutschen Chemischen Gesellschaft,* vol. 63, pp. 921-934, 1930.
[57] H. Staudinger and W. Heuer, "High polymer compounds, 93. Announcement. Decomposition of thread molecules of polystyrene.," *Berichte Der Deutschen Chemischen Gesellschaft,* vol. 67, pp. 1159-1164, 1934.
[58] H. Staudinger, "High polymere compounds 46th Announcement - Organic chemistry and colloidal chemistry," *Kolloid-Zeitschrift,* vol. 53, pp. 19-32, Oct 1930.
[59] T. Q. Nguyen and H. H. Kausch, "Effects of Solvent Viscosity on Polystyrene Degradation in Transient Elongational Flow," *Macromolecules,* vol. 23, pp. 5137-5145, Nov 26 1990.
[60] T. Q. Nguyen and H. H. Kausch, "Mechanochemical Degradation in Transient Elongational Flow," *Advances in Polymer Science,* vol. 100, pp. 73-182, 1992.
[61] S. N. Zhurkov, V. A. Zakrevskii, and E. E. Tomashevskii, "Formation of Free Radicals during Degradation and Deformation of Polymers Containing Sulfide Bonds," *Soviet Physics-Solid State,* vol. 6, pp. 1508-1510, 1964.
[62] S. N. Zhurkov, E. E. Tomashevskii, and A. Y. Savostin, "Mechanism Behind Breakdown of Polymers Investigated by Means of Electron Spin Resonance," *Doklady Akademii Nauk Sssr,* vol. 159, pp. 303-&, 1964.
[63] D. K. Backman and K. L. Devries, "Formation of Free Radicals during Machining and Fracture of Polymers," *Journal of Polymer Science Part a-1-Polymer Chemistry,* vol. 7, pp. 2125-&, 1969.
[64] J. Becht and H. Fischer, "Studies on Mechanically Loaded Synthetic Fibers," *Kolloid-Zeitschrift and Zeitschrift Fur Polymere,* vol. 240, pp. 766-&, 1970.

[65] S. N. Zhurkov and B. N. Narzullaev, "*Vremennaya Zavisimost Prochnosti Tverdykh Tel," *Zhurnal Tekhnicheskoi Fiziki,* vol. 23, pp. 1677-1689, 1953.
[66] S. N. Zhurkov, "Kinetic Concept of Strenght of Solids," *International Journal of Fracture Mechanics,* vol. 1, pp. 311-322, 1965.
[67] V. Schettino and R. Bini, "Molecules under extreme conditions: Chemical reactions at high pressure," *Physical Chemistry Chemical Physics,* vol. 5, pp. 1951-1965, 2003.
[68] R. H. Wentorf, "Behavior of Some Carbonaceous Materials at Very High Pressures and High Temperatures," *Journal of Physical Chemistry,* vol. 69, pp. 3063-&, 1965.
[69] J. Akella and G. C. Kennedy, "Phase Diagram of Benzene to 35 Kbar," *Journal of Chemical Physics,* vol. 55, pp. 793-&, 1971.
[70] L. Ciabini, F. A. Gorelli, M. Santoro, R. Bini, V. Schettino, and M. Mezouar, "High-pressure and high-temperature equation of state and phase diagram of solid benzene," *Physical Review B,* vol. 72, Sep 2005.
[71] L. Ciabini, M. Santoro, F. A. Gorelli, R. Bini, V. Schettino, and S. Raugei, "Triggering dynamics of the high-pressure benzene amorphization," *Nature Materials,* vol. 6, pp. 39-43, Jan 2007.
[72] L. Ciabini, M. Santoro, R. Bini, and V. Schettino, "High pressure photoinduced ring opening of benzene," *Physical Review Letters,* vol. 88, Feb 25 2002.
[73] V. Schettino, R. Bini, M. Ceppatelli, and M. Citroni, "Activation and control of chemical reactions at very high pressure," *Physica Scripta,* vol. 78, Nov 2008.
[74] D. Chelazzi, M. Ceppatelli, M. Santoro, R. Bini, and V. Schettino, "Pressure-induced polymerization in solid ethylene," *Journal of Physical Chemistry B,* vol. 109, pp. 21658-21663, Nov 24 2005.
[75] C. Murli and Y. Song, "Pressure-Induced Polymerization of Acrylic Acid: A Raman Spectroscopic Study," *Journal of Physical Chemistry B,* vol. 114, pp. 9744-9750, Aug 5 2010.
[76] Y. B. Gerbig, C. A. Michaels, A. M. Forster, and R. F. Cook, "In situ observation of the indentation-induced phase transformation of silicon thin films," *Physical Review B,* vol. 85, Mar 5 2012.
[77] D. Maugis, "On the contact and adhesion of rough surfaces," *Journal of adhesion science and technology,* vol. 10, pp. 161-175, 1996.
[78] K. L. Johnson and K. L. Johnson, *Contact mechanics*: Cambridge university press, 1987.
[79] R. P. Hennessy, "Exploration of hot switching damage and damage mechanisms in MEMS switch contacts," 2014.
[80] S. P. Timoshenko and J. N. Goodier, *Theory of Elasticity*, 3rd ed.: McGraw-Hill, 1970.
[81] J. A. Greenwood and J. B. Williamson, "Contact of Nominally Flat Surfaces," *Proceedings of the Royal Society of London Series a-Mathematical and Physical Sciences,* vol. 295, pp. 300-&, 1966.
[82] J. I. Mccool, "Predicting Microfracture in Ceramics Via a Microcontact Model," *Journal of Tribology-Transactions of the Asme,* vol. 108, pp. 380-386, Jul 1986.
[83] E. J. Abbott and F. A. Firestone, "Specifying surface quantity - a method based on the accurate measurement and comparison," *ASME Mechanical Engineers,* vol. 55, pp. 569-572, 1933.
[84] R. Holm, *Electric Contacts. Theory and Application. 4.ed*. New York: Springer, 1967.

[85] N. Agrait, A. L. Yeyati, and J. M. van Ruitenbeek, "Quantum properties of atomic-sized conductors," *Physics Reports-Review Section of Physics Letters*, vol. 377, pp. 81-279, Apr 2003.
[86] Y. V. Sharvin, "A Possible Method for Studying Fermi Surfaces," *Soviet Physics Jetp-Ussr*, vol. 21, pp. 655-&, 1965.
[87] G. Wexler, "The size effect and the non-local Boltzmann transport equation in orifice and disk geometry," *Proceedings of the Physical Society*, vol. 89, p. 927, 1966.
[88] A. Mikrajuddin, F. G. Shi, H. K. Kim, and K. Okuyama, "Size-dependent electrical constriction resistance for contacts of arbitrary size: from Sharvin to Holm limits," *Materials Science in Semiconductor Processing*, vol. 2, pp. 321-327, Dec 1999.
[89] V. Brand, M. S. Baker, and M. P. de Boer, "Contamination Thresholds of Pt- and RuO2-Coated Ohmic Switches," *Journal of Microelectromechanical Systems*, vol. 22, pp. 1248-1250, Dec 2013.
[90] D. P. D. Frank P. Incropera, Theodore L. Bergman, Adrienne S. Lavine, *Fundamentals of heat and mass transfer*. New York: John Wiley, 2007.
[91] H. D. Young, R. A. Freedman, T. R. Sandin, and A. L. Ford, *Univesity Physics*, 10 ed. vol. 2. San Francisco: Addison-Wesley, 1999.
[92] M. Ieda, "Dielectric-Breakdown Process of Polymers," *Ieee Transactions on Electrical Insulation*, vol. 15, pp. 206-224, 1980.
[93] R. Haag, M. A. Rampi, R. E. Holmlin, and G. M. Whitesides, "Electrical breakdown of aliphatic and aromatic self-assembled monolayers used as nanometer-thick organic dielectrics," *Journal of the American Chemical Society*, vol. 121, pp. 7895-7906, Sep 1 1999.
[94] J. Goldstein, D. Newbury, D. Joy, C. Lyman, P. Echlin, E. Lifshin, *et al.*, *Scanning Electron Microscopy and X-ray Microanalysis: Third Edition*: Springer US, 2003.
[95] J. F. Watts and J. Wolstenholme, *An Introduction to Surface Analysis by XPS and AES*: Wiley, 2003.
[96] A. C. Ferrari and J. Robertson, "Interpretation of Raman spectra of disordered and amorphous carbon," *Physical Review B*, vol. 61, pp. 14095-14107, May 15 2000.
[97] V. Brand, M. S. Baker, and M. P. de Boer, "Impact of Contact Materials and Operating Conditions on Stability of Micromechanical Switches," *Tribology Letters*, pp. 1-16.
[98] J. Zhu, K. B. Yeap, K. Y. Zeng, and L. Lu, "Nanomechanical characterization of sputtered RuO2 thin film on silicon substrate for solid state electronic devices," *Thin Solid Films*, vol. 519, pp. 1914-1922, Jan 3 2011.
[99] H. Lee, R. A. Coutu, S. Mall, and K. D. Leddy, "Characterization of metal and metal alloy films as contact materials in MEMS switches," *Journal of Micromechanics and Microengineering*, vol. 16, pp. 557-563, Mar 2006.
[100] M. S. Baker, J. A. Walraven, T. J. Headley, and R. A. Plass, *Final Report: Compliant Thermo-mechanical MEMS Actuators, LDRD# 52553*: United States. Department of Energy, 2004.
[101] W. W. Tyler and A. C. Wilson, Jr., "Thermal Conductivity, Electrical Resistivity, and Thermoelectric Power of Graphite," *Physical Review*, vol. 89, pp. 870-875, 02/15/ 1953.
[102] A. S. Vaughan, I. L. Hosier, S. J. Dodd, and S. J. Sutton, "On the structure and chemistry of electrical trees in polyethylene," *Journal of Physics D-Applied Physics*, vol. 39, pp. 962-978, Mar 7 2006.

[103] L. H. Germer and J. L. Smith, "Activation of Electrical Contacts by Organic Vapors," *Bell System Technical Journal,* vol. 36, pp. 769-812, 1957.
[104] C. N. Neufeld and W. F. Rieder, "Carbon contamination of contacts due to organic vapors," *Components, Packaging, and Manufacturing Technology, Part A, IEEE Transactions on,* vol. 18, pp. 399-404, 1995.
[105] A. Broue, T. Fourcade, J. Dhennin, F. Courtade, P. L. Charvet, P. Pons, *et al.*, "Validation of bending tests by nanoindentation for micro-contact analysis of MEMS switches," *Journal of Micromechanics and Microengineering,* vol. 20, Aug 2010.
[106] R. S. Porter and A. Casale, "Recent Studies of Polymer Reactions Caused by Stress," *Polymer Engineering and Science,* vol. 25, pp. 129-156, 1985.
[107] M. M. Caruso, D. A. Davis, Q. Shen, S. A. Odom, N. R. Sottos, S. R. White, *et al.*, "Mechanically-Induced Chemical Changes in Polymeric Materials," *Chemical Reviews,* vol. 109, pp. 5755-5798, Nov 2009.
[108] B. Krishnakumari, S. Naseem, and N. V. K. Dutt, "A Method of Estimating the Standard Gibbs Free-Energy of Formation," *Canadian Journal of Chemical Engineering,* vol. 71, pp. 489-491, Jun 1993.
[109] R. Chang, *Chemistry*, 8 ed. New York: McGraw-Hill, 2004.
[110] S. W. Chaikin, "On Frictional Polymer," *Wear,* vol. 10, pp. 49-&, 1967.
[111] B. Bhushan and F. W. Hahn, "Stains on Magnetic-Tape Heads," *Wear,* vol. 184, pp. 193-202, May 1995.
[112] S. Kumar and P. K. Srivastava, "Tribochemistry of lubrication issues of magnetic disk storage devices," *Tribology International,* vol. 38, pp. 687-691, Jun-Jul 2005.
[113] J. C. Smith, M. J. Furey, and C. Kajdas, "An Exploratory-Study of Vapor-Phase Lubrication of Ceramics by Monomers," *Wear,* vol. 181, pp. 581-593, Mar 1995.
[114] A. L. Barnette, D. B. Asay, J. A. Ohlhausen, M. T. Dugger, and S. H. Kim, "Tribochemical Polymerization of Adsorbed n-Pentanol on SiO2 during Rubbing: When Does It Occur and Is It Responsible for Effective Vapor Phase Lubrication?," *Langmuir,* vol. 26, pp. 16299-16304, Nov 2 2010.
[115] H. Over, "Surface Chemistry of Ruthenium Dioxide in Heterogeneous Catalysis and Electrocatalysis: From Fundamental to Applied Research," *ChemInform,* vol. 43, 2012.
[116] J. Assmann, V. Narkhede, N. A. Breuer, M. Muhler, A. P. Seitsonen, M. Knapp, *et al.*, "Heterogeneous oxidation catalysis on ruthenium: bridging the pressure and materials gaps and beyond," *Journal of Physics-Condensed Matter,* vol. 20, May 7 2008.
[117] V. Brand, M. P. de Boer, and M. Saleh, "Effects of electrical current and temperature on contamination induced degradation in ohmic switch contacts (to be submitted)," 2014.
[118] V. Brand and M. P. d. Boer, "Oxygen-Induced Graphitization of Amorphous Carbon Deposit on Ohmic Switch Contacts Improves Their Electrical Conductivity and Protects Them from Wear," *Journal of Micromechanics and Microengineering,* Unpublished results.
[119] J. Schwan, S. Ulrich, V. Batori, H. Ehrhardt, and S. R. P. Silva, "Raman spectroscopy on amorphous carbon films," *Journal of Applied Physics,* vol. 80, pp. 440-447, Jul 1 1996.
[120] D. Pantea, H. Darmstadt, S. Kaliaguine, L. Summchen, and C. Roy, "Electrical conductivity of thermal carbon blacks - Influence of surface chemistry," *Carbon,* vol. 39, pp. 1147-1158, 2001.

[121] S. Bhattacharyya, S. J. Henley, E. Mendoza, L. Gomez-Rojas, J. Allam, and S. R. P. Silva, "Resonant tunnelling and fast switching in amorphous-carbon quantum-well structures," *Nature Materials,* vol. 5, pp. 19-22, Jan 2006.
[122] E. Z. Luo, S. Lin, Z. Xie, J. B. Xu, I. H. Wilson, Y. H. Yu, *et al.*, "Studying the high-field electron conduction of tetrahedral amorphous carbon thin films by conducting atomic force microscopy," *Materials Characterization,* vol. 48, pp. 205-210, Apr 2002.
[123] T. C. Chieu, M. S. Dresselhaus, and M. Endo, "Raman Studies of Benzene-Derived Graphite Fibers," *Physical Review B,* vol. 26, pp. 5867-5877, 1982.
[124] F. Tuinstra and J. L. Koenig, "Raman Spectrum of Graphite," *Journal of Chemical Physics,* vol. 53, pp. 1126-&, 1970.
[125] J. Robertson, "Diamond-like amorphous carbon," *Materials Science & Engineering R-Reports,* vol. 37, pp. 129-281, May 24 2002.
[126] P. D. Wu, A. Debebe, and H. M. Yi, "Adsorption and Diffusion of C-6 and C-8 Hydrocarbons in Silicalite," *Zeolites,* vol. 3, pp. 118-122, 1983.
[127] Y. C. Chiang, P. C. Chaing, and C. P. Huang, "Effects of pore structure and temperature on VOC adsorption on activated carbon," *Carbon,* vol. 39, pp. 523-534, 2001.
[128] R. M. Davis, B. Mcdermott, and C. C. Koch, "Mechanical Alloying of Brittle Materials," *Metallurgical Transactions a-Physical Metallurgy and Materials Science,* vol. 19, pp. 2867-2874, Dec 1988.
[129] V. Brand and M. P. de Boer, "Oxygen-induced graphitization of amorphous carbon deposit on ohmic switch contacts improves their electrical conductivity and protects them from wear (submitted)," 2014.
[130] M. de Boer, R. Anderson, R. Shul, P. Clews, and M. Baker, "Wafer-level singulation, release and post-processing in surface micromachining," *Journal of Micromechanics and Microengineering,* vol. 20, p. 075007, 2010.
[131] J. J. Hauser, "Electrical, Structural and Optical-Properties of Amorphous-Carbon," *Journal of Non-Crystalline Solids,* vol. 23, pp. 21-41, 1977.
[132] J. D. Carey and S. R. P. Silva, "Disorder, clustering, and localization effects in amorphous carbon," *Physical Review B,* vol. 70, Dec 2004.
[133] D. Dasgupta, F. Demichelis, and A. Tagliaferro, "Electrical-Conductivity of Amorphous-Carbon and Amorphous Hydrogenated Carbon," *Philosophical Magazine B-Physics of Condensed Matter Statistical Mechanics Electronic Optical and Magnetic Properties,* vol. 63, pp. 1255-1266, Jun 1991.
[134] S. Osswald, E. Flahaut, H. Ye, and Y. Gogotsi, "Elimination of D-band in Raman spectra of double-wall carbon nanotubes by oxidation," *Chemical Physics Letters,* vol. 402, pp. 422-427, Feb 4 2005.
[135] Q. Zhang, D. Zhang, S. Jia, and W. Shong, "Microstructure and properties of some dispersion strengthened platinum alloys," *Platinum Metals Review(UK),* vol. 39, pp. 167-171, 1995.
[136] R. Saha and W. D. Nix, "Effects of the substrate on the determination of thin film mechanical properties by nanoindentation," *Acta Materialia,* vol. 50, pp. 23-38, Jan 8 2002.
[137] J. M. Kuchta, *Investigation of Fire and Explosion Accidents in the Chemical, Mining, and Fuel-related Industries: A Manual*: US Department of the Interior, Bureau of Mines, 1985.

[138] L. G. Britton, "Using heats of oxidation to evaluate flammability hazards," *Process Safety Progress,* vol. 21, pp. 31-54, March 2002 2002.
[139] M. G. Zabetakis, "Flammability characteristics of combustible gases and vapors," DTIC Document1965.
[140] L. A. Medard, *Accidental explosions: Physical and chemical properties*: Ellis Horwood, 1989.
[141] G. P. McKinnon, *Fire Protection Handbook,* 14 ed. Boston, MA, 1980.
[142] A. A. Shimy, "Calculating flammability characteristics of hydrocarbons and alcohols," *Fire Technology,* vol. 6, pp. 135-139, 1970.
[143] N. F. P. Association, *NFPA 325, Guide to Fire Hazard Properties of Flammable Liquids, Gases, and Volatile Solids*: National Fire Protection Association, 1994.
[144] M. Goethals, B. Vanderstraeten, J. Berghmans, G. De Smedt, S. Vliegen, and E. Van't Oost, "Experimental study of the flammability limits of toluene-air mixtures at elevated pressure and temperature," *Journal of Hazardous Materials,* vol. 70, pp. 93-104, Dec 31 1999.
[145] M. Vidal, W. J. Rogers, J. C. Holste, and M. S. Mannan, "A review of estimation methods for flash points and flammability limits," *Process Safety Progress,* vol. 23, pp. 47-55, Mar 2004.
[146] M. J. Moran and H. N. Shapiro, *Fundamentals of Engineering Thermodynamics,* 5th ed.: Wiley, 2004.
[147] Y. Okada and Y. Tokumaru, "Precise Determination of Lattice-Parameter and Thermal-Expansion Coefficient of Silicon between 300-K and 1500-K," *Journal of Applied Physics,* vol. 56, pp. 314-320, 1984.

Appendices:

APPENDIX I: Relating microswitch results to nanoswitches

Part 1: Estimating contact resistance

A theoretical approach outlined by Mikrajuddin et al. [88] enables a size-dependent electrical constriction resistance estimate for contacts of arbitrary area. This approach spans the Sharvin (ballistic electron transport) to Maxwell (diffusive electron transport) realm [88]:

$$R_C = \frac{4\rho K}{3\pi r_{eff}}\left[1 + \frac{3\pi}{8}\Gamma(K)\frac{r_{eff}}{l_e}\right] \quad \text{(A1)}$$

$$\Gamma(K) \approx \frac{2}{\pi}\int_0^\infty e^{-Kx} sinc(x)dx, \qquad K = l_e/r_{eff} \quad \text{(A2)}$$

The effective contact area radius (due to actual asperity contact), r_{eff}, is found using Abbott and Firestone's approach [83], assuming plastic deformation. A single contact asperity model is used (for an upper resistance estimate) [32]:

$$r_{eff} = \sqrt{F_c/H\pi}. \quad \text{(A3)}$$

For microswitches:

Force at contact, F_c = 125 µN
Effective radius, r_{eff} = 90 nm
Pt resistivity, ρ = 10^{-7} Ω-m
Electron mean free path, l_e = 40 nm
Knudsen number, K = 0.44
R_{c_micro} = 0.66 Ω

For nanoswitches:

Force at contact, F_c = 20 nN
Effective radius, r_{eff} = 1 nm
Pt resistivity, ρ = 10^{-7} Ω-m
Electron mean free path, l_e = 40 nm
Knudson number, K = 44
R_{c_nano} = 1,300 Ω

An empirical resistance calculation based on apparent contact area shows similar results for a nanoswitch. Considering that R_c is inversely proportional to apparent contact area:

$$\frac{R_{c\_nano}}{R_{c\_micro}} = \frac{1/A_{c\_nano}}{1/A_{c\_micro}} \quad \text{(A4)}$$

$$R_{c\_nano} = R_{c\_micro} * \frac{A_{c_{micro}}}{A_{c_{nano}}} = \mathbf{1,300\ \Omega} \quad \text{(A5)}$$

where, R_{c_micro} is 4 Ω and the apparent area of the microswitch contact, A_{c_micro}, is 25 x 2 µm^2. The apparent area for the nanoswitch contact, A_{c_nano}, is taken to be 0.4 x 0.4 µm^2.

Part 2: Estimating current density

Although, the contact area is smaller in nanoswitches, the contact pressure at individual asperities is limited by the material hardness and therefore does not depend strongly on scale [3]. Here we show that the current density, J (nA/nm^2), is similar (of the same order of magnitude) for microswitches and nanoswitches:

For our microswitch:

Electrical current in our switches is $I_{micro} = 10^7$ nA

Our contact area is A_{c_micro} = 25,000 x 2,000 nm^2

$$J_{micro} = \frac{I_{micro}}{A_{c\_micro}} = \mathbf{0.20}\,\frac{\mathbf{nA}}{\mathbf{nm^2}} \qquad \text{(A6)}$$

For a nanoswitch:

ECR found in Appendix I, R_{c_nano}=1,300 Ω

Contact area is A_{c_nano} = 400 x 400 nm^2

A reasonable voltage in a nanoswitch is V_{nano} = 0.1 V

Hence, $I_{nano} = V_{nano}/R_{c\_nano} = 7.7 \cdot 10^4$ nA

$$J_{nano} = \frac{I_{nano}}{A_{c\_nano}} = \mathbf{0.48}\,\frac{\mathbf{nA}}{\mathbf{nm^2}} \qquad \text{(A7)}$$

APPENDIX II: Estimating the flammability of benzene in microswitch test chamber

Microswitch reliability experiments are occasionally performed in an environment containing benzene gas and oxygen in a presence of an ignition source. To avoid an explosion it is therefore necessary to know the limits of safe operation. The main factors that need to be considered are whether the benzene concentration is safe, what temperature could cause ignition, whether there is enough oxygen to sustain combustion, and how the pressure within the system affects combustion. Other factors include the geometry of the chamber, gravitational field strength and direction of flame propagation.

Safe concentrations of benzene:

In order for ignition of benzene gas in air to be possible, the concentration of benzene must be within a particular range. This range is between what is known as the lower flammability limit (LFL) and the upper flammability limit (UFL). The LFL is defined as the minimum molar fraction (also volume fraction) of benzene in air that may cause ignition and UFL is defined analogously. The industrially accepted values for LFL and UFL for benzene in air at 1 atm and 25°C are 1.3% and 7.9%, respectively [137]. Several techniques that are based on experimental observation have been established in the 20th century to analytically estimate LFL and UFL. Although these methods provide relatively accurate results, today such analysis is usually done by calculating the adiabatic flame temperature numerically [138][2].

Understanding LFL is more relevant for our experimental setup because the benzene concentration used is 0.25% by volume in N_2. To help develop some intuition about what is taken in to account when finding LFL, a few analytical models are presented:

Lloyd's Rule:

As discussed by Britton and Zabetakis [138, 139], G. W. Jones has shown that at any temperature, the ratio of LFL to the stoichiometric concentration of alkanes in air is roughly constant. This became the foundation of the "Lloyd's Rule":

$$LFL(mol\ \%) = 0.55C_{st}$$

Where C_{st} is the stoichiometric concentration of fuel in air in the units of mol %. It was shown by Kuchta that:

$$C_{st} = \frac{100}{1 + 4.773S}$$

Where S is the molar ratio of oxygen to fuel in a stoichiometric equation for the combustion. For benzene this equation is:

$$C_6H_6 + 7.5O_2 \rightarrow 6CO_2 + 3H_2O$$

So we get S = 7.5, and thus:

$$LFL(mol\ \%) = 0.55 \times \frac{100}{1 + 4.773S} = 1.5\%$$

Larry's 1st Rule:

Another method to estimate LFL is known as Larry's 1st rule. This method uses an observation made by Le Chatelier and Boudouard as mentioned in Medard [140] that the molar heats of combustion (K) of LFL mixtures are roughly constant for different fuels:

$$K = LFL(mol\ \%) = \frac{\Delta H_C}{100} \cong -10.5 \pm 0.5 \left(\frac{kcal}{mol\ mixture}\right)$$

Where ΔH_c (kcal/mol fuel) is defined here as the net heat of combustion which equals the total heat of combustion less the (-10.5 kcal/mol) heat of condensation of water.

Considering that the value of "K" somewhat varies with both the homologous fuel group (e.g. hydrocarbons, oxygen containing fuels etc.) and with particular fuels within a group, a correction to the above equation is needed. This correction is based on the fact that the heat of oxidation is approximately constant for organic fuels [141]. The heat of oxidation differs from the heat of combustion only in that its units are (kcal/mol oxygen) instead of (kcal/mol mixture), that is:

Heat of combustion, K (lets now use K_1 for convenience): $K_1 \cong -10 \frac{kcal}{mol\ mixture}$

Heat of oxidation, K_2: $K_2 \cong -100 \frac{kcal}{mol\ oxygen}$

The heat of oxidation is also known to have the form of [138]: $K_2 \cong -\frac{\Delta H_C}{S}$

Figure A2.1 provides a sense of how much variability exists in K_1 and K_2 for different fuels.

Using the ratio of K_2 to K_1 we obtain: $\frac{K_2}{K_1} = \frac{\Delta H_C/S}{LFL*\Delta H_C/100} = \frac{100}{LFL*S}$

We also know from above that $\frac{K_2}{K_1} = 10$, this means that $LFL \cong \frac{10}{S}$.

This result is known as Larry's First Rule. It provides a more accurate estimate of LFL than K_1 or K_2 would individually. Using this method, the LFL value for benzene is 1.3%.

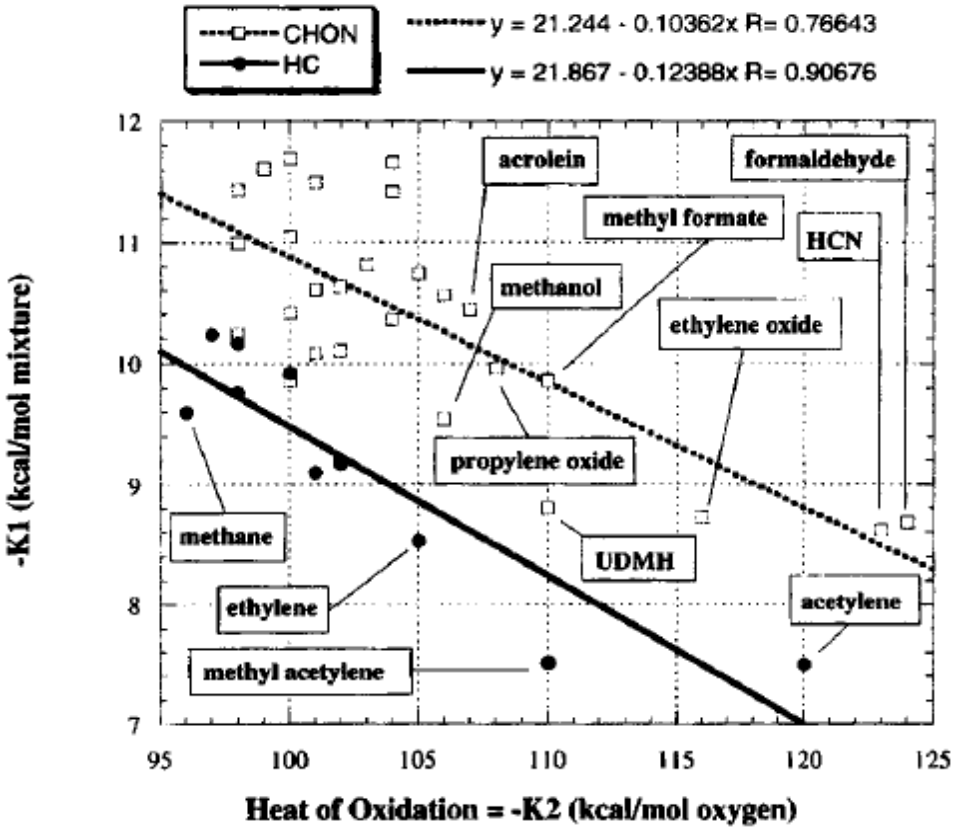

Figure A2.1: Dependence of the heat of combustion (K_1) on the heat of oxidation (K_2). Source: Britton, 2002 [138].

Shimy Method to find LFL:

According to Shimy [142] the lower flammability limits of hydrocarbons depend only on the number of carbon atoms in the chain regardless of the number of hydrogen atoms present. For benzene the following relationship is used:

$$LFL(mol\ \%) = \frac{8}{nC} = \frac{8}{6} = 1.33\%$$

Where nC is the number of carbon atoms in a benzene molecule.

Summary:

The LFL values in **Table A2.1** below were determined for standard conditions (1 atm pressure of air at 25°C) with the exception of Reported Value 1, which was obtained for a temperature of 100°C.

Table A2.1: Finding lower flammability limit of benzene with different methods

	Lower Flammability Limit (LFL) for C_6H_6
Larry's 1st Rule	1.33 %
Lloyd's Rule	1.49 %
Shimy Method	1.33 %
Reported Value 1 [137]	1.3%
Reported Value 2 [143]	1.2 %

Note: Reported value 1 was found experimentally and it has an error range of ±0.1. The setup to measure it consisted of an at least 5-cm diameter tube with an electrical spark ignition source.

Other considerations:

The aforementioned results alone cannot guarantee the safe operation of our experiment mainly because of the very specific testing conditions we have. In particular, our experiment is performed in an environment which has roughly 50% oxygen and the total chamber pressure is about ½ atm. Furthermore, the thermally actuated microswitches can serve as an ignition source not only because the TA legs can heat up to 450°C, but also the contacts can potentially become significantly hotter.

Temperature:

At standard ambient conditions the flammability limits are well established, however, at elevated temperature and pressure these data are limited. It is known that increasing the temperature of the system tends to decrease the LFL and increase the UFL, therefore increasing the flammability range. Although, I was not able to find much temperature data for benzene, I found some results for toluene-air mixtures. A Toluene molecule is a benzene ring with a methyl group attached, and it has a LFL and UFL values of 1.2% and 7.1% at STP respectively (very similar to benzene). According to Goethals et al. [144], at 250°C the LFL decreased to 0.83±0.02 %, they also showed that the temperature dependence of LFL was linear. This may suggest that a similar reduction in LFL may occur for benzene.

Autoignition Temperature:

The autoignition temperature (AIT) is the lowest temperature at which a fuel will ignite spontaneously without the presence of a spark. This means that at this temperature there is enough activation energy for the fuel to entirely combust. Increasing the pressure in the system or increasing the oxygen content will reduce AIT. For benzene the AIT is 560°C [137]. It is my understanding that ignition will not happen if the benzene concentration is below LFL even if the system temperature is above AIT.

Pressure:

If there is a pressure increase, it is often expected that the flammability range will become larger, however, this does not always hold [145]. For the case with toluene (which is similar to benzene from above), increase in pressure does not change the LFL [144]. This suggests that we should not be concerned about lower LFL of benzene at ½ atm total system pressure even though it might be implied otherwise from general trends for hydrocarbons.

Oxygen content:

According to Kuchta [137], increasing oxygen in the system will drastically increase the flammability range of hydrocarbon compounds. However, this increase is attributed to a large increase in the UFL, whereas the LFL remains about the same. The LFL for benzene in oxygen is very slightly lower (roughly the same) than the LFL for benzene in air. This means that even though the molar percentage of oxygen in our setup is higher than in air, it would not increase flammability. This makes sense because in either case (air or pure oxygen) there are more than enough oxygen molecules to react with all the benzene molecules (recall we have ~0.125 molar percent benzene).

Other factors such as chamber geometry and potential flame propagation direction are not significantly different from condition used to determine LFL at STP. These factors are therefore not expected to affect our LFL.

Considering that we have ~ 0.125% benzene (half of the gas is 99.75%N_2/0.25% C_6H_6 and the other half is 100%O_2) we are roughly 10 times below the LFL at STP. Even if the temperature were to increase to 250°C, we would still hold a factor of safety of more than six.

Worst case scenario calculation (if ignition occurs anyway):

Approach:

Although the discussion above suggests that we are comfortably in the safety zone, the lack of exact information on certain parameters such as AIT and LFL for specifically our setup outlines the need to find out what may happen if spontaneous combustion would occur. This is done using fundamental thermodynamic concepts as described by Moran and Shapiro [146].

We consider a worst case scenario where complete combustion of benzene occurs adiabatically such that no energy is transferred to the walls of the chamber and that no work is done by or on the gas mixture. It is further assumed that kinetic and potential energy effects are relatively negligible. This results in the first law of thermodynamics to be simply reduced to an energy balance where the internal energy of the reactants equals the internal energy of the products. By definition this internal energy can be expressed in terms of enthalpy (which is tabulated) and temperature. Since we know all of the initial conditions (enthalpies for reactants at STP), we can solve for the temperature of the products. The main difficulty here is that the

tabulated enthalpy values for the products depend on the final temperature. Nevertheless, an answer can be found by using an iterative approach:

Some numbers:

$V_{chamber} = 2(0.3)^3\ m^3 = 5.4E\text{-}2\ m^3$

$P_R = 101000$ Pa

$T_R = 298$ K

$$R = 8.314\ \frac{J}{mol * K}$$

$$n_{tot} = \frac{P * V_{chamber}}{R * T_R} = 2.2014\ mol$$

$$n_{O_2} = \frac{n_{tot}}{2} = 1.1007\ mol$$

$$n_{C_6H_6} = \frac{0.25}{100} * \frac{n_{tot}}{2} = 0.0028\ mol$$

$$n_{N_2} = \frac{n_{tot}}{2} - n_{C_6H_6} = 1.0979\ mol$$

The chemical equation for benzene is shown below:

$$C_6H_6 + 7.5 * O_2 \rightarrow 6 * CO_2 + 3 * H_2O$$

Considering we have only 0.0028 moles of benzene, the total reactants consumed and products created look like this:

$$0.0028 * C_6H_6 + 0.021 * O_2 \rightarrow 0.0168 * CO_2 + 0.0084 * H_2O$$

However, the form of the equation that is useful to us accounts for all of the molecules in the chamber before and then after the reaction:

$$1.0797 * O_2 + 1.0979 * N_2 + 0.0028 * C_6H_6 + 0.021 * O_2 \rightarrow 0.0168 * CO_2 + 0.0084 * H_2O + 1.0797 * O_2 + 1.0979 * N_2$$

Although the extra oxygen and nitrogen cancel out, it is important to keep in mind that they are there because their enthalpies are different before and after the reaction.

The First Law of Thermodynamics states that: $U_{products} - U_{reactants} = Q - W$

Since we assumed adiabatic combustion with no work involved, Q and W are zero. It is also useful to write the equation in molar basis:

$$\sum_{i}^{Products} n_i \bar{u}_i - \sum_{j}^{Reactants} n_j \bar{u}_j = 0$$

Since each component behaves as an ideal gas, the respective specific internal energies can be expressed in terms of specific enthalpy, i.e. $\bar{u} = \bar{h} - R * T$

$$\sum_{i}^{Products} n_i \left(\bar{h}_i - R * T_P\right) - \sum_{j}^{Reactants} n_j \left(\bar{h}_j - R * T_R\right) = 0$$

The enthalpy values in the tables are given relative to some arbitrary datum state where the enthalpy is set to zero. This approach is satisfactory for evaluations involving differences in enthalpy values between states of the same composition, for then arbitrary datums cancel. However since reactants disappear and products are formed, differences cannot be calculated for all the substances involved. Therefore what follows is used.

An enthalpy datum for reacting systems is established by assigning arbitrarily a value of zero to the enthalpy of the stable elements (usually diatomic gases and carbon) at a state called the standard reference state and defined by STP. For instance O_2 and N_2 at STP will have enthalpy of zero. Using this information and spectroscopic data it is possible to come up with enthalpies for other compounds at standard state. Where a particular enthalpy value equals the energy released or absorbed as a compound is formed from its elements (the compound elements all being at STP). This is known as the enthalpy of formation for a compound, $\bar{h}_f^\circ$.

The specific enthalpy of a compound at a state other than the standard state is found by adding the specific enthalpy change $\Delta\bar{h}$ between the standard state and the state of interest to the enthalpy of formation:

$$\bar{h}(T,p) = \bar{h}_f^\circ + \left[\bar{h}(T,p) - \bar{h}\left(T_{ref}, p_{ref}\right)\right] = \bar{h}_f^\circ + \Delta\bar{h}$$

Using these considerations we rewrite the energy balance:

$$\sum_{i}^{Products} n_i \left(\left(\bar{h}_f^\circ + \Delta\bar{h}\right)_i - R * T_P\right) - \sum_{j}^{Reactants} n_j \left(\left(\bar{h}_f^\circ + \Delta\bar{h}\right)_j - R * T_R\right) = 0$$

$$\sum_{i}^{Products} n_i \left(\bar{h}_f^\circ + \Delta\bar{h}\right)_i - \sum_{j}^{Reactants} n_j \left(\bar{h}_f^\circ + \Delta\bar{h}\right)_j - R * T_p * \sum_{i}^{Products} n_i + R * T_R * \sum_{j}^{Reactants} n_j = 0$$

$$\left\{0.0168 * \left(\bar{h}_f^\circ + \Delta\bar{h}\right)_{CO_2} + 0.0084 * \left(\bar{h}_f^\circ + \Delta\bar{h}\right)_{H_2O} + 1.0797 * \left(\bar{h}_f^\circ + \Delta\bar{h}\right)_{O_2} + 1.0979 * \left(\bar{h}_f^\circ + \Delta\bar{h}\right)_{N_2}\right\}_P - \left\{0.0028 * \left(\bar{h}_f^\circ + \Delta\bar{h}\right)_{C_6H_6} + 1.1007 * \left(\bar{h}_f^\circ + \Delta\bar{h}\right)_{O_2} + 1.0979 * \left(\bar{h}_f^\circ + \Delta\bar{h}\right)_{N_2}\right\}_R - R * T_p * (2.2028) + R * T_R * (2.2014) = 0$$

Recall, that for N_2 and O_2 $\bar{h}_f^\circ$ is zero. Also since $\Delta\bar{h}$ is only a function of temperature in this case, and the change in temperature for all the reactants is zero, so $\Delta\bar{h}_{\text{reactants}} = 0$. Therefore, the energy balance above reduces to:

$$\left\{0.0168 * \left(\bar{h}_f^\circ + \Delta\bar{h}\right)_{CO_2} + 0.0084 * \left(\bar{h}_f^\circ + \Delta\bar{h}\right)_{H_2O} + 1.0797 * \left(\Delta\bar{h}\right)_{O_2} + 1.0979 * \left(\Delta\bar{h}\right)_{N_2}\right\}_P - \left\{0.0028 * \left(\bar{h}_f^\circ\right)_{C_6H_6}\right\}_R - R * T_p * (2.2028) + R * T_R * (2.2014) = 0$$

And finally,

$$T_p = \frac{\left\{0.0168 * \left(\bar{h}_f^\circ + \Delta\bar{h}\right)_{CO_2} + 0.0084 * \left(\bar{h}_f^\circ + \Delta\bar{h}\right)_{H_2O} + 1.0797 * \left(\Delta\bar{h}\right)_{O_2} + 1.0979 * \left(\Delta\bar{h}\right)_{N_2}\right\}_P - \left\{0.0028 * \left(\bar{h}_f^\circ\right)_{C_6H_6}\right\}_R + R * T_p * (2.2014)}{2.2028 * R}$$

The final enthalpy values used are:

$$\left(\bar{h}_f^\circ\right)_{CO_2} = -393520\frac{J}{mol}$$

$$h_{298K}^{CO_2} = 9364\frac{J}{mol}$$

$$h_{500K}^{CO_2} = 17232\frac{J}{mol}$$

$$\left(\Delta\bar{h}\right)_{CO_2} = h_{500K}^{CO_2} - h_{298K}^{CO_2}$$

$$\left(\bar{h}_f^\circ\right)_{H_2O} = -241820\frac{J}{mol}$$

$$h_{298K}^{H_2O} = 9904\frac{J}{mol}$$

$$h_{500K}^{H_2O} = 16477\frac{J}{mol}$$

$$\left(\bar{h}_f^\circ\right)_{C_6H_6} = 82930\frac{J}{mol}$$

$$h_{298K}^{O_2} = 8682\frac{J}{mol}$$

$$h_{500K}^{O_2} = 14460 \frac{J}{mol}$$

$$h_{298K}^{N_2} = 8669 \frac{J}{mol}$$

$$h_{500K}^{N_2} = 14285 \frac{J}{mol}$$

To calculate T_P, an iterative process is followed. The result is $T_p \approx 500$ K = 227 °C.

The ideal gas law is used to find the final pressure that results from this temperature:

$$P_{final} = \frac{n_p * R * T_p}{V_{chamber}} = 169840\ Pa \cong 1.7\ atm$$

Based on this analysis we can conclude that the adiabatic combustion of benzene inside the chamber will produce a very noticeable effect. However, these numbers do not suggest a dangerous explosion could happen. The steel chamber and even the glass window within it, have been able to withstand higher pressures and higher temperatures.

It is important to point out that this worst case scenario is a significant overestimate of the situation because firstly, the complete combustion of benzene does not happen. It is well known that many significantly less exothermic by-product reactions occur during the combustion of benzene. Secondly, the assumed adiabatic conditions are an idealization because the relatively cold steel chamber may quickly absorb heat.

Methods for future work: Liquid benzene source

The flash point temperature is the temperature above which sufficient flammable vapor is generated to exceed the lower flammability limit. Therefore this information can be used to assess the level of risk of explosion in an experiment. This temperature can be found using the Clausius-Clapeyron equation and enthalpy of vaporization [145].

The meaning of ΔH_c and K

$C_6H_6 + 7.5O_2 \rightarrow 6CO_2 + 3H_2O$

Heat of combustion = enthalpy of reactants – enthalpy of products

$\left(\bar{h}_f^\circ\right)_{C_6H_6} = 82930 \frac{J}{mol}$

$(\bar{h}_f^o)_{O2} = 0$

$\left(\bar{h}_f^\circ\right)_{CO_2} = -393520 \frac{J}{mol}$

$\left(\bar{h}_f^\circ\right)_{H_2O} = -241820 \frac{J}{mol}$ - for water in gaseous phase

ΔH_c = [6(-393520)+3(-241820)-82930]/4.184 = -753 kcal/mol

This is the net heat of combustion for benzene

Net heat of combustion – water formed in gaseous state

Gross heat of combustion – water formed in liquid state

The latent heat of vaporization for water is 10.5 kcal/mol ($H_2O_{(l)} \rightarrow H_2O_{(g)}$)

(net heat of combustion) = (gross heat of combustion) – (latent heat of vaporization)

From definitions for Larry's first rule we saw:

$K=LFL(mol\%)\bullet\Delta H_C/100 \cong -10.5 \mp 0.5$ (kcal/mol mixture)

Where LFL for benzene is 1.3%

Calculating exact K for benzene we get:

$K_{benzene}$ = (1.3%)*(-753 kcal/mol)/100 = -9.85 (kcal/mol mixture)

This is indeed close to -10.5 (kcal/mol mixture)

APPENDIX III: Procedure for filling test chamber with benzene

Filling test chamber with benzene:

Before beginning it is imperative to check that the plastic hose is securely connected to the outlet of the scroll pump (P1) and also that it enters deep into the Exhaust tube at the ceiling.

The following description of steps assumes that the chamber (when closed) and all the gas lines connected to it initially have room air in them. It is further assumed that all the valves are initially closed.

Procedure with reference to Figure A3.1:

1) Open right angle valve (V1)
2) Turn on the scroll pump (P1) and monitor the pressure reading on the analog thermocouple gauge until it drops below 200 microns (200 mTorr or 2E-1 Torr). Note: This may take around 10 minutes if the pump has not been used in a while.
3) Now turn on the turbo pump (P2). If the pressure drops below 1E-5 Torr in the first hour then the system is probably functioning normally, and it is safe to begin a bakeout. After the bakeout let the system cool down to room temperature.
4) Close the right angle valve (V1) and turn off the turbo pump (P2). Wait for ~10 minutes to let the turbo pump rotor slowdown.
5) Open valves V3,V4,V5,V6,V7 and regulators R1,R2 to let the scroll pump suck out the room air from those gas lines. Wait until the pressure reading in the gas lines drops below 100 microns on the analog thermocouple gauge. Next, wait for additional 1 minute and close valve V7.
    a. Make sure that the reading on the Bourdon pressure gauge (G2) is at the minimum
    b. Make sure that the readings in both Bourdon pressure gauges at the regulators R1 and R2 are at the minimum
6) Purging the lines 3 times with N_2:
    a. Close V6 and R2, then open V8
    b. Adjust regulator R2 such that the pressure reading on the left Bourdon gauge is ~30 psig
    c. Open V6 to fill the gas lines with N_2 until G2 reads ~0 psig, then close V8.
    d. Open V7, and wait for 1 minute after G1 reads below 100 microns
    e. Close V7
    f. Open V8 to fill chamber with N_2 again (second time) until G2 reads 0 psig; then close V8 and repeat steps *d* and *e*.
    g. Repeat step *f* once more. At the end of this step all the lines should be empty.
7) Now we are ready to fill the chamber with benzene:
    a. Close V5 (just in case)
    b. Close V3
    c. Close R1 completely
    d. Open V9 to let benzene flow up to R1

    e. Slowly open R1 such that the left gauge on the regulator reads -20 psig (can increase R1 up to -7 psig if larger flow rate is desired)
    f. It is important to know that the check valve C1 will open if the pressure in the line is above atmospheric pressure.
8) Open V3 and the leak valve V2 to create a path between the gas lines and the evacuated chamber. Note that the amount of benzene entering the chamber can be further controlled by the leak valve.
    a. The amount of benzene in the chamber should not exceed -7 psig to make sure it does not leak out.
9) Close V2 (or V3) when the chamber has been filled to the desired level of benzene (e.g. -7psig).
10) Close V9 so that no more benzene is leaking from the cylinder
11) Clean the lines from benzene by purging them 4 times to the exhaust, while using N2 for refilling. This step is similar to step 6 (remember to open V5).
12) Testing of microswitches in benzene environment can be done now.
13) To clean out the benzene from the chamber (and the segment from V3 to V2 if the leak valve remained open in step 10), it would be necessary to purge the chamber 4 times with N_2.

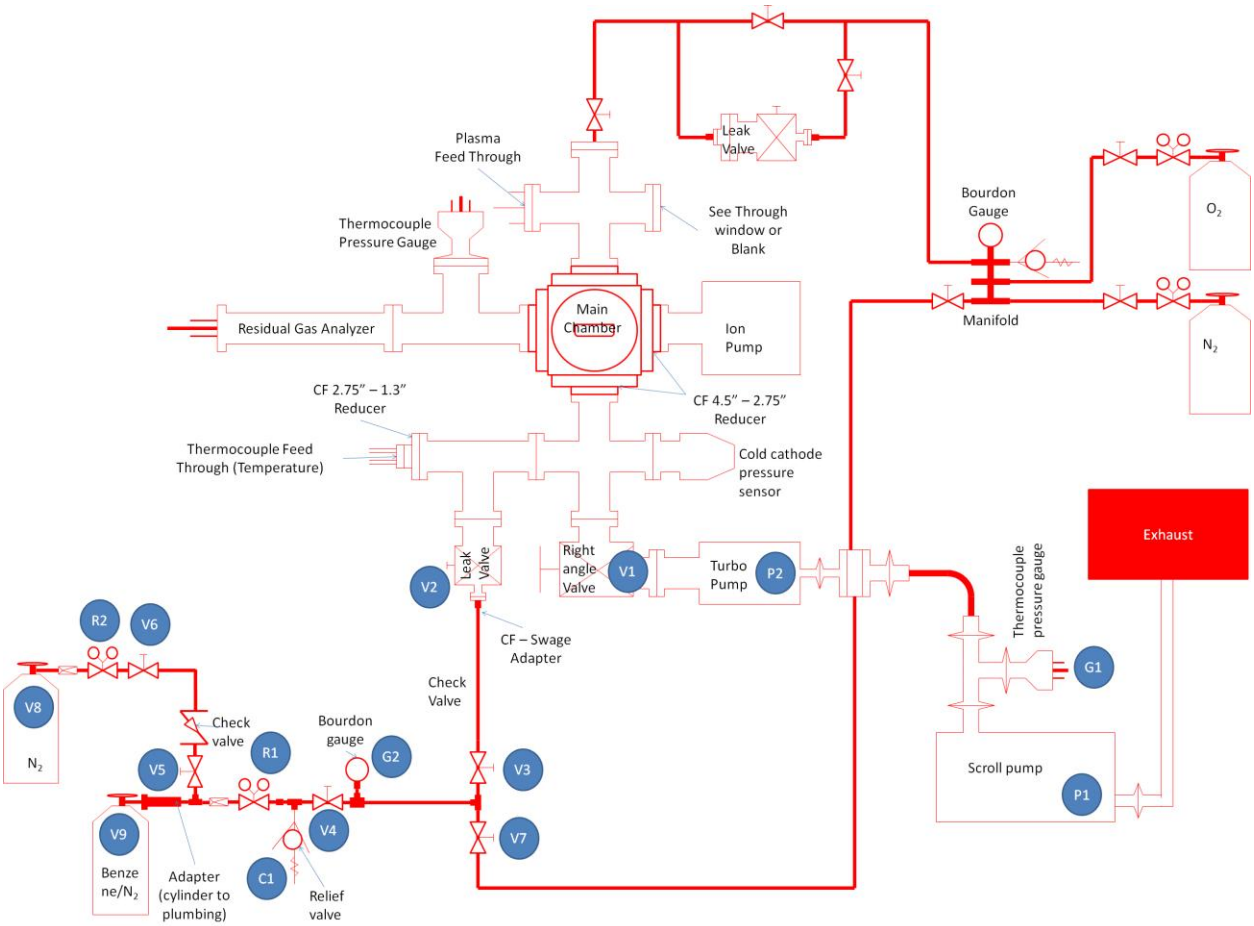

Figure A3.1: Chamber schematic.

APPENDIX IV: Chip layouts for Pt and RuO_2 switches

The layout of the Pt switches on a chip integrated in the ceramic 24 pin dual inline package (DIP) is shown in **Figure A4.1**. The six wire-bonded switches are labeled S1 through S6 on the chip. Each switch is shown to have four wires attached to each of its four pads, where the outer wires enable current transmission through the thermal actuator and the inner wires enable current transmission through the switch contacts. Other switches and components are present on the chip but are not wire-bonded to anything.

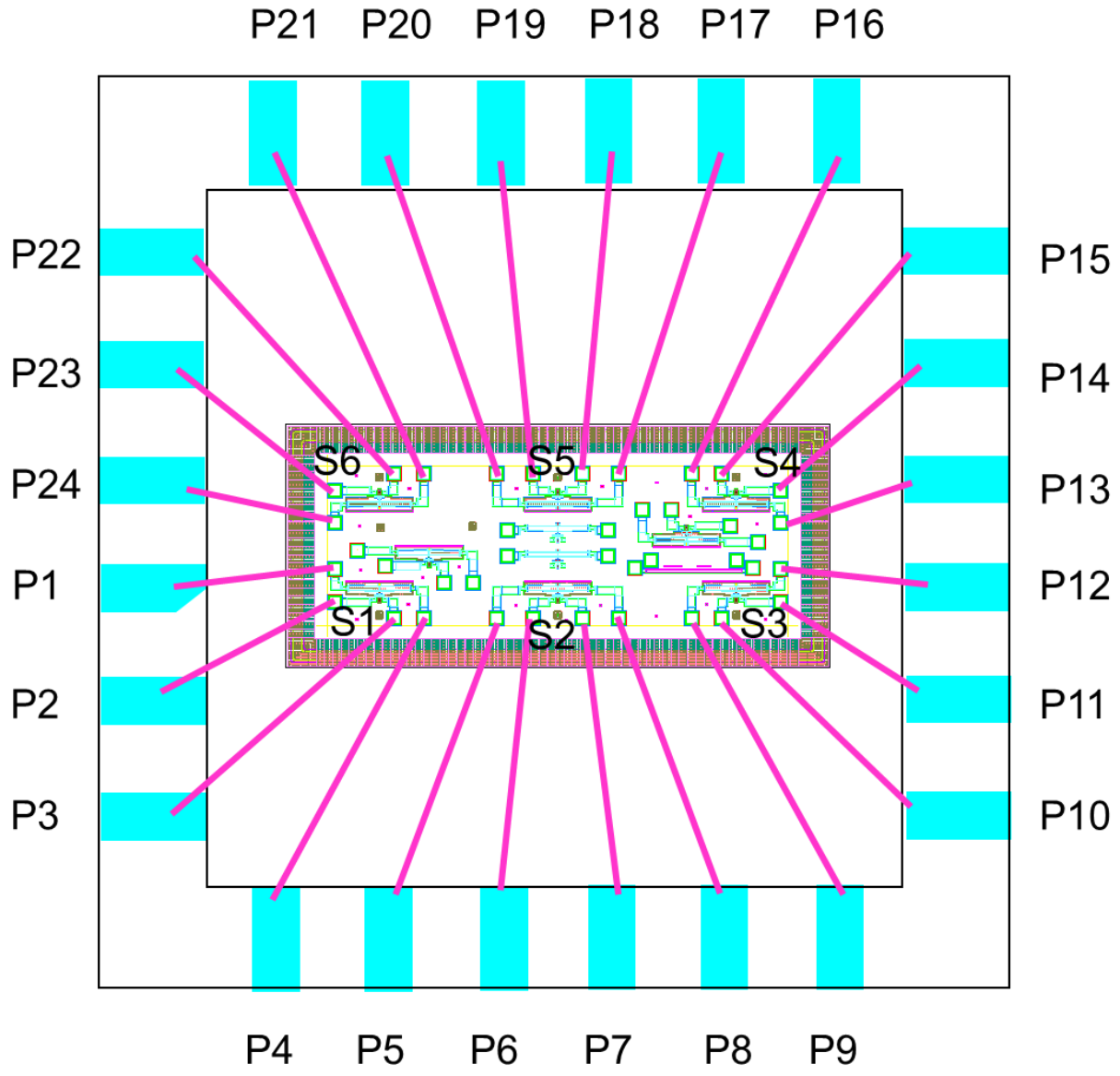

Figure A4.1: Layout of six Pt switches on a chip where each of them is wire-bonded to the DIP. Each of the switches is labeled S1 through S6.

The "open-state" switch contact gap spacing for each of the six devices is labeled in the small text boxes designating the switches, as shown in **Figure A4.2**. The devices located near the corners of the chip (S1,S3, S4, S6), have a gap spacing of around 6 microns. While the devices in the center of the chip (S2 and S5), have a much smaller gap spacing of around 3 microns. The top view optical images below the chip schematic in **Figure A4.2** shows the typical gap spacing along each row of devices. Notice how the central image has a shorter gap. It turns out that this lower gap spacing is a result of the bonding of the chip (with a 80 Sn-20Au solder) to the bottom of the DIP. When the chip is released from the DIP, all six devices have nearly identical gap sizes of 6 microns. The optical image at the bottom center of **Figure A4.2** shows the gap spacing of a central switch on a chip that was lifted from the DIP. Therefore it is presumed that the solder bond causes some curvature in the chip that in turn reduces the gap size of the devices in the middle.

The load applied by the contact bar on the opposing trace contacts for each of the six switches (labeled S1 through S6) during switch closure is shown above the small rectangular text boxes with the spacing gap spacing information. The devices in the lower row (S1 through S3), which have two pairs of thermal actuator legs, experience loading of around 200 μN. Whereas devices in the upper row (S4 through S6) experience twice as much load because they have twice as many thermal actuator legs. The fact that the upper row devices have twice as many thermal actuator legs is illustrated with the double-framed rectangle in **Figure A4.1**. It is also worth noting that the devices in the central column (S2 and S5), which have the lower contact gap spacing in the open state, also experience lower loading. These loads were calculated for 8 V applied across the thermal actuators using an ANSYS program written at Sandia National Laboratories [100].

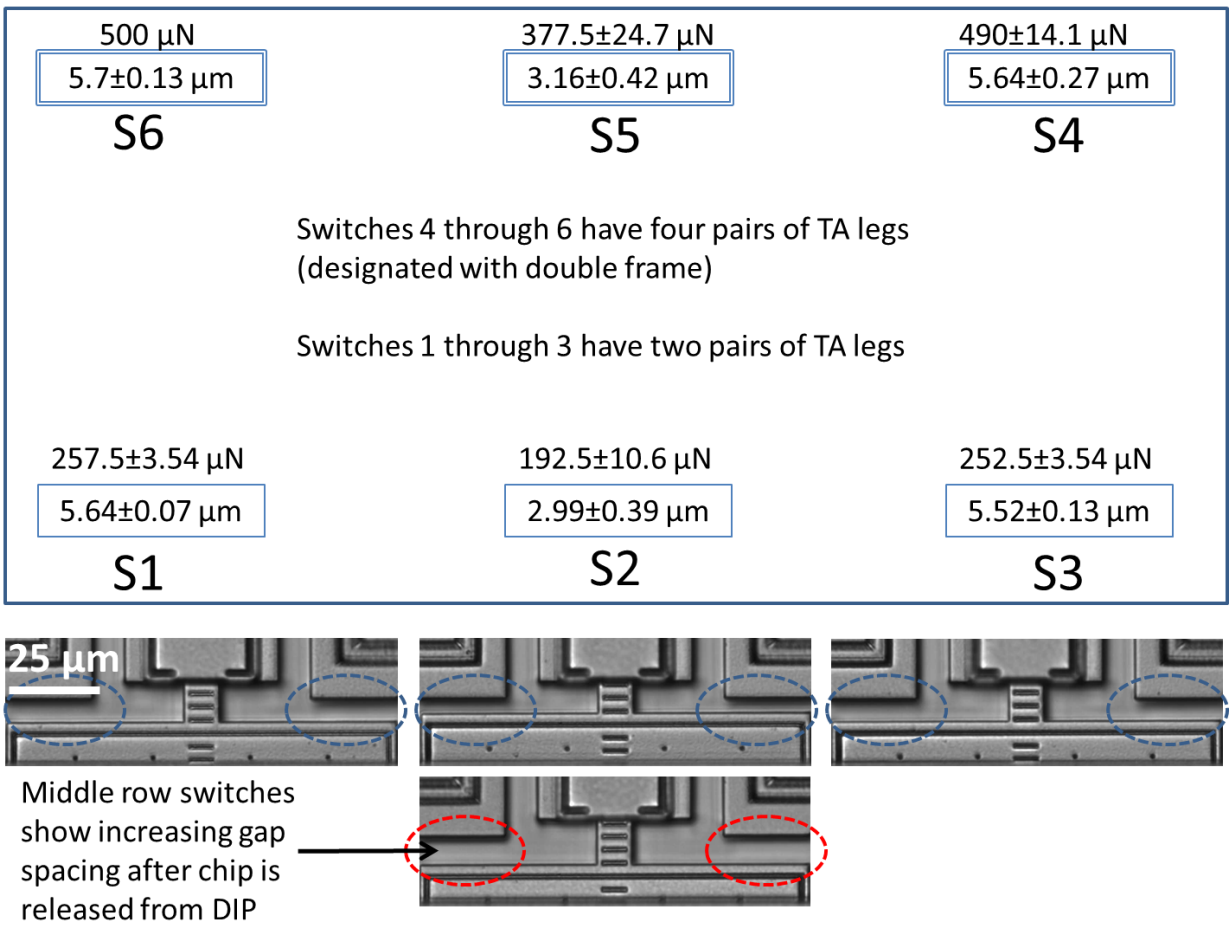

Figure A4.2: Contact gap spacing of each Pt switch in the open-state is shown in the small text boxes. The load applied by the contact bar on the trace contacts when the switches are closed is shown above those text boxes.

The layout of the RuO_2 switches on a chip integrated in the DIP is shown in **Figure A4.3**. This layout is different from the Pt chip. Notably 16 switches are on the chip yet only 6 of them are wire-bonded.

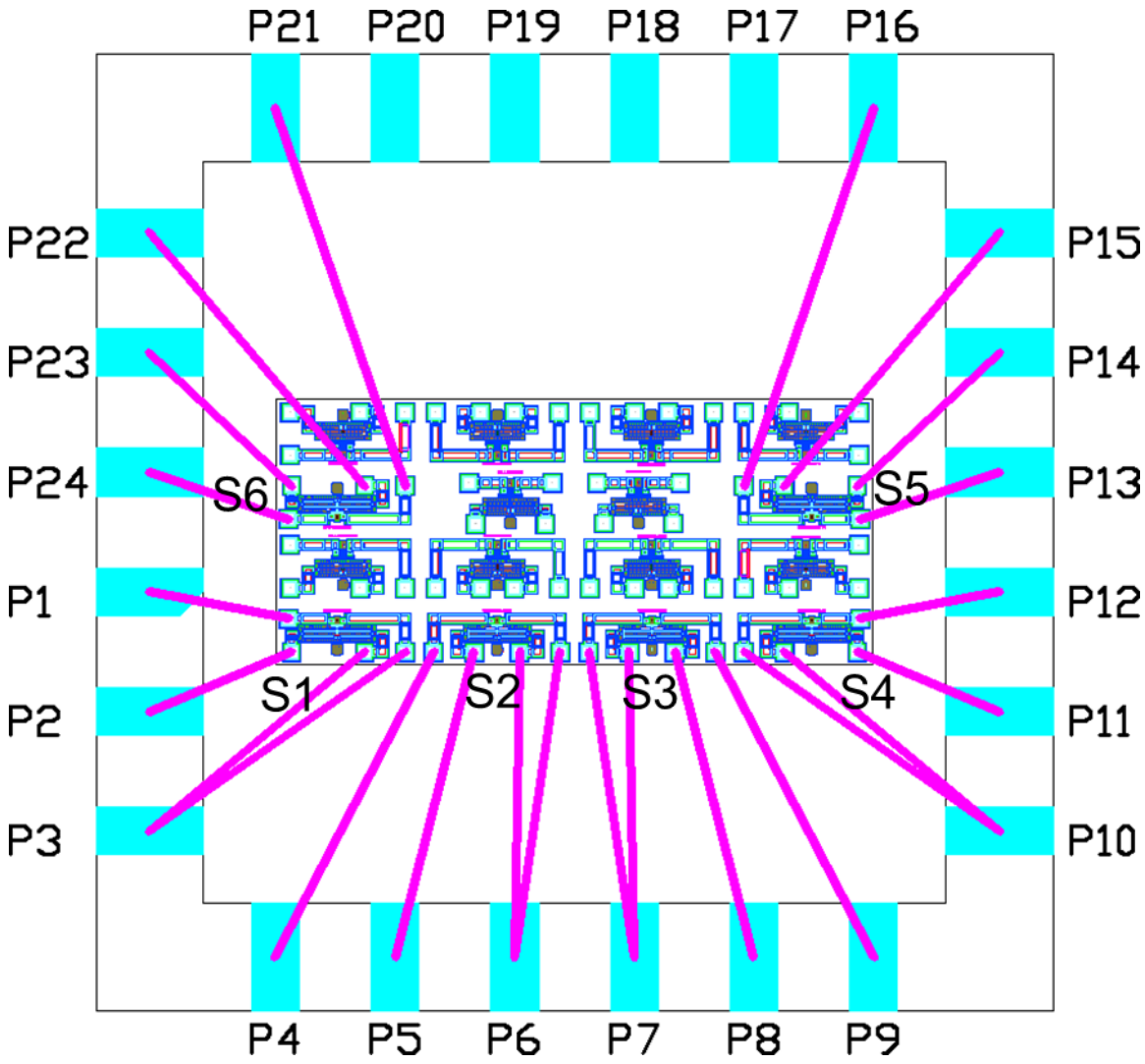

Figure A4.3: Layout of six wire-bonded RuO_2 switches on a chip where each of them is wire-bonded to the DIP. Each of the switches is labeled S1 through S6.

The schematic in **Figure A4.4** shows the gap spacing of each of the six wire-bonded switches when they are in the open state. The outer switches (S1, S4, S5, and S6) have a gap of about 8 microns, while the inner switches (S2 and S3) have a gap of about 6 microns. The solder bond between the chip and the DIP could also be responsible for the discrepancy between the gap size of outer and inner switches.

The load applied by the contact bar on the contact traces is around 200 μN for the outer switches and nearly 400 μN for the inner ones, as shown in **Figure A4.4**. Notably, the inner switches have thermal actuator leg length of 300 μm (hence the bold frame on the text boxes above S2 and S3) as compared to the 350 μm length in all other switches (it is also 350 μm for all Pt switches). This helps explain why the inner switches experience a higher load. Again, all loads were estimated using ANSYS.

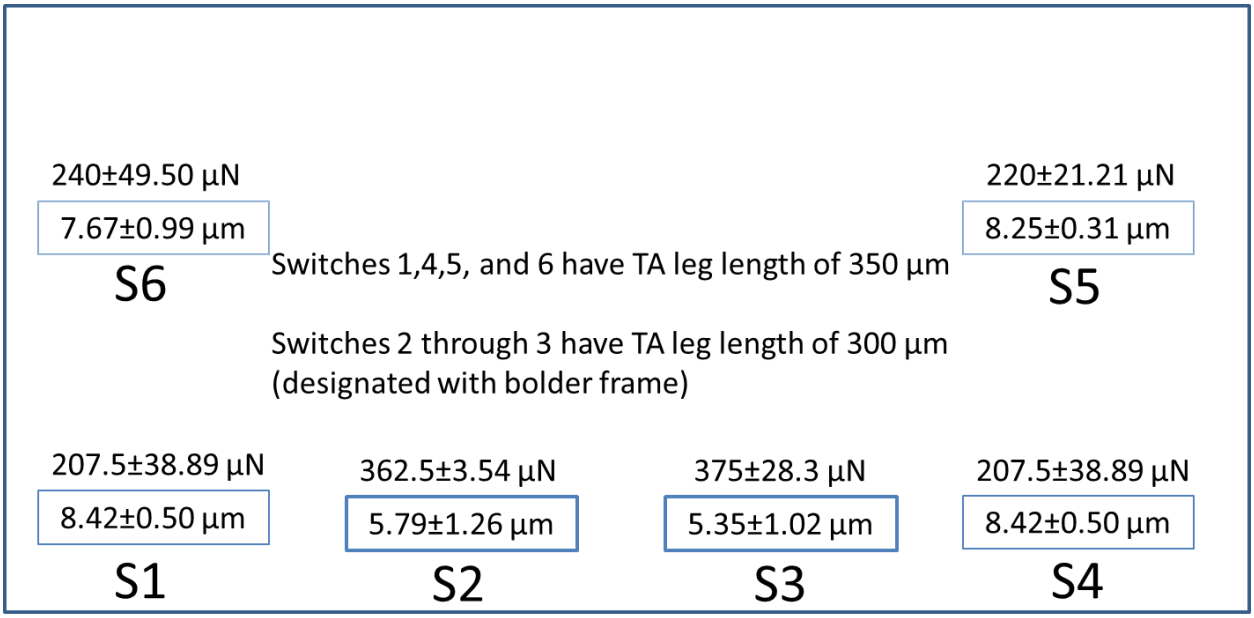

Figure A4.4: Contact gap spacing of each RuO_2 switch in the open-state is shown in the small text boxes. The load applied by the contact bar on the trace contacts when the switches are closed is shown above those text boxes.

For all load and gap displacement numbers obtained in this appendix, two chips with each coating were analyzed, so each listed value is the average for the two switches of the same type.

APPENDIX V: Finding minimum thermal actuator voltage to close the switch and proof of cold switching

Part I: Finding minimum voltage to close the switch

Upon the discovery of the contact spallation problem in the RuO_2 coated switches, we attempted to mitigate the challenge by utilizing lower contact loads. To do this, we first experimentally deduced the minimum thermal actuator voltage (V_{TA}) required to close the switch. This was done by increasing V_{TA} with 0.5 V increments starting at 4 V and stepping through to 9 V, while measuring the contact resistance R at each increment. Such a procedure was performed on three different switches on the same chip, as shown in **Figure A5.1**. The switch designated S2 has the shorter 300 µm TA leg length and the higher contact force than switches S3 and S4 (which have the 350 µm TA leg length). The minimum voltage required to close S2 is 6 V because that is when R is first measurable; however 6.5 V is needed to close S3 and S4. For each of the switches, R is reduced as V_{TA} is increased, presumably because better electrical contact is established.

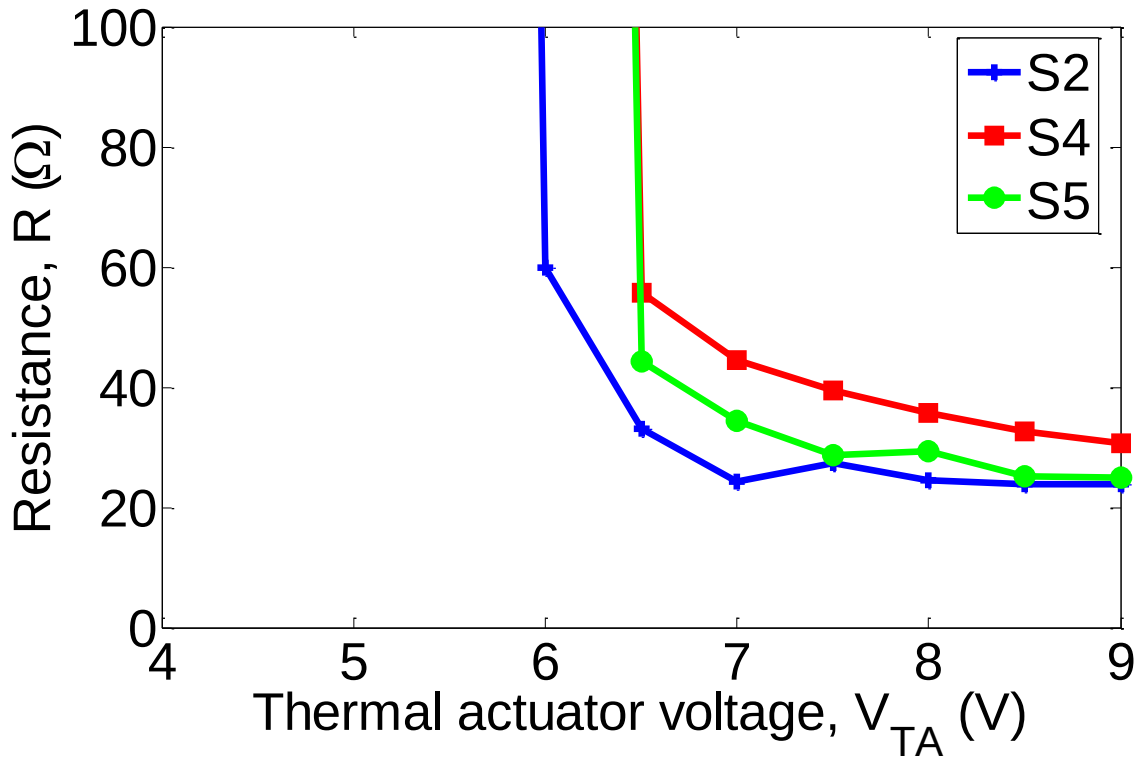

Figure A5.1: Contact resistance plotted as a function of thermal actuator voltage used to close the switch. The switch can be considered closed when the contact resistance is finite (i.e. when the data point is within the scale of the graph).

The Pt-coated switches also show a similar dependence of contact resistance on the thermal actuation voltage, that is, the resistance decreases with increasing voltage. For the devices on the corners of the chip (as shown in **Figure A4.2**), at least 5.8 V are required to close the switch. While the devices at the chip center (again **Figure A4.2**) 5 V can close the switch. The voltage required to close the central Pt switches is significantly lower than for any RuO_2 devices because the former have somewhat smaller open state contact separation gaps (compare **Figure A4.2** and **Figure A4.4**). In other words, switches with smaller open state contact separation gaps require lower actuation voltages.

Part II: Proof of cold switching

In order to have cold switching, the Labview program instructs the voltage across the switch contacts to be applied *after* applying the thermal actuator voltage, and to be removed *before* removing the thermal actuator voltage. However, it takes time for the thermal actuator to close the switch and it is important to verify that this indeed happens before the contact voltage is applied. Likewise, it is important to verify that the contact voltage is removed before the thermal actuator voltage is removed.

Referring to **Figure 2.3**, recall that the actuation voltage across the thermal actuator legs (V_{TA}) is 8 V while the 5 V contact voltage ($V_{contact}$) is applied across the electrical contacts and an in series 500 Ω current limiting resistor. The real voltage across the contacts is V_{out} and its magnitude depends on the value of the contact resistance, $R_{contact}$. As was detailed in reference [31], during each actuation cycle, $V_{contact}$ was applied once *during* the time interval the switch was closed to measure the $R_{contact}$ and once again when the switch was open to check that it is indeed open (since otherwise a low resistance would be measured). Hence during each actuation cycle, a voltage versus time plot would show a single square wave peak for V_{TA} and two square wave peaks for V_{out}. Using an oscilloscope, such plots were obtained for a variety of V_{TA} voltage settings shown in **Figures A5.2 through A5.4**.

The plots in **Figures A5.2 through A5.4** can confirm that cold switching is indeed performed as long as V_{TA} is high enough to close the switch. In these plots, the x-axis represents time where the horizontal side of each square is one ms. The y-axis is voltage and the vertical side of each square represents 5 V. Channel one measures the voltage-time response of the thermal actuator, while channel two measures the voltage-time response of the signal across the contact. Each cycle lasts 4 ms since the actuation frequency is 250 Hz.

The idea is that when $R_{contact} \ll 500\ \Omega$, it should NOT be possible to see $V_{out} \cong 5\ V$ AS LONG AS V_{TA} is applied. When $V_{contact}$ is set to 5 V, the V_{out} measurement would read anything near 5 V *only* when the switch is open. This can happen during the measurement interval (within an actuation cycle) when V_{TA} is set to zero (see **Figure A5.2**), or if $V_{TA} > 0\ V$ but the switch remains open (see **Figure A5.4**). The thing to watch out for is a large drop in the V_{out} voltage *at the beginning of the measurement interval* when the V_{TA} voltage is applied. In that case, if V_{out} starts at a value close to 5 V and drops down to a much lower value (e.g. 0.5 V, depending on $R_{contact}$), it means that the contact voltage was applied before the switch had enough time to close. In that case, it would be hot switching rather than cold switching.

In **Figures A5.2**, it can be seen that when V_{TA} is set to 8 V, V_{out} is always low and is roughly 0.5 V. While when V_{TA} is set to 0 V, V_{out} is always near 5 V. Also when plots of channels one and two were superimposed upon each other (see lower oscilloscope image in **Figures A5.2**), it is clearly seen that when the switch is in the closed state (i.e. $V_{TA} = 8\,V$), V_{out} is applied only within the interval that V_{TA} is applied. Therefore we definitely have cold switching in all of the experiments where cold switching was intended in this thesis. The reason why $V_{contact}$ is applied 0.6 ms after V_{TA} is applied is to ensure enough time is given for the switch to close before attempting to pass current through it. Even though $V_{contact}$ is removed just 1 ms before V_{TA} is removed, there is no possibility for hot switching (and arcing), so this smaller time interval does not affect the experiment.

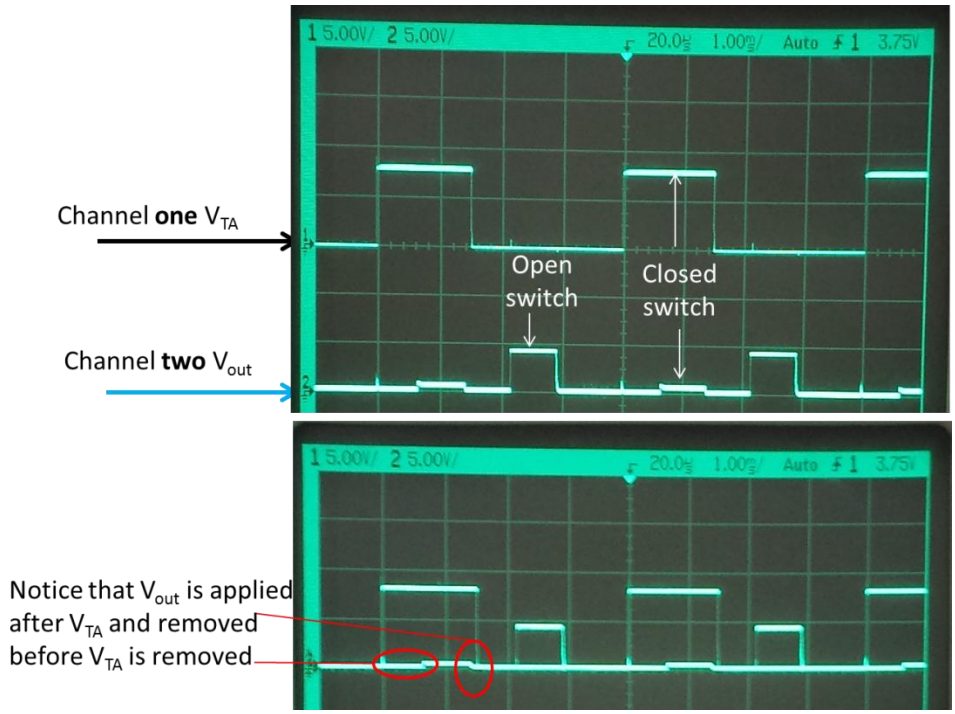

Figure A5.2: The applied voltages are $V_{TA} = 8\,V$ and $V_{contact} = 5\,V$. The top oscilloscope image illustrates V_{TA} in channel one and V_{out} in channel two. The x-axis is time, where the horizontal side of each square is 1 ms. The y-axis is voltage, where the vertical side of each square is 5 V. Each switch cycle lasts 4 ms. The lower oscilloscope image shows the signals from the two channels superimposed on each other to better illustrate the relative time each signal is applied.

The lowest V_{TA} at which the switch discussed above would close was 5.8 V. Again, V_{out} was much lower than 5 V during the entire interval when the switch was closed, as shown in **Figure A5.3**. This means that cold switching occurred in this case as well. The V_{out} value when the switch is closed is ~ 1V here, which is about twice higher than in **Figure A5.2**. This is because the contact resistance in the present case is twice as high ($R_{contact} = 50\,\Omega$ in **Figure A5.2** while $R_{contact} = 100\,\Omega$ in **Figure A5.3**).

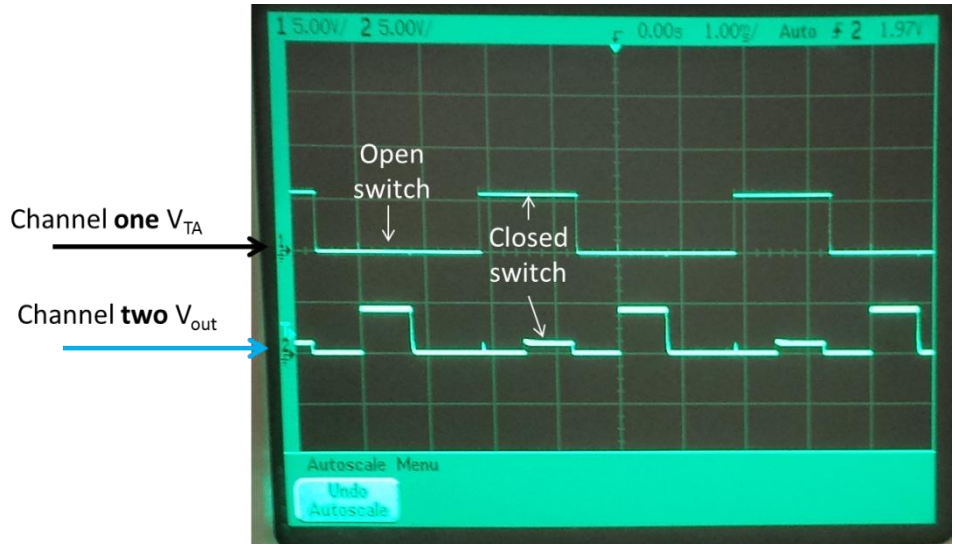

Figure A5.3: The applied voltages are $V_{TA} = 5.8\,V$ and $V_{contact} = 5\,V$. The top oscilloscope image illustrates V_{TA} in channel one and V_{out} in channel two. The x-axis is time, where the horizontal side of each square is 1 ms. The y-axis is voltage, where the vertical side of each square is 5 V. Each switch cycle lasts 4 ms.

When V_{TA} was set to 5 V, it was too low to close the switch. Hence, during the interval when V_{TA} was applied (i.e. when the switch was supposed to close) and during the interval when V_{TA} was set to 0 V, $V_{out}$was close to 5 V ($= V_{contact}$).

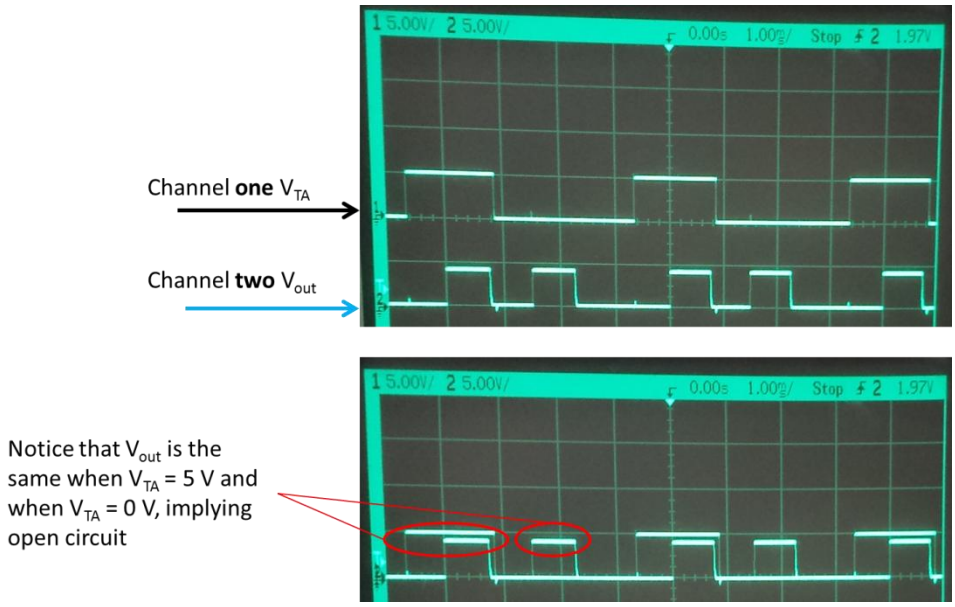

Figure A5.4: The applied voltages are $V_{TA} = 5\,V$ and $V_{contact} = 5\,V$. The top oscilloscope image illustrates V_{TA} in channel one and V_{out} in channel two. The x-axis is time, where the horizontal side of each square is 1 ms. The y-axis is voltage, where the vertical side of each square is 5 V. Each switch cycle lasts 4 ms. The lower oscilloscope image shows the signals from the two channels superimposed on each other to better illustrate the relative time each signal is applied.

It is important to point out that the V_{out} switches to a high impedance (Z) state when $V_{contact}$ goes to zero. To generate the plots of **Figures A5.2 through A5.4** it was therefore necessary to connect a 2500 Ω resistor in parallel with the electrical contacts in order to discharge the residual charge on the contacts when $V_{contact}$ goes to zero (the discharge cannot otherwise happen through the contacts because of an open circuit). In the absence of the 2500 Ω resistor, asymmetry in the square wave contact signal will happen because of leakage and a large RC time constant, since $R = Z$ is large. This does not affect the conclusion that cold switching occurs in our experiments because regardless of whether the 2500 Ω resistor is present, during the switch closure interval, V_{out} climbs from 0 V to 0.5 V 6 ms *after* V_{TA} is set to 8 V, and V_{out} reduces to 0 V 1 ms before V_{TA} is set to 0 V.

APPENDIX VI: Contact bar velocity estimate

A first order analysis for the average velocity of the contact bar as the switch closes follows. It is assumed that the thermal resistance is zero (time for heat to propagate is negligible) and that the time for the leg temperature to rise dominates the inertial response of the device.

Using the Pythagorean Theorem with reference to **Figure A6.1**, upon heating, it can be shown that the change in length of the TA legs for a displacement δ is

$$\Delta L = L_H - L_C \approx \frac{L}{2}\left(\frac{\delta}{L}\right)^2\left(1+\frac{2\delta_o}{\delta}\right) \quad , \qquad \text{(i)}$$

where L_C and L_H are the "cold" and "hot" lengths of the TA leg, L is the *horizontal*-distance from the pad to the shuttle connection, δ_o is the TA leg offset, and δ is the distance the shuttle moves (see **Figure A6.1**). The effective temperature of the TA leg is then determined by

$$\Delta T = \Delta L/(L_C\alpha) \quad , \qquad \text{(ii)}$$

where α is the temperature-averaged thermal coefficient of expansion.

The power injected into the TA legs is I^2R_{leg}, where I is the current and R_{leg} is the electrical resistance of a single leg. Assuming perfect thermal insulation, the change in heat of a TA leg is

$$\Delta H = \rho V c \Delta T = I^2 R_{leg} t_{cl} \quad , \qquad \text{(iii)}$$

where c is the specific heat capacity of polysilicon and m=ρV is the TA leg mass. Solving for t_{cl}, the time to close, gives

$$t_{cl} = \frac{\rho V c}{(I^2R)}\,\frac{1}{2\alpha}\,\frac{L}{L_c}\left(\frac{\delta}{L}\right)^2\left(1+\frac{2\delta_o}{\delta}\right) \quad . \qquad \text{(iv)}$$

For silicon ρ_{Si}=2330 kg/m^3. The leg volume is V=length•area=350•(2.25•5+2•2+2.5•5)•10^{-18} m^3 =350•27.75•10^{-18} m^3 = 9.7125•10^{-15} m^3, so m=$\rho_{Si}V$=2.263•10^{-11} kg.

Also c_{Si}=707 J/kg•K, R_{leg}=275 Ω (measured), I=V/R_{leg}=4 V/275 Ω=14.545 mA (one half leg pair). We shall take α_{Si}=3.5•10^{-6}/K [147]. Also, given δ_o=4.0 μm and δ=5.6 μm, L_c≈L=350 μm, we arrive at t_{cl}=25 μs. Then the velocity estimate is v≈δ/t_{cl}=5.63 μm/25 μs=0.23 m/s.

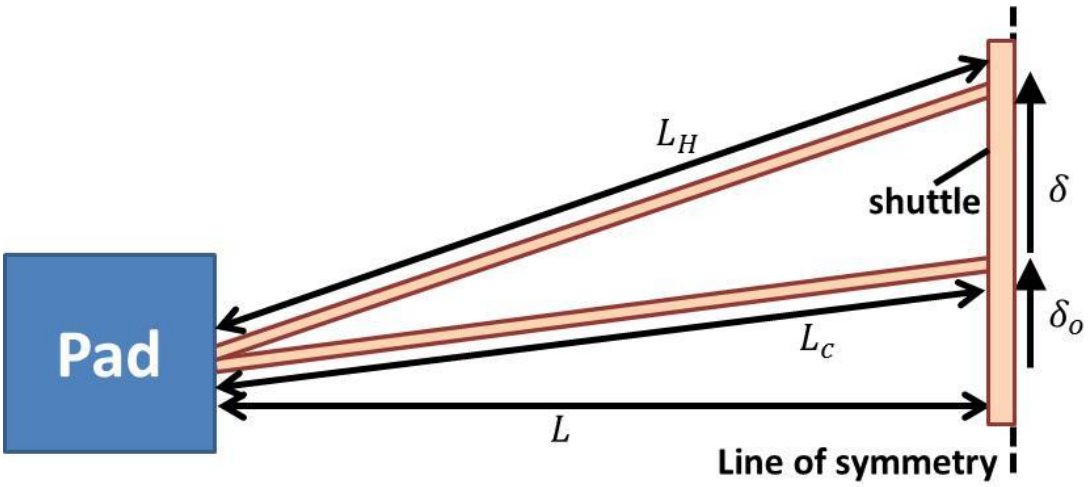

Figure A6.1: Thermal actuator geometry.